Reactive transport modeling in fractured media of nuclear glass for industrial application

Maria Repina

PSL UNIVERSITÉ PARIS

THÈSE DE DOCTORAT
DE L'UNIVERSITÉ PSL

Préparée à MINES ParisTech

Reactive transport modeling in fractured media of nuclear glass for industrial application

Modélisation du transport réactif dans les milieux fracturés de verre nucléaire d'intérêt industriel

Soutenue par
Maria REPINA
Le 27 février 2019

Ecole doctorale n° 398
Géosciences et Ressources Naturelles

Spécialité
Géosciences et géoingénierie

Composition du jury :

Tanguy, LE BORGNE Professeur, Université de Rennes 1	*Président*
Philippe, RENARD Directeur de recherche, Université de Neuchâtel	*Rapporteur*
Mickaele, LE RAVALEC Docteur HDR, IFP Energies Nouvelles	*Examinateur*
Frédéric, PLAS Directeur R&D, ANDRA	*Examinateur*
Vincent, LAGNEAU Professeur, HDR, MINES ParisTech	*Directeur de thèse*
Frédéric, BOUYER Ingénieur, CEA	*Examinateur*

MINES ParisTech | PSL

Remerciements

Tout d'abord je voudrais remercier Philippe Renard et Tanguy Le Borgne d'avoir accepté de relire cette thèse et d'en être les rapporteurs. La version définitive de ce mémoire a bénéficié de leur lecture très attentive et de leurs remarques précieuses. Je tiens à remercier Mickaele Le Ravalec d'avoir accepté d'être dans le jury et de m'avoir remarqué et encouragé dans le passé. Je remercie également Frédéric Plas d'avoir montré son intérêt pour ces travaux de recherche et d'avoir reconnu l'importance des résultats obtenus.

Je voudrais remercier tout particulièrement Vincent Lagneau qui m'a dirigé scientifiquement tout au long de ces trois années de thèse. Il a toujours été à l'écoute de mes nombreuses propositions, questions, doutes et il s'est toujours sincèrement intéressé à l'avancée de mes travaux. Les nombreuses discussions que nous avons eues ainsi que ses conseils sont pour beaucoup dans le résultat final de ce mémoire. Sa capacité d'analyse et son enthousiasme m'ont montré que le monde de la recherche pouvait être un univers passionnant. Enfin, ses relectures et corrections de cette thèse, souvent tard dans la nuit, ont été très appréciables.

Je remercie Frédéric Bouyer d'avoir encadré ce travail de thèse et de m'avoir accompagné dans ma vie d'immigrante russe dans le Sud de la France ☺. Il m'a aidé à m'intégrer dans la société, dans le labo et dans le monde des modélisateurs du transport réactif. Frédéric, merci de m'avoir laissé la liberté de m'exprimer en tant que chercheuse et de m'avoir permis d'orienter la thèse au cours de son déroulement. Merci pour votre ouverture d'esprit et pour votre soutien quand je faisais face à des difficultés scientifiques….

Vincent, Frédéric, cette thèse vous doit beaucoup. Merci pour votre audace dans la conception des objectifs de cette thèse, le résultat obtenu est un sourire aux audacieux !

Je remercie Pierre Frugier avec qui j'ai eu la chance de travailler sur l'application du modèle géochimique. Ses nombreuses connaissances en chimie et sa volonté de partager ces idées m'ont permis d'ouvrir la porte dans le monde de la géochimie.

Enfin, je remercie également toutes les personnes du labo LCLT pour leur gentillesse et leur disponibilité.

Je remercie tous les thésards du bâtiment 438 pour la bonne ambiance de travail et pour les bons moments passés ensembles. Entre autres Amreen, Sathya, Leila, Boris, Nicolas.

Amreen, thank you for your kindness and sincerity, I will always remember the evening I had to call you for the first time…. Certainly, every cloud has a silver lining !

L'équipe HR, merci de m'avoir accueilli lors de la préparation pour la soutenance.

Olivier Lerat, je ne peux pas ne pas me rappeler ton soutien. Merci pour ton amitié.

Maud, je vous serai toujours très reconnaissante, merci pour ce que vous avez fait pour nous. Ces moments que nous avons passés ensemble m'ont permis de décompresser, de prendre du recul, relativiser et, par conséquent, persévérer pour finir avec succès cette thèse.

Renaud, la réussite de ce travail est le résultat de ta patience et de ton attention. Merci d'avoir été présent et compréhensif. Cela signifie beaucoup pour moi.

Дорогие мои родители, низкий поклон вам за вашу любовь, уважение и безусловную поддержку. Даже будучи далеко, я никогда не чувствовала меня оставленной, вы разделили все взлеты и падения моей аспирантуры.
Лариса, Федор, не смею закончить эту главу, не поблагодарив вас. Ваша дружба, забота и поддержка служили тем незатухающим пламенем, что озаряло, бывало очень темные дни научных провалов и моих собственных смятений. Огромное спасибо за веру в меня.

RÉSUMÉ

Comprendre l'altération du verre nucléaire dans un réseau de fracture au sein d'un bloc de verre vitrifié est important pour la sûreté du conditionnement des déchets nucléaires (quantification des risques associés au relâchement des radionucléides). L'évaluation de la performance du stockage géologique des déchets nucléaires passe obligatoirement par la modélisation de l'altération aqueuse d'un bloc de verre nucléaire fracturé, l'échelle de temps envisagée (plusieurs milliers d'années) dépassant toute possibilité d'expérience directe. Cette thèse vise donc à combler le fossé entre les simulations d'écoulement et de transport à l'échelle du réservoir et la modélisation à l'échelle micrométrique des processus interfaciaux verre-eau, en apportant l'évaluation quantitative de la dégradation aqueuse du verre à l'échelle d'un bloc.

Pour aborder ce problème, les objectifs principaux de cette thèse ont été fixés comme suit : (i) la reproduction des résultats expérimentaux obtenus précédemment (pour quelques fractures modélisées de manière discrète en mode diffusif), (ii) l'analyse de l'impact des géométries de fractures sur la quantité de verre altéré pour quelques fissures modélisées de manière discrète, (iii) l'étude de la possibilité d'adaptation du modèle géochimique à la modélisation dans le cadre de l'approche milieu équivalent, (iv) la mise au point d'une méthodologie de caractérisation, (v) la modélisation géostatistique et géométrique de réseau de fractures à l'échelle d'un conteneur de verre, (vi) le calcul des paramètres équivalents diffusifs, hydrauliques et les paramètres qui contrôlent la cinétique de dissolution de verre, et au final, (vii) la modélisation de transport réactif à l'échelle d'un conteneur.

À titre illustratif, la méthodologie de la caractérisation de réseau fracturé proposée, basée sur le traitement des images, a été appliquée aux images bidimensionnelles (2D) de haute résolution de deux blocs de verre. Cette application a permis de mettre en œuvre à la fois les données directes obtenues par mesures des paramètres d'un réseau fracturé de verre vitrifié et les données indirectes explicatives issues des simulations thermomécaniques. L'application a abouti à la création de multiples réalisations de tessellation de réseaux fracturés équivalents qui ont ensuite été utilisées comme représentations physiques pour les calculs de la perméabilité équivalente, de la diffusion équivalente et des paramètres contrôlant la cinétique de dissolution de verre borosilicaté. L'évolution de la quantité de verre altéré obtenue en effectuant la modélisation de transport réactif appliquée à plusieurs réalisations de la tessellation de réseau fracturé équivalent a été comparée aux données expérimentales d'un essai d'altération aqueuse d'un conteneur non radioactif de verre nucléaire. Les résultats montrent que la méthodologie conçue offre une opportunité pour mieux comprendre l'impact de la fracturation sur l'altération aqueuse du verre vitrifié et constitue un outil fiable permettant de prendre en compte différents scénarios d'évolution du stockage.

MOTS CLÉS

Modélisation, corrosion du verre nucléaire, réseau de fractures, analyse d'images, changement d'échelle, milieu poreux équivalent

ABSTRACT

Understanding the alteration of nuclear glass in a fracture network of a vitrified glass block is important for the safe conditioning of nuclear waste (quantification of the risks associated with radionuclide release). Performance assessment of geological nuclear waste repositories entails modelling of the long-term evolution of the fractured nuclear glass block aqueous alteration, because the considered time scale, of several thousands of years, is beyond the range of any direct experimental perspectives. This dissertation aims then to bridge the gap between the reservoir-scale flow and transport simulations and the micron-scale modeling of the glass-water interfacial processes, by bringing the quantitative evaluation of the glass aqueous degradation at the block scale.

To tackle this issue, the main objectives of this thesis were fixed as follows: (i) reproduction of the experimental results previously obtained (for some fractures modeled in a discrete way in the diffusive mode),(ii) analysis of the impact of fractures geometries on the quantity of altered glass at the scale of some fractures modeled in a discrete way, (iii) investigation of the possibilities of the geochemical model adaptation for the equivalent homogenous modeling, (iv) establishment of a methodology for glass block fracture network characterization, (v) geostatistical and geometric modeling, (vi) calculation of the equivalent diffusive, hydraulic and glass dissolution kinetics controlling properties and (vii) upcoming reactive transport modeling at the scale of one canister.

As an illustrative example, the proposed image processing-based fracture network characterization methodology was applied to two-dimensional (2D) high-resolution images of two blocks of vitrified glass. This application brought into service both hard data obtained by direct measurement of the fracture network and soft physics-based explanatory data and resulted in the creation of multiple realizations of fracture network equivalent tessellation that were further used as physical representation for the calculation of the equivalent hydraulic, diffusive, and alteration kinetics - controlling properties. The evolution of the quantity of altered glass obtained by conducting reactive transport modeling applied to several realizations of the equivalent fracture network tessellation was compared with the experimental data of the aqueous alteration test of a non-radioactive full-scale nuclear glass canister. The results show that implementation of the devised procedure presents an opportunity for better understanding the impact of fracturing on aqueous alteration of borosilicate glass and provides a reliable tool enabling different scenarios of repository evolution to be accounted for.

KEYWORDS

Modeling, nuclear glass corrosion, fracture network, image analysis, upscaling, equivalent porous medium

Chapter 1: Introduction

CHAPTER 1: INTRODUCTION

List of figures

CHAPTER 1: INTRODUCTION

List of tables

CHAPTER 1: INTRODUCTION

Résumé du chapitre

Dans ce chapitre, les aspects liés au contexte du stockage de déchets nucléaires de haute activité à vie longue sont présentés. Ensuite, le procédé de la fabrication des conteneurs de verre vitrifié est exposé de manière succincte et la question de la fracturation du verre engendrée par son refroidissement dans le conteneur inox est abordée. Les questions scientifiques et les objectifs principaux de cette thèse sont détaillés. Ce chapitre se termine par la description de la structure de ce manuscrit.

1. Introduction

1.1. Background and Motivations

In the history of humanity the demand for energy has never been stronger than today. Even if in 2016 growth in energy consumption amounted to only half the average rate seen over the previous 10 years (Figure 1-1), it is still positive.

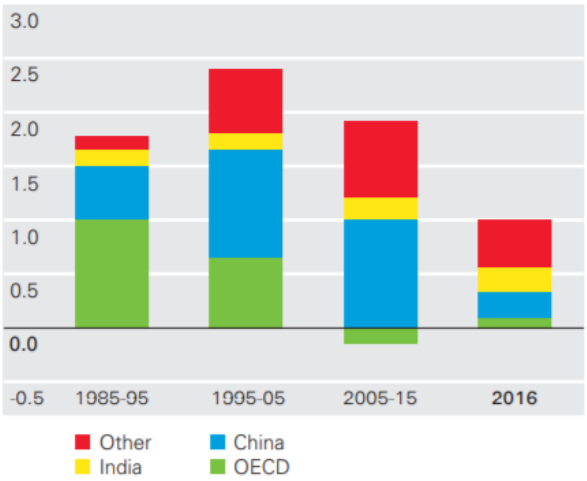

Figure 1-1 Energy consumption growth contributions to annual growth, %. Obtained from BP Statistical Review of World Energy 2017

It weighs more and more heavily on the natural resources (predominantly finite, like hydrocarbons). Over the last century, France has developed a large fleet of nuclear power generators in order to meet the growing demand while limiting its dependency to oil and gas importations. According to the BP 2017 statistical review of world energy (www.bp.com 2017), in 2016 total energy consumption in France amounted to 235 million tons of oil equivalent, with nuclear energy running to 91.2 million tons of oil equivalent. In 2016, France was responsible for 15.4 % of the world nuclear energy production.

In view of concerns on climate change, nuclear energy could play a significant role in the current energy transition. Fossil fuel energy is characterized by heavy carbon emissions that aggravate climate change. Coal power plants also emit large amounts of particles with real

and immediate impacts on human health. In that concern, from this environmental point of view, nuclear energy is much cleaner than fuel fossil energy.

Nevertheless, nuclear energy has several important drawbacks. Its development is heavily capitalistic and subject to onerous security restrictions. On top of that, and what is more crucial, nuclear energy sector leaves different kind of nuclear waste coming from the maintenance or operation of nuclear facilities. Thus, the wastes are regarded as a huge issue, especially since their management represents a technological challenge joined together with serious moral and ethical questionings.

From a scientific point of view, in France the management of nuclear wastes is based on the multi-barrier disposal concept implying that a series of engineered and natural barriers (container, buffer material around the container, metal envelops, sealing systems), will work together to contain and isolate used nuclear fuel from the environment

This research falls within the context of nuclear waste management, particularly for high level wastes, and strives for a better understanding of the behavior of the nuclear waste containing matrix of borosilicate glass over several thousands of years. In particular, it deals with the analysis of the glass fractured medium evolution. The study is based on the construction of a model of the fractured medium in view of a reactive transport modeling of its evolution. The methodology allows for the quantitative assessment of the degradation of the glass and the release of radionuclides under different scenarios of evolution, bridging the gap between laboratory scale (micrometer, years) and geological repository scale (meter for the block, tens of thousands of year).

1.2. General context: nuclear waste storage

1.2.1. Management of nuclear wastes

It is of common practice to classify nuclear wastes firstly, according to their level of radioactivity (from weak to highly radioactive) and secondly, according to the radioactive half-life of the main emitters that waste contains. Level of radioactivity and radioactive half-life define the dangerousness level and the duration of the nuisance that the waste can cause.

These two parameters cover a large range of activities and half-lives; therefore each type of nuclear waste requires special management.

In this connection it is worth remembering that in 1991 France passed a law, the Bataille Act, to organize the management of radioactive waste. Subsequently, it was extended by a new law passed on 28 June 2006. Within this legislative framework a major research program has been launched, with the main objective being to find the most appropriate way of managing the most highly radioactive wastes.

Nowadays in France, five waste categories are distinguished; their main characteristics are provided in Table 1-1

Table 1-1 Classification of radioactive waste and their storage/disposal solutions; information adapted from (andra.fr)

Category	Origin	Volume, %	Level of radioactivity, %	Preparation stage	Forseen disposal solution
Very-low-level waste (VLLW)	Operation and decommissioning of nuclear facilities; clean-up and remediation of historic sites polluted by radioactivity	27	<0.01	Some VLLW is subject to special processing like compaction, solidification, stabilization. Waste packages are labelled and stacked in vaults	Vaults are dug out of clay layer, a few meters below the surface
Low and intermediate level, short-lived radio-active waste (LILW-SL)	Maintenance and operation of nuclear facilities (clothing, tools, filters, etc.); by research or healthcare activities	63	0.02	Waste packages are compacted or solidified and then mixed with concrete before being placed in a concrete or metal container	In reinforced concrete near surface structures, that are later closed by a concrete slab, made watertight by a layer of impermeable resin
Low-level long-lived waste (LLW-LL)	Radium-bearing waste comes from the processing of various used minerals (e.g. metallurgy) Graphite waste originates from dismantling of the first generation of nuclear reactors	7	0.01	Graphite waste - in metal baskets that are later put then into concrete containers. Radium-bearing waste - in metal drums	Temporary stored on industrial producers sites
Intermediate-level waste, long-lived (ILW-LL)	Metal cladding structures surrounding nuclear fuel elements (hulls and end caps) or	3	4	Compacted into pucks and placed in containers (more or less similar to	Deep geological disposal at 500 metres

	residues from the operation of nuclear facilities			those used in vitrification facilities)	
High-level waste, long-lived (HLW LL)	Highly radioactive residue from the reprocessing of spent fuel used for power production, and waste from the defence sector	0.2	96	Stored temporarily in tanks before being calcined in the form of a powder and then incorporated into a molten glass. The mixture is poured into a stainless steel container	Deep geological disposal at 500 metres

Among the categories shown in Table 1-1, high level activity (HLA) and intermediate level (IL) activity long lived wastes are of specific concern, since the safety of their disposal solution has to be ensured for several thousands of years.

1.2.2. Geological storage

In consideration with the results of fifteen years of research spent studying and assessing various solutions for waste geological disposal carried out by ANDRA, the French Parliament opted for deep geological disposal and asked ANDRA to design Cigeo (Centre industriel de stockage géologique) - a deep geological disposal facility for radioactive waste.

According to the disposal scenario envisaged by ANDRA, the packages of vitrified glass containing high level long-lived radioactive wastes (HLLLW) will be stored in disposal cells of a repository to be built in Callovo-Oxfordian clay, located 500 m beneath the ground surface in Meuse / Haute-Marne, France.

Under the current concept (still in evolution), these cells would be blind micro-tunnels, 0.7 m of diameter and 100 to 150 m of total length (Figure 1-2). A steel lining is intended to facilitate the placement of packages during the operational phase (and their removal for possible recovery). Finally, a filler material should be injected between the liner and the host rock to enhance mechanical strength and reduce corrosion. The packages would be positioned separated from one another, so that heat production in the cell is compatible with thermo-hydro-mechanical targets (ANDRA 2016).

Depending on the administrative procedure and authorization process, Cigeo is expected to receive first batches of the stainless steel packages with inert vitrified glass (for

demonstration) between 2025 and 2030 in the framework of the industrial pilot phase, before an industrial phase by 2035.

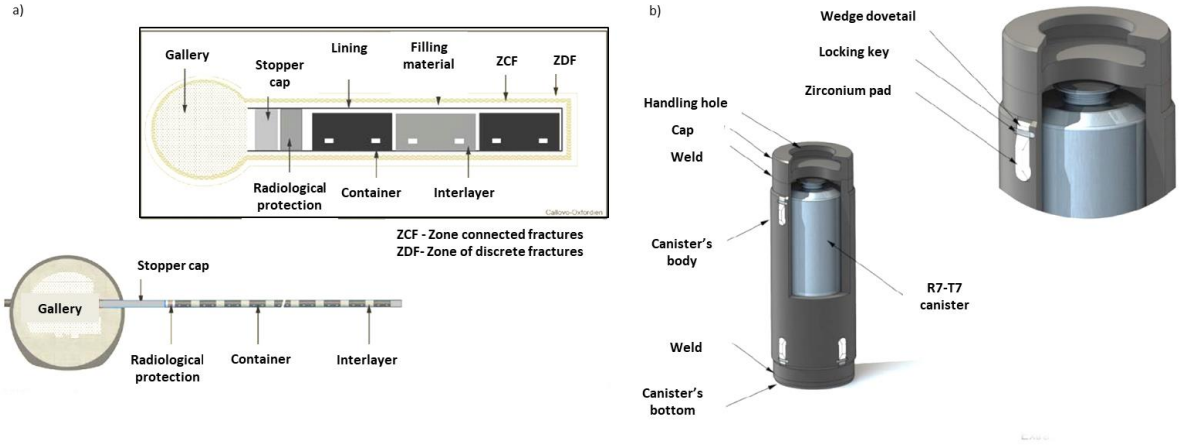

Figure 1-2 a) Schematic diagram of the HA cell; b) Illustration of an HA storage container for vitrified waste primary package type R7T7High-level long-lived waste disposal gallery in operating configuration. Obtained from (ANDRA 2016)

1.3. Conditioning of long-lived high- level (LLHL) radioactive waste

1.3.1. Manufacturing procedure of blocks of vitrified glass

The process of treatment of nuclear waste using vitrification at the industrial scale was initiated in 1978 at the Marcoule vitrification facility (Vernaz et al. 2014). The confinement process, detailed by (Bonniaud et al. 1980; Advocat et al. 2008), consists of two separate stages. The first stage involves calcination of the liquid fission product (FP) solutions at around 400°C. This is followed by a melting stage at around 1100°C in an induction-heated metallic reactor: the vitrification additive (glass frit) and the calcinated FP solution (calcinate) are mixed before being poured into a metallic container. In France, two types of melters are used to vitrify HLLL radioactive wastes: hot or cold crucible. In the melting pot (sometimes named hot crucible), glass is heated by thermal conductivity from the walls of the pot to the core the glass bath. Alternatively, with the cold crucible induction melter technology (CCIM), the principle is to induce electric currents directly within the glass to raise its temperature without heating the crucible. The direct-induction heating method allows the temperature to be increased (up to 1300°C) making it possible to obtain new waste containment matrices (*i.e.* for the vitrification of highly-corrosive UMo fission products, UOx fission products, etc.). Also, the CCIM technology allows the industrial vitrification throughput to be significantly increased: the higher the temperature, the faster the calcine digestion by the glass (neimagazine.com 2011).

Hot and cold crucibles give similar volume of glass SON68: in both cases about 400 kg is poured in two batches of 200 kg and the cooling takes place in natural environment without forced convection during about two days. That said, there are still some differences in

thermal parameters that differentiate these two procedures. Their graphical interpretation is given in Figure 1-3.

1. Duration of the inter-flows: about 10 h for the hot crucible, against about 6 h for the cold crucible.

2. Outside temperature: higher for the hot crucible, due to temperature maintenance in an oven (duration varies from case to case, in Figure 1-3 it makes up 50 000 s). In contrast, there is no preheating of the stainless steel casing for the cold crucible, and no external heating within the first hours. As a result, when the glass is solid, more important rate of fracturing is revealed for the hot crucible in comparison with the cold crucible.

3. Temperature of the glass melting: 1373 K for the hot crucible against 1 473 K for the cold crucible.

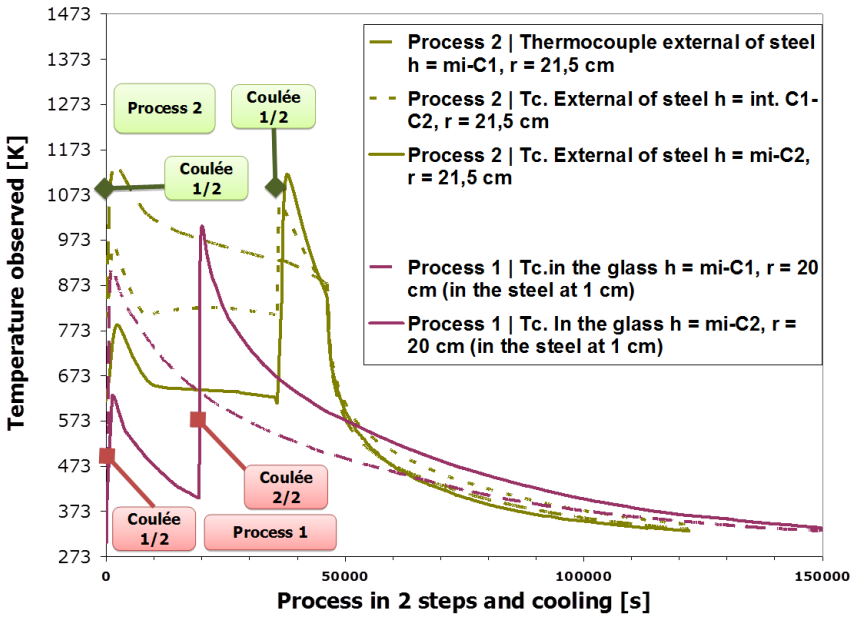

Figure 1-3 External temperature readings (close to steel) of the hot (process 2), and the cold (process 1) crucibles. For both of them the casting is effectuated in two steps, with total mass of a block being 400 kg). Adopted from (Barth 2013).

The resulting glass incorporating FP is then poured and solidifies inside stainless steel containers (type "CSD-V" - standard package of vitrified waste).

Downstream of the industrial process of vitrification, the packages are sealed and stored in ventilated wells during a sufficient storage period for initial cooling of the packages (up to 300 years). Later on, these packages are supposed to go to the underground storage facility.

1.3.2. Some studies on glass fracturing

Fracturing is a potential issue as it could increase the reactive surface accessible to underground water during the geological disposal phase of the vitrified wastes, after the stainless steel container has lost its integrity. A higher accessible surface in turn means an

increased radionuclide release rate. By conducting leaching experiments of a nuclear glass (Perez et al. 1989; Chomat 2008; Verney-Carron 2009) demonstrated that these surfaces, if they are part of a network of open cracks (in percolation), may also interact with water during the alteration of the packages in an aqueous medium.

That is why it seemed important to study the thermomechanical behavior of the nuclear glass. The research of (Barth 2013) resided in the implementation of a continuum damage mechanics model aimed at predicting the development of fracturing surfaces, originating as a result of the thermal and mechanical stresses related to the manufacturing procedure and evolving in course of a package life. It comprises such types of simulations as: thermal simulations, simulation of structural relaxation, and simulation of thermal damage.

(Bouyer et al. 2014) have illustrated the variation of the glass transition temperature according to the thermal history during cooling and solidification of the glass in the package. It was shown that the solidification front evolves in a characteristic way according to the process of glass melting (due to the distribution of thermal histories in the package). The model relaying on the assumption that the elastic energy associated with the stresses that are higher than the threshold stress is dissipated in the creation of new surfaces (Dube et al. 2010) was used to estimate the fracture surfaces of a glass block.

The results of the simulations of a glass block fabricated in a cold crucible without the thermal source due to radioactivity is planned to be used in our research in order to make a link between the observed fracture network morphology and the physical parameters that condition the development of the glass fracture network at scale 1.

1.4. Scientific questions and objectives

Modeling of flow and transport phenomena in fractured media has become a topical issue in Earth Sciences. The nuclear energy industry shows interest in this subject because fractures could eventually be responsible for the release of the radionuclides with the ground waters in deep geological wastes repositories. In fact, multiple researches strive to model the migration of radionuclides in fractures of host rocks surrounding deep geological repositories for high level wastes (ANDRA 2005a; Zhang 2018; Cvetkovic et al. 2004; ANDRA 2010, 2005b). With reference to these researches it is possible to state that at the reservoir scale the solute transport and the flow of the ground water bearing radionuclides are rather well understood.

At the same time, over the last thirty years, plenty of studies have focused on the performance of the glass under leaching (Pierce et al. 2014; Steefel 2015; Gin et al. 2013). Results of these experiments enabled better understanding of the mechanisms of glass alteration at the micro level and gave the foundation to elaborate glass reactivity with allowance for the alteration layer model (GRAAL), (Frugier et al. 2008). Despite the advancements made in studying solute transport and flow of the ground water in fractures and discoveries in the domain of borosilicate glass aqueous alteration, a crucial investigation

of the effect of block fracturing on the glass aqueous alteration has stayed rather limited so far.

The overarching aim of this research has therefore been to bring new light on the impact of fracturing on the quantity of altered glass at the scale of the glass package (scale 1). The dissertation is framed by the following scientific questions.

Question 1:

At the scale of some fractures, how to couple the geochemistry of glass alteration and the modeling of transport phenomena? What are the main mechanisms that drive the development of the altered glass layers and glass aqueous alteration?

Proposed solution: Taking control of GRAAL model, comparison of the results of reactive transport modeling to the results of the experiments conducted by Chomat (Chomat 2008), explanation of the results of modeling in light of the principles of GRAAL model and theoretical knowledge of nuclear glass corrosion.

Question 2:

What is the influence of fracture length, opening, number on the quantity of altered glass released?

Proposed solution: Conducting a sensitivity study in the framework of discrete fracture network modeling that enables to refine the knowledge of the impact of ideal fractures geometry on the evolution of the glass aqueous alteration.

Question 3:

Is it possible to adapt GRAAL model in order to conduct reactive transport modeling applied to a system of fractures described by an equivalent porous medium representation?

Proposed solution: "Upscaling" of the GRAAL model, carrying-out the modeling in the framework of "Fracture" and "Porous Medium" approaches in a diffusive mode. This step sets the stage for the geochemical modeling at the scale of a glass package. The main purpose is to prove that from the geochemical perspective it is feasible to replace CPU time consuming discrete fracture network representation by an equivalent fracture network representation provided that kinetics governing parameters such as, glass specific surface, glass mass per solution volume, half-saturation coefficient and equivalent fracture porosity are supplied for all meshes of the modeled equivalent medium.

Question 4:

What techniques should be applied to characterize a block fracture network? What are the approaches that will allow us to achieve the final objective of the quantity of altered glass

quantification in a relatively short period of time and without being extremely too cumbersome?

Proposed solution: Conception of the image-based fracture network characterization routine relying on the analysis of high quality images of vitrified glass block cross sections. It involves stages of fracture network extraction and its meticulous examination and it proposes the replacement of the fracture network representation by a "crystal" representation. The idea behind the adoption of the crystal representation is to be able to replicate block facture network by reproducing its segmented image (kind of object modeling via the techniques of anisotropic mesh growth). The devised workflow comprises steps of (i) characterization of fracture network as the scale of vitrified glass block, (ii) upscaling of permeability, diffusion and kinetics governing parameters and subsequent (iii) reactive transport modeling with consideration for variability of fracture network.

Question 5:

What data can be brought into play in order to supplement scarce hard data acquired at the stage of image analysis?

Proposed solution: Examination of the results of thermo-mechanical simulation as a model of a glass block elaborated in a cold-crucible without radioactive source term. Selection of an exhaustively known physical parameter whose transforms could supplement the raw data at the stage of the equivalent fracture network simulation. Analysis of the evolution of the chosen parameter and its derivatives with upcoming construction of the maps that reflect the anisotropy of fracture networks in consideration of the evolution of the internal state of the glass.

Question 6:

Is there any not lengthy and moderately time consuming way to extend the proposed 2D model towards a 3D model? What are the limitations of this approach?

Perspective for future: creation of a 3D model by applying a cylindrical symmetry. Regarding the knowledge of the fracture pattern of a transverse plane of fracture package, it could be obtained by applying the workflow devised in the course of this research. However, certain caution must be applied since the fracture network is likely to vary along the z-axis due to the presence of the different thermo-mechanical environments, i.e. zone of reliquefaction, free glass surface, bottom area of the package.

1.5. Dissertation structure

This section provides an overview of each chapter and explains their contributions to the achievement of the research goals.

Chapter 2

In this chapter, in a first step in § 2.1, the state of the art of the aqueous alteration of borosilicate nuclear glass is presented. The knowledge gained from the multiple experiments conducted at CEA and abroad is examined and the GRAAL glass corrosion model is presented. In § 2.2 we discuss the experimental results and the efforts made to characterize nuclear glass fracture networks at the scale of one container by static and dynamic measurements and then at the scale of a few fractures by optical microscopy and scanning electron microscopy. This chapter ends with the analysis of the theoretical bases of reactive transport and more precisely, in § 2.3 we pay attention to the principles of the coupled HYTEC reactive transport code used in this thesis, then we present some ideas on the origin of convection that might exist in storage conditions and we cite some limitations of reactive transport codes.

Chapter 3

This chapter aims to explain the issue of the glass fracture network analysis at the scale of a container. In § 3.1 we present the basics of mathematical morphology - the main tool for the characterization of glass fractured network, discussed in this thesis. In § 3.2 we look at the steps taken to obtain images of nuclear glass sections and we explain the reasons justifying the choice of ordinary imaging in relation to different types of microscopy and tomography. At the end of this chapter we reflect on the possibility of extending the proposed methodology to 3D applications and we indicate some technical obstacles that will be necessary to tackle.

Chapter 4

The fourth chapter begins with the recapitulation of the results of the glass aqueous corrosion experiments applied to simple systems of ideal fractures of nuclear glass. The second part of the chapter deals with the implementation of the Glass Reactivity with Allowance for the Alteration Layer Model (GRAAL) and its application as part of the discrete approach for some ideal cracks. In the last part of the chapter we examine the results of a sensitivity study aimed at studying the influence of number of cracks, their openings and their lengths as well as the volume of water and the degree of its agitation on the intensity of development of the dense passivating gel and of the porous non-passivating gel and, consequently, on the intensity of glass corrosion.

Chapter 5

This chapter represents the heart of the thesis and aims to explain in detail the image processing-based fracture network characterization workflow developed for carrying out reactive transport on a container scale by taking into account fracture network variability and different scenarios of storage evolution. This chapter is written in the form of two articles. In the first article in § 1.3 we see the application of the mathematical morphology in

order to (i) extract fracture network separately from pull-out zones and cavities of contraction, (ii) determine apertures for each branch of fracture network, (iii) perform image segmentation which intends to distinguish parts of the matrix separated by fractures and whose centroids are easy to find, and (iv) finally study the anisotropy of this segmented image by the theory of moments, from where the ratio of the axis lengths, the angle of rotation of each crystal and their barycenter are obtained. Then, in § 1.4 and 1.5 of the same article, we examine the steps of the quantitative analysis of the arrival map of the solidification front. This map and its derivatives are used to supplement the pointwise data of image analysis by the global spatial distribution of key parameters in order to perform geostatistical simulations and to predict network anisotropy. After, we proceed with the geostatistical simulations of crystal centers and crack openings, the results of which are used at the stage of the construction of equiprobable realizations of fracture network equivalent tessellations. The article ends with the demonstration of four simulated glass networks and two segmented images of UOx and UMo vitrified blocks.

In the second article in § 2 we examine the techniques proposed for calculating the equivalent parameters, such as coefficients of permeability and diffusion. We also look at how the parameters governing the kinetics of glass dissolution are calculated in the context of the equivalent porous model. The verification of these techniques is shown in § 3: it is carried out by means of the simulations of the reactive transport applied to a simplified network represented, on the one hand, by the DFN approach and on the other hand, by its equivalent porous model.

The application of the equivalent model at the scale of a container is addressed in § 4 of the second article, here the results of the reactive transport modeling conducted in diffusive and convective modes are shown and compared with the experimental results of the long-term aqueous alteration test of a block of nuclear glass. This experiment was realized at the CEA in the electrical static leaching unit.

This chapter concludes with the demonstration of the results of reactive transport modeling in conditions closer to those of the geological storage, i.e. applied to a lying on its side block in which the thermoconvection created by the release of waste heat is modeled. These simulations are conducted for three deadlines: 1000 years, 5000 years and 10 000 years after the canister is deposited in the storage cells.

Chapter 6

In this chapter, the question of the application of the model in the context of the storage of fractured glass blocks containing high-level nuclear waste is raised. We highlight the technical problems encountered during the application of the methodology and we reflect on the possibility of evolution of this methodology to be able, firstly, to extend towards 3D and, secondly, to take an account of storage conditions more realistic than those modeled in this thesis.

References

Advocat, Dussossoy, and Petitjean. 2008. 'Vitrification des déchets radioactifs', *Techniques de l'ingénieur Cycle du combustible nucléaire : combustibles usés et déchets radioactifs*, base documentaire : TIB457DUO.

ANDRA. 2005a. "Dossier 2005 Argile - Tome Architecture et Gestion du Stockage Géologique." In, edited by ANDRA, 1-497.

———. 2005b. "Dossier 2005 Argile - Tome Évolution Phénoménologique du Stockage Géologique." In, edited by ANDRA, 1-523.

———. 2010. "2006 - 2009 - 4 ans de recherches scientifiques à l'Andra pour les projets de stockage." In, edited by ANDRA, 1-48.

———. 2016. 'Rapport Andra CG-TE-D-NTE-AMOA-SR1-0000-15-0060 – « Dossier d'options de sûreté - Partie exploitation »'.

andra.fr, collectif. "Site internet de l'ANDRA." In.

Barth, Nicolas. 2013. 'Sur la modélisation et la simulation du comportement mécanique endommageable de verres borosilicatés sous sollicitation thermique', Université de Strasbourg.

Bonniaud, R., A. Jouan, and C. Sombret. 1980. 'Large scale production of glass for high level radioactive waste', *Nuclear and Chemical Waste Management*, 1: 3-16.

Bouyer, F, Véronique Doquet, Céline Mallet, Nicolas Barth, Emmanuelle Chabert, Neji Ben Ali, Andrei Constantinescu, Jérôme Fortin, Yves Guéguen, Daniel George, Yves Rémond, and Saïd Ahzi. 2014. "Synthèse sur la fracturation thermomécanique des verres R7T7 - Bilan du programme 2011-2014." In, edited by CEA, 1-201.

Carl I. Steefel, Lauren E. Beckingham, Gautier Landrot. 2015. 'Micro-Continuum Approaches for Modeling Pore-Scale Geochemical Processes', *Reviews in Mineralogy and Geochemistry*, 80: 217-46.

Chomat, L. 2008. 'Compréhension de l'altération à long terme des colis de verre R7T7 : étude du couplage chimie transport dans un milieu fissuré', Université Paris VI.

Cvetkovic, Vladimir, S. Painter, N. Outters, and J. O. Selroos. 2004. 'Stochastic simulation of radionuclide migration in discretely fractured rock near the Aspo Hard Rock Laboratory', *Water Resources Research*, 40: W02404.

Dube, Martine, Veronique Doquet, Andrei Constantinescu, Daniel George, Yves Remond, and Said Ahzi. 2010. 'Modeling of thermal shock-induced damage in a borosilicate glass', *Mechanics of Materials*, 42: 863-72.

Frugier, P., S. Gin, Y. Minet, T. Chave, B. Bonin, N. Godon, J.E. Lartigue, P. Jollivet, A. Ayral, L. De Windt, and G. Santarini. 2008. 'SON68 Nuclear glass dissolution kinetics: Current state of knowledge and basis of the new GRAAL model', *Journal of Nuclear Materials*, 380: 8-21.

Gin, S., A. Abdelouas, L.J. Criscenti, W.L. Ebert, K. Ferrand, T. Geisler, M.T. Harrison, Y. Inagaki, S. Mitsui, K.T. Mueller, J.C. Marra, C.G. Pantano, E.M. Pierce, J.V. Ryan, J.M. Schofield, C.I. Steefel, and J.D. Vienna. 2013. 'An international initiative on long-term behavior of high-level nuclear waste glass', *Materials Today*, 16: 243-48.

neimagazine.com, collectif of. 2011. 'cold crucible retrofit', *site of Nuclear Engineering International*.

Perez, Jr.J.M., and J.H.Jr. Westsik. 1989. "Effects of cracks on glass-leaching." In, edited by PNL, 1-19.

Pierce, Eric M., Pierre Frugier, Louise J. Criscenti, Kideok D. Kwon, and Sebastien N. Kerisit. 2014. 'Modeling Interfacial Glass-Water Reactions: Recent Advances and Current Limitations', *International Journal of Applied Glass Science*, 5: 421-35.

Vernaz, Étienne, and Jérôme Bruezière. 2014. 'History of Nuclear Waste Glass in France', *Procedia Materials Science*, 7: 3-9.

Verney-Carron, A. 2009. 'Etude d'analogues archéologiques pour la validation des modèles de comportement à long terme des verres nucléaires', Institut national polytechnique de Lorraine.

www.bp.com. 2017. 'BP Statistical Review of World Energy'.

Zhang, Chun-Liang. 2018. 'Thermo-hydro-mechanical behavior of clay rock for deep geological disposal of high-level radioactive waste', *Journal of Rock Mechanics and Geotechnical Engineering*.

Chapter 2: State of the art

CHAPTER 2: STATE OF THE ART

List of figures

CHAPTER 2: STATE OF THE ART

List of tables

Résumé du chapitre

Dans ce chapitre, dans un premier temps au § 2.1, l'état de l'art de l'altération aqueuse de verre nucléaire borosilicaté est présenté. Les connaissances obtenues par les expériences multiples menées au CEA et à l'étranger sont examinées et le modèle GRAAL de la corrosion du verre est présenté. Au § 2.2 sont abordés les résultats expérimentaux et les efforts accomplis jusque-là pour la caractérisation des réseaux de fractures de verre nucléaire à l'échelle d'un conteneur par les mesures de lixiviations statiques et dynamiques et ensuite, à l'échelle de quelques fissures, par la microscopie optique et la microscopie électronique à balayage. Ce chapitre se termine par l'analyse des bases théoriques du transport réactif et plus précisément, au § 2.3, nous mettons l'accent sur les principes du code couplé transport-chimie HYTEC utilisé dans cette thèse; puis nous présentons les phénomènes pouvant être à l'origine de la convection dans les conditions de stockage et nous exposons enfin quelques limites des codes de transport réactif.

2. State of the art

2.1. Borosilicate glass aqueous alteration

2.1.1. Knowledge derived from laboratory experiments

In the late 1970s France made the decision to use an alumino-borosilicate glass as a containment matrix because it has a great flexibility compared to crystalline structures, and it allows integration of many radionuclides by substitution of atoms of its structure. Borosilicate glass usually contains sodium with additions of other oxides like aluminum, calcium, lithium or zirconium. The study of the effects of glass composition on a wide range of properties like homogeneity, mixing temperature, viscosity, phase separation, crystallization, leaching behavior, resistance to irradiation, etc., led to the definition of two glass types: the industrial R7T7 glass (Table 2-1), considered in France as a reference for its confinement qualities, and its inactive analogue, referred to as SON68 glass (Table 2-2).

Table 2-1 Reference chemical composition of UOx glasses (% mass.).

Oxide	SiO_2	$B2O_3$	Na_2O	Al_2O_3	Li_2O	ZnO	CaO	Cr_2O_3	Fe_2O_3	P_2O_5	NiO	Oxides (FP + Zr + actinides) + Metallic particles	RuO_2+ Rh+ Pd
%	45.1	13.9	9.8	4.9	2.0	2.5	4.0	0.5	2.9	0.3	0.4	13.7	1.54

Table 2-2 Reference chemical composition of SON68 glasses (% mass.).

Oxide	SiO_2	B_2O_3	Na_2O	Al_2O_3	Li_2O	ZnO	CaO	ZrO_2	Fe_2O_3	Cs_2O	NiO	Nd_2O_3	MoO_3	Other
%	45.48	14.02	9.86	4.91	1.98	2.5	4.04	2.65	2.91	1.42	0.74	1.59	1.7	6.2

The interaction of nuclear glasses with water in a geological waste disposal is believed to happen after a few thousands of years, i.e. after the multiple barriers of the repository including the steel canister would have failed and groundwater from the surrounding geological medium would fill the repository. Glass gets corroded mainly due to reaction with water, which changes the physical structure of the glass surface, and releases its constitutive elements, including the radionuclides, into water. Laboratory experiments applied to modern glasses and study of the archeological glasses found in seawater beds or buried in cathedral construction sites have demonstrated that glass is capable of withstanding the corrosion for thousands of years (Verney-Carron et al. 2008; Sterpenich 1998).

In contact with water, glass is subjected to various phenomena like ion exchange (or interdiffusion), hydrolysis of the vitreous network, condensation of a part of the silica and poorly soluble elements and precipitation of secondary phases. The species solubilized during the alteration of the glass undergo local processes of condensation-precipitation. These processes are at the origin of the formation of silicate polymorphs, progressively reorganized into a porous and hydrated network called “gel”. The solution is also the place where precipitation reactions happen, leading to the formation of secondary phases, essentially clay and silicate.

Gel is the name given to the amorphous material formed by the establishment of a balance with a solution whose nature remains discussed. The gel can originate from several processes: in-situ condensation (Frugier 2008; Dran et al. 1988; Jegou et al. 2000) or precipitation (Jercinovic et al. 1990; Geisler et al. 2010; Hellmann et al. 2015) from elements released in solution by the hydrolysis of a glass network. Moreover, according to the current vision, these two mechanisms are not necessarily antagonistic and may coexist.

The gel limits the transport of the species to the alteration fronts (Rebiscoul et al. 2007); the closure of porosities is one of the reasons of gel’s passivation effect (Cailleteau 2008). The structure of the gel is likely to evolve over time towards the increase of its order at short distance and the decrease of its pore volume. In general, the denser the gel, the better its diffusive barrier properties (Grambow et al. 2001).

Recombination of the elements dissolved during the glass alteration gives rise to the precipitation of secondary phases. Alteration gel and secondary phases are aluminosilicates

containing cations present in the surrounding solution. According to the affinity of an element for one of the phases, either formation of secondary phases or gel (to the possible detriment of certain secondary phases) can take place, the affinity depending on environmental conditions and their evolution.

As for the terminology used in this thesis, gel refers to the amorphous weathering layer of glass at the glass / solution interphase. This gel may comprise two parts: passivating and non-passivating. The former with passivating properties called PRI for passivating reactive interphase. The non-passivating gel means a gel which has lost part of its initial constituents or whose passivation properties are negligible.

In the context on this research, we deal only with the aqueous alteration of glass under assumption of its full saturation with water in pH conditions not allowing the alteration to resume. However, we propose in the two following sections an overview of the mechanisms and the kinetic regimes for both environments: alteration in aqueous medium and in unsaturated vapor phase.

2.1.1.1. Full saturation with water

During the leaching process of a glass in an aqueous medium, the reaction mechanisms generate different alteration regimes as shown in Figure 2-1.

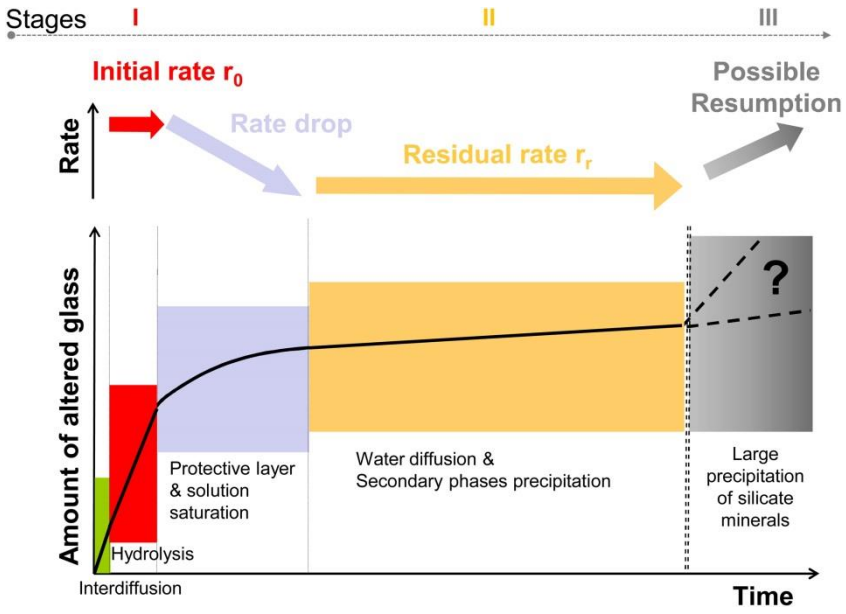

Figure 2-1 Alteration rate of glass in water over time and the different stages of alteration, obtained from (Gin 2013)

Their duration depends on the composition of the glass and the chemical conditions of its degradation. For each regime, the prevailing mechanisms are detailed as follows.

Initial rate regime

In the early stage of alteration, the mechanisms of interdiffusion and hydrolysis occur simultaneously. However, the interdiffusion regime is transient since it follows a diffusive process. So it's the velocity of hydrolysis that contributes mainly to the velocity of the initial alteration.

By definition, the initial glass alteration rate is the maximum dissolution rate of the glass obtained in the conditions far from the saturation, i.e. in a highly diluted medium where no diffusional barrier intervenes to slow down the alteration. The initial rate depends on pH and temperature in agreement with equation 2-1:

$$V_0(\mathrm{T}, \mathrm{pH}) = V_{0T_0} \times e^{-\frac{E_a}{RT}\left(\frac{1}{T}-\frac{1}{T_0}\right)} \times 10^{N_0 * \max(pH-7;0)}, \qquad 2\text{-}1$$

where E_a is the activation energy, V_0 is the initial glass hydration rate, No is the coefficient of the diffusion dependence on the pH, T is the current temperature, T_0 is the absolute zero temperature, R is the gas constant.

This equation is composed of three terms. The first is a constant rate measured at the initial temperature and pH equal to 7. The second and the third indicate the dependence on temperature and pH. The equation is valid for temperatures between 25 and 100°C and pH between 6 and 10. For illustrative purposes, two values of the initial rate for different pH and temperatures for SON68 glass are cited: 0.9 $g.m^{-2}.d^{-1}$ (T = 90°C, pH = 7), 5.5 $g.m^{-2}.d^{-1}$ (T = 90°C, pH = 9).

Rate drop regime

The rate drop is a complex regime that corresponds to the transition between the initial and the residual rates. The increase of concentrations in solution leads to the recondensation of part of the dissolved silicon in an amorphous, porous, and hydrated phase: the gel. The formation of this phase leads to a decrease of tracer elements departure rate, making the dissolution largely incongruent[1]. The fall of the rate is due to the decrease in the dissolution affinity of the glass and the formation of the passivating gel which limits the transport of dissolved silica from the glass / gel interphase to the solution. The passivating character of the gel increases with increasing concentrations in the solution that favors the recondensation of the elements within the gel. At this stage, the rate of the aqueous alteration of the glass can decrease by several orders of magnitude.

Residual rate regime

The regime of rate drop gives way to the so-called residual rate regime. This velocity evolves more or less in a long run. Two mechanisms are responsible for the residual rate regime:

[1] The dissolution of a mineral is congruent when its constituents are released simultaneously in solution. Their stoichiometric ratios in solution are then identical to those of the dissolving mineral

1. diffusion of elements coming from the alteration of the glass within the gel that results in the supersaturation at the hydrated glass / gel interphase;
2. formation of the secondary phases, which maintain residual hydrolysis by consuming certain elements, like silicon, aluminum, sodium and calcium.

In the case of French nuclear glass R7T7, when quasi-stationary silicon conditions are reached in the solution, a very low rate of alteration is found. To be precise, it is expected to be 4 orders of magnitude lower than the initial velocity at 90°C and pH 9, with values around 10^{-4} $g.m^{-2}.d^{-1}$.

Alteration resumption

The alteration resumption corresponds to an increase in the raterate of alteration, following the regime of the rate drop. The main mechanism related to the alteration resumption is secondary phase formation (as zeolites and Calcium Silicate Hydrates, C-S-H), which triggers or maintains the residual hydrolysis by consuming the forming elements of the alteration layer (aluminum, silicon, etc.). The development of these phases causes a pumping of the constitutive elements out of the gel. By doing this, it destabilizes and inhibits its passivating properties. According to the experimental and theoretical studies carried out so far, the phenomenon of alteration resumption depends essentially on the surface by volume ratio (S/V), pH, composition of the glass and the surrounding solution. The alteration resumption is favored in strongly basic pH conditions (pH > 10,5), high temperature and high S/V ratio (Fournier et al. 2014).

2.1.1.2. Vapor phase

After the break-up of the stainless steel container, vitrified waste alteration is likely to be initiated in unsaturated conditions resulting, in particular, from hydrogen production coming from the corrosion of the metal materials of the liner and the container (ANDRA-Collectif 2016). The reaction of glass with water vapor has been studied in Argonne National laboratory (ANL), Pacific Northwest National Laboratory (PNNL), Savannah River Laboratory (SRL) etc. It is acknowledged that currently the scientific database on the vapor hydration of nuclear glasses stays relatively limited.

From the experimental results conducted so far, it can be understood that the reactions occurring between glass and water are the same for alteration in aqueous medium and unsaturated water vapor. However, the rate controlling reaction mechanism and the driving force for alteration are different in both cases (Abrajano et al. 1989). The difference largely arises from the changes in the water chemistry, as a result of the extremely small volume of water available for reaction in the unsaturated case. The various results from the vapor hydration experiments suggest that the alteration in vapor phase is not simply an extreme case of the glass alteration in aqueous medium at a very high S/V (Abrajano et al. 1986). The precipitation of secondary phases seems to be the strongest driving force for alteration in vapor phase at high temperature. At high temperatures and low solution volume that gets

saturated rapidly, the conditions are thermodynamically favorable for the precipitation of secondary phases.

Given the lack of understanding of the geochemical behavior of the borosilicate glass under leaching in vapor unsaturated phase, it is crucial that more vapor hydration studies be conducted.

With the knowledge of these regimes, the geochemical modeling of glass dissolution is complex. It depends on saturation conditions (full saturation with water vs. vapor phase) and hydrodynamic regimes (solution renewal vs. static conditions).

2.1.2. General statements of GRAAL model

2.1.2.1. Theoretical basis of the geochemical modeling

The Glass Reactivity with allowance for the Alteration Layer Model was proposed to describe borosilicate nuclear glass alteration (Frugier 2008). The model was developed with a dual objective: (i) consideration of the coupling between the affinity effects in the kinetic law and the diffusion processes in the alteration layer and (ii) the establishment of precise material balance to calculate the distribution of the elements of the glass between the solution, the secondary phases and the gel. For this purpose, the GRAAL equations were implemented in a coupled chemistry-transport code HYTEC (Van der Lee et al. 2003).

The first hypothesis of the GRAAL model is the rapidity of the hydration reaction of the glass at the initial time. This phenomenon forces the elements of the glass (alkaline, boron) to pass into solution. The hydrolysis of silicon is slower, and it is the hydrolysis that conditions the glass initial dissolution rate. The difference between these two kinetics leads to the creation of the dealkalized hydrated glass layer at the glass-solution interphase. This layer or gel is gradually reorganized by hydrolysis / condensation phenomena and is called passivating reactive interphase (PRI). Each silicon atom present in the solution comes from the dissolution of the PRI. Along with the creation, this gel dissolves, as long as the solution is not saturated in the elements that constitute it: Si, Al, Ca, Zr.

GRAAL proposes the description of the gel formed on the surface of glass by condensation and precipitation of Si, Al, Zr and Ca. With a relatively simple formalism, the model accounts for the chemistry and solubility of the gel. It assumes that glass alteration is controlled by the PRI consisting of glass without any mobile elements in its composition (alkalis, boron, etc.). Apart from PRI, another amorphous layer is expected to be created during aqueous alteration (Figure 2-2). Frugier et al. are of the opinion that due to water diffusion in the glass, inter-diffusion between protons and alkali ions, some other amorphous interphases could be created.

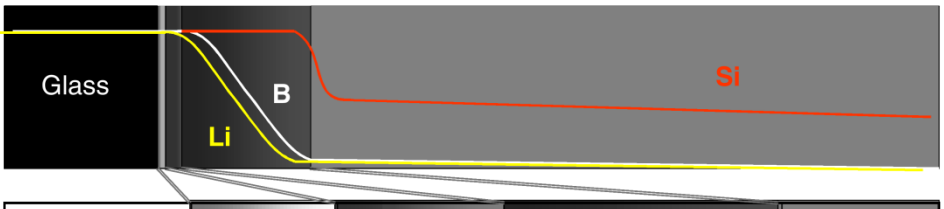

Zone : Glass	–1a– + H_2O	–1b– + H^+ - Li	–1c– + H_2O -Na Li B Mo IRP	–2– **Gel** also depleted in Si-Al-Ca…
Formation mechanism	Water diffusion	Exchange of alkali ions and protons	Reactive diffusion of all elements from solution or from crystallized phases, irrespective of their structural role	Hydrolysis / condensation. Rapid diffusion in pore water
Order of magnitude of possible thickness values "e"	Not observed. <1 nm if it exists	$e_{1b} << e_{1c}$ Approx. 1 nm	e_{1c} 3 to 300 nm D~1e^{-23} m^2.s^{-1}	e_2 Inversely proportional to S/V in a closed system
	Hydration	**Alkali interdiffusion**	**PRI**	**Depleted gel**

Figure 2-2 Diagram of the different amorphous phases and mechanisms of their generation (obtained from Frugier et al., 2008)

In this research, we consider two main alteration layers (porous gel and passivating dense gel) and we strive to model the generation of these two layers by executing a reactive transport modeling inside different fracture media. The verification of the GRAAL model undertaken at the first stage of the research was done by results comparison with the thickness of altered glass measured by means of SEM (Chomat 2008).

According to (de Combarieu 2007; Godon et al. 2012), passivating reactive interphase comprises all gel forming elements (Si, Ca, Al, Zr). This zone is characterized by a concentration gradient both of the mobile elements (alkalis, B) and of the elements that limit the formation of crystallized phases (Zn, Ni, etc.). NMR and X-ray absorption spectrometry show that it is the layer in which the silica network is more polymerized that in the initial glass. This in situ reorganization of the glass constituent elements causes the reactivity to control the concentrations and to passivate the underlying pristine glass.

On the other hand, when the glass is sufficiently altered by the renewal of a pure water solution or when the glass, that has to be dissolved to saturate the solution, has the thickness comparable to the characteristic diffusion thickness, another type of gel – depleted in Si, Al and Ca is formed. This part of the gel is porous and no longer passivating.

In the GRAAL model, the transport properties of the PRI are modeled by a constant diffusion coefficient for the elements of the glass. Accordingly, the flow of mobile elements transported through PRI is proportional to the diffusion coefficient and inversely proportional to the thickness of the PRI. Therefore, the GRAAL model makes the assumption

of a balance between the non-passivating gel and the solution and between the external interphase of the PRI and the solution.

The GRAAL model uses two kinetic equations for the PRI grouped in equation 2-2.

$$\frac{dx}{dt} = r_1 - r_2 = \frac{D_{PRI}}{x_{PRI}} - v_0\left(1 - \frac{Q_{PRI}}{K_{PRI}}\right), \qquad 2\text{-}2$$

This equation states that the PRI is (i) formed from the glass with a rate r_1 which is a function of its thickness - x_{PRI} and PRI diffusion coefficient - D_{PRI}, and (ii) dissolves with a rate r_2 according to a classical affinity law in which v_0 – is the initial rate, Q_{PRI} - is the activity product of the PRI and K_{PRI} – is the PRI activity product at saturation.

As it was stated in (Frugier et al. 2018), in order to limit the creation kinetics of the protective layer, that is, to avoid the appearance of the infinite rate when $x_{PRI} = 0$, a constant hydration rate is introduced in the definition of r_1 in Equation 2-3:

$$r_1 = \frac{D_{PRI}}{x_{PRI}} = \frac{r_h}{1 + x_{PRI}\frac{r_h}{D\frac{\pi}{2}}}, \qquad 2\text{-}3$$

where r_h is the hydration rate, it is higher than the initial dissolution rate. This is totally compatible with the experimental observations: the dissolution rate of mobile ions is higher than the dissolution rate of silicon ions. However, due to the very low diffusion coefficient value of nuclear glasses, the hydratation rate governs the alteration rate for only a few seconds of alteration. The parameter is not measurable experimentally and has almost no effect on the modeling results.

The GRAAL model allows us to compute the gel thickness provided that we know the concentration of a certain pole or a group of poles. The formalism of this model postulates the notion of the equivalent thickness, i.e. the glass thickness that should be dissolved to achieve the measured concentration of a given element in solution. It is calculated based on the mass balance equation between the quantity accumulated in the solution and the quantity released by the glass dissolution, as given by (2-4):

$$\frac{de_i}{dt} = \frac{d}{dt}\left(\frac{C_i}{\rho_{PS} x_i S_p C_v}\right), \qquad 2\text{-}4$$

where e_i is the equivalent alteration thickness for element i; C_i is the concentration of this element in solution; ρ_{PS} is the glass density; x_i is the mass fraction of the element i in the glass; S_p is the glass specific surface, C_v is the mass of the glass in a unit volume

Amorphous layer's end-members stoichiometry, both the one of PRI and those used to describe the amorphous non protective gel, have been chosen with two constraints: The first constraint is that the model must account for the analyzed concentrations of the elements in the fluid, that is the composition and the solubility of the amorphous layer. The second constraint arises from software limitations: a single end-member can passivate the glass according equation 2-3. In the GRAAL the Si rich end-members are chosen because silicon is

the main element and its condensation is mandatory for passivation to occur (Frugier et al. 2018).

For the computation of the equivalent thickness of the dense gel (PRI), the governing concentration is the SiAl concentration, because the major part of this layer is occupied by Si and Al (according to the formalism of the GRAAL, the PRI is represented as $SiO_2Al_{0.033}(OH)_{0.1}$).

SEM measurements provide the total thickness of the amorphous layer. Regarding reactive transport modeling, this total thickness can be calculated from the total concentration of SiZrCa and SiZrNa found in the solution. These two poles comprising Zr are chosen because Zr solubility is low. This allows us to suppose that all Zr liberated from the glass is preserved (condensed) inside the amorphous layer, that it does not pass into solution. With respect to the composition of the chosen glass, Zr can form only two species SiZrCa and SiZrNa, sum of the concentrations of which is necessary to estimate the equivalent thickness of the total altered layer.

Other parameters frequently used to characterize the glass alteration are the quantity of altered glass per day (2-5) and its ratio to the maximum quantity of altered glass per day (2-6):

$$QAG = \frac{C_{i(t)}}{x_i * \frac{S}{V} * t}, \qquad 2\text{-}5$$

$$\frac{QAG_{(Vcurrent)}}{QAG_{max(V_0)}}, \qquad 2\text{-}6$$

The current quantity of altered glass per day QAG [g/(m²×day)] is calculated knowing the concentrations C_i either of total dissolved boron concentration $(B(OH)_3)aq$ or total dissolved silica concentration $(SiO_2)aq$ in the resulting solution at time t. In (2-5), x_i is the mass fraction of the tracer element in the glass, S is the glass surface and V is the volume of the analyzed solution. In this thesis, the terms "Quantity of altered glass per day" and "Alteration rate" are used interchangeably.

The maximum quantity of altered glass per day QAG_{max} is computed in accordance with (2-7):

$$QAG_{max} = k^+ * \exp^{\frac{-Ea}{R}\left(\frac{1}{T_0} - \frac{1}{T_{exp}}\right)} * 10^{-(pH)*n}, \qquad 2\text{-}7$$

where R is the ideal gas constant, Ea is the activation energy defined experimentally, n is the constant determining the dependence to pH, T_0 is the absolute zero temperature, T_{exp} is the experiment temperature, k^+ is the dissolution rate of PRI in pure water. It should be noted that (2-7) is valid for temperature values between 25°C and 100°C and pH between 6 and 10.

2.1.2.2. GRAAL implementation in a reactive transport code

The HYTEC computational code developed by MINES ParisTech was chosen for

implementing the GRAAL model. This implementation did not demand any software adaptation since the GRAAL formalism is totally consistent with the reactive transport code HYTEC. HYTEC is based on the geochemical code CHESS and the flow, heat and transport library R2lib.

The principal requirements for HYTEC to handle GRAAL equations, were the availability of the Monod type equation, the ability to use the concentration of a solid (glass) as a variable of the equation and an adaptive time step (Frugier et al. 2018). That is, the time step needs to be small at the beginning of the calculation when the protective layer is thin to prevent its immediate dissolution.

The passage from GRAAL model to HYTEC is realized by treating Equation 2-3 as a Monod type equation and by using general kinetic formulation to describe the dissolution equation (Table 2-3).

Table 2-3 Correspondence between the parameters of the GRAAL model and of HYTEC code

	GRAAL model	HYTEC code
Parameter	PRI thickness	PRI concentration
Primary solid alteration rate controlled by protective layer's thickness	$\frac{D_{PRI}}{x_{PRI}} = \frac{r_h}{1 + x_{PRI}\frac{r_h}{D_{PRI}\frac{\pi}{2}}}$ $D_{PRI}(T, pH) = D_0 \times [OH^-]^{n'} \times e^{-\frac{E'_a}{RT}}$	$r_h \frac{half - saturation}{half - saturation + C_{PRI}}$ W term specifying the dependence on pH
Protective layer's dissolution rate	$k^+ \times [H^+]^n \times e^{-\frac{E_a}{RT}} \times \left(1 - \frac{Q_{PRI}}{K_{PRI}}\right)$	Rate, solid saturation Y- term specifying the dependence on the saturation state , activity W-term specifying the dependence on the pH

Note to the Table 2-3: definition of all variables is specified in the following paragraphs.

The concentration of the protective layer (C_{PRI}) calculated by HYTEC in each cell of modeled glass geochemical unit is proportional to the thickness of the protective layer x_{PRI} - principal GRAAL parameter (Equation 2-8):

$$X_{PRI} = \frac{C_{PRI}}{\rho_{PRI} S_{sp} C_v}, \qquad 2\text{-}8$$

where ρ_{PRI} is the protective layer's molar densty, S_{sp} is the specific surface area of the glass (named primary solid), C_v is the concentration of the primary solid in the calculation cell.

The mass balance is written for each element belonging to the glass and the PRI as defined in Equation 2-9:

$$F_i = \frac{i_{PRI}\rho_{PRI}x_{PRI}}{i_{PS}\rho_{PS}x_{PS}} \qquad 2\text{-}9$$

where F_i is the fraction of the element from the primary solid found in the PRI, i_{PRI} and i_{PS} are the molar fractions of element i in the PRI and in the primary solid, x_{PRI} and x_{PS} are the thicknesses of the protective layer and of the primary solid that was altered.

Equations 2-8 and 2-9 enable user to calculate half-saturation term that makes part of the Monod-type equation presented in Table 2-3:

$$half - saturation = \frac{D\frac{\pi}{2}}{r_h} F_i \frac{i_{PS}}{i_{PRI}} \rho_{PS} S_{sp} C_v = \frac{D\frac{\pi}{2}}{r_h} \rho_{PS} \frac{i_{PS}}{i_{PRI}} S_{sp} C_v \ , \qquad 2\text{-}10$$

In Equation 2-10, D is the interdiffusion coefficient that varies with temperature and pH as defined in Equation 2-11.

$$D(T, pH) = D_0 \times [OH^-]^{n'} \times e^{-\frac{E'_a}{RT}} \qquad 2\text{-}11$$

where D_0 is the interdiffusion constant, E'_a is the activation energy associated to the interdiffusion coefficient, n' is the pH-dependence factor.

One example of HYTEC file (htc.) is shown below. It includes the specification of the database, the flow type, the type of discretization and choice of solver, the definition of all geochemical units associated to all zones specified in the mesh file.

```
database = chess_graal.tdb
flow-regime = saturated, stationary
solver-regime = vertex
grid-regime = vertex fissure_vertex_carre_verre.msh

# Geometry definition
# -------------------
zone 1 {
   permeability = value or NA when the value is read from the externally provided table
   diffusion = value or NA when the value is read from the externally provided table
   porosity = value or NA when the value is read from the externally provided table
   geochem = water
}
zone 2 {
   permeability = value or NA when the value is read from the externally provided table
   diffusion = value or NA when the value is read from the externally provided table
   porosity = value or NA when the value is read from the externally provided table
   geochem = glass
}
```

In addition, the definition of the composition of assigned geochemical units and overall

definition of the chemistry block (directly related to the formalism of GRAAL) is to be done inside the htc input file.

To fill this part, user needs to specify the parameters governing the primary solid alteration rate (Figure 2-3 lines 3-35) and the protective layer's dissolution rate (Figure 2-3 lines 38-48). Within HYTEC, the following syntax is adopted: the law of glass dissolution is written in three term: (i) inter-diffusion applied to glass (product of rate and half-saturation, Figure 2-3 lines 3-19), (ii) velocity of retro-diffusion applied to PRI (the same parameters as for inter-diffusion, Figure 2-3 lines 20-35) and (iii) velocity of hydrolysis of PRI (which concerns the initial velocity of dissolution, PRI ionic product and solubility, Figure 2-3 lines 38-48).

```
1 # KINETIC (for geochemical zone # 105)
2 # ---------------------
3 # Applied to glass, describes a congruent dissolution of the primary solid
4 extend mineral CJ4_105 {
5   kinetics {
6     area = CJ4_105
7     rate = -1.05e-4 mol/m2/s
8     monod {
9        species = SiAl
10       half-saturation = 9.173295e-14 molal
11       power1 = -1
12       power2 = 1
13    }
14    w-term {
15      species = OH[-]
16      power = -0.649
17    }
18  }
19 }
20 # Applied to PRI, describes a backward precipitation of the protective layer
21 extend mineral SiAl {
22    kinetics {
23    area = CJ4_105
24    rate = 1.8872e-5 mol/m2/s
25    monod {
26       species = SiAl
27       half-saturation = 9.173295e-14  molal
28       power1 = -1
29       power2 = 1
30    }
31    w-term {
32      species = OH[-]
33      power = -0.649
34    }
35    }
36
37
38 # Classical dissolution reaction, applied to PRI
39    kinetics {
40     area = CJ4_105
41     rate = -3.05e-12 mol/m2/s
42     y-term, species = SiAl
43     w-term {
44       species = H[+]
45       power = -0.4
46     }
47   }
48   }
```

Figure 2-3 Fragment of HYTEC script specifying kinetics of glass dissolution in one geochemical zone.

The first group of parameters specifies the Monod-type equation and the dependence on the pH. The second group of parameters is used to designate pH and temperature dependence of the initial PRI dissolution rate and the exponential rate drop when the concentrations approach saturation of the PRI.

2.1.2.3. Modeling options proposed by GRAAL model

In the scope of the GRAAL model, two approaches may be followed:

1. Fracture approach
2. Porous medium approach

Fracture approach

1. This approach is used when modeled fractures are described explicitly, it falls in the framework of the discrete modeling (Figure 2-4).
2. It assumes that there are 2 zones inside a modeled system: a glass zone and a fracture zone.
3. From the physical point of view, the fracture zone brings properties of liquid medium (as it is filled with water); the glass zone shows properties of liquid medium also. The glass zone is modeled by a film of a unit mesh thickness, in which all the glass is concentrated. This glass zone is seen as a source of material immediately available at the glass / water interface.
4. There are two geochemical units: water and glass.
5. The transport of material could be monitored in two perpendicular axes (dX, dY).

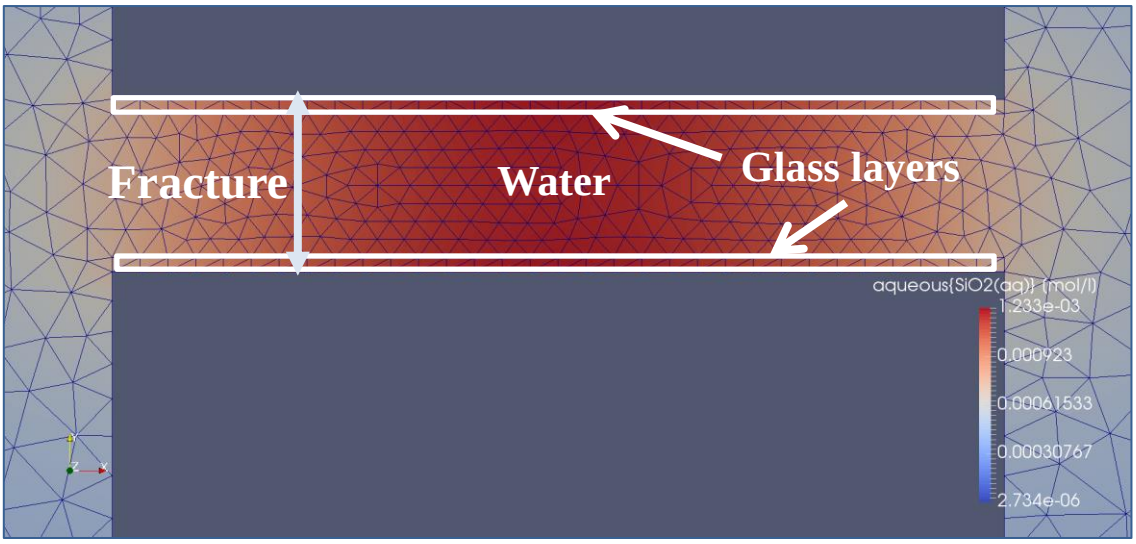

Figure 2-4 Representation of fracture modeling approach: two geochemical zones are defined.

Porous medium approach

1. This approach is used when modeled fractures are described implicitly; it falls in the framework of the homogenized modeling and is used for the equivalent porous medium modeling (Figure 2-5 right).
2. It assumes that there are N zones inside a modeled system: homogenized zones of

water and glass.

3. These zones have properties of equivalent porous medium. Their calculation is shown in Section 5.3.3
4. There are N geochemical units, where N is the number of the meshes of the porosity grid. The necessity to create several geochemical units is explained by the varying porosity that makes glass concentration and half-saturation term vary accordingly.
5. In this approach, transport along dY axis could be neglected, because the gradient of the dissolution rate is insignificant. However it is possible to monitor the transport of material along dX.

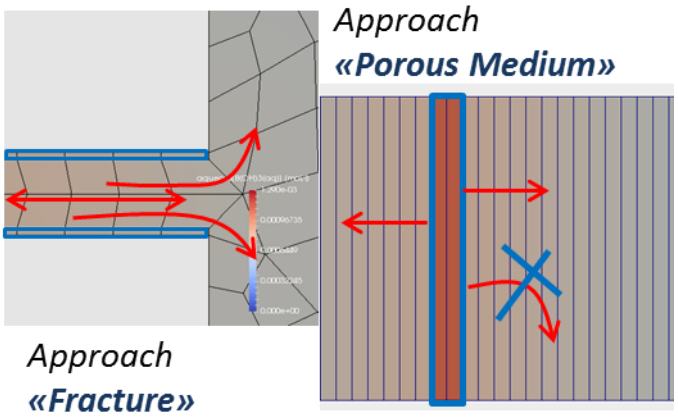

Figure 2-5 Differences between "Fracture" and "Porous Medium" modeling approaches

The passage from "Fracture" to "Porous medium" approach includes:

i. calculation of the equivalent parameters of the specific glass surface, the glass mass per unit volume, the half-saturation factor;
ii. computation of the porosity grid, showing the ratio of the volume of fractures over the volume of fractures and matrix together in each mesh of the equivalent porous medium system.

The parameters governing the kinetics of the glass dissolution are specified in the section "geochemical units" of the htc file, while the grids of the porosity, the hydraulic conductivity and the pore diffusion are provided in the form of the table including the coordinates of the mesh nodes and the corresponding parameter values. This file is read externally.

Here below, the examples of the application of "Fracture" and ''Porous medium" approaches for one, three and five fractures, are presented. Figures 2-6, 2-7 and Table 2-4 provide some details about the way in which the simulations were conducted, and the approaches were changed.

It should be noted that the same physical representations will be met in Section 4.2, when we will deal with the reproduction of the experimental results obtained by Chomat. Here our idea is to show that "Fracture" and "Porous medium" approaches are compatible, i.e. to

demonstrate that the GRAAL model is applicable for modeling glass fracture network represented by its equivalent porous medium.

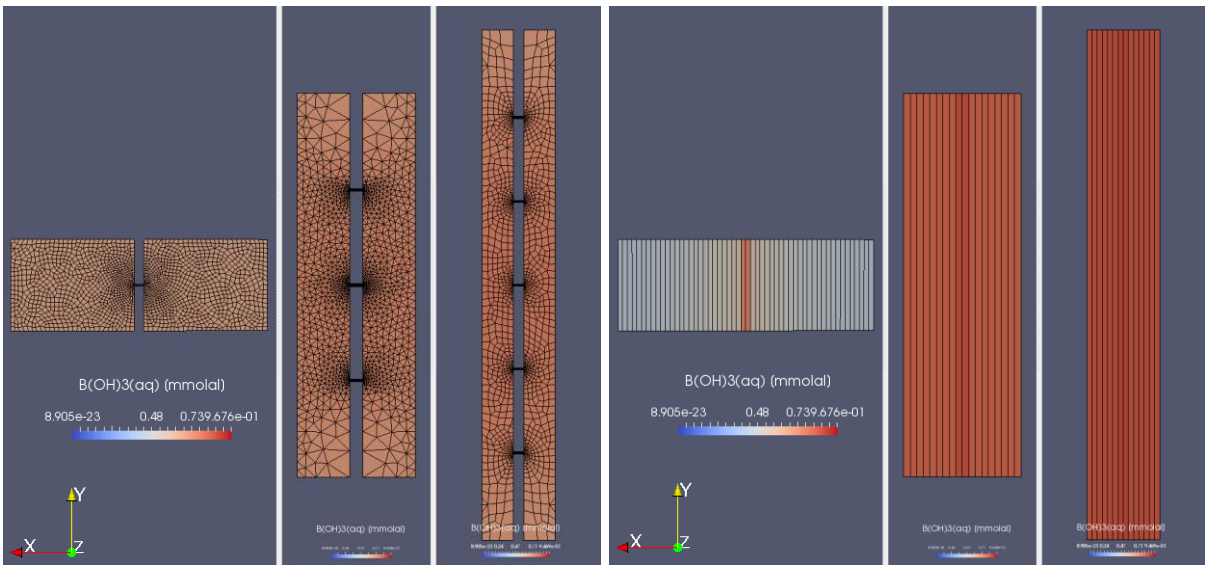

Figure 2-6 Examples of systems used to study the aqueous alteration of the glass by applying discrete and homogenized equivalent approaches. The three first models describe fractures, glass and water-filled recipients explicitly, water and glass geochemical units are separate. The three last models represent their equivalent counterparts with fractures being described in an indirect way by introducing porosity value in a system. The volume of water in two recipients remains identical for each pair of models (DFN- homogeneous).

Table 2-4 Comparative table of the geometry-related parameters governing the kinetic of glass alteration.

Model	Geometries of modeled system	Mass of glass	Experience volume V_{exp}	Glass specific surface S_p	Glass mass per unit volume C_v	Half-saturation	Porosity
Fracture	a,b,c	M_{glass}	$a \times 1m \times (o/2)^2$	$a \times 1m / M_{glass}$	M_{glass} / V_{exp}	$K \times S_p \times C_v$	1
Porous Medium	a,b,c	$M_{glass} \times N_g$	$a \times 1m \times o \times N_g$	$a \times 1m \times N_g / M_{glass} \times N_g$	$M_{glass} \times N_g / V_{exp}$	$K \times S_p \times C_v$	$V_{fr} / V_{fr} + V_g$

[2] Half of the aperture is used because one wall of fracture "sees" only one half of the fracture opening.

Notes for Table 2-4: a is the fracture length (in porous medium approach a was equal to the length of the porous medium system); b is the length of the recipient filled with water; c is the height of the compound filled with water, o- is the fracture opening; ε is the thickness of the glass layer in contact with the fracture; ϱ is the glass density; m_{glass} is the user-defined (or experimental) mass of glass; N_g is the number of modeled glass plates, N_f is the number of modeled fractures; A is the fracture aperture, $K=D_{PRI}\times\rho_{PS}\frac{i_{PS}}{i_{PRI}}$ where i_{PRI} is the molar fractions of elements in the PRI and i_{PS} - in the glass, ρ_{PS} *is the* glass molar density and D_{PRI} is the e diffusion coefficient of PRI; $V_{fr} = a\times1m\times A\times N_f$; V_g is the user-defined (or experimental) volume of glass.

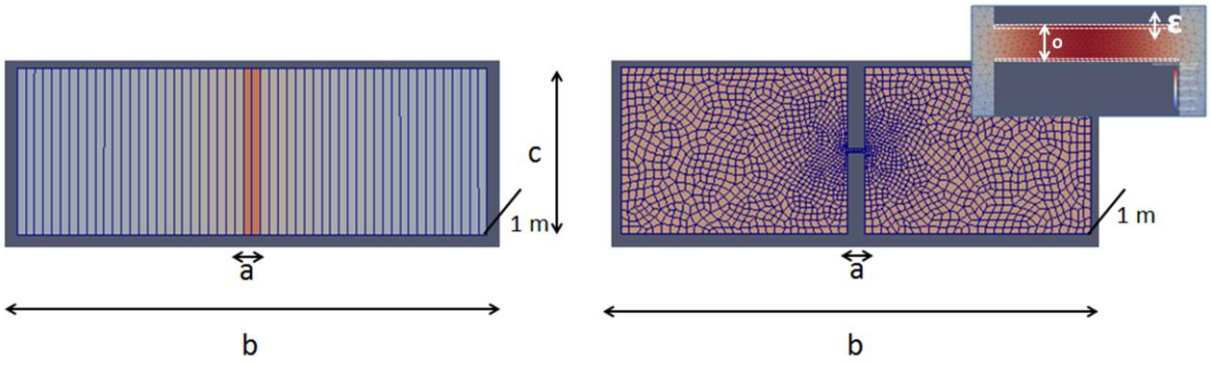

Figure 2-7 Image accompanying Table 2-4. Case "1 modeled fracture" in the scope of "Porous Medium" (left image) and "Fracture" (right image) approaches

It should be noted that:

1. By default in HYTEC, in 2D simulations, the third dimension (depth) is equal to 1 m.
2. Ɛ is a purely modeling parameter representing the thickness of the film of glass covering fracture (Figure 2-7) for the DFN approach. For all cases presented here, Ɛ is taken constant and equal to 10 μm. It was shown that this value needs to be small enough with respect to the fracture aperture (Repina 2016). For fractures whose opening is higher than 100 μm, it was advised to take Ɛ equal to 10 μm as a tradeoff between the time of calculation and the accuracy of calculations.
3. Since in the case of "Porous medium approach" the material transport is not limited in dY direction in contrast to the "Fracture" approach, it was proposed to run a supplementary case (1 fracture, discrete model) where the water homogenization is amplified by increasing its coefficient of diffusion. This allows the reservoirs of water to be modeled as an agitated reactor with homogeneous concentrations.

Figure 2-8 provides the results obtained by conducting RTM in the framework of "fracture" and "porous medium" approaches in diffusive mode. It is apparent from the curves, showing the ratio of the quantity of altered glass (QAG, equation 2-6) over the maximum quantity of altered glass (QAG_{max}, equation 2-7) and the curves of average pH in water, that two tested approaches give quit similar results for the cases of three and five fractures. There

is, however, some difference between the profiles of QAG/QAG$_{max}$ and pH for the case of 1 fracture modeled by fracture and porous medium approaches. It is expected to be related to the diffusion process. In fact, for both models, a unique coefficient of diffusion was taken: $D_x=D_y=D_w$, where D_w – is the water self-diffusion coefficient. Certainly, the question of the calculation of the equivalent diffusion coefficient must be considered in the future. It will be dealt with in Section 5.

The supposition that the difference between two models comes from an unadapted coefficient of diffusion of the porous medium model is confirmed by the results of modeling. Indeed, once the homogenization of water is favored, the similar QAG is obtained by both approaches. To sum up, the results of the modeling indicate that GRAAL model can be applied to model glass aqueous in fractured media in both discrete and equivalent porous medium. However, certain attention should be payed to the calculation of the equivalent hydraulic and diffusive properties of the equivalent model.

Input parameters used to conduct the modeling are provided in Table 2-5.

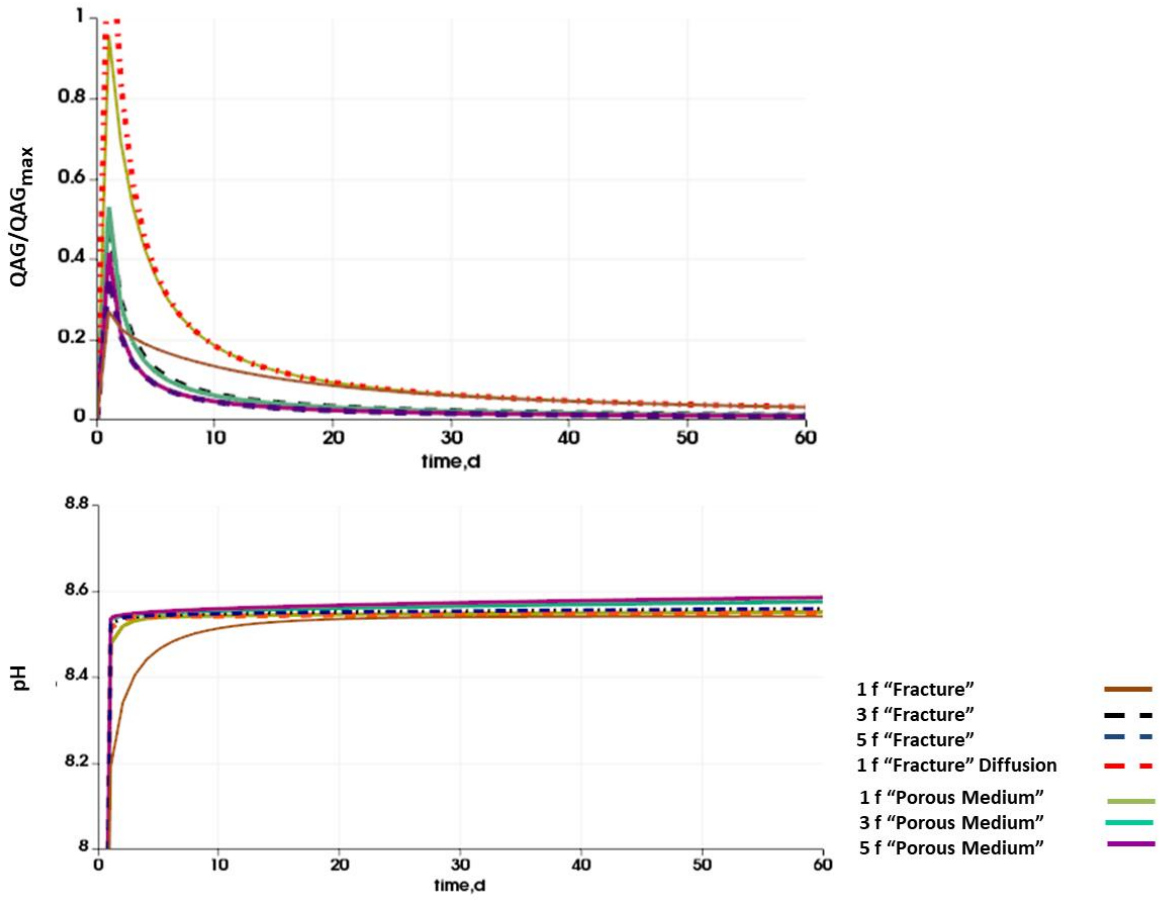

Figure 2-8 Results of RT modeling in the context of "Fracture" and "Porous medium" approaches of GRAAL model

Table 2-5 Summary of the input parameters of the modeled cases

Name	Modeling approach	Number of	Fracture aperture,	Fracture length,	Water diffusion	Volume of	S/V, 1/m

		fractures	μm	cm	coefficient, m^2/s	water, ml	
1f « Fracture »	Fracture (discrete)	1	120	0.0625	10^{-9}	97.5625	2e+04
3f « Fracture »	Fracture (discrete)	3	120	0.0625	10^{-9}	91.9875	2e+04
5f « Fracture »	Fracture (discrete)	5	120	0.0625	10^{-9}	115.063	2e+04
1f «Fracture»_ Diffusion	Fracture (discrete)	1	120	0.0625	10^{-8}	97.5625	2e+04
1f « Porous Medium»	Porous medium (homogeneous equivalent)	1	120	0.0625	10^{-9}	97.5	2e+04
3f « Porous Medium»	Porous medium (homogeneous equivalent)	3	120	0.0625	10^{-9}	91.8	2e+04
5f « Porous Medium»	Porous medium (homogeneous equivalent)	5	120	0.0625	10^{-9}	114.75	2e+04

2.2. Experimental studies and modeling efforts aiming at the fracture network characterization

2.2.1. Fracturing ratio by static and dynamic measurements

Fracture network characterization is a subject of prime importance since fractures could be responsible for the increase of the reactive surface and, very probably, would provide preferential paths for the migration of elements in solution. This characterisation can be based on static (cartography or imagery), or dynamic (analysis of the flow circulating under different conditions through the studied fracture network) measurements that optimally should be conducted together.

Since, for a long time, glass canister fracture network morphology characterization has not been on the agenda, the intensity of the glass block fracturing has been only characterized by a relatively simple and practical for chemical purposes parameter, named fracturing ratio (FR) and defined by equation 2-12:

$$FR = \frac{\text{total measured surface}}{\text{external surace of package}} = 1 + \frac{\text{internal surface}}{\text{external surface of package}}, \qquad 2\text{-}12$$

where the outer surface of the package is the geometric surface of the cylinder of the glass package, and the inner surface is the surface developed by the entire network of cracks

inside the glass block. The total measured surface is the sum of the internal surface and the external surface of the package.

The techniques for evaluating the internal surface of the crack network are either based on dynamic leaching experiments using the measurement of the quantity of glass altered, or based on physical measurements allowing the fractured surface to be access directly. Each technique has its assumptions and its own limitations. For example, in case of measurements by leaching, only the part of the network accessible to water in the time limit of the experiment (useful surface) can be accounted for. On top of that, when determining the useful ratio of fracturing by leaching experiments, a homogeneous and constant rate of glass alteration is presumed.

Regarding the FR estimation by granulometric sorting, it comes along with the physical damaging of the block that often results in the opening of cracks, or even generation of new cracks. Concerning the tomographic technique, its main limitation relates to a spatial resolution that is dependent on the size of the camera recording the different images at different scans. Thus, by conducting tomography at the scale of glass canister, only part of cracks (most opened) can be captured. However, it is of common practice to sample separately the most interesting areas in order to come up with the characterization of their structure with high precision.

The alteration of the fractured glass block makes it possible to estimate the quantity of altered glass by equation 2-13:

$$\text{Quantity of altered glass} = \text{QAG} = \iint_{\text{Surface, time}} V(r,\theta,z)\, dS(r,\theta,z)\, dt, \qquad 2\text{-}13$$

where V(r, θ, z) is the rate of alteration at a given instant and at a given point of the glass block, S(r, θ, z) is the surface in contact with water (surfaces of cracks). As the velocity regime is not known at all times, and the surfaces are not always known, the estimated fracturing ratio determined by leaching experiments is named the useful fracturing ratio, assuming that the rate regime of the experiment $\bar{V}$ is known, constant and uniform. Then, $QAG = \bar{V}\ S_{measured}$. For the initial rate regime, the useful fracturing rate then becomes: $\tau_0 = \frac{QAG/V_0}{S_{external}}$. For the residual velocity regime, the useful fracturing rate then becomes: $\tau_r = \frac{QAG/V_r}{S_{external}}$. It should be noted, that the QAG is generally determined experimentally by chemical analyzes.

Two full scale SON68 blocks were tested in Soxlhet studies to acquire the initial rate of alteration (alteration in dynamic mode of water renewal), (Minet et al. 1999, 2003). Results showed that the useful fracturing ratio specific to this rate regime is close to 5. Other Soxhlet tests on highly damaged blocks yielded useful fracturing ratio in residual rate regime between 24 and 65 (Minet et al. 2003).

Physical measurement by tomography was applied to 4 blocks at scale 1. The obtained fracturing ratio was between 4 and 15 (Goebbels et al. 1998; Sené et al. 1999).

Finally, granulometry tests performed on 2 blocks gave a fracturing rate equal to 15 (Moncouyoux et al. 1991).

While the fracturing ratio values determined by these two groups of methods are of the same order of magnitude, they do not provide any insight about the morphology of the fracture network. For the purposes of reactive transport modeling, it is certainly penalizing, owing to the fact that processes of transport and flow happening inside fracture are strongly controlled by the fracture network inherent parameters, like fracture aperture distribution, fracture connectedness, density (de Dreuzy 2008; Chomat 2008; Davy et al. 2006).

2.2.2. Optical microscopy, scanning electron microscopy (SEM)

Optical microscopy and scanning electron microscopy are two frequently used methods when studying the products of the glass alteration. In the framework of the study carried out in CEA/LCLT that focused on a long-term (7.5 years) full-scale glass block alteration conducted in static conditions on the SON68[3] glass block (Minet et al. 2013), these two microscopy techniques enabled the characterization of the crack network, including the measurement of the cracks apertures and the measurement of the altered layer thickness inside these cracks.

The post-mortem observations of several transversal cross-sections of the ALISE block (see Section 5) aimed at fracture mapping, fracture parameters reporting and measurement of the thickness of altered glass found on the fracture lips.

The overview of the fissure network of disk #6 is shown in Figure 2-9. It was obtained by drawing cracks visible to the naked eye, with the help of an illuminated magnifying glass. In accordance with the map, an internal zonation from the center to the periphery of the glass canister was reported.

By naked eye observations, a radial zonation was proposed, it includes:

- a peripheral zone near the edges of the block, with a higher density of cracks;
- an intermediate zone with less cracks;
- a central zone near the centre of the inner crack network, where bubbles of “gas porosity” are present.

[3] Inactive glass, simulating French nuclear glass R7T7, historically the most studied

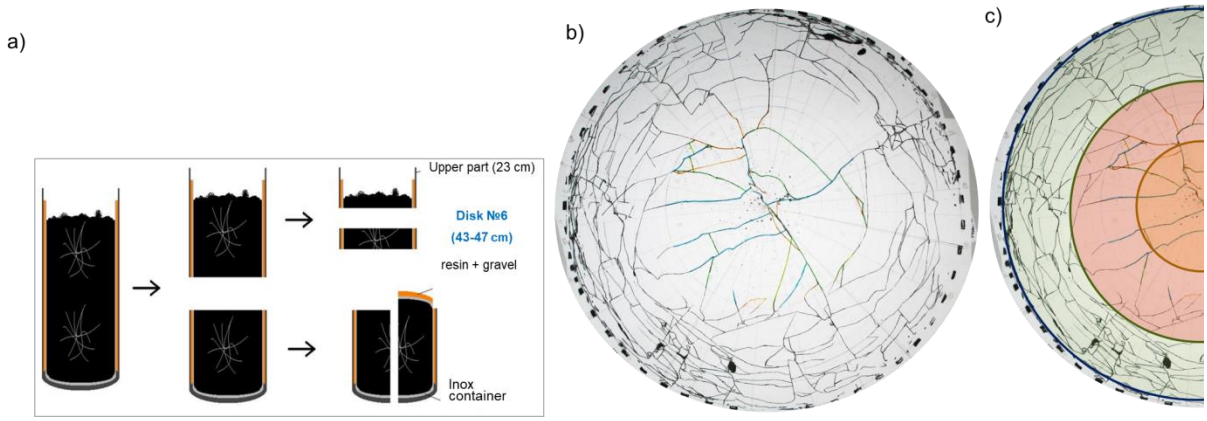

Figure 2-9 a) Schematic view of the cutting of the block; b) Map of the network of fissures of the disc #6; c) Radial zonation subjectively chosen to characterize fractures, $R_{central}$=R_{interm}=R_{periph}=7cm

Later, in order to carry out detailed observations of the internal parts of the block by microscopy techniques, disc # 6 was cut by means of a diamond saw. It should be noted that a resin coating was made to minimize any additional fracturing that could have been caused by cutting (Section 5).

Next, to make the samples observable at the SEM, each of them was first manually polished with diamond discs down to 1 µm grain size, then metallized with a uniform platinum layer. Three selected pieces of glass belonging to different regions of the disc were examined in detail (Figure 2-10). In that respect, the fracture lengths were manually measured using a double decimetre ruler on the enlarged images, whereas crack openings as well as the thicknesses of the altered films were measured using the microscope imaging software.

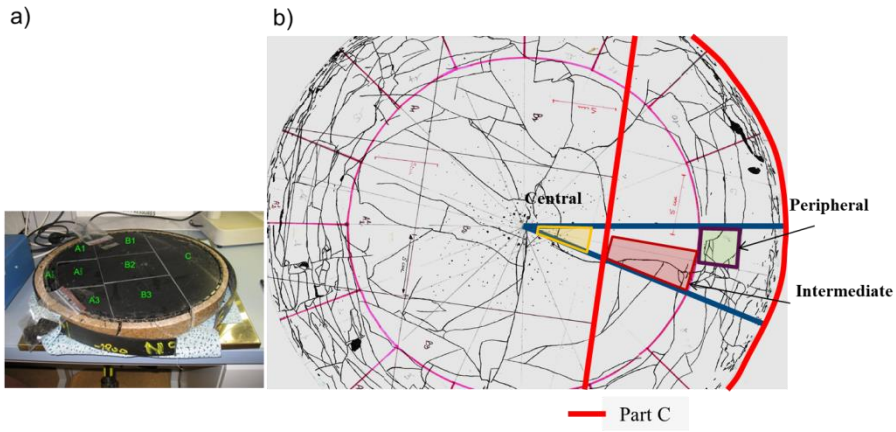

Figure 2-10 a) view of the disc #6 split in several parts, b) fragment of the map of the network of fissures with localized central, intermediate and peripheral zones.

The observations showed that the alteration film was present in each examined fracture, even the smallest one, suggesting that water could penetrate the entire network. The statistics for three samples are given in Table 2-6. It should be noted that only 4 fractures

were recorded by analysing the sample of the central zone, which certainly puts at risk the soundness of its results. The relative uncertainty of the measurements was reported close to 10% for length, aperture and alteration film thickness measurements[4].

From the data presented in Figure 2-11, it can be noted that firstly, for samples of peripheral and intermediate zones, aperture increases with length; secondly, mean altered glass thickness of the sample from the intermediate zone is higher than the mean altered glass thickness of the sample from the peripheral zone for all families of openings; thirdly, most of the fractures located in the peripheral zone had apertures lower than 10 µm and mean altered glass thickness close to 4-5 µm; fourthly, most of the fractures located in the intermediate zone had apertures close to 50 µm and mean altered glass thickness close to 7-10 µm. Concerning the central zone where only 4 fractures were found, no conclusion whatsoever could be drawn.

Table 2-6 Observation results on peripheral, intermediate and central zone samples, adapted from (internal CEA communication Yves MINET et al. 2013)

Sample	Surface (cm^2)	S_{sample}/S_{zone}	Nb. of fractures	Areal density (cm^{-2})	Mean length (cm)	Mean aperture (µm)	Mean thickness of glass altered layer (µm)
Peripheral	11,3	0.015	102	9.0	0.35	77	3.9
Intermediate	29,1	0.063	51	1.8	0.70	90	12.8
Central	9,55	0.062	4	0.42	1.39	33	3.7

N.B. Mean thickness of glass altered layer and mean aperture are weighted by cumulated fracture length

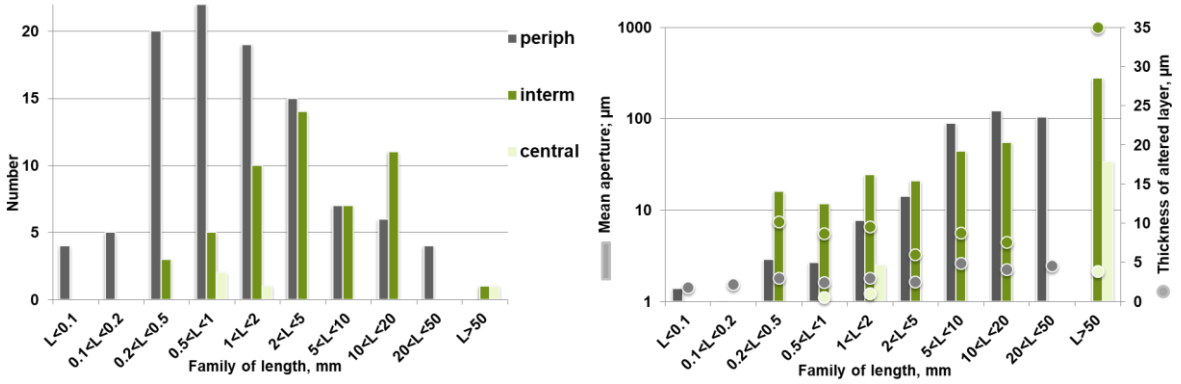

Figure 2-11 Histograms of : a) the number of fractures belonging to each family length; b) the mean aperture and the mean thickness of altered layer in fractures belonging to each family length

The overall conclusions derived from the microscopy observations are: 1. fracture network of a scale of glass block is highly inhomogeneous and interconnected; 2. fracture openings have a very large variability, at least 3 orders of magnitude (opening from a fraction of µm to a few hundreds of µm).

[4] Except for smaller apertures and thicknesses, for which an absolute uncertainty is about 1 µm

Although it was important to obtain results of such precision, this local sampling is still insufficient for the purposes of reactive transport modelling at the glass canister scale. In addition, it is possible to question the representativity of the chosen glass pieces together with the reasoning of the disk radial zonation.

2.2.3. FRAGMA

Techniques employed so far for fracture network characterization turned out to be inappropriate for the characterization of a network at the scale of a glass package. Thus, Crevoisier et al. (Crevoisier et al. 2011) argued that, although tomography has been as a powerful tool for fracture numerical description at scale 1, its digital representation is not adapted as an input mesh for large scale reactive transport simulations. Moreover, a 3D model of the network reconstructed from a series of 2D tomography images is considered to be non-complying with the technical imperatives of any efficient numerical simulation (non-continuous fissures, not closed topology of a constructed geometrical domain, presence of geometrical elements of highly variable sizes).

Subject to the above constraint, FRAGMA was put in place (Crevoisier et al. 2011). FRAGMA is the software able to generate a realistic 2D geometry of the fissure network inside the glass based on mechanistic analogies.

The principles of the fracture network generator are primary based on geometrical analogies revealed by observations at different resolutions (from the naked-eye to tomography analyses). FRAGMA also takes into account possible local relaxation and stress variation during fissure propagation via stochastic law determining whether fracture stops or continues growing. As regards the input data for the fracture network construction presented in Figure 2-12a, it was obtained by the analysis of the characteristics of one glass semi-cylinder 2D cross-section given by tomography. A weighting of the obtained distribution laws by stochastic parameters was further used to represent the heterogeneities of the material and the variations inherent to the industrial techniques of glass block elaboration.

The algorithm coded in FRAGMA follows several steps: 1. definition of geometric analogues; 2. generation of the median lines of the cracks, comprising the insertion of the initiation points and the segments representing the median lines of the fractures propagated from the points of initiation; 3. explicit fracture generation by attributing opening values to the middle segments; 4. insertion of the segments representing fracture walls.

Two realizations of the fracture network at the scale of the semi-disc and the glass block are shown in Figure 2-12b-c.

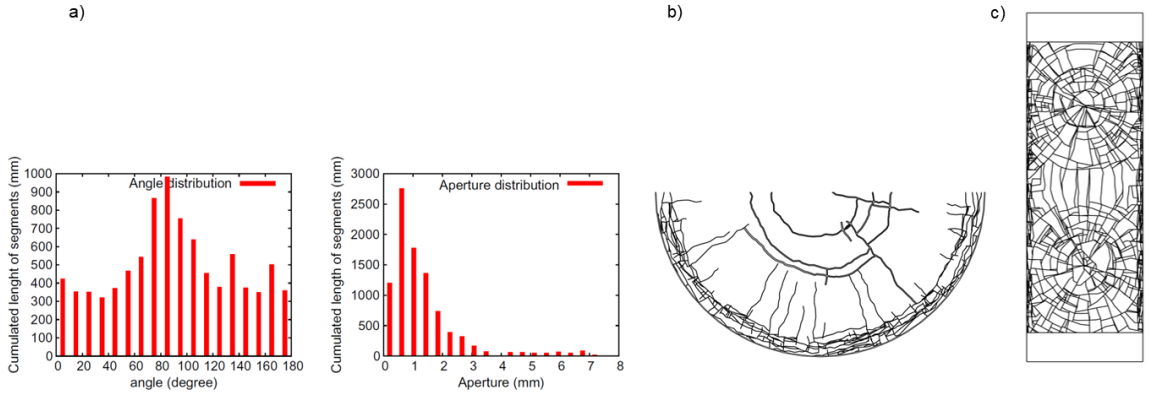

Figure 2-12 Glass fracture network stochastic geometries construction by FRAGMA code: a) distributions of apertures and directions (with respect to the radial direction) obtained by the characterization of a glass semi-cylinder 2D cross-section given by tomography; b) fissure network of a semi-disc; c) simplified fissure network of a glass block at scale 1

Certainly, the modeling effort of (Crevoisier et al. 2011) was important; it probably could be used to create a model for further reactive transport modeling. However, it is likely to be too computationally demanding since it provides a discrete fracture network. Moreover, it relies on input data provided by a meticulous characterization of a glass block at scale 1. In fact, at this step the elaboration of the methodology comprising (i) characterization of fracture network as the scale of vitrified glass block, (ii) calculation of equivalent diffusion, hydraulic and glass aqueous alteration kinetics governing parameters and subsequent (iii) reactive transport modeling with consideration for variability of fracture network is seen as a primordial exercise that can no longer be postponed.

2.3. Reactive transport modeling

2.3.1. General overview

Reactive transport (RT) as a research focus has appeared relatively recently with the publication of Reviews in Mineralogy and Geochemistry 34: Reactive Transport in Porous Media (Lichtner 1996), but rapidly gained the recognition of the Earth and environmental science community. Its multi-disciplinary topics stay at the crossroad of geochemistry, hydrology, and engineering applications. Firstly dealt with the contaminant hydrology, reactive transport principles have expanded to become broadly utilized throughout the Earth and environmental sciences. RT is now employed to address a wide variety of natural and engineered systems across diverse spatial and temporal scales, in cooperation with advances in computational capability, quantitative imaging and reactive interphase characterization techniques (Steefel, Beckingham, et al. 2015; Xiao 2018). Reactive transport modeling (RTM) has shown to be an essential tool for the analysis of coupled physical, chemical, and biological processes in Earth systems, and has the additional potential to integrate the results from fundamental research (Steefel et al. 2005; MacQuarrie et al. 2005). Using a modern reactive transport approach, it is possible to provide predictive capabilities for Earth and environmental systems that go beyond the empirical models that are still in wide use today.

CHAPTER 2: STATE OF THE ART

Commonly used reactive transport codes include following modules: transport, flow, geochemistry and microbiology (Steefel, Appelo, et al. 2015). Table 2-7 summarizes the flow and the transport capabilities of the most frequently used, widely available RT codes. Table 2-8 summarizes their geochemical and microbial capabilities. Table 2-9 provides a list of numerical characteristics of the codes.

With reference of the data set out in these tables, it is evident that the choice of the calculation code depends on the characteristics of the medium under study (saturated flow, multiphase flow, multiple continua, reaction induced porosity-permeability change, etc.) and its ability to reproduce a modeled phenomenon.

The coupling between modules is considered in the governing equations describing reactive transport in porous media. The equations are based on the conservation of energy, solvent mass, solute mass, and momentum (the Navier–Stokes equation applicable to flow at the pore scale, Darcy's law applicable to flow in porous media at the continuum scale, and Cauchy's equation describing the deformation of the solid phase), and a variety of constitutive laws for key parameters. As reported by (Steefel et al. 2005), the principal feedbacks between the equations/processes include:

1. Coupling between energy and fluid flow: it is primarily performed through the advection of heat and the effect of temperature on the fluid density;
2. Coupling between the flow (conservation of momentum) and the conservation of fluid or solid mass: it is typically treated by solving the two together to obtain the flow field or the deformation of the solid phase.
3. The effect of dissolution or precipitation of minerals on concentrations of solutes and the mass of minerals;
4. Coupling between fluid flow and solute concentrations: this is primarily effectuated through the advection of solutes and/ or colloids and the effect of concentration on fluid density and through modifications in the porosity and permeability as a result of mineral dissolution or precipitation.
5. Coupling between temperature (conservation of energy) and solute concentrations through the effects of temperature on the thermodynamics and on reaction rates and the effect of chemical reactions on the thermal regime where heats of reaction are significant.

There are three different types of models depending on the scale of interest to describe reactive transport in porous media 1) continuum models, 2) pore scale models, and 3) hybrid models involving a combination of scales.

The continuum equations are often obtained by averaging over a representative elementary volume (REV) resulting in effective macroscale parameters. According to continuum models, the flow is described in terms of Darcy's law with velocity proportional to the pressure gradient; and the uniform reaction rates within the control volume are supposed. Pore scale

models include pore network (Meakin et al. 2009; Steefel et al. 2013) and lattice Boltzmann models (Kang et al. 2003; Kang et al. 2007). They are applied when the pore scale gradients and processes (i.e. wormholing) must be captured and accounted for. Multiple continuum (hybrid) models (Battiato et al. 2011; Weinan E. et al. 2003) which combine pore scale and continuum scale behavior begin to be payed attention to because systems, involving multiple characteristic length scales, require the separate description of these continua.

Regarding the representation of fractured porous media, a number of different conceptual frameworks can be mentioned. They include: discrete fracture model (DFM), equivalent continuum model, variations of dual and multiple continuum models (double porosity (2Φ) – single permeability (1K), double porosity (2Φ) – double permeability (2K) etc.). Incorporating chemical reaction in these models of fractured media very often requires an extension of the techniques to represent flow and transport; and, as a matter of fact, it necessitates greater computational effort to be solved: this is particularly the case for the DFM.

The term discrete fracture model refers to a model in which the positions of fractures and their characteristics are explicitly defined. The flow and transport equations are usually solved separately for fractures and matrix. The coupling between both media is ensured via a coupling term. A successful application of 2D RTM in DFM was demonstrated in (Ghogomu et al. 2000). The model comprised two parallel fractures connected by a third perpendicular fracture, all located within a porous matrix. Although the model did not take into account the feedback between reactions and fracture and matrix properties, it showed the influence of fractures and porous matrix when coupled with multicomponent transport on complex flow fields and irregular spatial distribution of chemical species in the fractured system. Discrete fracture models allow precise quantification of many flow and transport phenomena that are not fully captured by applying continuum models. A great advantage of the discrete fracture approach is that it can account explicitly for the effects of individual fractures on flow and transport. As a consequence, discrete fracture models are popular for studies and applications on limited number of fractures, whereas their application for large-scale flow and transport problems is restricted due to their high computational capacities demand.

Dual (multiple) continuum models are referred to when a fracture network model is represented as a composition of two (multiple) coexisting continua, i.e. fracture and matrix. In these models, the communication representing the mass exchange between media is established via a coupling term. This term considers the surface area between continua and the flux between them; as a consequence, it necessitates the knowledge of the matrix block equivalent geometries that might be difficult to define precisely (Lichtner 2000). Inside this group of models, it is of common practice to distinguish dual permeability models (2Φ – 2K), which are mentioned when in both media, fractures and matrix, flow takes place, in contrast to double porosity (2Φ – 1K), where matrix is supposed to be diffusive only so that only

mobile-immobile-type solute transport modeling is considered. Although dual continuum models have seen vast application in the petroleum engineering literature (Bourbiaux B. 2002; J. Bourbiaux et al. 1997), for purposes of the reactive transport modeling, their applications stay limited so far. One of the remarkable example that is worth citing is the research by Glassley (Glassley et al. 2003), in which a 2Φ – 2K formulation was used with the aim to describe more accurately fracture-matrix interactions when investigating geochemical evolution of the Yucca mountain waste repository. This dual continuum formulation was chosen because of the practical infeasibility of collecting data for parametrizing DF model. Meanwhile, it should be noted that, even this "simplified" continuum formulation was only feasible with implementation of the code on massive parallel computers. Having said that, it is possible to conclude that dual continuum models are likely to be most applicable to densely fractured systems where the explicit fracture representation is too computationally onerous.

Single continuum (equivalent porous medium) models suppose equal fracture and matrix solute concentrations, but possible different mineral concentrations (Lichtner 2000). Berkowitz (Berkowitz 2002) stated that they are applicable when either the fracture network is dense and highly interconnected, or when the interaction between the fracture network and the porous/permeable matrix allows sufficient interaction to establish a local equilibrium. Application of this model demands the computation of the equivalent hydraulic and diffusive properties obtained, at the stage of parameters upscaling, by considering both fracture and matrix media. As noted in (MacQuarrie et al. 2005), single continuum formulation cannot be applied to any type of fractured media and should be considered with caution. Regarding the applications, the work of (Steefel et al. 1994) touched upon the use of the equivalent continuum model to conduct the RTM in single-phase hydrothermal systems in fractured rock. Some key assumptions, comprising: (i) porosity and permeability update only for fractures and (ii) matrix non-participation in fluid flow and reactive transport, made possible a relatively easy definition of equivalent properties based on the geometry of fracture set.

In this research, we dealt with the reactive transport modeling of borosilicate glass alteration performed in HYTEC reactive transport code at the scale of some fractures up to a glass canister. Regarding the modeling approaches, both discrete and equivalent single continuum (1Φ-1K) models were used. RTM for relatively simple fracture systems was effectuated in the framework of the DFN modeling approach, whereas the application of the RTM at the block scale was conducted in accordance with the equivalent modeling approach. In fact, although the strong coupling (iterative, sequential) scheme, as outlined below in the following section, makes HYTEC particularly useful for the modeling of long-term leaching of solidified wastes (Trotignon et al. 2007a; De Windt et al. 2007), the difficulty in coupling transport, flow and geochemistry modules, when conducting RTM applied to fractured media modeled explicitly, stays pertinent. Even though the choice of the equivalent 1Φ – 1K model could be

argued taking into account a strongly anisotropic fracture network of a glass block and, as a consequence, the complications associated with the determination of the unique representative elementary volume (REV), we found that in the current conditions (availability of computational power, time left for realization, development of the code) the adoption of the single continuum equivalent model was reasonable. Moreover, when considering this equivalent formulation, we took into account the impermeability of the glass matrix and the possibility to adapt the GRAAL geochemical model to the equivalent porous medium representation. Further discussions regarding limitations of currently available RT codes and justification of the chosen modeling approaches could be found in Section 2.3.4.

Table 2-7 A comparison of key flow and transport features of reactive transport modeling codes. Obtained from (Steefel, Appelo, et al. 2015)

Capabilities/features	PHREEQC	HP1/HPx	PHT3D	OpenGeoSys	HYTEC	ORCHESTRA	TOUGHREACT	eSTOMP	HYDROGEOCHEM	CrunchFlow	MIN3P	PFLOTRAN
Dimensions	1D	1,2,3D	1,2,3D	1,2,3D	1,2,3D	1D	1,2,3D	1,2,3D	1,2,3D	1,2,3D	1,2,3D	1,2,3D
Flow												
Saturated flow	Yes	Yes	Yes	Yes	Yes	Yes	Yes	Yes	Yes	Yes	Yes	Yes
Richards equation	No	Yes	No	Yes	Yes	Yes	Yes	Yes	Yes	No	Yes	Yes
Multiphase–multicomponent flow	No	No	No	No	Yes	No	Yes	Yes	Yes	No	No	Yes
Variable density flow	No	No	Yes	Yes	Yes	No	Yes	Yes	Yes	Yes	Yes	No
Non-isothermal flow	No	No	No	Yes	No	No	Yes	Yes	Yes	No	Yes	Yes
Transport												
Advection	Yes	Yes	Yes	Yes	Yes	Yes	Yes	Yes	Yes	Yes	Yes	Yes
Molecular diffusion	Yes	Yes	Yes	Yes	Yes	Yes	Yes	Yes	Yes	Yes	Yes	Yes
Electrochemical migration	Yes	No	No	No	No	Yes	No	No	No	Yes	Yes	No
Dispersion tensor	Diagonal	Diagonal	Diagonal	Diagonal	Diagonal	Diagonal	No	Diagonal	Full	Diagonal	Diagonal	Diagonal
Gas phase advection	No	Yes	No	Yes	Yes	Yes	Yes	Yes	Yes	Yes	Yes	Yes
Gas phase diffusion	No	Yes	No	Yes	Yes	Yes	Yes	Yes	Yes	Yes	Yes	Yes
Colloids	Yes	No	No	Yes	Yes	Yes	Yes	No	Yes	No	No	Yes
Multiple continua	Yes	Yes	No	Yes	Yes	Yes	Yes	No	No	Yes[a]	Yes[b]	Yes

Table 2-8 A comparison of key geochemical and microbial features of reactive transport modeling codes. Obtained from (Steefel, Appelo, et al. 2015)

Capabilities/ features	PHREEQC	HP1/HPx	PHT3D	OpenGeoSys	HYTEC	ORCHESTRA	TOUGHREACT	eSTOMP	HYDROGEOCHEM	CrunchFlow	MIN3P	PFLOTRAN
Geochemistry												
Extended Debye-Hückel	Yes	Yes	Yes	Yes	Yes	No	Yes	Yes	Yes	Yes	Yes	Yes
Davies activity model	Yes	Yes	Yes	Yes	Yes	Yes	No	Yes	Yes	Yes	Yes	No
Pitzer activity model	Yes	Yes	No	Yes[a]	No	No	No	Yes	No	No	Yes	No
Non-isothermal geochemistry	Yes	Yes	Yes	Yes	Yes	Yes	Yes	Yes	Yes	Yes	Yes	Yes
Surface complexation[b]	DDL, Non-edl	DDL, Non-edl	DDL, Non-edl	DDL, Non-edl	DDL, CC	DDL	DDL, CC	DDL, Non-edl	DDL, Non-edl	DDL, Non-edl	Non-edl	Non-edl
Ion exchange	Yes	Yes	Yes	Yes	Yes	Yes	Yes	Yes	Yes	Yes	Yes	Yes
Aqueous–gas exchange	Yes	Yes	Yes	Yes	Yes	Yes	Yes	Yes	Yes	Yes	Yes	Yes
Kinetic mineral precipitation–dissolution	Yes	Yes	Yes	Yes	Yes	Yes	Yes	Yes	Yes	Yes	Yes	Yes
Mineral nucleation	Yes	Yes	Yes	Yes	No	Yes	No	No	No	Yes	No	No
Mineral solid-solutions	Yes	Yes	Yes	Yes	No	Yes	Yes	Yes	Yes	Yes	No	No
Equilibrium isotope fractionation	Yes	Yes	Yes	Yes	Yes	Yes	Yes	No	Yes	Yes	No	No
Kinetic isotope fractionation	Yes	Yes	Yes	No	No	Yes	Yes	No	Yes	Yes	Yes[c]	No
Aqueous kinetics	Yes	Yes	Yes	Yes	Yes	Yes	Yes	Yes	Yes	Yes	Yes	Yes
Radioactive decay chains	Yes	Yes	Yes	Yes	Yes	Yes	Yes	Yes	Yes	Yes	Yes	Yes
Microbial												
Monod kinetics	Yes	Yes	Yes	Yes	Yes	Yes	Yes	Yes	Yes	Yes	Yes	Yes
Thermodynamic	Yes	Yes	Yes	Yes	Yes	Yes	Yes	Yes	Yes	Yes	Yes	No
Biomass growth	Yes	Yes	Yes	Yes	Yes	Yes	Yes	Yes	Yes	Yes	Yes	Yes

Table 2-9 A comparison of key geochemical and microbial features of reactive transport modeling codes. Obtained from (Steefel, Appelo, et al. 2015)

Capabilities/features	PHREEQC	HP1	PHT3D	OpenGeoSys	HYTEC	ORCHESTRA	TOUGHREACT	eSTOMP	HYDRO-GEOCHEM	CrunchFlow	MIN3P	PFLOTRAN
Coupling												
Reaction-induced porosity–permeability	No	Yes	No	Yes	Yes	Yes	Yes	Yes	Yes	Yes	Yes	Yes
Coupled heat of reaction	No	No	No	Yes	No	No	Yes	No	Yes	No	No	Yes
Coupled deformation/ compaction[a]	No	No	No	Yes	No	No	C-E	No	EGM	C-E	No[b]	Yes
Reaction consumption of phase (H_2O, CO_2)	Yes	Yes	Yes	Yes	Yes	Yes	Yes	Yes	Yes	Yes	No	Yes
Electrical double layer transport	Yes	No	No	No	No	Yes	No	No	Yes	Yes	No	No
Numerical Scheme												
Operator splitting	Yes	Yes	Yes	Yes	Yes	Yes	Yes	Yes	Yes	Yes	No	Yes
Global implicit	No	No	No	No	No	No	No	No	No	Yes	Yes	Yes
High Peclet number transport	Yes	No	Yes	Yes (FCT)[c]	No	Yes	No	Yes	Yes	Yes	Yes	Yes
Spatial discretization[d]	MC	FEM	FVM, MMC	FEM	FVM	MC	FVM	FVM	FEM, MMC	FVM	FVM	FVM
Time discretization[e]	TW	TW	TW	BE	TW	FE/ RK	BE/CN	BE	TW,Mid	BE	BE	BE
Computational												
Parallelization	No	No	No[f]	Yes	Yes	Yes	Partial	Yes	No	No	Yes	Yes
Inverse estimation	Yes	With PEST[g]	With PEST[g]	With PEST[g]	No	No	Yes	No	No	With PEST[g]	With PEST[g]	With PEST[g]
Graphical user interface	Yes	Yes	Yes	Yes	No	Yes	No	No	No	No	No	No
Open source	Yes	No	No	Yes	No	No	No	No	Yes	No	No	Yes

Notes to Table 2-7: [a]Not available in CrunchFlow, but available in CrunchFlowEDL ; [b]Not available in MIN3P-THCm, but dual porosity model is available in MIN3P-Dual

Notes to Table 2-8: [a]Not available in OGS, but OGS has built-in interphases to different geochemical and biogeochemical solvers (GEM, PHREEQC, ChemApp, BRNS) that can implement Pitzer activity model ; [b]DDL denotes Diffuse Double Layer, non-edl denotes Non-Electrostatic model, and CC denotes Constant Capacitance ; [c]Not available in MIN3P-THCm, but available in a customized version of MIN3P

Notes to Table 2-9: C-E denotes compaction-erosion, and EGM denotes Equilibrium Geo-Mechanics Model; Simplified 1-D approach following Neuzil; FCT refers to linearized algebraic flux corrected transport; MC denotes mixing cell, FEM denotes Finite Element Method, FVM denotes Finite Volume Method and MMC denotes Modified Method of Characteristic or backward particle tracking; BE denotes Backwards Euler, TW denotes time weighted difference including forward difference, backward difference, and Crank-Nicolson (CN) Central Difference, Mid denotes Mid difference, and RK denotes Runge-Kutta ; An MPI-based parallel version of PHT3D has been developed and is in the testing phase ; PEST denotes Parameter Estimation Software Toolkit

2.3.2. Origin of thermo convection

On time scales inaccessible at the laboratory, the modeling appears to be the most attractive method to study convection – one of the phenomena that could potentially govern the long-term aqueous glass alteration.

In glass packages, the convection would result from the heat source due to radioactive decay. The heat would diffuse, giving rise to a temperature gradient within a package. A great number of researches reported that when the temperature of a fluid is higher at the bottom than at the top, convection currents are created instantly (Manneville 2006; Guy et al. 2008). Since there is a density gradient between the top and the bottom, gravity acts trying to pull the cooler, denser liquid from the top to the bottom. This gravitational force is opposed by the viscous damping force in the fluid. This leads to the formation of rolls, the so-called Rayleigh-Bénard cells.

Bouyer (internal CEA communication, 2017) investigated the conditions that could favor the convection in the underground waste storage environment. By carrying out computational fluid dynamics calculations in TrioCFD code (http://www-trio-u.cea.fr/) with two sources of data, such as the temperature at the boundaries of the overpack (Figure 2-13) and the thermal power density of packages as a function of time (Table 2-10), he obtained temperature maps of a nominal glass canister at 1.000 y and 10.000 y after its disposal (Figure 2-14).

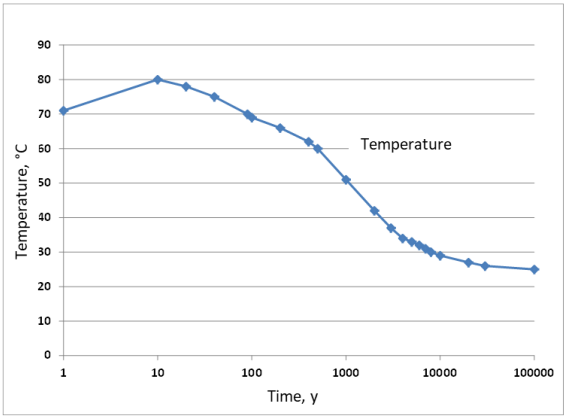

Figure 2-13 Temperature at the overpack boundaries as a function of time (adapted by F. Bouyer from (ANDRA-Collectif 2016)).

Table 2-10 Power density released by a glass package (Godon 2004)

Time (y)	*0*	*50*	*100*	*1000*	*10 000*	*100 000*
Power density (W/m³)	*16573*	*4267*	*1740*	*173*	*0,266*	*0,266*

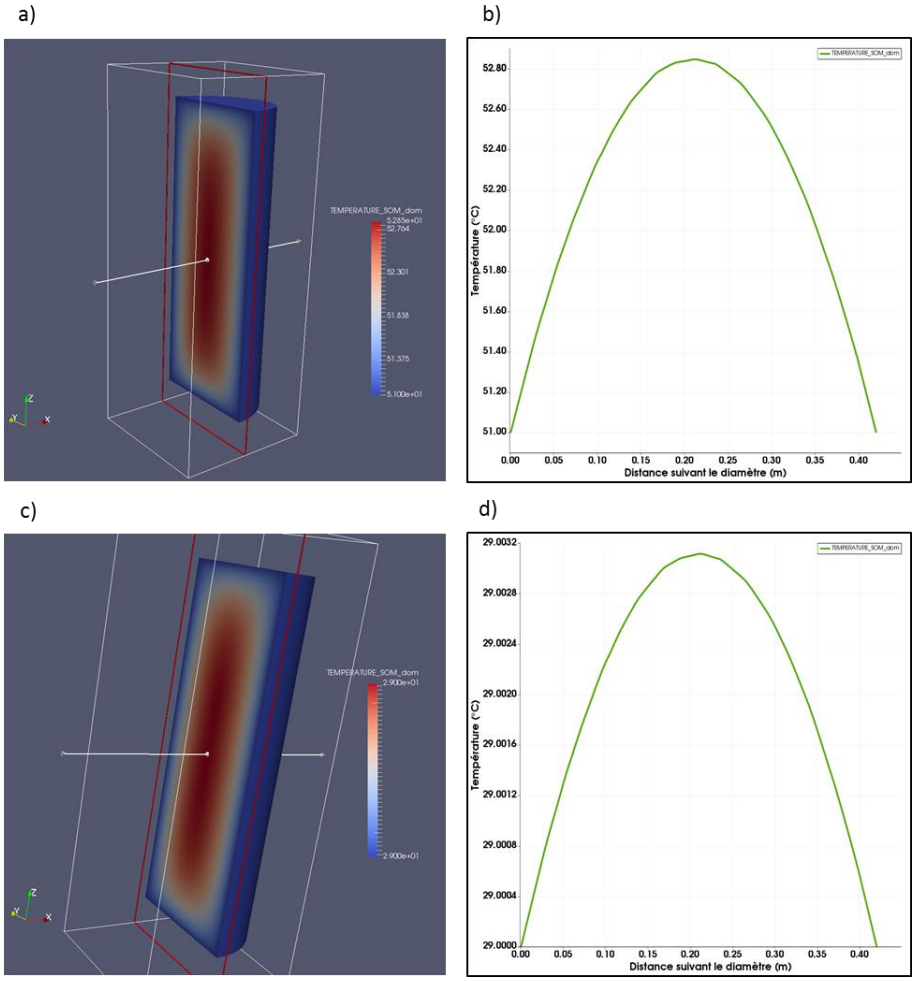

Figure 2-14 Temperature map calculated for a glass canister – a;b): the temperature field and the profile at 1.000 year after the canister disposal; c,d): the temperature field and the profile at 10.000 year after the canister disposal

Afterwards, by considering the effect of temperature on the fluid density via the Boussinesq approximation (see Section 2.3.3 equation 2-23), Bouyer estimated water velocity inside a vertical fracture crossing the transversal glass canister cross section of 42 cm (Figure 2-15), with fracture aperture varying from 40 μm to 1000 μm.

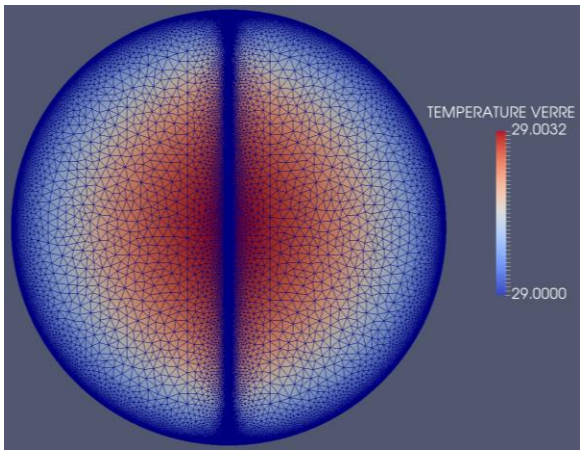

Figure 2-15 Mesh of a modeled glass block section with a crack of 40 μm. Temperature field at 10.000 y.

The Péclet number (adimensional number describing whether the transport of species is essentially governed by diffusion or convection) was calculated: Bouyer reported that for the case of a package with temperature and heat output conditions at 1.000 years, convection always seemed to be predominant, at least up down 40 μm aperture. Regarding the case of a package with temperature boundary conditions at 10.000 years, convection was found negligible for cracks of less than 100 μm opening.

Moreover, it was noticed that the presence of the apical voids or the cavities of contraction, formed at the end of the cooling the glass block, could favor the convection, that would activate the dissolution of the glass, until the saturation would be reached, if the velocity of the fluid in the clay remained very small and negligible.

Given the reported findings, it is probable that during the periods of full saturation, the alteration of glass blocks in repository conditions will be governed by three mechanisms: molecular diffusion, kinematic dispersion, thermo-convection (density flow). The prerequisites for the existence of these three mechanisms are proven to take place inside a glass cracks medium. That is why final runs of RTM should be conducted in both diffusive and convective modes.

2.3.3. HYTEC reactive transport code

HYTEC is a reactive transport code developed by the reactive hydrodynamics group at MINES ParisTech (van der Lee, 2003). It was constructed around another geochemical code CHESS in order to connect a grid module with modules of resolution of flow, thermic and transport problems.

This code relies on the method of the separation of operators (operator-splitting based code) (Lagneau 2013b). It implies the resolution of the flow equation at the beginning of the time-step, subsequent iterative solution of chemistry, transport and porosity problems with the ultimate update of the field of permeability according to porosity change for a next time-step flow-problem resolution[5].

The chosen approach to solving chemical systems is based on the principal component formalism that implies that the unknowns are restricted to the total concentrations of a certain number of basis species. The resolution of the advection /dispersion equation in porous media is required to be done for all components according to (2-14), (2-15).

$$\frac{\partial \Phi c}{\partial t} = \mathcal{T}(c) - \frac{\partial \Phi \bar{c}}{\partial t}, \qquad 2\text{-}14$$

$$\boldsymbol{\mathcal{T}}(c) = \mathrm{div}\,(De \cdot \overline{\mathrm{grad}\, c} - c\bar{U}), \qquad 2\text{-}15$$

Where Φ is the porosity; De is the effective dispersion/diffusion coefficient equal to D×Φ; $\boldsymbol{\mathcal{T}}$ is the transport operator, c is the concentration of a total mobile fraction for the considered element, $\bar{c}$ is the concentration of total immobile fraction for the same element (for example, minerals).

The sequential resolution consists in numerical solving of transport, then chemistry through the resolution of the transport for one time-step and following resolution of the speciation, using the local values of the total concentrations according to (2-16).

$$\frac{\Phi^{\zeta} c_j^{t+\delta t,2i+1} - \Phi^{t} c_j^{t}}{\delta t} = \boldsymbol{\mathcal{T}}(c_j) - \frac{\Phi^{\zeta} c_j^{-t+\delta t,2i} - \Phi^{-t} c_j^{-t}}{\delta t}, \qquad 2\text{-}16$$

Where c_j^{-t}, c_j^{t} is the solution known at the current time and $c_j^{t+\delta t,2i}, c_j^{-t+\delta t,2i}$ is the estimation of the chemical module for the new time step at the previous iteration 2i. In comparison with the fully coupled method of the equation resolution, the solving physical and reactive transport separately greatly reduces the memory requirements and, in case of very large problems, it is seen as the only feasible solution.

The speciation is calculated in each node of the system. It is used to estimate the fixed and mobile fractions and calculate the mineral volumes. The calculation is performed by the geochemical code CHESS (van der Lee 1998), based on several equations, such as the mass-action law equation (2-17) providing an algebraic link between the primary and the secondary species, the mass-balance equation (2-18) and kinetic law (2-19)

[5] It should be noted that in our research, the effect of fracture clogging with newly precipitated secondary phases it not taken into account.

$$[S_j] = K_j \prod_{i=1}^{Np} [S_i]^{\alpha_{ji}}, \quad 2\text{-}17$$

where S_j is the activity of species j, K_j is the thermodynamic reaction constant, Np is the number of species involved, S_i is the activity of the basis species i needed to form the species j, α_{ji} is the associated stoichiometric coefficient.

$$S_{i-TOT} = \sum_{j=1}^{N_s} \alpha_{ji} S_j, \quad 2\text{-}18$$

where Ns is the number of all species in the system.

$$\frac{d[M]}{dt} = kA_v \prod_i (A_i)^{a_i} \left(\left(\frac{Q}{K_s}\right)^p - 1\right), \quad 2\text{-}19$$

According to equation 2-19, the variation in mineral concentration is proportional to (i) the intrinsic kinetic constant of the reaction k, negative in case of dissolution and positive in case of precipitation, and to (ii) the volumetric surface of the mineral A_v. At first approximation, the reaction rate can be assumed proportional to the area of the solid. The term $\left(\frac{Q}{K_s}\right)^p - 1$ (where p - an empirical parameter) is related to the notion of saturation: in that respect, precipitation happens if Q > Ks, otherwise dissolution takes place. The term $\prod_i (A_i)^{a_i}$ integrates the activity of the dissolved species A_i and a_i shows the dependence of the rate reaction on the chemistry of dissolution.

Solution of geochemical equilibrium is calculated with reference to a thermodynamic database; in this research, the adapted CTDP[6] database is used.

Flow module is available in HYTEC in saturated (stationary, transitory regimes) as well as unsaturated and two-phase forms.

Mathematical basis for single phase flow in saturated stationary regime is represented by the continuity equation (2-20) and the generalized Darcy equation (2-21)

$$\mathrm{div}\left(\rho \vec{U}\right) + \frac{\partial \Phi \rho}{\partial t} + \rho q = 0\,, \quad 2\text{-}20$$

where $\vec{U}$ is the Darcy velocity, K is the hydraulic conductivity, ρ is the fluid density, Φ is the porosity, q is the volumetric source term.

$$\vec{U} = -K \cdot \overrightarrow{\mathrm{grad}}\,(h)\,, \quad 2\text{-}21$$

where h is the hydraulic head.

A module of variable density flow was also developed in HYTEC (Lagneau 2013a): it relies on the equation of mass conservation and Darcy's equation (2-22) where the contributions of pressure and gravity are separated:

[6] The public CTDP thermodynamic database adapted at LCLT, Marcoule by adding the definition of nuclear glasses (SON68, ISG etc.).

$$\begin{cases} S_s \frac{\partial p}{\partial t} + \rho g q = \mathrm{div}\left[\frac{\rho g k}{\mu}\left(\overrightarrow{\mathrm{grad}}(p) + \rho g \ \overrightarrow{\mathrm{grad}}(z)\right)\right] \\ \vec{U} = -\frac{k}{\mu}\left(\overrightarrow{\mathrm{grad}}(p) + \rho g \ \overrightarrow{\mathrm{grad}}(z)\right) \end{cases}, \qquad 2\text{-}22$$

where S_s is the storage coefficient, p is the pressure, ρ is the fluid density, k is the intrinsic permeability.

In order to consider the variation of water densities as a function of temperatures (motor to thermo-convection), the Boussinesq approximation (2-23) is used:

$$\frac{\rho}{\rho_0} = 1 - \alpha\left(T - T_0\right), \qquad 2\text{-}23$$

where α is the thermal expansion coefficient, T is the temperature.

In HYTEC, discretization scheme of the hydrodynamic module can be chosen between centered (by default for the dispersion) and upstream (by default for the advection). Time discretization is one-step and can be set from fully explicit to implicit (semi-implicit Crank Nicholson scheme by default).

For the explicit scheme in pure transport, the time step is subjected to the Courant-Levy criterion, which postulates that the higher the dispersivity and/or the space discretization, the smaller the admissible time step. HYTEC resolution scheme also includes a heuristic control of time step based on the number of coupling iterations required to reach convergence between transport and chemistry. If convergence is reached rapidly (typically less than 20 coupling iterations), HYTEC increases the timestep (5%) and reduces it otherwise. If convergence is not reached after 60 coupling iterations, HYTEC goes back to the previous time step, and starts over with a reduced time step (-30%). If the time step becomes very small (microseconds or less), HYTEC gives up, announcing an error of non-convergence.

Moreover, since 2014, a precise control of time step is available in HYTEC versions (Lagneau 2014). It helps the user to adapt the time step manually to avoid an error. So it is possible to control maximum and minimum time step according to the easiness of convergence, i.e. locally modify start time step value as well as maximum time step value to pass through local difficult periods when convergence is not assured.

HYTEC is based on a finite volume discretization of the governing coupled partial differential equations that link flow, solute transport, and multicomponent equilibrium and kinetic reactions in porous and/or fluid media. The choice of the finite volume method is justified in (Lagneau 2013b) in view of the coupling with chemistry. In fact, in algorithms with operator-splitting principle, each cell is considered as an independent chemical reactor where concentrations of different chemical elements are uniform. As for finite volume method, concentrations are not interpolated between cells but assigned at the centers. Furthermore, conservation of flux is guaranteed, which is of high importance for reactions based on mass balance.

However, in the current HYTEC version the use of the externally generated vertex centered mesh is also possible. The external vertex - centered mesh is created by a three-dimensional mesh generator with built-in pre- and post-processing facilities, named GMSH (Geuzaine et al. 2009). The move from the cell-vertex mesh (generated by GMSH) to the cell-centered approach adopted in HYTEC is performed on a dual of the mesh, which properties are calculated internally. It is constructed in a way that the degrees of freedom are placed at the center of dual elements. Then the equations are integrated over these new control volumes. The adoption of an externally generated grid is explained by the fact that GMSH is found to be efficient, it enables users to cope with abstract geometries, it possesses different types of solvers that could be easily applied, it enables the construction of a grid with varying mesh size etc.

To sum up, for the purposes of this research, HYTEC reactive transport code was used. The simulations of the aqueous alteration of the borosilicate glass of simplified composition (ISG glass) were conducted in saturated stationary and saturated transitory regimes. Theses simulations were conducted in both diffusive and convective mode. Convection was originated from either term source reflecting the radioactive decay that will occur inside a glass canister in repository conditions, or by imposing temperature gradient between opposite walls of the modeled systems. The change of the porosity and its feedback on permeability and diffusion, as a consequence of clogging or dissolution, were not considered in this study. The glass dissolution was considered isovolumetric, that is, all dissolved glass was assumed to be spent on the generation of the alteration gel.

2.3.4. Limits of reactive transport codes

With reference to multiple researches mentioned earlier, it is clear that subsurface RTM has developed drastically in the last 15 years. It is now possible to study a wide range of complex coupled phenomena with a number of different codes. Development of operator splitting numerical schemes and evolution of computer science make it possible to run more complex cases with increasing number of meshes constituting a grid of a model. As regards the RTM of complex fracture porous media, the development of codes is still in progress. Nevertheless, there are already several codes (Table 2-7) capable of treating multiple continua.

However, the examples of RTM applications to complex fracture networks are still rare. The introduction of multiple continua requires the complexification of the grid, the increase of the number of meshes to be treated, and usually the decrease of the mesh size (when meshing fractures). In the domain of computational fluid dynamics (CFD), it is no longer an issue. Indeed, there is multitude of examples showing the results of CFD calculations conducted on multi-million cell grids. In contrast to CFD applications, RTM deals with the coupling of the flow / transport and geochemical phenomena that represent an extra challenge. In fact, in presence of multiple component species, number of equations to be solved increases considerably (de Dieuleveult et al. 2009), and because all these equations

should be solved in each mesh, this exercise become challenging or even impossible to be accomplished without resorting to powerful massively parallel computers. Moreover, some supplementary difficulties could come from the geochemical model itself. For instance, according to the formalism of GRAAL geochemical model (Section 2.1.2) used in this study, glass aqueous alteration is controlled by a dense gel showing its passivating power when the retention rate of the Si and Al elements is enough. This passivating gel forms from the glass with a speed that is a function of its thickness and its diffusion coefficient, and dissolves according to a classical affinity law involving the initial velocity, and the ionic and solubility products of the gel. It means that in order to start up the calculation, it is necessary to achieve quickly a certain level of SiAl concentration in each mesh that becomes problematic in the case of fine meshes. As a consequence, due to the highly non-linear nature of the equations involved, the iterative sequential solution scheme of the code sometimes fails to converge or, in order to avoid the non-convergence, it is forced to reduce the time-step (Section 2.3.3). Although it allows to bypass the failure, it extends significantly the time of calculation, that, in a case like our, where the simulation time is of order of several tens of years minimum, becomes penalizing. It is especially relevant to the simulations run in presence of convection, when another restrictive criterion, named Courant Number, should also be respected.

To sum up, although the evolution of RTM codes is impressive, RTM applied to a fractured media of a glass block remains challenging. On the one hand, for the time being, it is impossible to run RTM applied to a discrete model of fractures at scale of a glass canister, while on the other hand, the determination of a unique REV within this highly anisotropic fracture network is delicate and its replacement by an equivalent porous media requires the provision of the equivalent hydraulic and diffusive properties; as well as the adaptation of the geochemical model. The techniques used to come up with the equivalent porous media model will be addressed in Section 5.

References

Abrajano, T., J. K. Bates, and C.D. Byers. 1986. 'Aqueous corrosion of natural and nuclear waste glasses I. Comparative rates of hydration in liquid and vapor environments at elevated temperatures', *Journal of Non Crystalline Solids*, 84: 251-57.

Abrajano, T.A., Jr., J.K. Bates, and J.J. Mazer. 1989. 'Aqueous corrosion of natural and nuclear waste glasses. II. Mechanisms of vapor hydration of nuclear waste glasses', *Journal of Non-Crystalline Solids*, 108: 269-88.

Advocat, Dussossoy, and Petitjean. 2008. 'Vitrification des déchets radioactifs', *Techniques de l'ingénieur Cycle du combustible nucléaire : combustibles usés et déchets radioactifs*, base documentaire : TIB457DUO.

ANDRA-Collectif. 2016. "Dossier d'options de sûreté - Partie après fermeture (DOS-AF)." In, 1-467. ANDRA.

ANDRA. 2005a. "Dossier 2005 Argile - Tome Architecture et Gestion du Stockage Géologique." In, edited by ANDRA, 1-497.

———. 2005b. "Dossier 2005 Argile - Tome Évolution Phénoménologique du Stockage Géologique." In, edited by ANDRA, 1-523.

———. 2010. "2006 - 2009 - 4 ans de recherches scientifiques à l'Andra pour les projets de stockage." In, edited by ANDRA, 1-48.

———. 2016. 'Rapport Andra CG-TE-D-NTE-AMOA-SR1-0000-15-0060 – « Dossier d'options de sûreté - Partie exploitation »'.

andra.fr, collectif. "Site internet de l'ANDRA." In.

Barth, Nicolas. 2013. 'Sur la modélisation et la simulation du comportement mécanique endommageable de verres borosilicatés sous sollicitation thermique', Université de Strasbourg.

Battiato, Ilenia, Daniel M. Tartakovsky, Alexandre M. Tartakovsky, and Timothy Scheibe. 2011. *Hybrid models of reactive transport in porous and fractured media*.

Beckingham, L., C. Peters, W. Um, K. Jones, and W. Lindquist. 2013. *2D and 3D imaging resolution trade-offs in quantifying pore throats for prediction of permeability*.

Berkowitz, B. 2002. 'Characterizing flow and transport in fractured geological media: A review', *Advances in Water Ressources*, 25: 861-84.

Bonniaud, R., A. Jouan, and C. Sombret. 1980. 'Large scale production of glass for high level radioactive waste', *Nuclear and Chemical Waste Management*, 1: 3-16.

Bourbiaux B., Basquet R., Cacas M-C, Sarda S. 2002. 'An Integrated Workflow to Account for Multi-Scale Fractures in Reservoir Simulation Models: Implementation and Benefits', *Conference and oil show*.

Bouyer, F, Véronique Doquet, Céline Mallet, Nicolas Barth, Emmanuelle Chabert, Neji Ben Ali, Andrei Constantinescu, Jérôme Fortin, Yves Guéguen, Daniel George, Yves Rémond, and Saïd Ahzi. 2014. "Synthèse sur la fracturation thermomécanique des verres R7T7 - Bilan du programme 2011-2014." In, edited by CEA, 1-201.

Cailleteau, C. 2008. 'Influence de la morphologie du gel sur la cinétique d'altération des verres nucléaires: rôle du calcium et du zirconium.', Thèse de l'école polytechnique de Paris.

Caubit, C., G. Hamon, A. P. Sheppard, and P. E. Øren. 2009. 'Evaluation Of The Reliability Of Prediction Of Petrophysical Data Through Imagery And Pore Network Modelling', *Petrophysics*, 50: 13.

Chomat, L. 2008. 'Compréhension de l'altération à long terme des colis de verre R7T7 : étude du couplage chimie transport dans un milieu fissuré', Université Paris VI.

Christian, Thiery. 2013. 'Tomographie à rayons X', *Techniques de l'ingénieur CND : méthodes globales et volumiques*, base documentaire : TIB585DUO.

Crevoisier, D., F. Bouyer, and S. Gin. 2011. 'Semi-stochastic generator (FRAGMA) of 2D fractured media by mechanistic analogy. Application to reactive transport in a fractured package of vitrified nuclear waste', *Computational Materials Science*, 50: 1387-98.

Cvetkovic, Vladimir, S. Painter, N. Outters, and J. O. Selroos. 2004. 'Stochastic simulation of radionuclide migration in discretely fractured rock near the Aspo Hard Rock Laboratory', *Water Resources Research*, 40: W02404.

Davy, Philippe, Olivier Bour, Jean-Raynald de Dreuzy, and Caroline Darcel. 2006. *Flow in multiscale fracture networks*.

De Chiffre, L., Simone Carmignato, J. P. Kruth, Robert Schmitt, and Albert Weckenmann. 2014. *Industrial applications of computed tomography*.

de Combarieu, G. 2007. 'Altération du verre de confinement de déchets type R7T7 en condition de stockage géologique.', Université Paris XI - UFR Scientifique d'Orsay.

de Dieuleveult, C., J. Erhel, and M. Kern. 2009. 'A global strategy for solving reactive transport equations', *Journal of Computational Physics*, 228: 6395-410.

de Dreuzy, Jean-Raynald. 2008. 'Modélisation des écoulements et du transport dans les milieux fortement hétérogènes et fracturés - Mémoire HDR', Université de Rennes 1.

De Windt, Laurent, Rabia Badreddine, and Vincent Lagneau. 2007. 'Long-term reactive transport modelling of stabilized/solidified waste: from dynamic leaching tests to disposal scenarios', *Journal of Hazardous Materials*, 139: 529-36.

Dran, J.C., G. Della Mea, A. Paccagnella, J.C. Petit, and Laurent Trotignon. 1988. 'The aqueous dissolution of alkali silicate glasses : reappraisal of mechanisms by H and Na depth profiling with high energy ion beams', *Physics and Chemistry of Glasses*, 29: 249-55.

Dube, Martine, Veronique Doquet, Andrei Constantinescu, Daniel George, Yves Remond, and Said Ahzi. 2010. 'Modeling of thermal shock-induced damage in a borosilicate glass', *Mechanics of Materials*, 42: 863-72.

Fournier, M., S. Gin, and P. Frugier. 2014. 'Resumption of nuclear glass alteration: State of the art', *Journal of Nuclear Materials*, 448: 348-63.

Frugier, P., S. Gin, Y. Minet, T. Chave, B. Bonin, N. Godon, J.E. Lartigue, P. Jollivet, A. Ayral, L. De Windt, and G. Santarini. 2008. 'SON68 Nuclear glass dissolution kinetics: Current state of knowledge and basis of the new GRAAL model', *Journal of Nuclear Materials*, 380: 8-21.

Frugier, P., Gin, S., Minet, Y., Chave, T., Bonin, B., Godon, N.,Lartigue, J.E., Jollivet, P., Ayral, A., De Windt, L., Santarini, G. 2008. 'SON68 Nuclear glass dissolution kinetics: Current state of knowledge and basis of the new GRAAL model', *Journal of Nuclear Materials*, 380: 8-21.

Frugier, Pierre, Yves Minet, Natarajan Rajmohan, Nicole Godon, and Stéphane Gin. 2018. 'Modeling glass corrosion with GRAAL', *npj Materials Degradation*, 2: 35.

Geisler, T., A. Janssen, D. Scheiter, T. Stephan, J. Berndt, and A. Putnis. 2010. 'Aqueous corrosion of borosilicate glass under acidic conditions: A new corrosion mechanism', *Journal of Non-Crystalline Solids*, 356: 1458-65.

Geuzaine, Christophe, and Jean Francois Remacle. 2009. 'Gmsh: A 3-D finite element mesh generator with built-in pre- and post-processing facilities', *International Journal for Numerical Methods in Engineering*, 79: 1309-31.

Ghogomu, N. F., and René Therrien. 2000. *Reactive mass transport modeling in discretely-fractured porous media*.

Gin, S., A. Abdelouas, L.J. Criscenti, W.L. Ebert, K. Ferrand, T. Geisler, M.T. Harrison, Y. Inagaki, S. Mitsui, K.T. Mueller, J.C. Marra, C.G. Pantano, E.M. Pierce, J.V. Ryan, J.M. Schofield, C.I. Steefel, and J.D. Vienna. 2013. 'An international initiative on long-term behavior of high-level nuclear waste glass', *Materials Today*, 16: 243-48.

———. 2013. 'An international initiative on long-term behavior of high-level nuclear waste glass', *Materials Today*, 16: 243-48.

Glassley, William, John Nitao, and Charles Grant. 2003. *Three-dimensional spatial variability of chemical properties around a monitored waste emplacement tunnel*.

Godon, N. 2004. "Dossier de Référence sur le Comportement à Long Terme des Verres Nucléaires." In, edited by CEA, 292.

Godon, N., S. Peuget, F. Bouyer, F. Angeli, S. Depierre, O. Pinet, M. Tribet, B. Boizot, J.M. Delaye, J.L. Dussossoy, N. Ollier, S. Gin, C. Jégou, and Ribet I. 2012. "Référentiel scientifique sur le comportement à long terme des déchets vitrifiés : résultats de la R&D menée en collaboration avec les producteurs de déchets." In, edited by CEA, 1-425.

Goebbels, J., P. Reimers, M. Aouri, P. Jollivet, E. Vernaz, C. Lierse, K. Krebs, E. Kaciniel, and W. Stöwer. 1998. "Non-destructive examination of nuclear radioactive waste packages by advanced radiometric methods." In, edited by Commission européene, 97.

Grambow, B., and R. Muller. 2001. 'First-order dissolution rate law and the role of surface layers in glass performance assessment', *Journal of Nuclear Materials*, 298: 112-24.

Guy, Lauriat, and Gobin Dominique. 2008. 'Convection naturelle Cas particuliers', *Techniques de l'ingénieur Modélisation mécanique*, base documentaire : TIB400DUO.

Hellmann, R., S. Cotte, E. Cadel, S. Malladi, L.S. Karlsson, S. Lozano-Perez, M. Cabie, and A. Seyeux. 2015. 'Nanometre-scale evidence for interfacial dissolution-reprecipitation control of silicate glass corrosion', *Nature Materials*, 14: 307-11.

J. Bourbiaux, B., M. C. Cacas, S. Sarda, and J. C. Sabathier. 1997. *A Fast and Efficient Methodology to Convert Fractured Reservoir Images Into a Dual-Porosity Model*.

Jegou, C., S. Gin, and F. Larche. 2000. 'Alteration kinetics of a simplified nuclear glass in an aqueous medium: effects of solution chemistry and of protective gel properties on diminishing the alteration rate', *Journal of Nuclear Materials*, 280: 216-29.

Jercinovic, M.J., S.A. Kaser, R.C. Ewing, and W. Lutze. 1990. 'Comparison of surface layers formed on synthetic basaltic glass, French R7T7 and HMI borosilicate nuclear waste form glasses-

materials interface interactions tests, Waste Isolation Pilot Plant.' in V.M. Oversby and P.W. Brown (eds.), *Scientific Basis for Nuclear Waste Management XIII* (Mater. Res. Soc: Pittsburgh, PA, USA).

Kang, Qinjun, Peter C. Lichtner, and Dongxiao Zhang. 2007. 'An improved lattice Boltzmann model for multicomponent reactive transport in porous media at the pore scale', *Water Resources Research*, 43.

Kang, Qinjun, Dongxiao Zhang, and Shiyi Chen. 2003. 'Simulation of dissolution and precipitation in porous media', *Journal of Geophysical Research: Solid Earth*, 108.

Lagneau, V. 2013a. *Développement d'un module écoulements densitaires dans Hytec*.

———. 2013b. 'Simulation of coupled geochemical reactions and hydynamical processes in porous media -- application to CO2 storage and Uranium exploitation', Université Pierre et Marie Curie - Paris VI.

———. 2014. "Gestion fine pas de temps et sorties dans HYTEC." In, 1-13.

Lichtner, Peter. 2000. *Critique of dual continuum formulations of multicomponent reactive transport in fractured porous media*.

Lichtner , Steefel, Oelkers. 1996. *Reactive Transport in Porous Media* (Mineralogical Society of America).

MacQuarrie, K.T.B., and K.U. Mayer. 2005. 'Reactive transport modeling in fractured rock: A state-of-the-scieence review', *Earth-science Reviews*, 72: 189-227.

Manneville. 2006. 'Rayleigh-Bénard Convection: Thirty Years of Experimental, Theoretical, and Modeling Work.'.

Matheron, G. 1967. 'Eléments pour une théorie des milieux poreux'.

Meakin, Paul, and Alexandre M. Tartakovsky. 2009. 'Modeling and simulation of pore-scale multiphase fluid flow and reactive transport in fractured and porous media', *Reviews of Geophysics*, 47.

Minet, Y., and N. Godon. 1999. "Synthèse des connaissances sur la fracturation des blocs de verre de type R7T7 et AVM." In, edited by CEA, 1-53.

———. 2003. "Leaching full-scale fractured glass blocks." In *American Ceramic Society - 104th meeting*, 275-82.

Moncouyoux, J.P., A. Aure, and C. Ladirat. 1991. "Investigation of full scale high-level waste containment glass blocks - Task 3 : Characterization of radioactive waste forms - A series of final reports (1985-89)-N°24." In, edited by Commission of the European Communities, 1-91.

neimagazine.com, collectif of. 2011. 'cold crucible retrofit', *site of Nuclear Engineering International*.

Perez, Jr.J.M., and J.H.Jr. Westsik. 1989. "Effects of cracks on glass-leaching." In, edited by PNL, 1-19.

Pierce, Eric M., Pierre Frugier, Louise J. Criscenti, Kideok D. Kwon, and Sebastien N. Kerisit. 2014. 'Modeling Interfacial Glass-Water Reactions: Recent Advances and Current Limitations', *International Journal of Applied Glass Science*, 5: 421-35.

Rebiscoul, D., F. Rieutord, F. Né, P. Frugier, R. Cubitt, and S. Gin. 2007. 'Water penetration mechanisms in nuclear glasses by X-ray and neutron reflectrometry.', *Journal of Non-Crystalline Solids*, 353: 2221-30.

Sené, M.R., M. Bailey, B. Illerhaus, J. Goebbels, O. Haase, A. Kulish, and J.L. Chouchan. 1999. "Characterisation of accessible surface area of HLW glass monoliths by high energy accelerator tomography and comparison with conventional techniques." In, edited by European Commission, 1-99.

Serra, J. 1969. 'Introduction à la Morphologie Mathématique', *Cahiers du Centre de Morphologie Mathématique*: 160.

———. 1982. 'Image Analysis and Mathematical Morphology', *Academic Press*.

Soille, Pierre. 2003. *Morphological Image Analysis: Principles and Applications* (Springer-Verlag New York, Inc.).

Steefel, C., L. Beckingham, and G. Landrot. 2015. 'Micro-Continuum Approaches for Modeling Pore-Scale Geochemical Processes', *Reviews in Mineralogy and Geochemistry*, 80: 217-46.

Steefel, C., Beckingham, L., Landrot G. 2015. 'Micro-Continuum Approaches for Modeling Pore-Scale Geochemical Processes', *Reviews in Mineralogy and Geochemistry*, 80: 217-46.

Steefel, C. I., C. A. J. Appelo, B. Arora, D. Kalbacher, O. Kolditz, V. Lagneau, P. C. Lichtner, K. U. Mayer, J. C. L. Meeussen, S. Molins, D. Moulton, D. Shao, J. Simunek, N. Spycher, S. B. Yabusaki, and G. T. Yeh. 2015. 'Reactive transport codes for subsurface environmental simulation', *Computational Geosciences*, 19: 445-78.

Steefel, C.;, S.; Molins, and D. Trebotich. 2013. *Pore Scale Processes Associated with Subsurface CO2 Injection and Sequestration*.

Steefel, Carl I., Donald J. DePaolo, and Peter C. Lichtner. 2005. 'Reactive transport modeling: An essential tool and a new research approach for the Earth sciences', *Earth and Planetary Science Letters*, 240: 539-58.

Steefel, Carl, and Antonio Lasaga. 1994. *A Coupled Model for Transport of Multiple Chemical-Species and Kinetic Precipitation Dissolution Reactions with Application to Reactive Flow in Single-Phase Hydrothermal Systems*.

Sterpenich, J. 1998. 'Altération des vitraux médiévaux - Contribution à l'étude du comportement à long terme des verres de confinement', Doctorat, Université Henri Poincaré.

Trotignon, L., V. Devallois, H. Peycelon, C. Tiffreau, and X. Bourbon. 2007. 'Predicting the long term durability of concrete engineered barriers in a geological repository for radioactive waste', *Physics and Chemistry of the Earth, Parts A/B/C*, 32: 259-74.

van der Lee, J. 1998. "Thermodynamic and mathematical concepts of CHESS." In, edited by Ecole des Mines de Paris and Fontainebleau.

Van der Lee, Jan, Laurent De Windt, Vincent Lagneau, and Patrick Goblet. 2003. 'Module-oriented modeling of reactive transport with HYTEC', *Computers & Geosciences*, 29: 265-75.

Vernaz, Etienne. 2009. 'Nuclear Waste Conditioning', *CEA DFN Monographs*.

Vernaz, Étienne, and Jérôme Bruezière. 2014. 'History of Nuclear Waste Glass in France', *Procedia Materials Science*, 7: 3-9.

Verney-Carron, A. 2009. 'Etude d'analogues archéologiques pour la validation des modèles de comportement à long terme des verres nucléaires', Institut national polytechnique de Lorraine.

Verney-Carron, A., S. Gin, and G. Libourel. 2008. 'A fractured roman glass block altered for 1800 years in seawater: Analogy with nuclear waste glass in a deep geological repository', *Geochimica et Cosmochimica Acta*, 72: 5372-85.

Weinan E., and Bjorn E. 2003. 'The Heterognous Multiscale Methods', *Commun. Math. Sci.*, 1: 87-132.

www.bp.com. 2017. 'BP Statistical Review of World Energy'.

Xiao, Y.; Whitaker, F.; Xu, T.; Steefel, C. 2018. 'Reactive Transport Modeling: Applications in Subsurface Energy and Environmental Problems ': 540.

Zhang, Chun-Liang. 2018. 'Thermo-hydro-mechanical behavior of clay rock for deep geological disposal of high-level radioactive waste', *Journal of Rock Mechanics and Geotechnical Engineering*.

Chapter 3: From objectives to their realizations

CHAPTER 3: FROM OBJECTIVES TO THEIR REALIZATIONS

List of figures

CHAPTER 3: FROM OBJECTIVES TO THEIR REALIZATIONS

List of tables

CHAPTER 3: FROM OBJECTIVES TO THEIR REALIZATIONS

Résumé du chapitre

Ce chapitre s'attache à expliquer la problématique de l'analyse des réseaux de verre fracturé à l'échelle d'un conteneur. Au § 3.1, sont présentées les bases de la morphologie mathématique, *i.e.* l'outil principal pour la caractérisation des réseaux de verre fracturé examinés dans cette thèse. Au § 3.2 sont exposées les démarches effectuées pour l'obtention des images de coupes de verre nucléaire et nous justifions le choix de l'imagerie ordinaire par rapport aux autres techniques : la microscopie et la tomographie. À la fin de ce chapitre, nous examinons la possibilité d'étendre la méthodologie proposée à des applications en 3D et indiquons quelques verrous techniques auxquels il faudra faire face pour y parvenir.

3. From objectives to their realizations

3.1. Basics of mathematical morphology and presentation of the image processing-based fracture network characterization method

In this research, mathematical morphology was used to characterize fracture networks of two blocks of vitrified glass.

Developed in the 1960s (Matheron, 1967; Serra, 1969), mathematical morphology is currently applied in many domains, such as biomedical imaging, document processing, pattern recognition, remote sensing, microscopy, robot vision, internal structure description of reservoir rock , etc., both in two and three dimensional applications. Its high demand in the geosciences is easy to explain since it offers a nondestructive approach of heterogeneous medium characterization when coupled with non-intrusive analysis: *e.g.* micro-tomography (Tokan-Lawal et al., 2015), scanning electron microscopy (Al-Kharusi and Blunt, 2008; Jouini et al., 2011), ordinary digital imaging (Chatterjee et al., 2010).

As mathematical morphology is based on the assumption that any image consists of structures which can be handled by the set theory, these sets are used to analyze important network attributes, such as porosity, connectivity and size of objects that make up the object under study, *e.g.* a fracture network in a nuclear glass canister.

Here below, a few fundamental notions from mathematical morphology are described. They were used to realize the first part of the elaborated fracture network characterization method described later.

i. There are several types of discrete images, depending on the type of numerical information associated with each image pixel. The value of a pixel of a binary image is either 1 or 0 depending on whether the pixel belongs to the foreground or to the background. The range of the values of the pixels of a grayscale image is extended from 0 to 2^n - 1 for pixel values coded on n bits. Both type of images, grayscale and binary images, were used in this work.

ii. Morphological operators aim at extracting relevant structures of the image considered as a set. This is realized by probing the image with another set of known shape called structuring element (SE). The shape of the SE is usually chosen according to some preliminary knowledge about the geometry of the relevant and irrelevant image structures. In our applications, hexagon and line segment structuring elements were used.

iii. Dilation, erosion, closing, opening are major transformations used to probe the image under study.

The erosion of an image f by a structuring element B is denoted by $\varepsilon_B(f)$ and is defined as the minimum of the translations of f by the vectors -b of B (Figure 3-1a). Or to put it simply, the eroded set is the locus of points where the answer to the question "*Does the structuring element fit the set?*" is affirmative.

The dilation of an image f by a structuring element B is denoted by $\delta_B(f)$ and is defined as the maximum of the translation of f by the vectors -b of B (Figure 3-1b). Like for the erosion, the dilated set is the locus of points where the answer to the question is affirmative, however the question slightly changes and becomes: "*Does the structuring element hit the set?*"

Given these definitions, it becomes clear that any erosion of an image is equivalent to a complementation of the dilation of the complemented image with the same structuring element (and vice versa). Both erosion and dilation can be decomposed, that is, eroding/dilating with a structuring element of size n is equivalent to eroding/dilating n times with the corresponding SE of size 1.

The opening γ of an image f by a structuring element B is denoted by $\gamma_B(f)$ and is defined as the erosion of f by B followed by the dilation with the reflected SE $\check{B}$ (Figure 3-1c). The idea behind the morphological opening is to dilate the eroded image to recover as much as possible the original image.

The closing of an image f by a structuring element B is denoted by $\phi_B(f)$ and is defined as the dilation of f with a structuring element B followed by the erosion with the reflected SE $\check{B}$ (Figure 3-1d). The idea behind the morphological closing is to build an operator able to recover the initial shape of the image structures that have been dilated. This is achieved by eroding the dilated image.

As it can be noticed from the definitions, opening an image is equivalent to closing the complement of this image and then complementing the resulting image, which means that the two are dual transformations with respect to set complementation. Opening and closing are idempotent transformations. This means that in contrast to dilation and erosion, their successive applications do not further modify the image. Opening and closing are increasing transformations; they preserve ordering relations between images. Opening is an anti-extensive transformation; its application results in removal of some pixels, whereas closing is extensive and adds some pixels. In

order to define openings with specific selection properties, one can use various morphological openings and take their supremum[7] as a final result.

In the course of this study, such transformations as morphological opening, morphological closing, supremum of linear openings, opening by reconstruction were used.

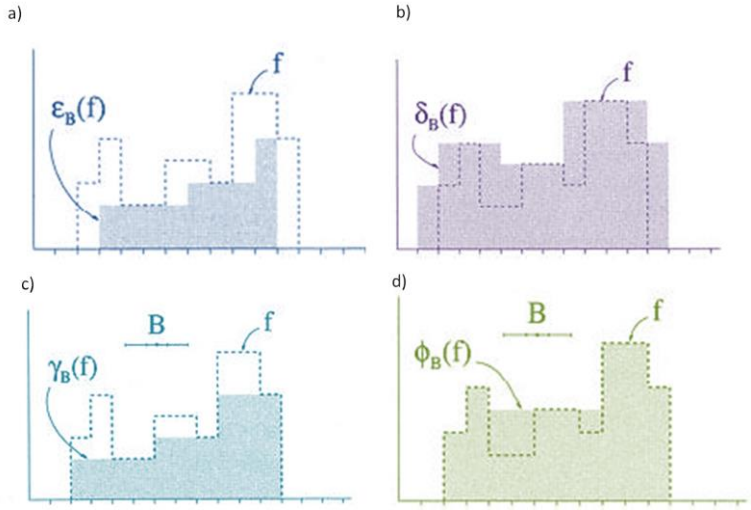

Figure 3-1 Result of morphological a) erosion εB(f), b) dilation δB(f), c) opening γB(f), d) closing ϕB(f) of the image f. Structuring element B used for the pairs dilation and closing, erosion and opening is the same. Obtained from (Soille, 2003)

iv. Top hat transformations unite white top-hat and black top-hat transformations and belong to a class of operators named residues. The first transformation, defined as the difference between the image *f* and its opening $\gamma_\lambda(f)$ with a structuring element of the size = λ, allows to extract white and narrow features from the image, whilst the second transformation, defined as the difference between the image closing $\phi_\lambda(f)$ and the image itself *f*, extracts black and narrow features. The shape and size of the structuring element used for top-hat transforms depend on the morphology of the structures to be extracted. Top hat transformations perform correction of uneven illumination by mitigating illumination gradients and enhancing the contrast. In this study, black top hat transformation was applied to grayscale images at the stage of image pre-processing to remove slow trends and to perform contrast enhancement. This operator brought out fractures whose thickness is half the chosen size of the SE and, as a consequence, it facilitated the separation of the glass matrix and the fracture network. Regarding the selection of the size of the SE, it can be found in Section 5.1.

v. Geodesic reconstruction allows the reconstruction of all connected components of an image *g* from a marker image *f*. It is effectuated by iterating geodesic dilatations of *f*

[7] In this document, "supremum" and "union" as well as "infimum" and "intersection" are used as interchangeable synonyms; supremum (or point-wise maximum) and infimum (or point-wise minimum) replace the union and the intersection set operators for grayscale images.

with respect to g until stability (Figure 3-2 a,b). One of the questions appearing before executing geodesic reconstruction is related to the selection of an appropriate pair of mask/marker images. As a matter of fact, it is always recommended to obtain a marker image by performing some appropriate transformations of the mask image itself by considering the expected result. Geodesic reconstructions are found in many applications, such as the removal of objects connected to an image border, the removal of holes of a binary image etc. Moreover, one more transformation, based on geodesic reconstruction, opening by reconstruction, is important to mention: in contrast to simple opening, this transformation preserves the contours of the objects that have not been removed by the erosion (binary image) and removes unconnected light features (grayscale image). In this research, operations of geodesic reconstruction and opening by reconstruction were applied.

vi. Skeleton is a compact representation obtained by thinning of the object to a set of lines condensing the information of the original object while keeping its homotopy (topology preservation). The skeletal points and their distance to the boundary of the set enable the reconstruction of the set. There are several techniques to perform skeletonisation. In this research, we used a skeleton by maximal balls and a skeleton by homotopic thinning. Regarding the skeleton by maximal balls, it is defined by the centers of maximal balls, where a maximal ball B is considered maximal in X object if there exists no other ball included in X and containing B (Figure 3-2 d). The quench function, calculated together with the skeleton by maximal balls, associates the radius of the ball to the ball center. A second type of the skeleton, used in our applications, is the L-skeleton by homotopic thinning. It is obtained by performing the sequential thinning with six rotations of L structuring element (Golay's alphabet, (Serra, 1982)) until stability. This skeleton is always connected, of unit thickness and is less prone to generating spurious branches due to irregularities of object frontiers.

vii. Multiple points are used for detecting connections between one-pixel width curves such as those obtained after the homotopic skeletonisation. They were useful in separating fracture ramifications.

viii. Bounding box represents the smallest enclosing box for an object. Its dimensions, named Feret diameters, are the distances between the parallel planes restricting the object. For the purposes of aperture calculation, all bounding boxes were turned with respect to the rotation angle of the object (presented by a fracture ramification) whose size was measured. After, minimal Feret diameter corresponding to a fracture ramification aperture was measured.

ix. Distance function is defined as the length of the shortest path drawn on the Euclidian grid between two points. In the digital version, each section at level i of the distance function of a set X corresponds to the erosion of size i-1 of X. It this research, distance function was used to provide continuous measurements of fracture apertures. Values of distance function lying on the traces of L-skeleton by homotopic thinning were

used to calculate aperture averages for each fracture ramification and for each set of fractures belonging to a crystal (Section 5.1).

x. Image segmentation is defined as its partition into different regions, each one having certain properties. There are essentially two approaches depending on whether the core of the segments (*i.e.* region growing techniques) or their boundaries (*i.e.* edge detection techniques) are looked for. In this study we worked with the combination of both techniques, presented by the watershed transformation. To be precise, to avoid an over-segmentation of the image, we used a marker-controlled segmentation by watershed transformation that consists in finding boundaries of the catchment basins (influence zones of imposed minima) of the image under study (Figure 3-2c).

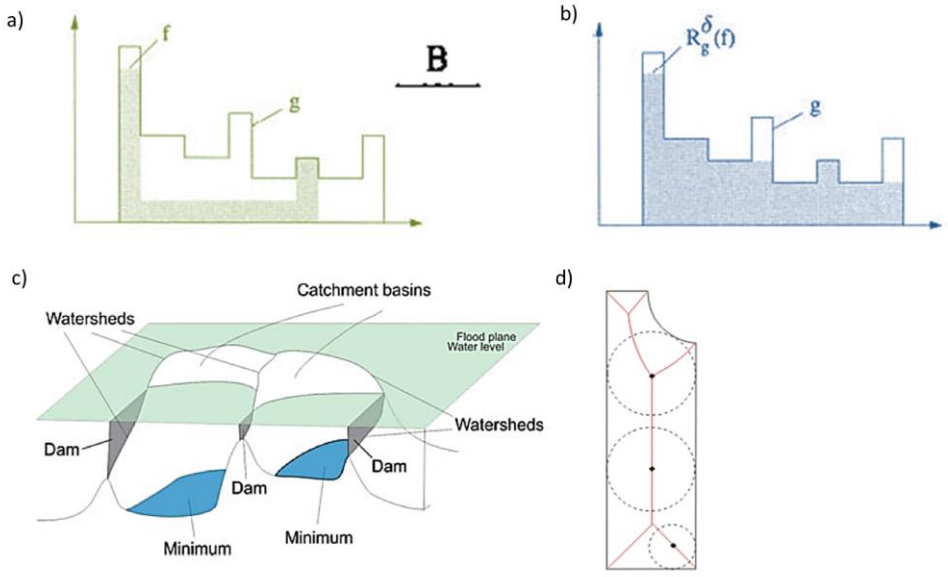

Figure 3-2 a) marker image b)result of geodesic reconstruction c) minima, catchment basins, and watersheds on the topographic representation of a grey scale image d) maximal balls and skeleton by maximal balls (in red). Figures a, b have been obtained from (Soille, 2003).

3.2. Materials

3.2.1. Objects

In order to be capable of performing RT simulations at the scale of an entire glass canister, we elaborated an image processing-based fracture network characterization workflow that enables us to (i) characterize a glass block fracture network, (ii) establish a link between a physical parameter representing an internal state of glass structural relaxation and an internal structure of the block fracture network, (iii) generate multiple realizations of equivalent fracture networks by considering the variability of the fracture network parameters such as fracture distribution and apertures, (iv) calculate coefficients of equivalent diffusion, permeability and kinetics governing parameters, (v) run RT simulations

for N realizations of equivalent fracture networks. The first part of the proposed workflow is devoted to the characterization of the morphology of the fracture networks via extensive analyses of high-resolution photographies. It is performed by using mathematical morphology tools.

To demonstrate the feasibility of the proposed workflow, its application to two images of the longitudinal cross-sections of specimens of non-radioactive packages of vitrified glass was carried out. Two packages were produced at the Vitrification Production Facilities in Marcoule in a cold crucible induction furnace: uranium-molybdenum (UMo) and uranium oxides (UOx) (Vernaz, 2009). Molten glass was injected in a steel canister 1.1 m high with an internal diameter of 0.42 m. The injection from the crucible occurred in two stages, with each casting being half of 400 kg in total. The duration between the two castings was between 6 and 10 h. Once the packages were made, they were removed and were placed into a room in which the cooling progressed further with no implication of forced airflow. Soon after their fabrication, the canisters were cut in two parts along their long axis. Some precautions were taken to preserve the integrity of the intrinsic fracture network. Hence, a viscous resin was poured on top of the UMo glass block (Figure 3-3) prior to the sawing operations. However, the resin could not fill the entire network. In a similar manner, the integrity of the UOx block (Figure 3-4) was expected to be guaranteed by pouring on top of the package a batch of concrete. But unfortunately, the concrete could not fully penetrate the network either.

Amongst the blocks cut and available, we chose those which seem to preserve their integrity at best. Despite these precautions, we realize that these blocks are not perfect. It is clear that it would have been necessary to prepare these blocks differently and to attempt better resin impregnation before the blocks' cutting. This could have required more time of preparation and was beyond the scope of this study. Nevertheless, in this work we assumed that the fracture networks separated from the pullout zones were representative and fully appropriate to serve as objects for further modeling. Having said that, it is suggested that in the future the proposed workflow is applied to glass blocks, with better preservation of the fracture network.

A series of photos of the two block halves, at 200 kg with dimensions of 430 mm × 1335 mm, were shot in the CEA facilities in Marcoule. The methodology developed in this study is presented by using the UMo image (Figure 3-5). The UOx fracture network (extracted from the image shown in Figure 3-6) is presented subsequently when comparing the results of the equivalent network construction to the real fracture networks. The image parameters for both blocks are indicated in Table 3-1.

Table 3-1 Characteristics of the examined images

Name of image	Size (px) of input image	Resolution (mm)	Assembly of N images
UMo	6144 × 2430	0.17	1

UOx	6592 × 2856	0.1443	1

Figure 3-3 Raw image of the UMo block of vitrified fractured glass.

Figure 3-4 Raw image of the UOx block of vitrified fractured glass.

Figure 3-5 Grayscale image of the UMo block of vitrified fractured glass. Dimensions: 1044 mm × 413 mm.

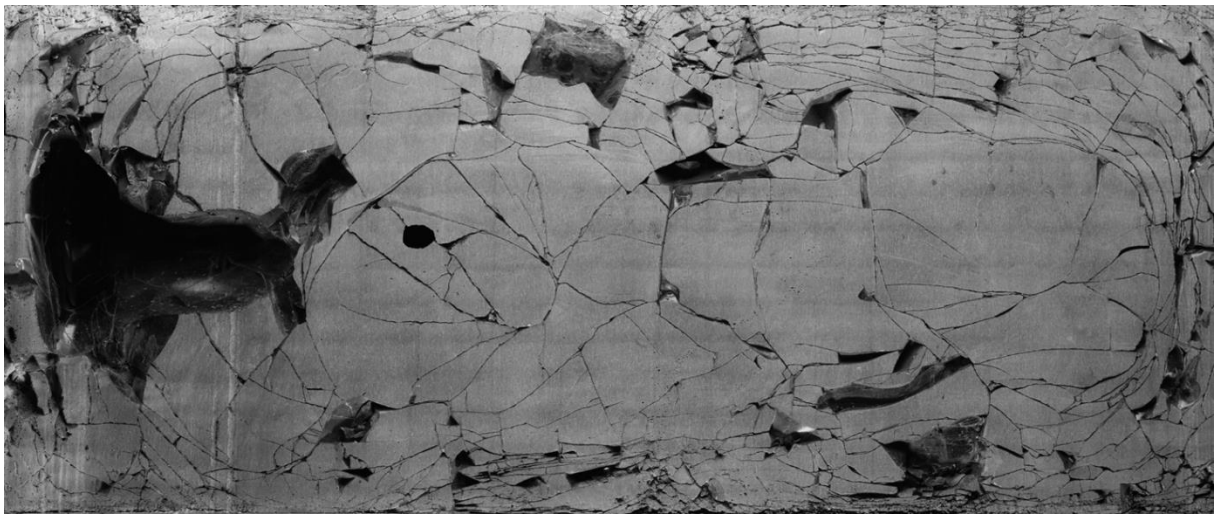

Figure 3-6 Grayscale image of the UOx block of vitrified fractured glass. Dimensions: 952 mm × 412 mm.

3.2.2. Justification of the choice

There is a number of techniques based on object imaging, that are commonly used to characterize internal structure of porous media, including fractured porous media: Scanning Electron Microscopy (SEM), Focused Ion Beam-Scanning Electron Microscopy (FIB-SEM), X-ray Computed Tomography (X-ray microCT, X-ray macroCT), Small Angle Neutron Scattering (SANS), Magnetic Resonance Imaging (MRI) etc. 2D and/or 3D images obtained by these techniques can be analyzed to extract reactive transport model parameters, such as porosity, fracture aperture, mineral volume fractions, surface areas, that afterwards enable the predication of diffusivity and permeability (Beckingham, Peters, Um, Jones, & Lindquist, 2013; Caubit, Hamon, Sheppard, & Øren, 2009; Steefel, Beckingham, & Landrot, 2015). Spatial resolution limits stated by the manufacturers of the imaging equipment varies from some mm down to some nm (FIB-SEM, SANS) and are principally determined by the size and number of detector elements, the source-object-detector distances, and the method of imaging applied (Christian, 2013). In general, however, these techniques are limited by the size of the samples that are accepted for the analyses.

As mentioned in Section 2.2, in the past, the tomographic imaging of a half of the glass canister transversal cross - section (Figure 3-7) was carried out. It was performed by the TOMO ADOUR X-ray CT system (http://www.tomoadour.com) with a 450 kV X-ray tube. The post-processed reconstructed 3D fracture network was used to calculate the fracturing ratio and to capture the connectivity of the network in 3D. Regarding the choice of the object size, (Chomat, 2008) argued that, given the spatial resolution of the final tomographic images that was related to the size of the imaged object and the size of the detector, the conduction of the tomographic survey applied to an entire glass canister was impractical, that is why only a small part of the glass canister was inspected (half of the glass canister transversal cross of 20 cm height).

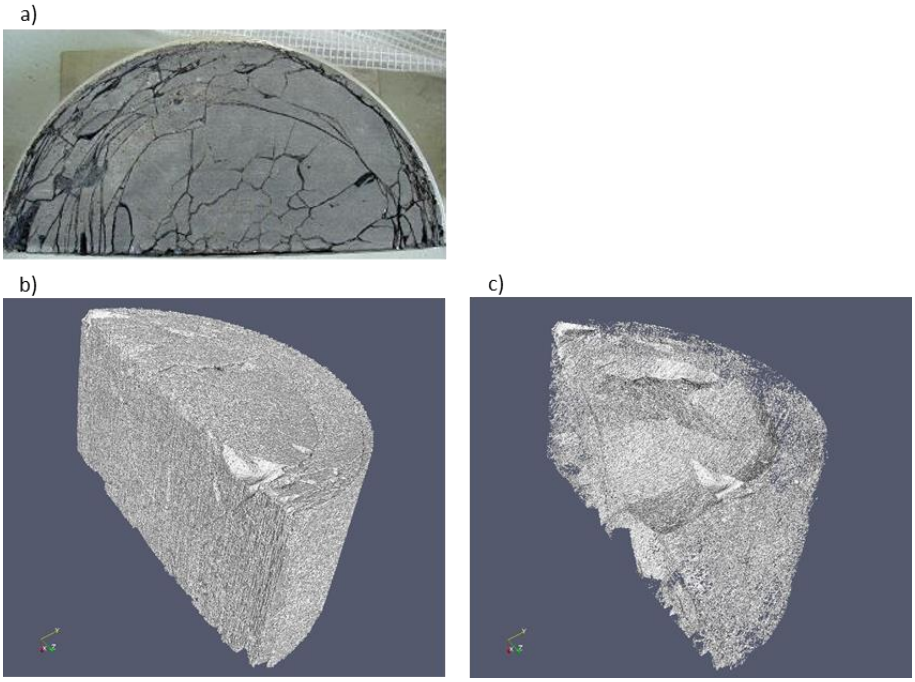

Figure 3-7 a) Top view of the transversal cross-section 20 cm high with the diameter of 42 cm, used for tomographic analysis; b) reconstituted 3D fracture network; c) imaged sample with external surfaces

Moreover, even for this small specimen, whose volume made up only one tenth of the glass block, value of special resolution was lower than desired. In fact, the analysis carried out by TOMO ADOUR X-ray CT system with size of the detector 2048 × 2048 pixels (internal CEA DEN technical report, 2012/01) had a limit of minimum spatial resolution equal to 0.21 mm. This means that below this limit of spatial resolution, the two walls of the fractures were not detected.

A number of authors explained the issue of the spatial resolution of CT imaging. Figure 3-8 shows typical ranges of spatial resolution and size of imaged objects for the tomographic systems.

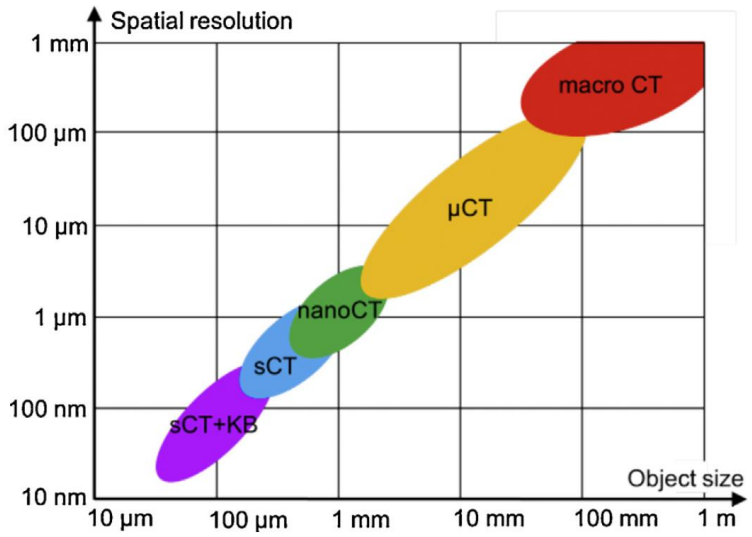

Figure 3-8 Typical spatial resolutions and object sizes (diameter) for macro-CT, micro-CT, nano-CT, synchrotron CT (sCT) and synchrotron CT with Kirkpatrick–Baez (KB) mirrors (sCT + KB). Obtained from (De Chiffre, Carmignato, Kruth, Schmitt, & Weckenmann, 2014).

In general, the spatial resolution of CT reconstructions is the highest for the techniques with the lowest focal spot size, such as micro-CT, nano-CT, synchrotron-CT and synchrotron-CT + KB. However, these techniques can be applied uniquely to small-size objects, up to some millimeters in diameter. For objects of larger size, macro-CT method is appropriate. But it possesses some restrictions too. In CT scanning of large objects, the main limiting factor is related to the material attenuation coefficient, which limits the maximum accumulated material thickness that can be penetrated (De Chiffre et al., 2014). In order to increase the maximum penetrable thickness, X-ray tubes with high voltage are employed. At the present time, commercial standard tubes are typically limited to 450 kV (used to image the half of the glass canister transversal cross – section), but special tubes up to 800 kV become available. For higher energies, linear accelerator X-ray sources are also requested.

However, by increasing the size of the imaged object, one increases the complexity of its data processing (3D reconstruction, surface generation, scale correction), that becomes hardly manageable for complex media like fracture porous media. In this context, (Crevoisier, Bouyer, & Gin, 2011) stated that although tomography can be a powerful tool for fracture numerical description at the scale of an entire glass block, its digital representation is not adapted as an input mesh for large scale RT simulations. Furthermore, a 3D model of the network reconstructed from a series of 2D tomography images is considered to be non-complying with the technical imperatives of an efficient numerical simulation. For example, non-continuous fissures, non-closed topology of a constructed geometrical domain, and presence of geometrical elements of highly variable sizes common for 3D reconstructed images of fracture network make the use of these resulting images difficult, if not impossible.

In view of the limitations related to the size of the object acceptable for CT imaging, the spatial resolution limitations for objects of decimetre/metre size, the difficulty in using the

reconstructed 3D images for subsequent numerical simulations, we decided to opt for a high-quality ordinary digital imaging.

First, although, high-quality ordinary imaging is also concerned with the spatial resolution issue, it is easier to tackle this issue, provided that the appropriate equipment is used. Figure 3-9 illustrates the way the photography of two inactive packages of vitrified fractured glass was conducted. Some precautions were taken to obtain photos that could be used to conduct their detailed examination. Indeed, the quality of the imaging is key for a correct processing: flaws and defect require additional treatment (more work), and lead to poorer description (decreased quality description). The following conditions drew our attention.

(i) Flatness of the surface, the device had to be parallel to the cutting plane: it was ensured by using a level and a rail for the camera.
(ii) Imposed adapted diffused lighting originating from several sources: it was implemented to avoid the possibility to mix up real fractures with shadows generated by cracks and unevenness of the surface

Second, imaging of the glass canisters whose size and weight is considerable, was possible by the ordinary imaging technique. Thirdly, for glass canisters of 400kg, that are extremely difficult to transport due to their weight and security issues, this technique was seen as a good compromise. Fourthly, despite the fact that the ordinary imaging did not produce a 3D reconstruction of the interior structure of the glass canisters, there is still a possibility to unite images of different transversal and longitudinal cross sections to come up with their 3D models that could be used at the stage of RTM. This question will be touched upon in the following section.

Figure 3-9 Working process undertaken to realize a series of high-quality ordinary images of fracture network of two inactive vitrified nuclear glass canisters.

3.2.3. Extension toward a simplified three-dimensional model and price to pay

Although this research focuses on the construction and the application of a 2D model of nuclear glass fracture network at scale 1, its extension toward a simplified 3D model is feasible. Given that glass canisters have a natural symmetry axis, being perfect cylinders, and that the cylindrical symmetry has been used for the thermo-mechanical simulations at scale 1 (Section 2.2), one of the less lengthy solutions is the use of cylindrical coordinates, when constructing a 3D simplified model of a fracture network. Its realization is possible even when only one representative longitudinal model is available. This model requires the grids of all necessary parameters, such as porosity, permeability tensor, diffusion tensor, alteration kinetics governing parameters. Its sketch is represented in Figure 3-10a.

However, as it was mentioned in the preceding section, by unifying information obtained by analyzing images of longitudinal and transversal cross-sections of glass canisters, it is realistic to construct a more complex 3D model. This is especially appealing, since almost all tools necessary to accomplish this exercise are already prepared. First, the knowledge of the fracture pattern of a transverse plane of a fracture package can be obtained by applying the workflow elaborated in the course of this research (Section 5). Second, the data required for geostatistical modelling are identified. Moreover, the maps of the solidification front arrival times necessary to support the image analysis results can be procured easily and the way in

which they should be analyzed is already known. Besides, the algorithm used to generate the anisotropic Voronoï tessellation (realized in RGeostats package) should potentially be able to do it in 3D after some proper adaptations are made. These additional implementations concern the creation of the connected 3D fracture planes. From our point of view, based on the knowledge of position of cell centers and scaling factors in 3 directions and under the hypothesis that fracture planes grow radially toward the canister axis, it would possible to obtain 3D tessellation of equivalent fracture network (Figure 3-10b). Nevertheless, it should be noticed that although the fracture network in the transversal direction is likely to vary along the z-axis owing to the presence of the different thermo-mechanical environments such as a zone of re-liquefaction (in the middle) or a stress-free surface (at the top), it would be rather difficult to take this heterogeneity into account by the existing tools. Furthermore, it would certainly make the model sufficiently more complex and, as a consequence, computationally demanding, without considerably changing the result of the RT modeling. However, it could be interesting to create realizations of 3D equivalent tessellation based on the data obtained by analyzing two transversal cross sections and one longitudinal cross section. The transversal cross sections should belong to two different castings, in order to capture the difference of the fracture network morphology related to the two-stage manufacturing procedure.

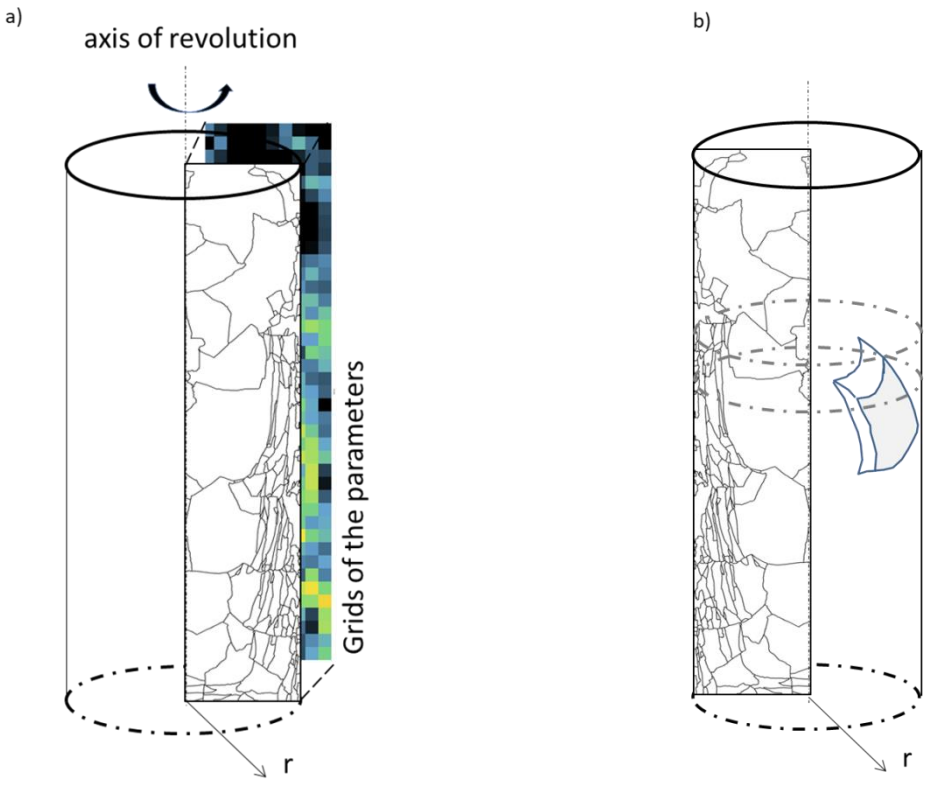

Figure 3-10 Conceptual representations of a) a simplified 3D model with cylindrical coordinates b) the idea how to construct a 3D fracture network surfaces under the assumption of their radial growth

Unfortunately, the creation of this true 3D model is not foreseen in the framework of this research, because, firstly there is no transversal section of glass block available for the

analysis, and secondly their preparation is beyond the scope of this study due to time limitations. Regarding the disc of the block ALISE whose map of the network was drawn by naked eye and later on analyzed by SEM (Section 2.2.2), it was polished with diamond disc of fine size. This resulted in the creation of many artificial scratches that are difficult to separate from the real fractures (Figure 3-11).

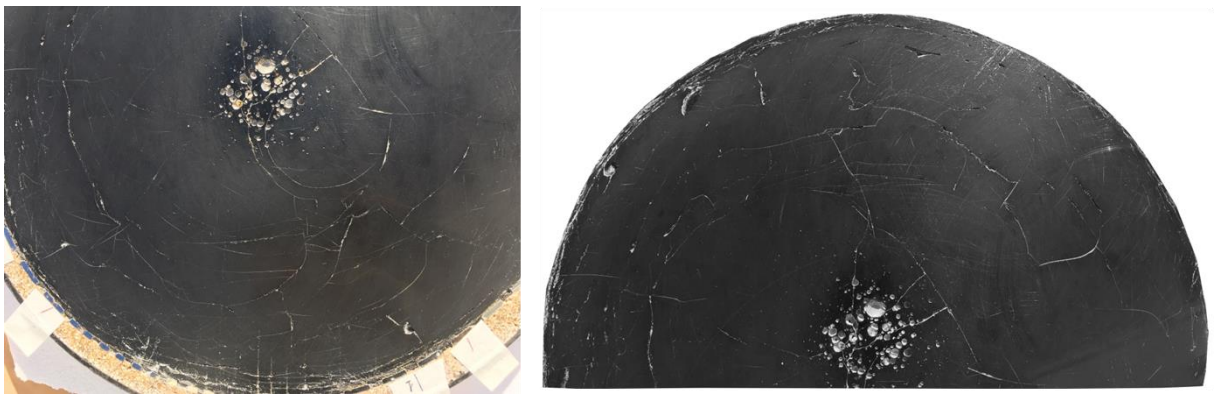

Figure 3-11 Non-professional images of the parts of one transversal disc of the ALISE block (full diameter =42cm).

Presence of artificial fractures created by the disc polishing makes its application very hard, even impossible. In the future it is necessary to prepare a new set of transversal cross-sections whose fracture network should be analyzed by the proposed image processing-based fracture network characterization workflow (Section 5).

In consideration of the above-mentioned limitations of the scanning tomography techniques and the imperatives for conducting the reactive transport modeling at the scale of the entire glass block, a new methodology was elaborated. It relies on the input of the pre-prepared grayscale high-quality images of glass block cross-sections and results of the thermo-mechanical modeling of the viscoelastic behavior and the damage behavior, evolving in response to the structural relaxation of the glass. The workflow combines (i) image analysis, (ii) analysis of a physical parameter indicative of glass internal structural relaxation, (iii) geostatistical modeling, (iv) reproduction of equivalent fracture network tessellations, (v) calculation of equivalent permeability, diffusivity and kinetics governing parameters. It is viewed as a powerful tool that enables the combination of hard and soft data in pursuit of nuclear glass block fracturing characterization and modeling. As such, it provides the basis for future investigation of the impact of fracturing on the aqueous alteration of borosilicate nuclear glass with consideration for the variability of the fracture network and under different scenarios of repository evolution.

References

Beckingham, L., Peters, C., Um, W., Jones, K., & Lindquist, W. (2013). *2D and 3D imaging resolution trade-offs in quantifying pore throats for prediction of permeability* (Vol. 62).

Caubit, C., Hamon, G., Sheppard, A. P., & Øren, P. E. (2009). Evaluation Of The Reliability Of Prediction Of Petrophysical Data Through Imagery And Pore Network Modelling. *Petrophysics, 50*(04), 13.

Chomat, L. (2008). *Compréhension de l'altération à long terme des colis de verre R7T7 : étude du couplage chimie transport dans un milieu fissuré.* Université Paris VI,

Christian, T. (2013). Tomographie à rayons X. *Techniques de l'ingénieur CND : méthodes globales et volumiques, base documentaire : TIB585DUO*(ref. article : p950).

Crevoisier, D., Bouyer, F., & Gin, S. (2011). Semi-stochastic generator (FRAGMA) of 2D fractured media by mechanistic analogy. Application to reactive transport in a fractured package of vitrified nuclear waste. *Computational Materials Science, 50*(4), 1387-1398.

De Chiffre, L., Carmignato, S., Kruth, J. P., Schmitt, R., & Weckenmann, A. (2014). *Industrial applications of computed tomography* (Vol. 63).

Matheron, G. (1967). Eléments pour une théorie des milieux poreux. (Masson, Paris).

Serra, J. (1969). Introduction à la Morphologie Mathématique. *Cahiers du Centre de Morphologie Mathématique*(Ecole des Mines de Paris), 160.

Serra, J. (1982). Image Analysis and Mathematical Morphology. *Academic Press*.

Soille, P. (2003). *Morphological Image Analysis: Principles and Applications*: Springer-Verlag New York, Inc.

Steefel, C., Beckingham, L., & Landrot, G. (2015). Micro-Continuum Approaches for Modeling Pore-Scale Geochemical Processes. *Reviews in Mineralogy and Geochemistry, 80*(1), 217-246. doi:10.2138/rmg.2015.80.07

Vernaz, E. (2009). Nuclear Waste Conditioning. *CEA DFN Monographs*.

Chapter 4: Reactive transport modeling in the framework of discrete approach applied to some fractures

CHAPTER 4: REACTIVE TRANSPORT MODELING IN THE FRAMEWORK OF DISCRETE APPROACH APPLIED TO SOME FRACTURES

List of figures

CHAPTER 4: REACTIVE TRANSPORT MODELING IN THE FRAMEWORK OF DISCRETE APPROACH APPLIED TO SOME FRACTURES

List of tables

Résumé du chapitre

La première partie de ce chapitre récapitule les résultats des expériences d'altération aqueuse de fractures idéales de verre SON68. La deuxième partie concerne la prise en main du modèle géochimique de corrosion de verre GRAAL et son application dans le cadre de l'approche discrète pour quelques fissures idéales. Dans la dernière partie du chapitre, nous examinons les résultats d'une étude de sensibilité visant à étudier l'influence du nombre de fissures, de leurs ouvertures et de leurs longueurs ainsi que le volume d'eau et de son agitation sur le développement du gel dense passivant et du gel poreux non passivant et, par conséquent, sur l'altération du verre.

4. Reactive transport modeling in the framework of discrete approach applied to some fractures

4.1. Experimental data of the reactive transport in some ideal fractures

The goal of this chapter is to recapitulate the results of the laboratory experiments on the aqueous alteration of the simple fracture networks. These results are important to consider as they represent the experimental test-bed of our research and they were referred to when discussing the validity of the reactive transport models presented in this research.

Although studies of the behavior of the fractured glasses in contact with water were initiated in Marcoule at the LCLT laboratory nearly ten years ago, currently there are only some results of experimental works conducted in the scope of the thesis of (Chomat 2008), that could be used as a tool for calibration and verification of the accuracy of our first reactive transport models.

Results of the experimental studies of the glass aqueous alteration inside one/two fracture(s) of different apertures (inside the range 40-520 μm) and positions (horizontal/vertical) are available at LCLT. They are represented by the Scanning Electron Microscopy (SEM) measurements of the thickness of the altered glass layer.

The first set of the experiments for one fracture was realized by using a static reactor (Figure 4-1) of certain volume (from 58 to 100 ml) filled by the chosen solution (NaOH 0.25 mol/l or pure water). In this set of experiments two plates of glass of 24×24×3 mm^3 separated by 40, 60, 82, 170 and 550 μm (aperture of the modeled fracture) were submerged into the solution for the period of up to 290 days. The glass plates were placed either horizontally or vertically and the alteration was studied in the predominantly static conditions (there were only some trials performed in a dynamic mode with the goal to accelerate the development of the gel in the initially pure water and to observe the impact of the generated velocity on the glass alteration).

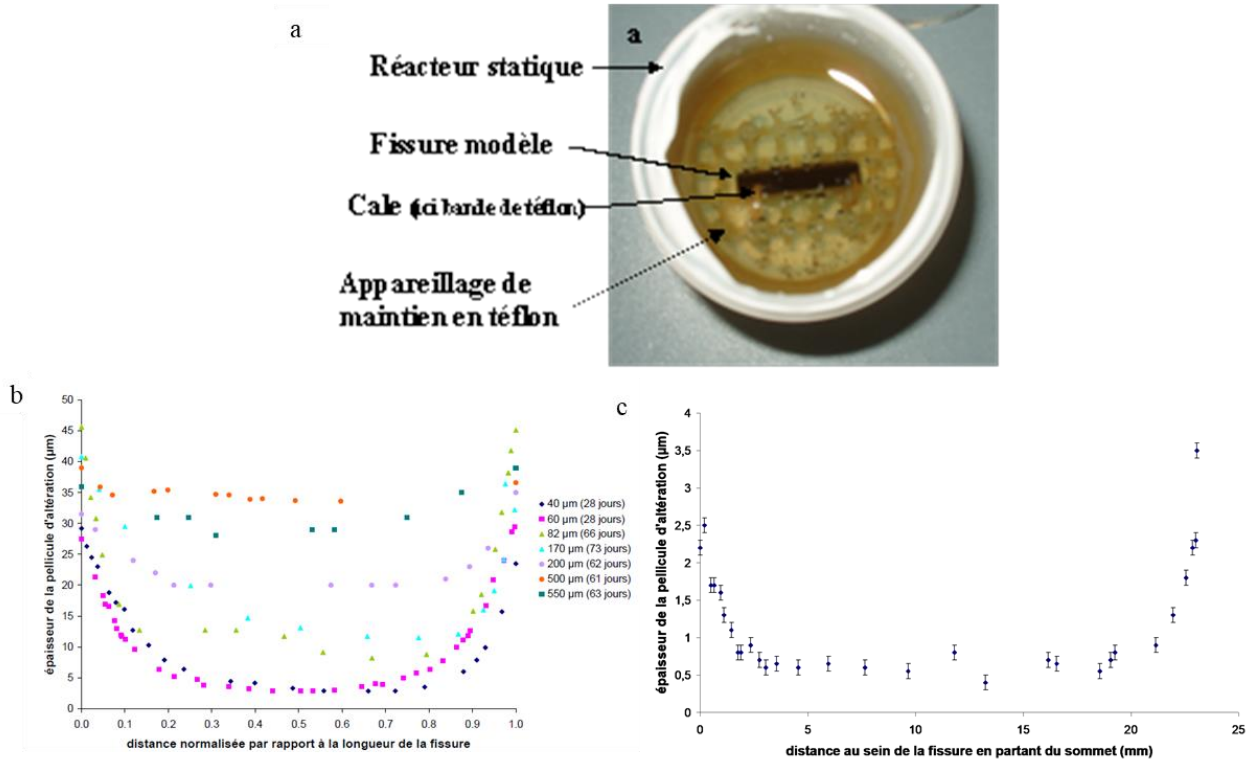

Figure 4-1 a): Device used for the experiments in the diffusive mode for one fracture altered in a basic or a neutral solution; b): Profiles of the thickness of the altered glass along horizontal fractures of varying apertures. Experimental specifications: volume of solution - 100 ml, solution temperature – 90 C, solution composition - 0,25 mol/l of NaOH; c) Profile of the thickness of the altered glass along a fracture of 100 µm altered during 203 d in initially pure water. Obtained from (Chomat 2008)

The second set of the experiments was conducted in the ambition to observe the effect of the thermo-convection provoked by the temperature difference between two compartments filled with water. The device (Figure 4-2) represented two stainless steel compartments of 500 ml each, separated by the bloc of SON68 glass. To create two fissures of given aperture (in the range 40-200 µm), two glass samples were fixed together, with the separation between them indicating the studied fracture aperture. The thermo-isolation of the device was designed to ensure a fixed temperature gradient. The value of the temperature difference was maintained at 4±1 °C. By analyzing the concentration of the tracer KCl (3 mol/l), added into a hot compartment, the average velocity of the solution movement for different fracture apertures (from 60 to 200 µm) was calculated, in a range of 5.7×10^{-6} to 3.5×10^{-4} m/s order of magnitude.

At the postmortem stage, it was noted that the thickness of the film of the altered glass was affected by the flux stimulated by the thermo-convection. According to (Chomat 2008), the thickness of the film developed on the interface with the upper fracture varied from 6.5 to 2 µm (diminishing along the direction of the flow). As for the lower fracture, the effect of the flow was less pronounced. The film thickness was reported equal to 2.5 to 1.8 µm.

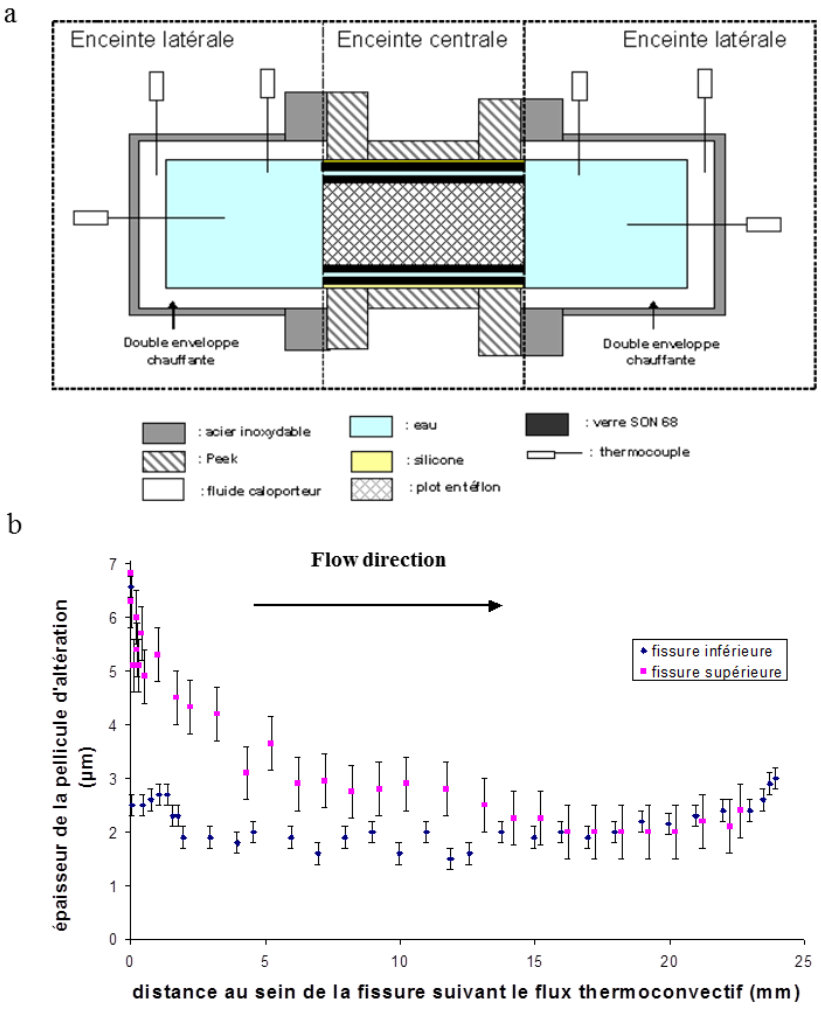

Text below Figure 4-2a: Stainless steel, water, glass SON68, thermo-plastic, silicone, temperature device, heat transfer medium, block of Teflon (translation from left to right, top to bottom)

Figure 4-2 a) Scheme of the device used for the experiments with two fractures in the thermo-convection mode (dimensions are not respected); b) Profiles of the thickness of the altered glass along the horizontal fractures of 200 µm aperture, at the 28th day of the experiment. Obtained from (Chomat 2008)

To study the influence of the disposition and the amount of the fractures on the coupling between transport and chemistry, Chomat's thesis dealt with some more complex systems: one of them is presented below.

In this experiment, the network of the interconnected fractures (Figure 4-3) was represented by two horizontal and one vertical fissures of equal aperture (40 µm). Two copies of this set were separately dropped into 230 ml of NaOH 0.25 mol/l solution for 78 days and into 250 ml of initially pure water for 212 days.

a b

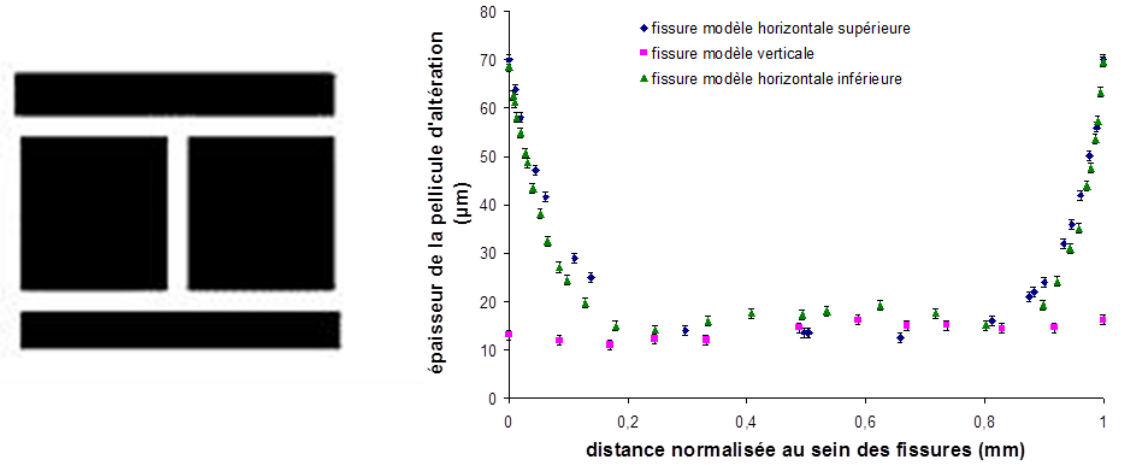

Figure 4-3 a) Network of three interconnected fractures; b) Profile of the thickness of the altered glass for three fractures (horizontal upper, horizontal lower and vertical). Specifications of the experiment: volume of solution - 230 ml, solution composition - 0.25 mol/l NaOH, duration of experiment - 78 days.

Main conclusions of the experimental test-bed of the thesis:

1. Development of the gel is stimulated in pH basic environments; thus, at the end of two-month experiment inside single fractures having apertures in the range 170 - 550 µm, the altered layers were 15 - 40 µm. While for one fracture of 100 µm aperture altered in pH neutral solution the thickness was from 0.7 to 4 µm for 203 and 290-days experiments.

2. In horizontal fractures altered in basic solutions, the profiles of the altered layer were symmetric, with the intensity of the alteration being 4-5 times higher towards the edges.

3. In a vertical fracture, the effect of asymmetry of the altered layer profile was explained by the influence of the convection originated by the gravity segregation;

4. The higher the aperture of the fracture, the more homogeneous the alteration of the glass. Based on the SEM measurements of the altered glass thickness, it was argued that the profiles of the gel traced along the fracture started to be flat for fractures with apertures > 250 µm.

5. The thickness of the film of the altered glass was affected by the thermo-convection flow. The glass alteration layer was more developed in the upper fracture.

6. The experiment with three interconnected fractures altered in a basic solution, showed the influence of the position and the orientation of the fractures on the intensity and the pattern of the gel development. Thus, it was discovered that the precipitation of the secondary phase was more important for the lower horizontal fracture, more intense alteration close to the tips of the fractures was noticed for the horizontally oriented fractures.

7. Experiments conducted in neutral solution were not numerous and often unsuccessful, the developed alteration layers were too small to be observed in SEM.

4.2. Reproduction of the experimental results

First tests of the reactive transport modeling applied to glass fractured media were conducted in the scope of the deterministic discrete approach. The idea was to verify the representativity of the Glass Reactivity with Allowance for the Alteration Layer Model (GRAAL) by simulating aqueous alteration in initially pure water inside one fracture in the framework of "Fracture approach" (Section 2.1.2). To do this, the experimental observations (Section 4.1) were compared with the modeling results.

We decided to start by the simulation of the alteration in initially pure water even if the majority of experiments conducted by Chomat were executed in a strongly basic solution (with pH close to 12-13). This is explained by the fact that the basis GRAAL model (Frugier 2008; Minet et al. 2010) is designed to treat the alteration of glass only in the environments where pH is below 10; for solutions of strongly basic pH (higher than 10.5), one should take the model developed in the framework of other researches (Fournier 2015; Fournier et al. 2014; Gin et al. 2001). Indeed, the alteration in basic solution differs significantly, that means that the data-base, used for modeling, composition of gel poles, secondary phases, parameters of kinetics, etc. must be changed to model the aqueous alteration of the borosilicate glasses in the highly alkaline media.

In the case of Cigeo, it is highly improbable to have strongly basic environment (pH> 10.5) for a long period of time: the environment in the vicinity of the glass should be limited to the canister, steel liner, bentonitic cement and the Callovo-Oxfordian clay. These elements impose pH<10; even the bentonitic "cement" was devised to limit the pH pressure on glass. That allowed us to consider neutral environment while running reactive transport simulations.

The geometries of the modeled systems have been taken by analogy with Chomat experiences. Firstly, we modeled two glass plates of 2.5 cm × 2.5 cm × 0.3 cm altered in 100 ml of a pure water solution. It should be noted that, to respect the total glass volume, we had to recalculate the length of the modeled fractures. It was necessary since by default in HYTEC, in 2D simulations, the third dimension (depth) is equal to 1 m. That is, the length the fracture was calculated as (2.5 cm × 2.5 cm × 0.3 cm) / (2.5 cm ×100 cm) and equaled to 0.0625 cm. By doing that, we obtained the surface equal to that of the glass plates used in the experiment. However, we admit that by decreasing the length of the fracture we will probably lose, to a certain extent, the transport effect. The influence of local chemical conditions, such as saturation in silica, inside a long fracture, is expected to be more important compared to a fracture whose length is shorter.

CHAPTER 4: REACTIVE TRANSPORT MODELING IN THE FRAMEWORK OF DISCRETE APPROACH APPLIED TO SOME FRACTURES

The first reactive transport modeling tests in diffusion mode were successfully conducted as part of the discrete modeling for a one, three and five model fractures. The parameters of the modeled systems are shown in Table 4-1.

Table 4-1 Recapitulative table of the modeled systems

Case name	N fractures	Length, cm	Aperture, μm	Total volume of water, m^3
1f _short	1	0.0625	120	10E-05
3f _short	3	0.0625	120	10E-05
5f _short	5	0.0625	120	10E-05

In accordance with the description of the Fracture approach, discussed in Section 2.1.2.3, fractures were described explicitly, i.e. all parts of the system (reservoirs with water, fracture, glass films at the interface with fracture) were meshed (Figure 4-4). It should be noted that glass films had thickness of one mesh layer and served as a source of material available immediately. In Hytec input file, two geochemical units were specified: glass unit was assigned to the glass meshes and water geochemical unit was set to fracture and reservoir meshes. The parameters necessary to specify dissolution law (Section 2.1.2.2) of the glass of simplified composition (ISG) were calculated as defined in Table 2-4.

During the analysis of the results of modeling the attention was brought to the evolution of the following parameters: total dissolved boron concentration in water, total dissolved silica concentration in water, SiAl concentration in glass, SiZrCa concentration in glass, pH, saturation index of silica in water. The total dissolved boron concentration and the total dissolved silica concentration were observed to characterize the intensity of glass dissolution. It should be noted that total dissolved boron concentration is indicative of glass alteration rate during the whole alteration, whereas total dissolved silica concentration is used when the dissolution is congruent, that is at the beginning of the alteration.

The SiAl concentration averaged inside a glass plate was used to calculate the PRI equivalent thickness (or thickness of dense gel), as defined in Equation 4-1. According to the GRAAL formalism, the major part of this layer is occupied by Si and Al. The SiZrCa concentration averaged inside a glass plate was utilized to estimate the alteration layer total thickness (or thickness of altered glass) and after compared with the thickness of altered glass obtained by MEB. The alteration layer total thickness includes the thickness of dense gel and the thickness of porous gel. SiZrCa pole was chosen due to low Zr solubility; this allows us to consider that Zr stays always inside the alteration layer and does not pass into solution. The equivalent thickness was calculated using Equation 4-1.

$$\frac{de_i}{dt} = \frac{d}{dt}\left(\frac{C_i}{\rho_{PS} x_i S_p C_v}\right), \qquad 4\text{-}1$$

where e_i is the equivalent alteration thickness for element i; C_i is the concentration of this

element in solution; ρ_{PS} is the glass density; x_i is the mass fraction of the element i in the glass; S_p is the glass specific surface, C_v is the mass of the glass in a unit volume

As an illustrative example, distributions of the total boron concentration and the concentration of SiZrCa after 50 days of glass alteration are demonstrated in Figure 4-4b-c.

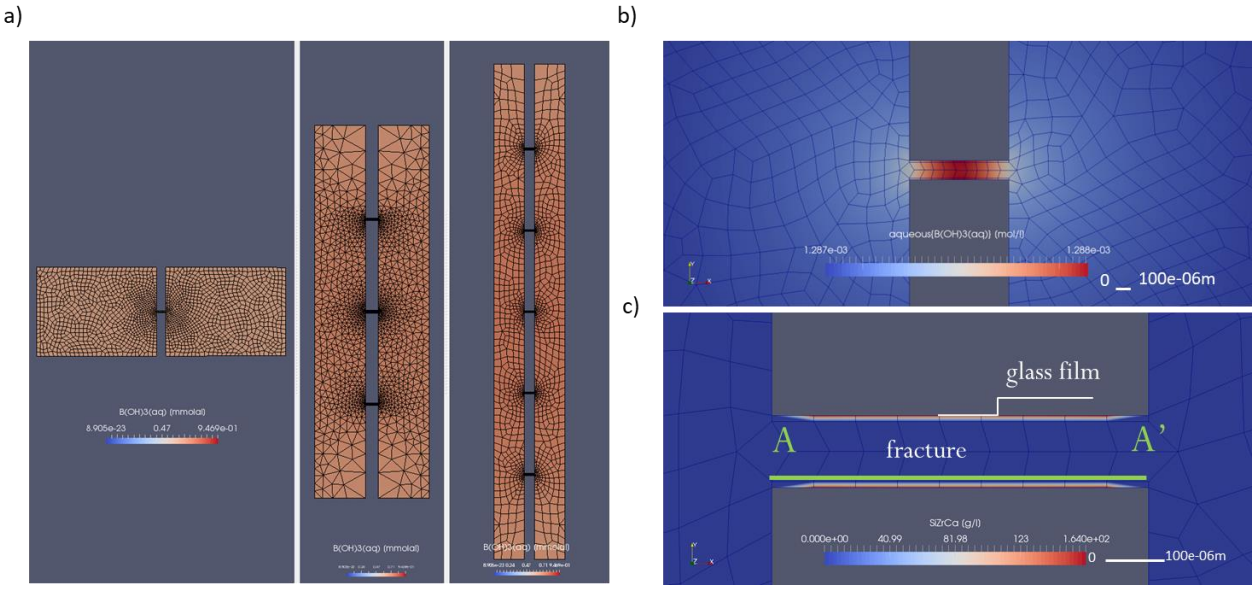

Figure 4-4 a) Example of physical representations of modeled systems: cases 1,3,5 short fractures b) distribution of total boron concentration after 50 days of alteration; modeled case – "1f_ short"; c) distribution of SiZrCa concentration in a glass film; modeled case – "1f_ short".

The results of the modeling presented in Figure 4-5 proved to be close to the expected values. Simulations of the alteration in pure water of the model fractures have shown that the thickness of the gel is in agreement with the experimental results discussed in the previous section. Indeed, according to SEM measurements, the thickness of altered glass on the wall of one fracture of 100 μm aperture altered in initially pure water during 203 d. was of the order of several μm (Figure 4-1c).

The first results of the modeling presented in Sections 2.1.2.3 and 4.2 proves the soundness of the GRAAL application for the reproduction of simple cases of RT in fractured systems. Parameters describing the kinetics of glass alteration are proven to be well adjusted.

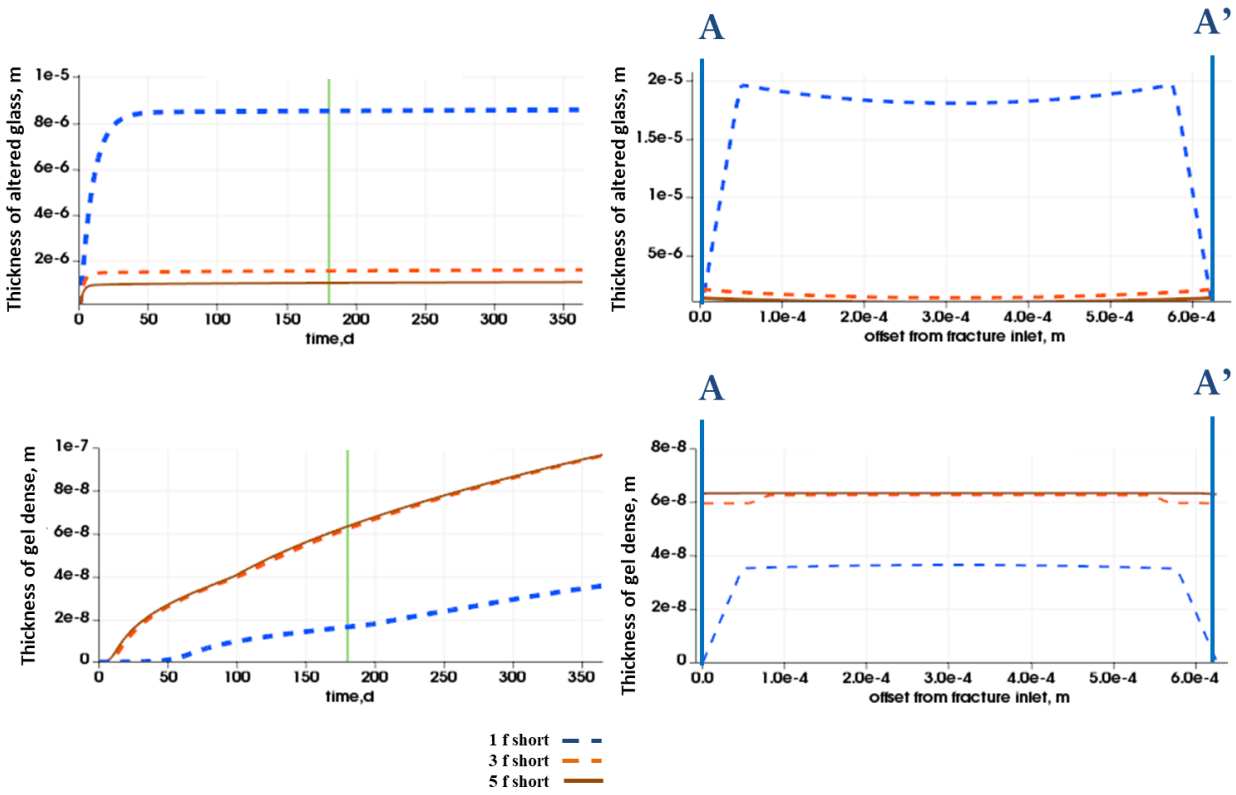

Figure 4-5 Modeled geometries: one, three, five fractures of 0.0625 cm length, total volume of water-filled reactors connected to fracture(s) from two sides was 100 ml.

a) Evolution of the altered glass layer thickness over time for different modeled systems
b) Profiles of the thickness of the altered glass along one fracture (profile A-A' in Figure 4-4c) in systems composed of one, three and five identical fractures, 180th day of aqueous alteration
c) Evolution of the dense layer thickness over time for different modeled systems
d) Profiles of the thickness of dense layer along one fracture (profile A-A' in Figure 4-4c) in systems composed of one, three and five identical fractures, 180th day of aqueous alteration

4.3. Sensitivity study of fracture geometry related parameters on the aqueous alteration of glass

Next, the sensitivity study revealing the effect of major parameters influencing the dissolution kinetics of glass (GRAAL model) was conducted. Three types of effects were studied: mass (or concentration) effect, transport effect and homogenization effect. It was realized by performing HYTEC simulations with changing parameters of:

1. Number of fractures (mass effect);
2. Fracture length (transport effect) ;
3. Opening of fractures (transport effect);
4. Coefficient of diffusion (homogenization effect) ;
5. Volume of water confined in two reservoirs (concentration effect).

The next part of this Section offers the findings emerged from the sensitivity analysis of the

aqueous alteration of ISG glass in initially pure water. Table 4-2 indicates the parameters of the modeled cases presented in this Section.

Table 4-2 Recapitulative table of the systems modeled in the scope of the sensitivity study

Case name	N fractures	Length, cm	Aperture, µm	Total volume of water, m^3	Diffusion coeff in water, m^2/s
1fis_30_short	1	0.0625	30	10.00E-05	10^{-9}
1fis_30_long	1	0.3125	30	10.00E-05	10^{-9}
1fis_120_short	1	0.0625	120	10.00E-05	10^{-9}
1fis_120_long	1	0.3125	120	10.00E-05	10^{-9}
3fis_120_short	3	0.0625	120	10.00E-05	10^{-9}
5fis_120_short	5	0.0625	120	10.00E-05	10^{-9}
3fis_120_long	3	0.3125	120	10.00E-05	10^{-9}
5fis_120_long	5	0.3125	120	10.00E-05	10^{-9}
5fis_120_short_250ml	5	0.0625	120	25.00E-05	10^{-9}
Diff_1fis_short	1	0.0625	120	10.00E-05	10^{-8}
Diff_3fis_short	3	0.0625	120	10.00E-05	10^{-8}
Diff_5fis_short	5	0.0625	120	10.00E-05	10^{-8}

1. **Increasing the number of fractures that terminate in two tanks filled with water decreases the reaction affinity**. It results in the increase of the SiO_2(aq) concentration at the front of the hydrolysis and the stimulated development of the protective gel. In turn, the protective gel decreases the intensity of the degradation.
2. **Increasing the number of fractures gives the same effect as increasing the S/V ratio, where S is the glass surface available for alteration, V is the water volume.** The duration of the velocity drop regime is related to the S/V ratio: the higher the S/V ratio, the quicker the arrival at the silica saturation of the water. This means that less porous gel forms due to the increase of the number of fractures, as its development is impeded by the dense gel. In contrast, dense gel continues to develop even if its increase is small (order of nm) (Figure 4-6).

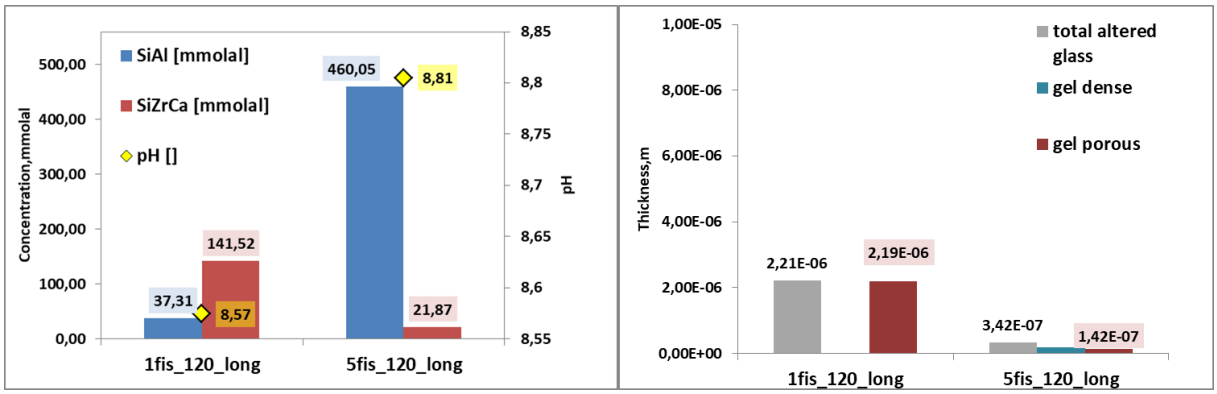

Figure 4-6 Modeled geometries: 1 fracture and 5 fractures of 120 μm opening and 0.3125 cm length. Left: Average concentrations (mmol) of SiAl and SiZrCa after 5 years inside a glass plate, average pH after 5 years inside a glass plate. Right: Thicknesses of altered glass, dense gel and porous gel for two cases after 5 years

3. **Increasing the fracture length decreases the formation of porous gel in the center.** This results from the decrease of the reaction affinity, that is, the achievement of the saturation in silica in the center of a long fracture due to local fluid confinement. From Figure 4-7, it is clear that the precipitation of the dense gel was more significant in the center of the long fracture in comparison to the short fracture. This development of passivating gel restrains glass dissolution that is indicated by the increase of the SiAl saturation index.

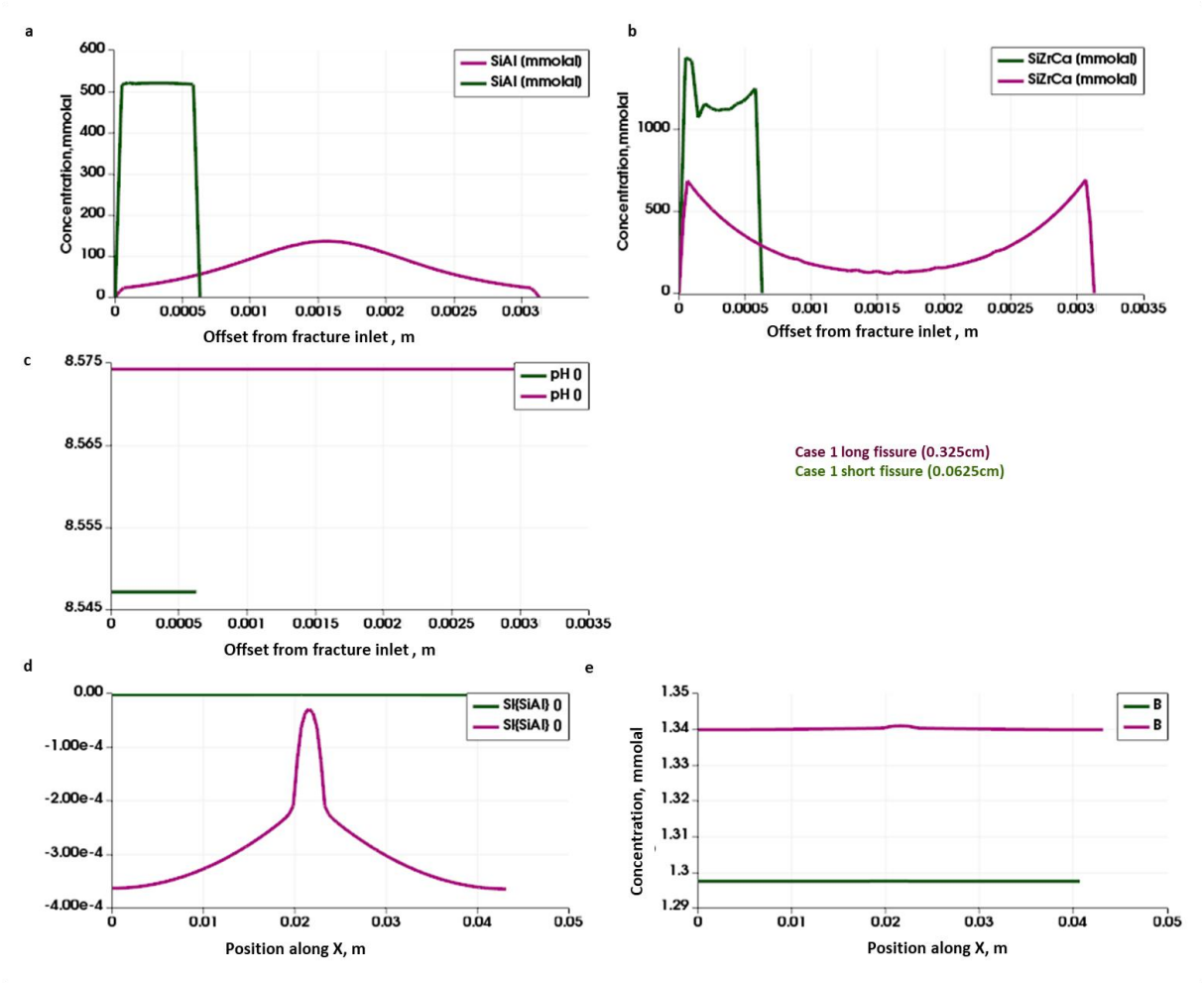

Figure 4-7 Demonstration of the transport effect and the effect of the rection affinity. Modeled geometries: 1 fracture with length of 0.0625 cm (green line) and 0.3125 cm (purple line).

a, b) concentrations of SiAl and SiZrCa along a fracture after 1825j of alteration. In the middle of the fracture the porous gel is formed less easily due to the passivation by the dense layer;
c) profile of pH after 1825 d of glass alteration at the interface glass – water;
d) saturation indices (SI) of SiAl along two reservoirs and a fracture at the end of 5 years; negative SI of SiAl indicates that SiAl ion activity product is less than SiAl equilibrium constant, that is the environment is undersaturated in SiAl, whereas neutral SI of SiAl shows that the solution is in equilibrium;
e) profile of total dissolved boron concentrations. They are traced along two reservoirs and a fracture at the end of 5 y alteration

4. **The rate of glass dissolution is governed by the medium**. pH has a strong influence on the dissolution rate; a low pH (0.1 pH unit) deviation causes a fairly significant change in initial dissolution rate and thus, it affects the glass alteration regime. It should be emphasized that pH in the solution becomes more basic when the S/V of the test is higher. The link between the concentration of SiO_2(aq) in water and pH is directly proportional (Figure 4-8). The porous gel is preferably formed when the initial dissolution regime is longer (case of 3 short fractures), while the dense gel is built up gradually for both modeled

systems during the aqueous alteration (Table 4-3).

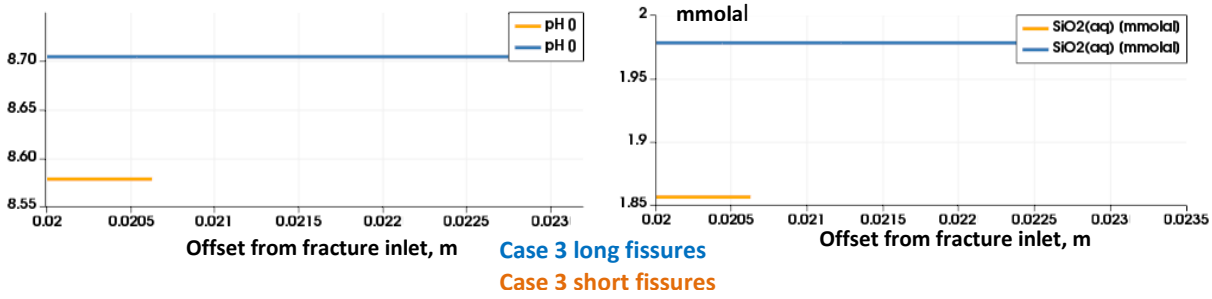

Figure 4-8 Modeled geometries: 3 fractures with length of 0.0625 cm (orange) and 0.3125 cm (blue). pH and aqueous concentration of SiO_2 along a fracture after 1250 days. These images demonstrate the existence of a link between the concentration of SiO_2 (aq) in water and pH.

Table 4-3 Average values of the concentrations of the major poles constituting the depleted (porous) and passivating (dense) layers in a glass plate. Modeled geometries: 3 fractures with lengths of 0.0625 cm (short) and 0.3125 cm (long).

Case	Total glass surface, m^2	Total water volume, m^3	Average SiAl, mmolal	Average SiZrCa, mmola
3 short fractures	6.25E-09	10.00E-05	427	108
3 long fractures	3.13E-08	10.00E-05	400	28

5. **Increased dissolved boron is observed in solution when glass dissolution is favored** (Figure 4-9). In fact, boron is used as a tracer of the alteration because it is not retained in the glass and does not take part of any gel.

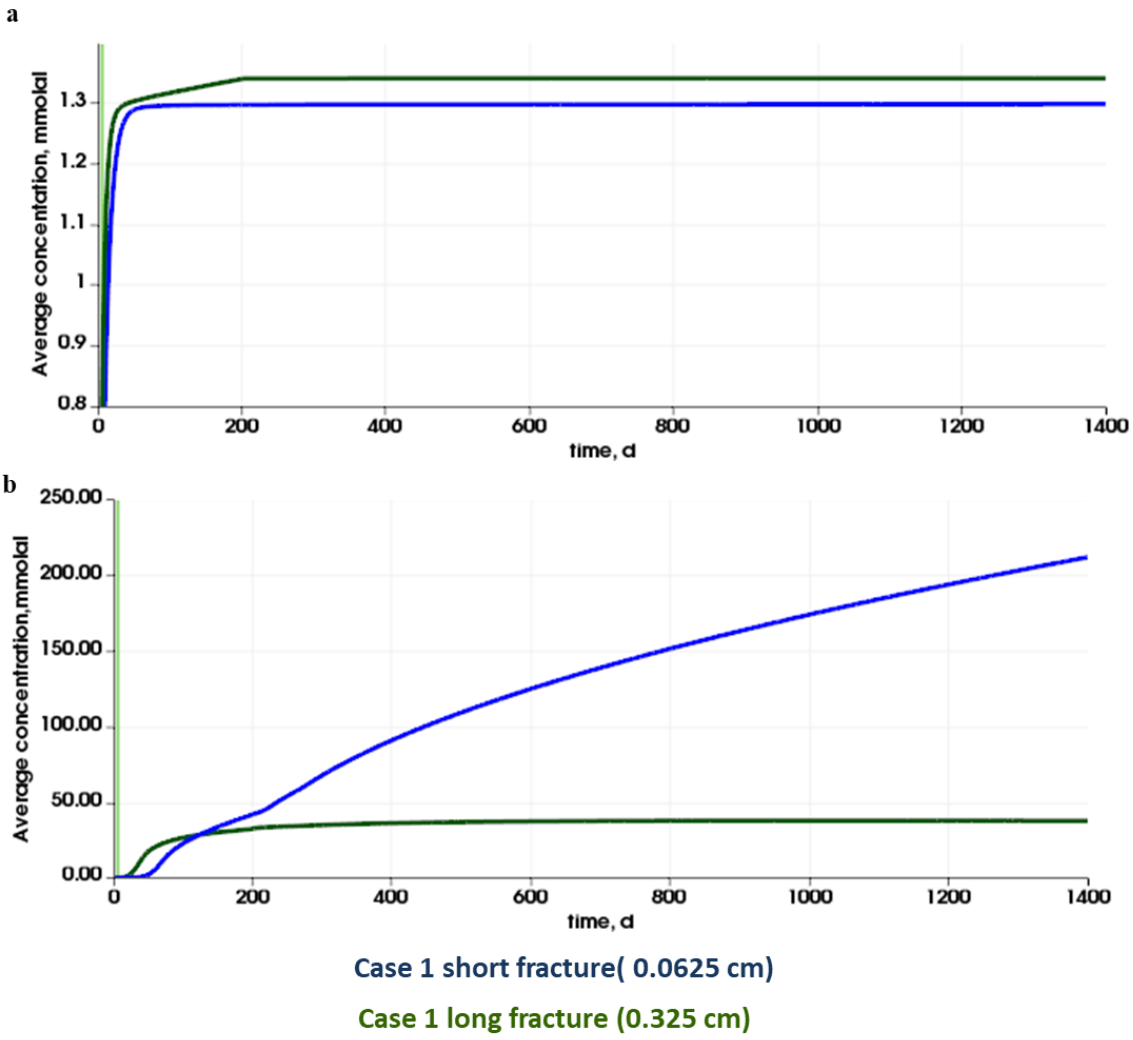

Figure 4-9 Modeled geometries: 1 fracture with lengths of 0.0625 cm (blue) and 0.3125 cm (green).

a) evolution of the average concentration of all aqueous species containing boron in solution;
b) evolution of the average SiAl concentration. Dense gel was more developed in the case 1 short fracture, it explains the fact that less boron was found in solution.

6. **The aqueous alteration of the glass can be different for the internal** (in the center of a fracture) **and external** (near reservoirs) **parts of the fracture,** as indicated in Figure 4-10. At first, the intense interdiffusion is slowed down when the thickness of the hydrated layer becomes more visible. The interdiffusion is more prominent in the middle of the fracture and governs the development of the PRI, whereas porous gel growth is more stimulated by the process of hydrolysis, so the thickness of the porous gel is important at the ends of the fracture where the solution is less confined, see Figure 4-11.

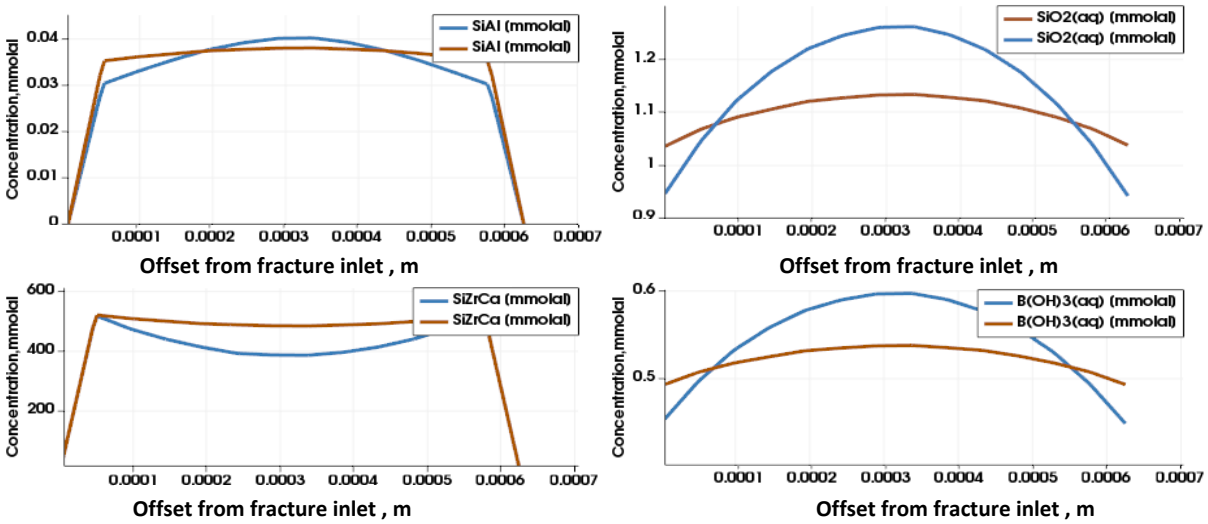

Figure 4-10 Modeled geometries: 1 short facture (0.0625 cm) of 120 µm and 30 µm apertures. Concentration profiles of SiAl, SiZrCa, SiO_2, $B(OH)_3$ in solution on the "glass- water" interface along a fracture after 5 days of aqueous alteration

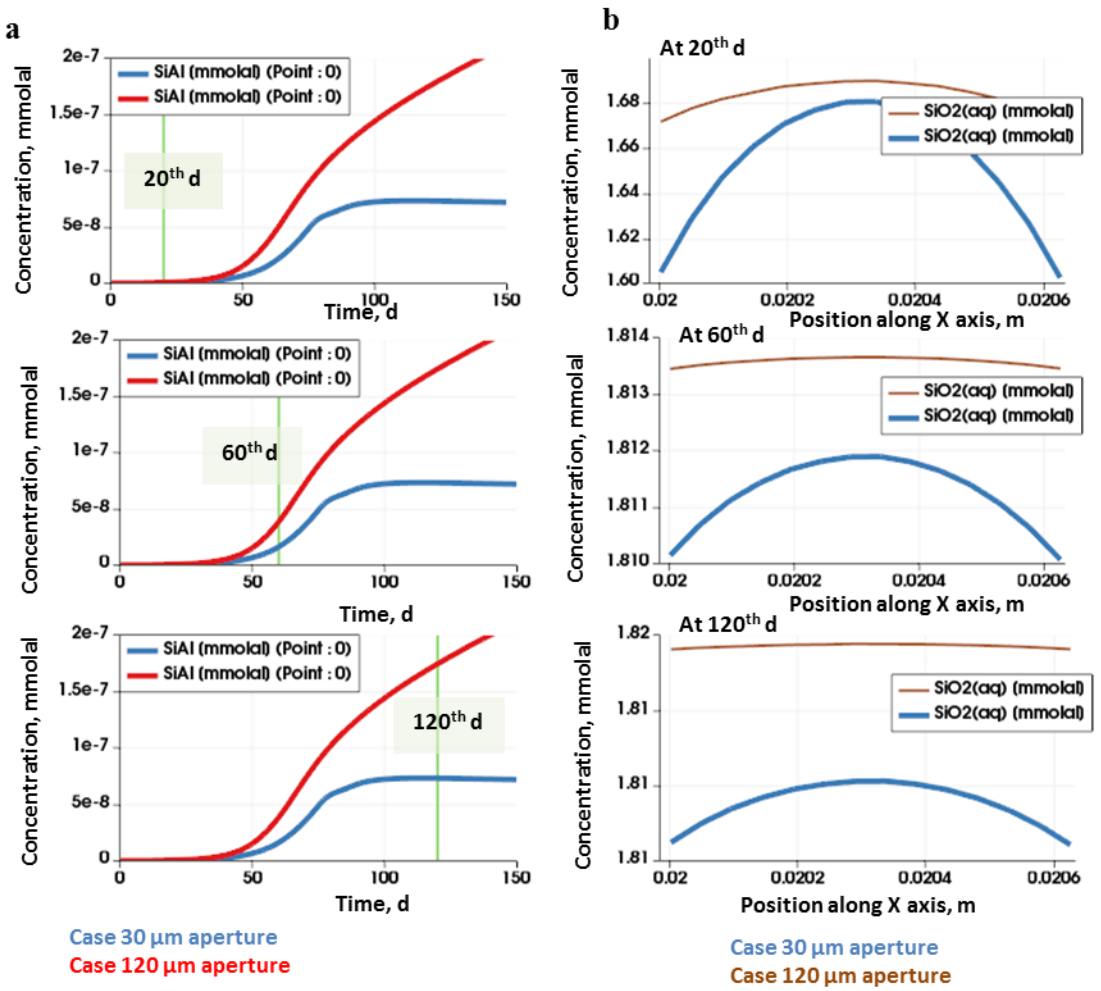

Figure 4-11 Modeled geometries: 1 short facture (0.0625 cm) of 120 µm and 30 µm aperture.

a) evolution of SiAl concentration of vs. time. It reveals that after 80 days the value of SiAl concentration remains stable for the case 1 fracture of 30 µm opening (blue curve).
b) profiles of SiO2(aq) along glass-water interface. It appears clear that in both cases the development of hydrated gel is regulated by the concentration of silica at the glass-water interface (images of the states for the following time steps: 20 d, 60 d, 120 d).

8. **Increasing the diffusion coefficient in water has the effect of restricting the aqueous alteration (passivating and non-passivating),** as seen in Figure 4-12 and Figure 4-13. Indeed, the homogenization of the solution, provoked by the increase of the diffusion coefficient in the water, plays an essential role by acting on the chemical conditions. Given that there is no renewal of water; the agitation, favored by the increase of the diffusion coefficient, causes the increase of the reactional affinity and, as a consequence, the anticipated development of the dense gel (in the first hours). It serves as a curb to slow the growth of the porous gel that globally determines the outcome of the aqueous alteration.

a

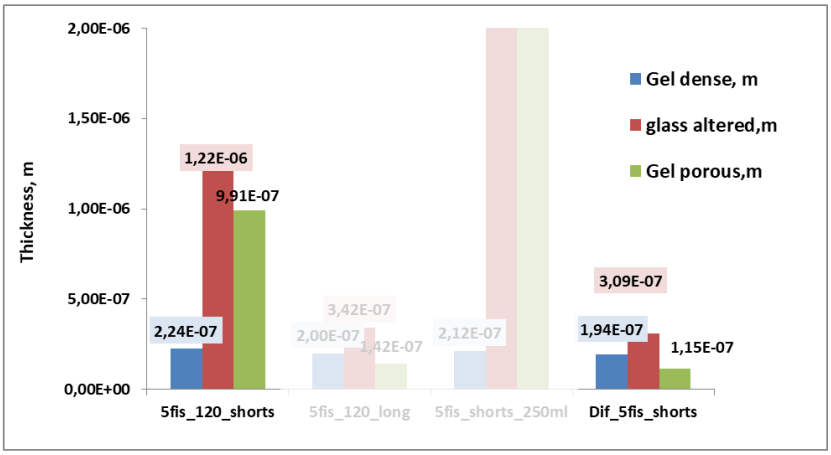

b

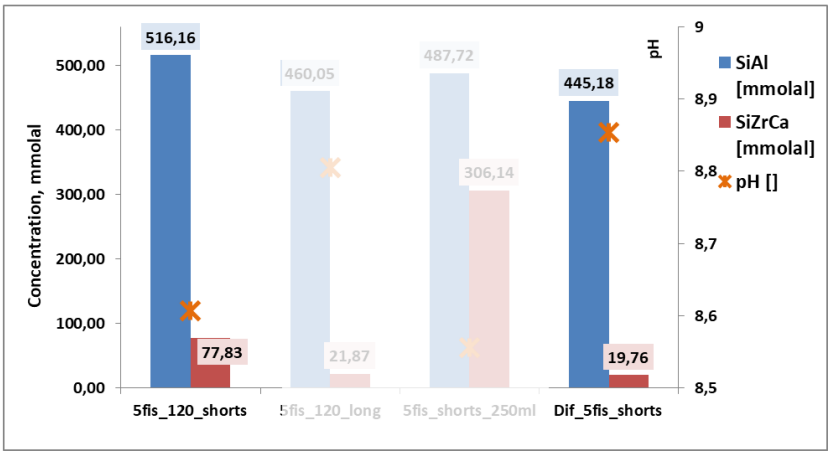

Figure 4-12 Modeled geometries: 5 short fractures (0.0625 cm long), for the first model (5fis_120_short) the diffusion coefficient is equal to 1E-09 m²/s in each water tank; for the second model (Dif_5fis_short) the diffusion coefficient is increased up to 1E-08 m²/s in order to homogenize water

a) bar chart of the average thickness of dense, porous films and overall altered glass(m) after 1825 days of glass alteration;
b) bar chart of the average concentrations of the major poles SiAl, SiZrCa (mmolal) in glass and pH in solution after 1825 days of glass alteration;

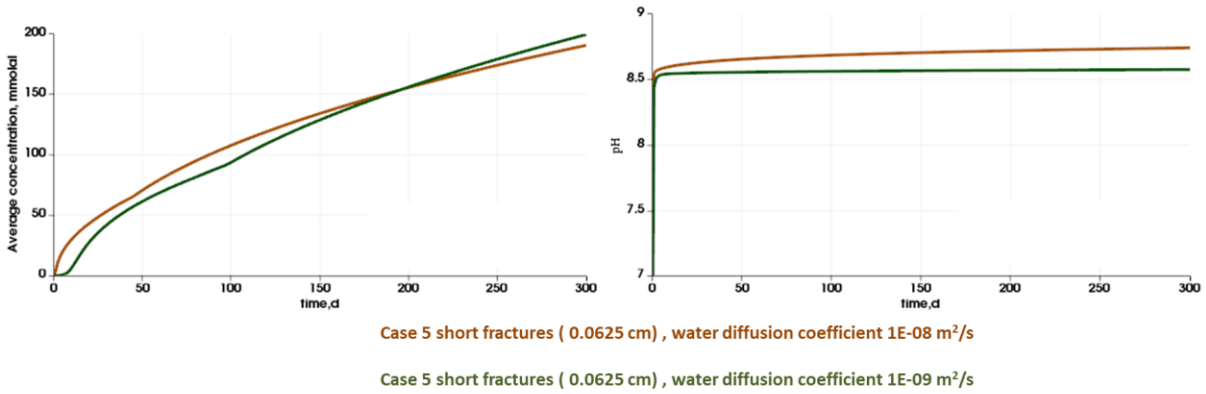

Figure 4-13 Modeled geometries: 5 short fractures, for the first model the diffusion coefficient is equal to 1E-09 m^2/s in each water tank; for the second model the diffusion coefficient is increased up to 1E-08 m^2/s in order to homogenize water

a) evolution of SiAl in the first days of the alteration; after 200 days, the development of the protective gel slows down, but these first days determine the trends of the aqueous alteration;
b) evolution of pH over time; pH increase is observed in the water when the diffusion is more stimulated.

9. **Increased tank volume lead to increased glass alteration**. As the volume of water in the tanks increases, silica diffuses more easily diffused out of the fractures, so that its concentration decreases in fractures. Therefore, there is a delay in the development of the protective gel, while the porous gel develops progressively since there is no restriction due to the reactive affinity.

Together, the results of this sensitivity provide important insight into the influence of the fracture geometry related parameters on the glass aqueous alteration and they suggest the following.

a. Increase of fractures number without changing the water volume of the system causes a slowdown of the development of the porous gel; however, this correlation is not constant. The slowdown of the growth of the porous gel is not identical if we compare the results of the simulations for a pair 1 fracture - 3 fractures, then, a pair 3 fractures - 5 fractures. The increase of the fracture number results in the stimulation of the protective gel development because of the decrease in the reaction affinity (influence of the concentration of silica in the solution).

b. Fracture elongation reveals both the effect of transport and the effect of reaction affinity. Since the chemical conditions are not identical inside a fracture and at its ends, the dense gel develops more in the middle of the fracture where the inter-diffusion process dominates. The hydrolysis effect is seen at the fracture tips where the stimulated development of the depleted (porous) gel is noticed.

c. The higher the S/V ratio, the higher the pH. Consequently, it increases the initial dissolution rate of the glass. As soon as the solution becomes saturated with silica, the system tends towards a state of equilibrium. This modeling conclusion is in accordance with the equation 4-2 describing the dissolution of the glass:

$$\frac{dE}{dt} = r_{dis}\left(1 - \frac{C_{si}(t)}{C_{sat}}\right), \qquad 4\text{-}2$$

where E –is the PRI thickness at time t, r_{dis} – is the rate of PRI dissolution in pure water , $C_{si}(t)$ – is the solution concentration in silica at time t, C_{sat} – is the saturation concentration, when the solution is at equilibrium with the PRI.

d. The larger the volume of the tanks filled with water, the more the passivation effect by the protective gel is delayed. That is, the increase of the volume of water favors the development of the porous gel.

Figure 4-14 provides the summary of the sensitivity study results.

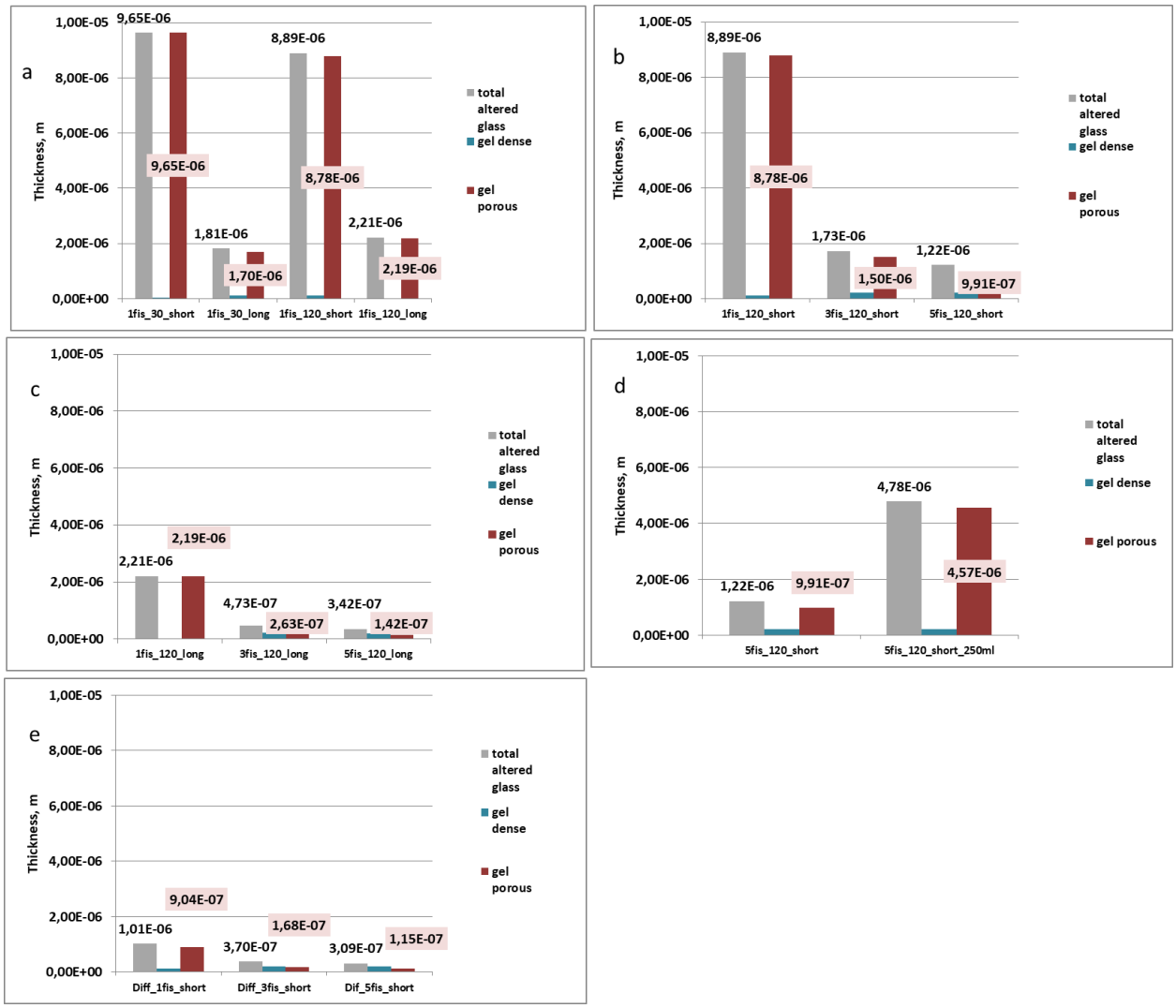

Figure 4-14 Bars charts resuming the results of the reactive transport modeling for the studied cases represented in Table 4-2.

References

Chomat, L. 2008. 'Compréhension de l'altération à long terme des colis de verre R7T7 : étude du couplage chimie transport dans un milieu fissuré', Université Paris VI.

Fournier, M. 2015. 'Etude des mécanismes à l'origine des reprises d'altération. Modélisation et évaluation de l'impact sur les verres de confinement.', Université de Montpellier.

Fournier, M., S. Gin, and P. Frugier. 2014. 'Resumption of nuclear glass alteration: State of the art', *Journal of Nuclear Materials*, 448: 348-63.

Frugier, P., Gin, S., Minet, Y., Chave, T., Bonin, B., Godon, N.,Lartigue, J.E., Jollivet, P., Ayral, A., De Windt, L., Santarini, G. 2008. 'SON68 Nuclear glass dissolution kinetics: Current state of knowledge and basis of the new GRAAL model', *Journal of Nuclear Materials*, 380: 8-21.

Gin, S., and J.P. Mestre. 2001. 'SON 68 nuclear glass alteration kinetics between pH 7 and pH 11.5', *Journal of Nuclear Materials*, 295: 83-96.

Minet, Y., B. Bonin, S. Gin, and P. Frugier. 2010. 'Analytic implementation of the GRAAL model: Application to a R7T7-type glass package in a geological disposal environment', *Journal of Nuclear Materials*, 404: 178-202.

Chapter 5: From block image analysis to reactive transport modeling

CHAPTER 5: FROM BLOCK IMAGE ANALYSIS TO REACTIVE TRANSPORT MODELING

CHAPTER 5: FROM BLOCK IMAGE ANALYSIS TO REACTIVE TRANSPORT MODELING

CHAPTER 5: FROM BLOCK IMAGE ANALYSIS TO REACTIVE TRANSPORT MODELING

List of figures

CHAPTER 5: FROM BLOCK IMAGE ANALYSIS TO REACTIVE TRANSPORT MODELING

List of figures for the article "Coupling image analysis and thermo-mechanical simulation results to produce a model of the fracture network in a nuclear glass canister"

CHAPTER 5: FROM BLOCK IMAGE ANALYSIS TO REACTIVE TRANSPORT MODELING

List of figures for the article "Reactive transport modeling of the glass alteration in a fractured vitrified nuclear glass canister: from upscaling to experimental validation"

CHAPTER 5: FROM BLOCK IMAGE ANALYSIS TO REACTIVE TRANSPORT MODELING

List of tables

CHAPTER 5: FROM BLOCK IMAGE ANALYSIS TO REACTIVE TRANSPORT MODELING

List of tables for the article "Coupling image analysis and thermo-mechanical simulation results to produce a model of the fracture network in a nuclear glass canister"

CHAPTER 5: FROM BLOCK IMAGE ANALYSIS TO REACTIVE TRANSPORT MODELING

List of tables for the article "Reactive transport modeling of the glass alteration in a fractured vitrified nuclear glass canister: from upscaling to experimental validation"

CHAPTER 5: FROM BLOCK IMAGE ANALYSIS TO REACTIVE TRANSPORT MODELING

Résumé du chapitre

Ce chapitre expose le séquencement de toutes les actions (workflow) : il explique en détail la méthodologie allant de la caractérisation et la modélisation du réseau de verre fracturé pour en arrivant *in fine* au transport réactif à l'échelle d'un bloc industriel, en prenant en compte la variabilité du réseau et différentes conditions d'altération (stockage, expérience échelle 1 ALISE). Ce chapitre est écrit dans le format de deux articles. Dans le premier au § 1.3, nous étudions l'application de la morphologie mathématique dans l'objectif (i) d'extraire le réseau de fissures séparément des zones d'arrachement et des retassures, (ii) de déterminer les ouvertures des fissures pour chaque ramification des fissures, (iii) d'effectuer la segmentation de l'image qui a pour but de distinguer les parties de la matrice séparées par les fractures et dont les barycentres sont aisés à déterminer, et (iv) finalement d'étudier l'anisotropie de cette image segmentée par la théorie des moments, et en déduire l'angle de rotation pour chaque cristal et leur barycentre. Ensuite, au § 1.4 et 1.5 du même article, nous étudions les étapes de l'analyse quantitative de la carte du front de solidification, provenant de simulations thermomécaniques de la solidification du bloc de verre. Cette carte et les analyses qui en ont résulté, sont utilisées afin de compléter les données ponctuelles de l'analyse d'image par la distribution spatiale globale des paramètres clés en vue d'effectuer des simulations géostatistiques et de prédire l'anisotropie du réseau. Nous procédons par la suite aux simulations géostatistiques des centres de cristaux et des ouvertures de fissures, dont les résultats sont utilisés pour les réalisations de la tessellation du réseau équivalent de fissures. L'article se termine avec la simulation de quatre réseaux de verre fracturés et de deux images segmentées, pour les deux blocs vitrifiés UOx et UMo.

Dans le deuxième article, au § 2, sont examinées les techniques pour calculer les paramètres équivalents, tels que la perméabilité et le coefficient de diffusion. Nous regardons aussi comment les paramètres, qui gouvernent la cinétique de dissolution de verre, sont calculés dans le cadre du modèle poreux équivalent. La vérification de ces techniques est apportée au § 3 ; elle est effectuée au moyen de simulations de transport réactif appliquées à un réseau simplifié représenté, d'un côté, par l'approche DFN et de l'autre côté, par son modèle poreux équivalent.

L'application du modèle équivalent au cas d'un bloc échelle 1 est présentée au § 4 du deuxième article : les résultats des simulations du transport réactif en mode diffusif et en mode convectif sont montrés et sont comparés aux résultats expérimentaux d'un essai d'altération aqueuse d'un bloc de verre. Ce test a été réalisé au CEA dans l'appareillage de lixiviation statique (ALISE).

Ce chapitre se termine par les résultats de simulations du transport réactif d'un bloc échelle 1 dans les conditions proches à celles du stockage géologique, c'est-à-dire, pour un bloc en position horizontale, au sein duquel la thermoconvection créée par le dégagement de chaleur due à la radioactivité est prise en compte. Ces simulations traitent les échéances 1 000, 5 000 et 10 000 ans après mise en stockage des conteneurs dans les galeries souterraines.

CHAPTER 5: FROM BLOCK IMAGE ANALYSIS TO REACTIVE TRANSPORT MODELING

5.1. Fracture network characterization by mathematical morphology

5.2. Geostatistical and geometric modeling

Sections 5.1 and 5.2 are presented in the form of an article entitled "Coupling image analysis and thermo-mechanical simulation results to produce a model of the fracture network in a nuclear glass canister". It was accepted for publication in April 2019 in the Journal of Nuclear Materials. Some additional information is given below.

Description of a thermo-mechanical simulation used in the study

The overview of the thermo-mechanical model (Barth 2013) used to simulate multiple realizations of the equivalent fracture network tessellation is given in the Section 1.2 of the above-mentioned article. Below some supplementary information on the modeling stages undertaken in the course of the thermo-mechanical simulations is provided.

The protocol used to carry out the thermo-mechanical simulations was composed of two stages: first, the thermal analysis of materials and second, the mechanical analysis based on thermal maps calculated at the first stage. This approach supposed that there was no feedback between the mechanical deformations and the thermal exchanges within the package.

One complete thermo-mechanical modeling run included:

i. complete thermal analysis of the package, coupled with an inverse analysis. This analysis provided the complete temperature map evolving in time with consideration of different materials comprising the package;
ii. viscoelastic analysis that took into account structural viscoelastic relaxations of the glass;
iii. calculation of the glass phase change;
iv. mechanical analysis of the entire system, considering the temperature map and phase changes as a function of time.

The boundary conditions imposed for the simulations are those derived from the temperature readings of the experiment applied to a glass canister carried out in Marcoule, CEA. In this experiment, recordings of three thermocouples placed at ¼, ½ and ¾ the height of the glass block were monitored and analyzed.

The idea behind the inverse analysis was to determine values of the thermal flows based on the values of the temperatures imposed as boundary conditions, by adjusting coefficients of heat exchange happening in the glass (Barth et al. 2014).

Once the data intrinsic to the materials were obtained, it enabled the realization of the simulations with other operating conditions, including the simulations with the term source due to the nuclear radioactivity.

CHAPTER 5: FROM BLOCK IMAGE ANALYSIS TO REACTIVE TRANSPORT MODELING

Use of the thermo-mechanical simulation as a proxy for image analysis

In this research, the results of the viscoelastic analysis were used to complement the photography information and by doing so, establish a link between the observed morphology of the glass fracture network and the evolution of physical parameters resulted in the creation of the crack network. In particular, the calculated map of the arrival times of the solidification front was valuable.

The position of the solidification front was obtained by analyzing the delay between the fictive temperature and the glass temperature at each time step. In fact, it is very difficult to determine the glass transition temperature (T_g) directly because its value depends on two fundamental phenomena that cannot be summed up in a single variable expressed by the temperature. On the one hand, T_g is influenced by the thermal history T(t) of the glass network and on the other hand, the vitreous transition depends on the property of the glass under consideration (*e.g.* specific volume, thermal conductivity, specific heat capacity, viscoelasticity, refractive index, etc.). For this reason, it is often helpful to use the fictive temperature (T_f) generalized by Narayanaswamy and Moynihan in the model "TNM" (Tool-Narayanaswamy-Moynihan) (Moynihan et al. 1976; Narayanaswamy 1971). The state of structural relaxation, obtained through T_f, quantifies the progress of structural relaxation over the thermal history T(t). The fictitious temperature T_f is calculated in every point of the volume of glass. The internal glass properties change in a different way according to the state of the glass, which can be liquid, solid or semiliquid / semisolid. First, when $T = T_f$ and $T >> T_g$ the glass is considered to be in the liquid phase. Second, when $T_f >> T$ the glass is in the solid state and shows properties of a solid medium. It should be noticed that T_f can continue to evolve leading to the stabilization or solid state relaxation of the glass. Third, when T_f begins to show the delay with respect to the cooling taking place according to T, the glass is considered in the liquid-solid transition state.

In consideration of the T_f and T evolution, it was possible to determine at each time step of the simulation the evolution of the position of the solidification front. On the basis of these data, the map of the arrival times of the solidification front was built. This parameter was chosen because it is the cooling rate, related to the liquid/solid phase transition that was demonstrated to be a major parameter governing the glass package fracturing. Indeed, the higher the cooling rate, the quicker the transition of the phases and the stronger the structural perturbation of the glass resulting in the more intensive matrix fracturing.

Title: Coupling image analysis and thermo-mechanical simulation results to produce a model of the fracture network in a nuclear glass canister

Authors : Maria Repina[a,b], Didier Renard[b], Frédéric Bouyer[a,8], Vincent Lagneau[b]

[a] CEA, DEN, DE2D, SEVT, LCLT Marcoule, F 30207 BAGNOLS SUR CEZE Cedex, France

[b] MINES ParisTech - PSL Research University, Centre de Géosciences 35, Rue Saint-Honoré F 77305 FONTAINEBLEAU Cedex, France

Abstract

Understanding nuclear glass alteration in a fracture network of a block of nuclear glass is critical in predicting the release of the radionuclides in the subsurface and is relevant for the security of nuclear waste disposal. Here, we present an image processing-based fracture network characterization workflow that enables us to characterize a glass block fracture network, establish a link between a physical parameter representing an internal state of glass structural relaxation and an internal structure of the block fracture network, and generate multiple realizations of equivalent fracture networks by considering the variability of the fracture network parameters such as fracture distribution and apertures. The proposed workflow includes the following stages: (i) fracture network extraction, (ii) measurement of apertures of all distinct ramifications of the fracture network, (iii) image segmentation, (iv) anisotropy characterization, (v) passage to segment representation with the intention of modeling block equivalent fracture networks by using an algorithm of mesh growth, (vi) geostatistical modeling of average apertures and variables responsible for fracture spatial distribution, and (vii) simulation of equiprobable realizations of fracture network equivalent tessellations. Given this processing, the workflow is able to provide data for further steps including upscaling of diffusivity and permeability, and it facilitates reactive transport modeling at the glass block scale. As an illustrative example, we apply the proposed sequence of actions to a two-dimensional (2D) high-resolution image of two blocks of nuclear glass. This application brings into service both hard data obtained by direct measurement of the fracture network and soft physics-based explanatory data and considers the variability in the fracture network. The results show that implementation of the devised procedure presents an opportunity for better understanding of the impact of fracturing on aqueous alteration of glass.

Keywords

Nuclear waste, fracture network, image analysis, thermo-mechanical simulation, equivalent model, nuclear glasses.

Introduction

Vitrification of radioactive waste has been acknowledged as a feasible and reliable application to condition high-level long-lived nuclear fission products in geological disposal facilities on time scales

[8] Corresponding author CEA, DEN, DE2D, SEVT, LCLT, Marcoule, F 30207 BAGNOLS SUR CEZE Cedex, France
E-mail address: frederic.bouyer@cea.fr (BOUYER Frederic)

of up to millions of years. This process involves calcination of liquid fission product solutions followed by a melting stage at around 1100 °C in a metallic vessel in which the molten glass and the calcinated fission product solution are directly heated by electromagnetic induction before being poured into a metallic container. As the glass cooling and solidification occur, the stress increase stemming from the mechanical equilibrium between the internal liquid glass and external solidified glass causes the development of a fracture network. The thermal gradient is very important at the beginning of the cooling along the walls of the stainless steel container that results in the creation of a dense fracture network. After, when the gradient fades, a less dense radially growing fracture network creates in the center of the block.

The chemical performance and alteration of glass under leaching has been extensively studied during the last thirty years (Pierce et al. 2014; Carl I. Steefel 2015; Gin et al. 2013). The results of these experiments have provided a better understanding of the mechanisms of glass alteration at the micro level and facilitated elaboration of the glass reactivity with allowance for the alteration layer (GRAAL) model (Frugier et al. 2008). The modeling of flow and transport phenomena in fractured media is a topical issue in Earth sciences. The nuclear energy industry has shown interest in this subject because fractures could eventually enable the release of radionuclides in the ground waters of deep geological waste repositories. In fact, multiple studies have modeled the migration of radionuclides in fractures of host rocks surrounding deep geological repositories for high-level waste (ANDRA 2005; Zhang 2018; Nykyri et al. 2008; Cvetkovic et al. 2004).

By merging the lessons learned from both fields, it is possible to imagine quantitative simulations of the coupled chemical evolution of the glass and the migration of fluids and solutes within its fracture network at the block scale. To that end, good characterization of the fracture network is a key step before quantifying the long-term immobilization properties of the matrix. However, a discrete fracture model is considered to be too computationally demanding for conducting the reactive transport modeling (RTM) applied to a block of nuclear glass; instead, construction of an equivalent fracture network model and determination of its equivalent hydraulic and diffusive parameters are necessary.

In this article, a new methodology is introduced to characterize a fracture network of a glass package at scale 1 and to simulate multiple realizations of its equivalent representation to enable estimation of the uncertainties of the quantity of altered glass (QAG) resulting from the uncertainties of the fracture network-related parameters such as diffusion, permeability, and porosity. Beginning with high-resolution photography of the cross-section of an inactive glass container, the methodology used here relies on the combination of mathematical morphology techniques and geostatistical analysis to build a model of the fracture network. The results from thermo-mechanical simulations of the cooling phase of the glass (Barth 2013) are also used, particularly the calculated arrival times of the solidification front.

The paper is organized in the following manner. Section 1, Material and methods, presents an overview of the steps involved in the characterization methodology of the image processing-based fracture network and includes (i) characterization of a glass block fracture network by using mathematical morphology approaches, (ii) numerical analysis of a physical parameter proved to be indicative of a glass block fracturing pattern, (iii) geostatistical exploratory analysis and modeling of fracture geometry-related parameters, and (iv) creation of multiple realizations of a glass block

equivalent fracture network. Section 2, Results, details the implementation of the methodology on the high-resolution photography of a section of an inactive glass container. The fracture networks of the training block images are compared with the realizations of equivalent fracture networks. Section 3, Discussion, covers the potential applications of this methodology. Finally, the conclusions and the perspectives of this study are given in Section 4.

1 Material and methods

The complete workflow consisted of several steps, as shown in Figure 1: 1) fracture network image analysis, 2) creation of a proxy model via analysis of the map of arrival times of the solidification front, 3) geostatistical modeling, and 4) construction of multiple realizations of fracture network equivalent tessellations. Application of the model, including upscaling of diffusion, permeability, and parameters governing the kinetics of glass dissolution, and subsequent RTM are beyond the scope of this paper but will be covered in a forthcoming article. Although major verification of the feasibility of the model is addressed in the second part of the research, where the results of the RTM are compared with the experimental data, in the Results section it is shown that the distribution and the anisotropy of fracture network static parameters are honored and reproduced. The variation of the fracture density is respected, and the distribution of the fracture apertures is preserved.

The workflow asks for input of the pre-prepared grayscale image and progresses through seven stages: (i) fracture network extraction, (ii) measurement of fracture apertures, (iii) image segmentation, (iv) anisotropy characterization of the segmented image, (v) calculation of average aperture for each zone (segment) of the segmented image, (vi) construction of a proxy model based on the analysis of the map of the arrival times of the solidification front (Barth 2013), (vii) geostatistical modeling of the position of mesh seeds and averaged aperture values, and (viii) simulation of equiprobable realizations of fracture network equivalent tessellations.

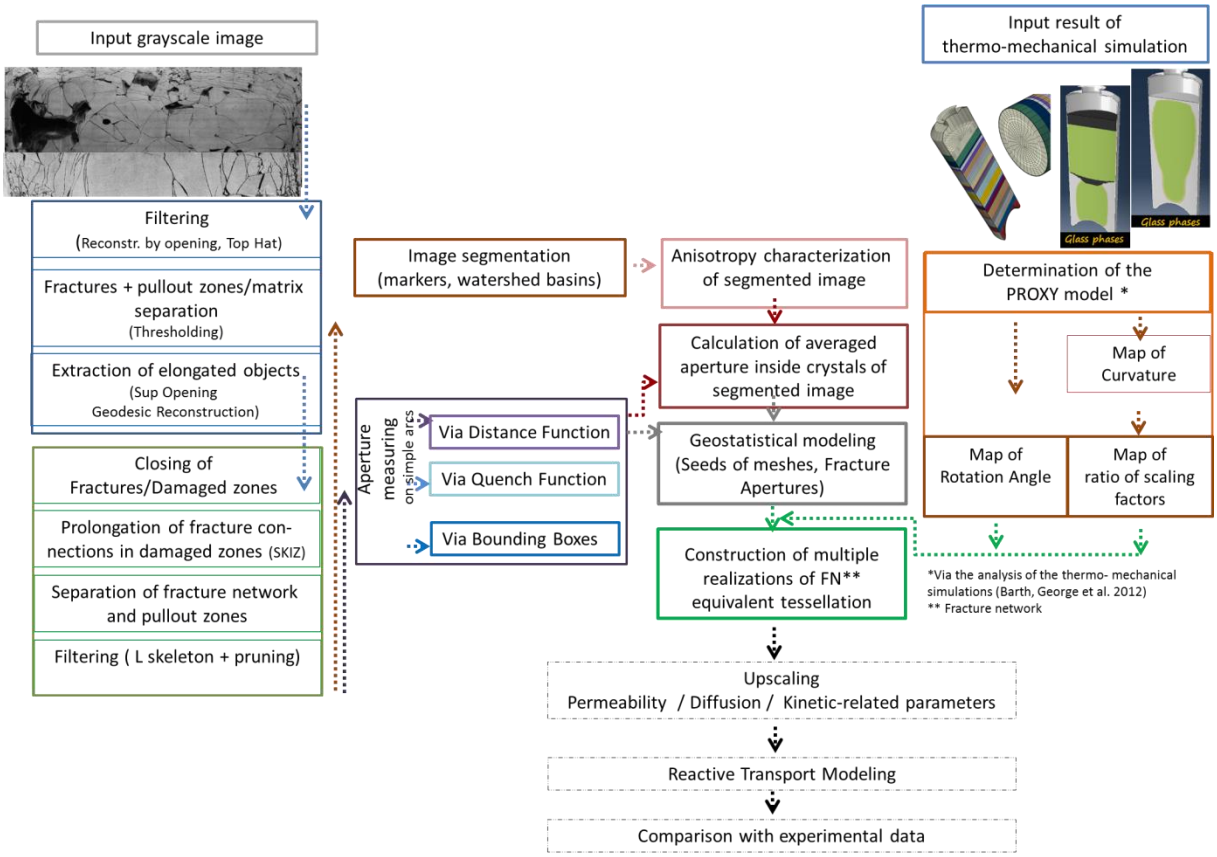

Figure 1 Image processing-based fracture network characterization method. The parts contoured with dashed lines are not presented in this paper.

Free libraries MAMBA[9] and Smil[10] written in C and Python were adopted to conduct morphological image analysis. Analysis of the map of the arrival times of the solidification front was conducted in Python, R, and Paraview. For geostatistical exploratory analyses, simulations of equivalent tessellations were performed in R, specifically the RGeostats package[11].

1.1.Glass block section

In our research, morphological mathematics methods were engaged to characterize the morphology of the fracture networks via extensive analysis of high-resolution photography. The images of the longitudinal cross-sections of specimens of non-radioactive packages of nuclear glass were used as a testbed for this study. Two packages were produced at the Vitrification Production Facilities in Marcoule in a cold crucible induction furnace: uranium-molybdenum[12] (UMo) and uranium oxides[13] (UOx) (Vernaz 2009). Molten glass was poured in a steel canister 1.1 m high with an internal diameter of 0.42 m. The injection from the crucible occurred in two phases, with each casting being half of the nominal volume of 400 kg in total. The duration between the two castings was close to 6 h. After a waiting time of about 2 h below the furnace, the package was removed and was placed into a room in which the cooling progressed further with no implication of forced airflow.

[9] http://www.mamba-image.org.html
[10] http://smil.cmm.mines-paristech.fr/doc/index.html
[11] http://rgeostats.free.fr/
[12] This is a vitrocrystalline matrix with 13 wt% molybdenum oxide developed to confine solutions used for UMo fuel treatment
[13] This is ordinary industrial glass for confining fission products arising from UOx fuel treatment

Soon after their fabrication, the canisters were cut in two parts along their long axis. Some precautions were taken to preserve the integrity of the intrinsic fracture network. Hence, viscous resin was poured on top of the UMo glass prior to the sawing operations. However, resin could not fill the entire network. In a similar manner, the integrity of block UOx was not fully assured during the cutting operations; the batch of grout poured on the top of the glass package could not penetrate the network.

Nevertheless, we assumed in this work that the resultant fracture networks separated from the pullout zones were representative and fully appropriate to serve as objects for further modeling.

A series of photographs of the two block halves, at 200 kg with dimensions of 430 mm × 1335 mm, were shot at different resolutions. The methodology developed in this study is presented by using the UMo image (Figure 2) and includes a complete process from extraction of the fracture network to simulation of its multiple equivalent realizations. The UOx image is presented subsequently when comparing the results of the equivalent network construction to the real fracture networks. The image parameters for both blocks are indicated in Table 1.

Table 1 Characteristics of the examined images

Name of image	Size (px) of input image	Resolution (mm)	Assembly of N images
UMo	6144 × 2430	0.17	1
UOx	6592 × 2856	0.1443	1

Figure 2 Grayscale image of the UMo bloc of vitrified fractured glass. Dimensions: 1044 mm × 413 mm.

1.2. Thermo-mechanical simulation

The thermo-mechanical model used to complement the photography information is based on the results of the thermo-mechanical fracturing program (Barth et al. 2014; Barth et al. 2012) of the VESTALE project initiated and financed by the French Atomic Energy Commission (CEA), National Agency for Radioactive Waste Management (ANDRA), and Orano (previously Areva). The objective of the program was to develop a tool for simulating the fracturing of nuclear borosilicate glass used for radionuclides confinement. For this purpose, the finite element method was used to model the viscoelastic behavior and the damage behavior, evolving in response to the structural relaxation of the glass. This program was established to build models from the thermo-mechanical parameters determined experimentally on SON68 glass, as given by CEA, and to provide simulations on the scale

1 package with the most representative scenarios of the industrial process. The 3D representation of the thermo-mechanical model is shown in Figure 3a.

Although the simulation results showed the evolution of the glass fracture network surface due to radiogenic heating, it is not expected to be significantly different from the fracture networks analyzed in this research (Barth 2013) The radioactivity has the effect of slightly reducing the fracturing of the blocks. The inactive glass used in this study can therefore be considered conservative in the sense that radioactive glass would develop a similar or reduced fracture network.

The position of the solidification front was obtained by analyzing the delay between the fictive temperature (T_f) and the glass temperature at each time step T(t). In fact, it is very difficult to determine the glass transition temperature (T_g) directly because its value depends on two fundamental phenomena that cannot be summed up in a single variable expressed by the temperature. On the one hand, T_g is influenced by the thermal history T(t) of the glass network and on the other hand, the vitreous transition depends on the property of the glass under consideration (*e.g.* specific volume, thermal conductivity, specific heat capacity, viscoelasticity, refractive index, etc.). For this reason, Barth used T_f generalized by Narayanaswamy and Moynihan in the model "TNM" (Tool-Narayanaswamy-Moynihan) (Moynihan et al. 1976; Narayanaswamy 1971). The state of structural relaxation, obtained through T_f, quantifies the progress of structural relaxation over the thermal history. T_f is calculated in every point of the volume of glass. The internal glass properties change in a different way according to the state of the glass, which can be liquid, solid or semiliquid / semisolid. In consideration of the T_f and T evolution, it was possible to determine at each time step of the simulation the position of the solidification front (Figure 3b). The assembled map of the arrival times of the solidification front (Section 1.4) will be used to supplement pointwise data from the image analysis with global spatial distribution of the key parameters.

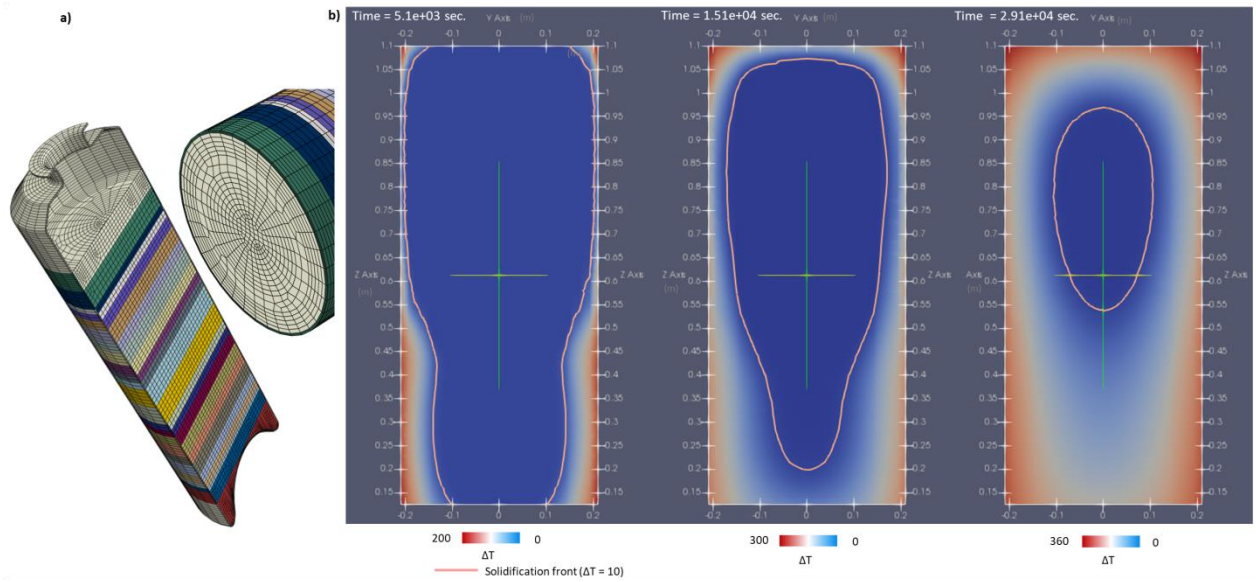

Figure 3 Results of thermo-mechanical study: a) three-dimensional (3D) mesh of the package for thermo-mechanical simulations showing longitudinal and transverse sections, obtained from (Barth 2013); b) Variable expressing the delay between the fictive temperature and the temperature inside the glass (ΔT= Tf – T),

indicating the glass internal state (blue: liquid; red: solid). Evolution of the solidification front approximated by the isoline of the delay ΔT= 10.

1.3. Fracture network characterization by mathematical morphology

Mathematical morphology methods were used to characterize the fracture network of a block of nuclear glass. First developed by Matheron (Matheron 1967) and Serra (Serra 1969) in 1960s, it is currently applied to many domains in which image processing in both two and three dimensions is requested. Its high demand in the geosciences is easy to explain because it offers a nondestructive approach of heterogeneous medium characterization by combining non-intrusive analysis such as micro-tomography (Tokan-Lawal et al. 2015), scanning electron microscopy (Al-Kharusi et al. 2008; Jouini et al. 2011), and ordinary digital imaging (Chatterjee et al. 2010). Because mathematical morphology is based on the assumption that any image consists of structures that can be handled by the set theory; these sets are studied to determine important network attributes such as the porosity, connectivity, and size of objects that comprise the fracture network.

1.3.1. Fracture network extraction

Image processing includes several steps and aims to extract the fracture network to be studied afterward. In the first step, the chosen images are cropped so that the stainless steel container edges are removed and only the glass matrix remains. The images are then transformed into grayscale images of 8 bit/pixel. The gray images are filtered via opening by reconstruction, defined as that by erosion of the image using a hexagon as structuring element followed by a morphological reconstruction (Vincent 1993). This operator enables elimination of light reflections that cannot contain the structuring element, leaving other image features unaltered.

The fracture network is then extracted by the following operations:

1) Black top hat transformation, defined as the difference between the closing of the image and the image itself, is performed by a hexagon structuring element of size 20 to remove slow trends and to perform contrast enhancement. This operator brings out fractures whose thickness is half the chosen size; as a consequence, it facilitates the separation of the glass matrix and the fracture network.
2) Thresholding based on the histogram of the image is conducted to separate the clear gray background of a glass matrix from the foreground dark gray fracture network together with the pullout zones.
3) Supremum[14] of linear openings by reconstruction is performed to preserve objects (fractures) greater in size than the chosen opening size in at least one direction. This operator ensures conservation of the elongated fractures, with the noise coming from the thresholding removed. All retained fractures are reconstructed to their real forms by geodesic reconstruction.

As mentioned previously, both fractures and pullout zones created during the sawing operation[15] are present in the foreground. The next step is devoted to their separation from the fracture network so that the artificially created pullout zones are removed. For this purpose, the operators used are

[14] In this article, “supremum” and “union” as well as “infimum” and “intersection” are used as interchangeable synonyms; supremum (or point-wise maximum) and infimum (or point-wise minimum) replace the union and the intersection set operators for grayscale images.
[15] The bloc has been split in two longitudinal cross-sections to expose the existing fracture network.

closing, which closes fractures that are thinner than the pullout zones, and hole filling, which closes the pullout zones. Because certain fractures cross the extracted pullout zones, their prolongation is assured by tracing the skeleton of influence zones. This operation does not add redundant connections but enables preservation of the connectivity of some fine fractures in the artificially damaged zones. Final slight filtering is performed by extraction of the fracture skeleton, followed by removal of the skeleton ramifications and the geodesic reconstruction of the resulting skeleton.

1.3.2. Measurement of fracture apertures

Fracture aperture is a principal network characteristic governing the intensity of the glass aqueous alteration. Three methods based on morphological mathematics are proposed for measuring the fracture apertures.

1.3.2.1. Discrete way of aperture measurement via bounding boxes

The first method is based on measuring the Feret diameters of each rotated bounding box containing a single, non-connected labeled component, or each simple branch, of the fracture network. The separation of the network into non-connected branches is performed by subtraction of the dilated multiple points[16] from the extracted fracture network (Figure 4, Figure 5a).

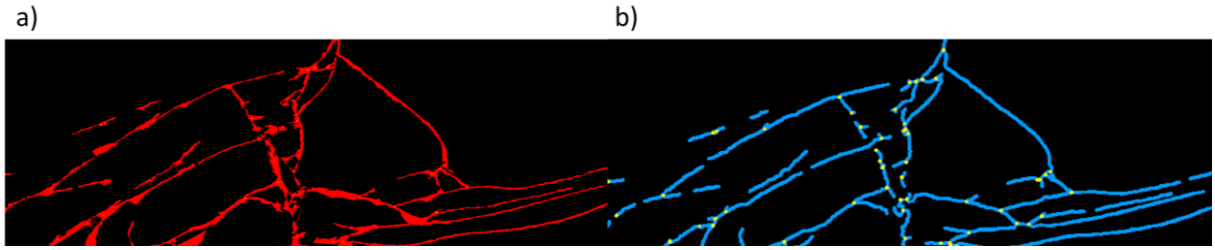

Figure 4 Preparation of fracture network for aperture measurement via the bounding boxes approach

a) Fragment of UMo image with dimensions of 318.9 mm × 122.2 mm; b) multiple points at the locations of fracture branching shown in yellow. For visibility in this image, the multiple points and the skeleton by homotopic thinning are dilated with a hexagon structuring element of size equals to three.

It should be noted that each bounding box, *i.e.* the rectangle that circumscribes its corresponding fracture, is aligned with the inertia tensor computed from the second-order moments of this fracture (Equation 4). This makes the values of minimum Feret diameter indicative of the average fracture aperture.

[16] The procedure of multiple point extraction is described in section 1.3.2.2

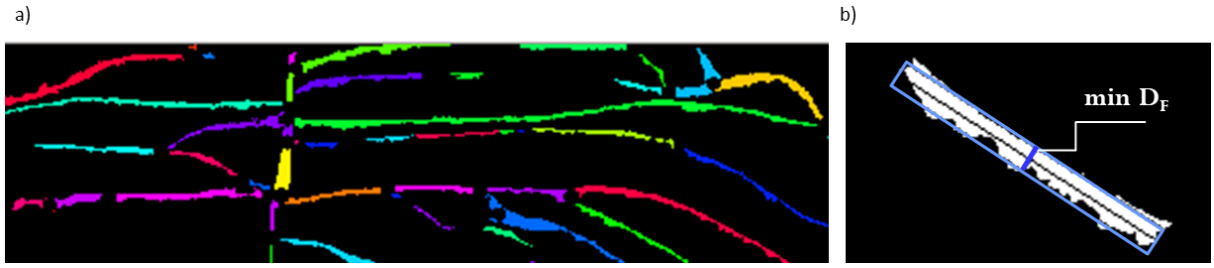

Figure 5 a) Fragment of UMo image with dimensions of 68 mm × 19.9 mm. Patchwork palette was used to mark the fracture ramifications separated by dilated multiple points; b) Each ramification was circumscribed by a bounding box in which the minimum Feret diameter (min D_F) was used to measure the fracture aperture average. The shown ramification has min D_F = 12 px (2.04 mm).

1.3.2.2. Continuous way of measurement via quench and distance functions

The second and third methods rely on the techniques of homotopic thinning. In the framework of these methods, the aforementioned problem of the fracture network separation is resolved by implementing several operations:

1) homotopic thinning with the L structuring element (Serra 1982);
2) removal of the skeleton's endpoints (pruning);
3) extraction of multiple points at the intersections of fracture branches; and
4) subtraction of multiple points from the resulting L-skeleton.

After implementing this sequence of operations, we obtained simple arcs that represent disconnected ramifications of the fracture network. For each ramification, its barycenter and aperture average will be found subsequently.

We used two techniques of aperture measurement: the quench function[17] (Figure 6a), associated with the skeleton of maximal balls, and the distance function (Figure 7), recorded on the traces of simple arcs[18]. Both of these functions give the (n + 1) value, where

- for the first technique, n is the size of the maximal disc put at point i on the skeleton by maximal balls; and
- for the second technique, n is equivalent to the level of the distance function.

These techniques of measurement thus provide information on the thickness of the fracture branches in a continuous manner. However, the averaged apertures of the fractures are not expected to be identical for several reasons. First, on the periphery of fractures, the traces of skeleton branches are expected in which the quench function values are equal to 1. This occurs because fracture walls are not ideal flat lines, and the skeletonization by maximal balls is highly sensitive to even small variations in its boundaries. These irrelevant branches of the skeleton (Figure 6b) should not be considered in the course of aperture average computation. This step can be

[17] This function represents the locus of the skeletal points together with their minimal distance to the fracture walls.

[18] The skeleton by homotopic thinning with removed multiple points of the skeleton gives a multitude of disconnected ramifications named simple arcs.

performed by finding the intersection of the traces of simple arcs and the skeleton of maximal discs[19].

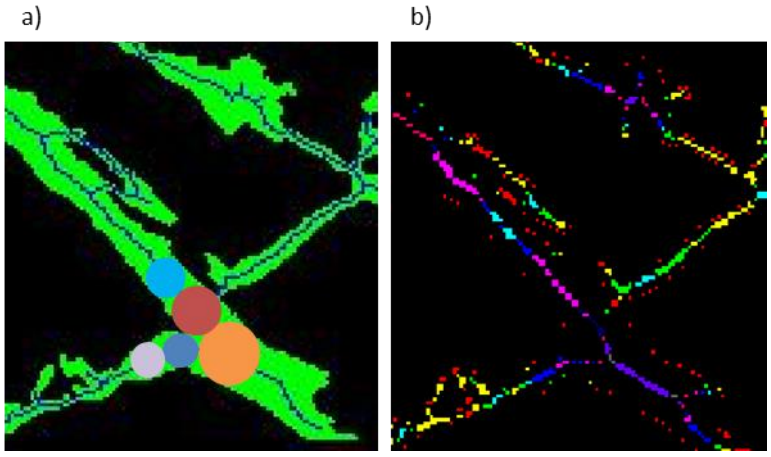

Figure 6 Fragment UMo image with dimensions of 27 mm × 30.3 mm: a) sketch showing superposition of fractures and the skeleton by homotopic thinning with overlapped maximal balls in which the radii are recorded to evaluate the fracture aperture average; b) patchwork palette application to visualize the quench function that represents the locus of the skeletal points with associated values of the radii of maximal balls.

It should be noted that the aperture average value measured by this technique is not always available for all simple arcs. For some simple arcs, intersection of the trace of skeleton by simple arcs and the trace of the skeleton by maximal balls does not exist. This issue can be resolved by reading the values of distance function directly on the traces of the simple arcs without calling upon their intersections with the skeleton by maximal balls. The distance function of the fracture network image is calculated by using the MAMBA image library.

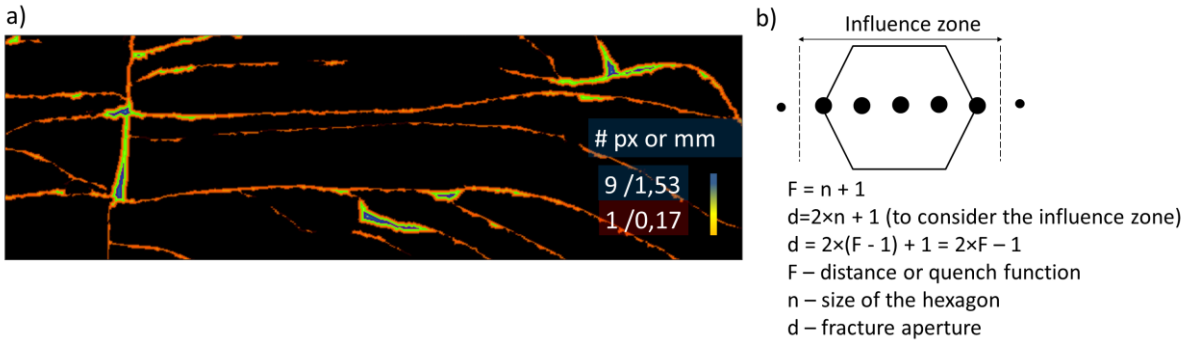

Figure 7 a) Fragment of UMo image with dimensions of 127.2 mm × 43.5 mm. The visualized distance function used the values read on the traces of the simple arcs to calculate the fracture aperture average; b) sketch showing a hexagon structuring element and an influence zone taken into account when calculating quench and distance functions.

[19] Even if the L homotopic skeleton and the maximal balls skeleton do not always occupy the same position, they still have overlapping points.

The values of average aperture of each fracture network ramification were calculated by formula (1):

$$\sum(2(F-1)+1)/nb = \sum(2F-1)/nb, \quad (1)$$

where F is the value of the distance function or quench function read on the trace of the corresponding simple arc, and nb is the number of points making up the trace. In formula (1) on the left-hand side, one comes from the fact that there is an influence zone (Figure 7b) that is considered when measuring fracture width.

1.3.3. Image segmentation

In mathematical terms, segmentation is the partition into disjoint nonempty sets known as segments (Soille 2003). Usually, an image that has been segmented is represented as a label image that enables separate processing of all compound elements including disjoint sets named segments, as discussed below.

The main objective of the segmentation is to define segments that represent parts of the glass matrix separated by the extracted early fracture network.

This is realized by a sequence of operations based on watershed transformation (Beucher 1982).

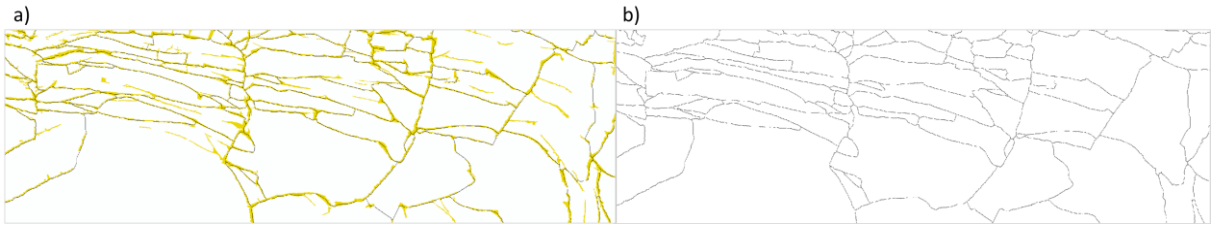

Figure 8 Fragment of UMo image with dimensions of 314.8 mm × 98.6 mm): a) part of the fracture network and b) its corresponding watershed lines.

To avoid oversegmentation, we imposed markers represented by the labeled maxima of the reconstructed half distance function. The development of individual tiny segments positioned inside large segments is prevented by applying the supremum of the small size opening at the marker construction stage. The edges of the catchment basins delineate the glass segments (Figure 8).

1.3.4. Characterization of the segmented image

This section details the use of the segments obtained as a result of image segmentation. Introduction of the representation by segments facilitates geostatistical simulation of the block fracture network, which makes uncertainty estimation possible.

The concept behind the adoption of the representation by segments is that it enables replication of the block facture network by reproducing its segmented image. That is, our objective is to portray a previously extracted fracture network by reproducing parts of the matrix separated by this network via any type of tessellation that could reconstruct, or model, (i) the internal texture of the segmented image to identify the relationships between segments and (ii) the spatial structure and distribution of average fracture aperture. The internal structure of the segmented image is determined by the position of segment centers, the rotation angles of the segments, and the segment shape factor.

Here, we focus on the characterization of the segmented image by first- and second-order moments. This approach is widely used in image analysis(Flusser et al. 2009; Jan Flusser 2016) and was adopted from the mechanics of rigid and deformable bodies (Lubarda et al. 2011).

The characterization includes computation of the following parameters: lengths of the main axes (A, B) of each segment, segment rotation angles (theta), and positions of segment centers. The rotation angle is defined as the angle associated with the largest axis of a segment and a horizontal plane and is positive when the major axis is turned in a counterclockwise direction.

Image moments are defined as weighted averages of the pixels' intensities (i, j). In our case, we are concerned with the segmented binary image in which the (p,q)[20] moment $M_{p,q}$ gives equation (2):

$$\boldsymbol{M_{p,q}} = \sum_{i,j \in Obj} \boldsymbol{i^p j^q}, \quad (2)$$

The first-order normalized moments give the coordinates of the barycenter in the horizontal and vertical directions, and the second-order central moments determine the equivalent ellipse, furnishing the orientation and the dimensions of the major and minor axes.

The three central moments of second-order central moments ($\mu_{1,1}, \mu_{0,2}, \mu_{2,0}$) form the inertial tensor of the rotation of the object about its gravity center, expressed by equation (3):

$$\boldsymbol{cov(object)} = \begin{bmatrix} \boldsymbol{\mu_{2,0}} & \boldsymbol{\mu_{1,1}} \\ \boldsymbol{\mu_{1,1}} & \boldsymbol{\mu_{0,2}} \end{bmatrix}, \quad (3)$$

The main inertial axes corresponding to the semi-major and semi-minor axes of the ellipse are derived from the eigenvalues of this tensor.

The orientation of the object is defined as the tilt between the x-axes and the axis, around which the object is rotated with the minimal inertia and is calculated by expression (4):

$$\boldsymbol{\theta = 0.5\, arctan \frac{2\mu_{1,1}}{\mu_{2,0} - \mu_{0,2}}}, \quad (4)$$

For all segments, the position of segment barycenter (X_i, Y_i), axis length (A_i, B_i), and rotation angle ($theta_i$) are computed and further exploited at the stages of the geostatistical modeling (Section 1.5.2) and the creation of fracture network equivalent tessellation (Section 1.5.1)[21].

1.3.5. Calculation of aperture average inside crystals of the segmented image

Despite the high accuracy of the continuous approach of aperture measuring and its judicious results, processing of the fracture network via simple arc representation is problematic. In fact, the aperture values of each fracture ramification kept at their centers are not usable, at least directly, in the framework of the segment representation approach. In fact, at the stage of fracture network modeling by the technique of mesh growth, we expect to determine the positions of the mesh boundaries in which the thickness values need to be provided at the centers of the meshes.

The aperture average of the fractures associated with each segment should therefore be calculated. As discussed in Section 1.3.2, we first separated the fracture network into its simple constituents, and we then calculated the aperture average for all ramifications via one of the proposed approaches such as bounding boxes, quench function, or distance function. To calculate the aperture average inside the segments of the segmented image, we used the results of the aperture measurements via distance function because this continuous method of fracture aperture measurement is considered to be more accurate, and the distance function approach is believed to be less biased in comparison to the quench function approach. Afterward, the fractures were grouped according to their position in the segments. All fractures with simple arc centers positioned inside a segment are used to

[20] p,q denote the order of a moment

[21] Voronoï anisotropic tessellation built in RGeostats package, Mines ParisTech

calculate the aperture average assigned to that segment barycenter position (Figure 9). The operation is repeated for all segments.

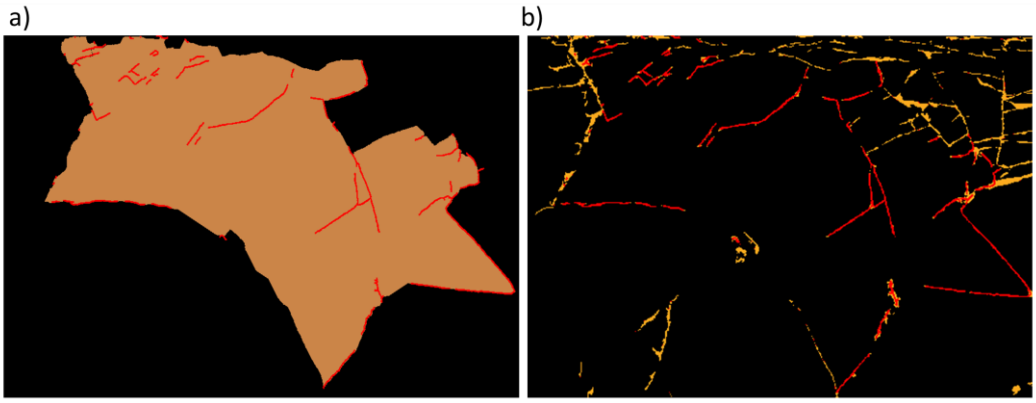

Figure 9 Fragment of UMo image, where fractures belonging to the chosen segment are identified.

a) Superposition of a chosen segment (in beige) and arcs (in red, dilated for better visibility with a hexagon structuring element of size equals to two) retained for measurement of the aperture average assigned to the segment barycenter. The fragment's dimensions are 138.6 mm × 97.4 mm;
b) Fractures in red are retained for measurement of the aperture average assigned to the segment barycenter. The fragment's dimensions are 134.0 mm × 96.6 mm.

1.4.Analysis of the solidification front map

In geostatistical modeling, it is recommended to make use of all available soft data that can supplement the raw data, particularly if the raw data are scarce and are difficult to interpret. As previously mentioned, the raw data include the values of parameters obtained by image analysis of one block of nuclear glass such as the values of apertures and positions of segment centers. This database cannot be considered as exhaustive. Moreover, it should be noted that the analyzed block could be very likely damaged at the cutting stage. Thus, photography analysis is supplemented with the results of the thermo-mechanical simulations (Section 1.2) to provide a physically meaningful parameter that helps to constrain the spatial structure and distribution of the parameters of the fracture network.

For this purpose, an exhaustively known parameter has been identified whose transforms can supplement the raw data at the stage of the equivalent fracture network simulation. Of particular interest are the knowledge of the direction of the fractures and the aspect ratio of the cells. These data can be determined through analysis of the segmented image by first- and second-order moments (Section 1.3.4). However, these pointwise data known only at the segment centers are not sufficient for construction of an equivalent tessellation. Indeed, values of the rotation angles and the ratio of the scaling factors of the meshes should be provided in the form of a continuous map.

Numerous studies (Crevoisier et al. 2011; Barth et al. 2012) have reported the fabrication process of a full-scale package specimen containing nuclear glass, which is a close analogue of the block analyzed in our study. According to the previous research, the map of the solidification front arrival times indicates that fissuring occurs first along the perimeter of the package and then propagates radially to the block center (Crevoisier et al. 2011). The network density is highest on the periphery owing to the highest intensity of the temperature drop that initiates fracturing immediately after the bloc fabrication ends. In contrast, the fracture density is significantly lower close to the package core,

where the temperature remains homogeneous. In addition, the upper part of the package is less fractured because it represents a stress-free surface, where dissipation of the external energy is not limited.

After analyzing several variables that describe the thermo-mechanical evolution of the internal state of glass after being poured in a rigid canister, we decide to select a variable referred to throughout this paper as the solidification front. This variable indicates the temperature delay between the fictive temperature[22] and the temperature inside the glass and serves to indicate the transition from liquid to solid state inside the glass.

First, we assembled a map of the arrival times of the solidification front by selecting front positions for all ranges of time values existing in the thermo-mechanical model. Later, we interpolated the arrival time values by applying kriging estimation with a linear model. The result is shown in Figure 10a.
Second, we calculated the angles between the axis parallel to the block axis and all pairs of neighboring points of the solidification front sequentially for each arrival time. We used the same angle convention as mentioned earlier. Then, we interpolated the values of the rotation angle by applying kriging estimation with a linear model. The map of the fronts line rotation angles is presented in Figure 10b.
Third, we proceeded with analysis of the lines of the glass solidification fronts by calculating their curvature using the formula of the Menger curvature (5) (Pajot 2002) for each set of three points of the solidification front:

$$\boldsymbol{c(x,y,z) = \frac{1}{R} = \frac{4*S}{|x-y||y-z||z-x|}}, \qquad (5)$$

where S is the surface of the triangle spanned by the x, y, and z points.

At this stage, we followed the concept such that in the first approximation, the shapes of the solidification fronts determine the shapes of the glass matrix segments. That is, fractures divide the glass into segments such that along the long sides of the block, it is probable that elongated segments meet with A/B >> 1. However, in the zone of the re-liquefaction at the boundary between the first and the second castings and in the zone of the first casting in the middle of the block, the fractures have identical lengths in two dimensions (A/B ≈ 1). In fact, when estimating the A/B ratio of scaling factors, it is useful to employ observations that can be explained by the physics of glass structural relaxation. To be precise, we used the map of front line curvature, presented in Figure 10c, as an external drift in order to generate the map of the A/B[23] ratio of the mesh scaling factors. The external drift kriging technique (Hudson 1993) implies that the overall shape of the target variable is given by an external drift map, whereas residuals are responsible for the fluctuations around this drift.

[22]According to Barth [9], the state of structural relaxation obtained through fictive temperature quantifies the progress of structural relaxation as a function of thermal history.
[23] A and B are lengths of the main axes of each mesh of equivalent fracture network tessellation.

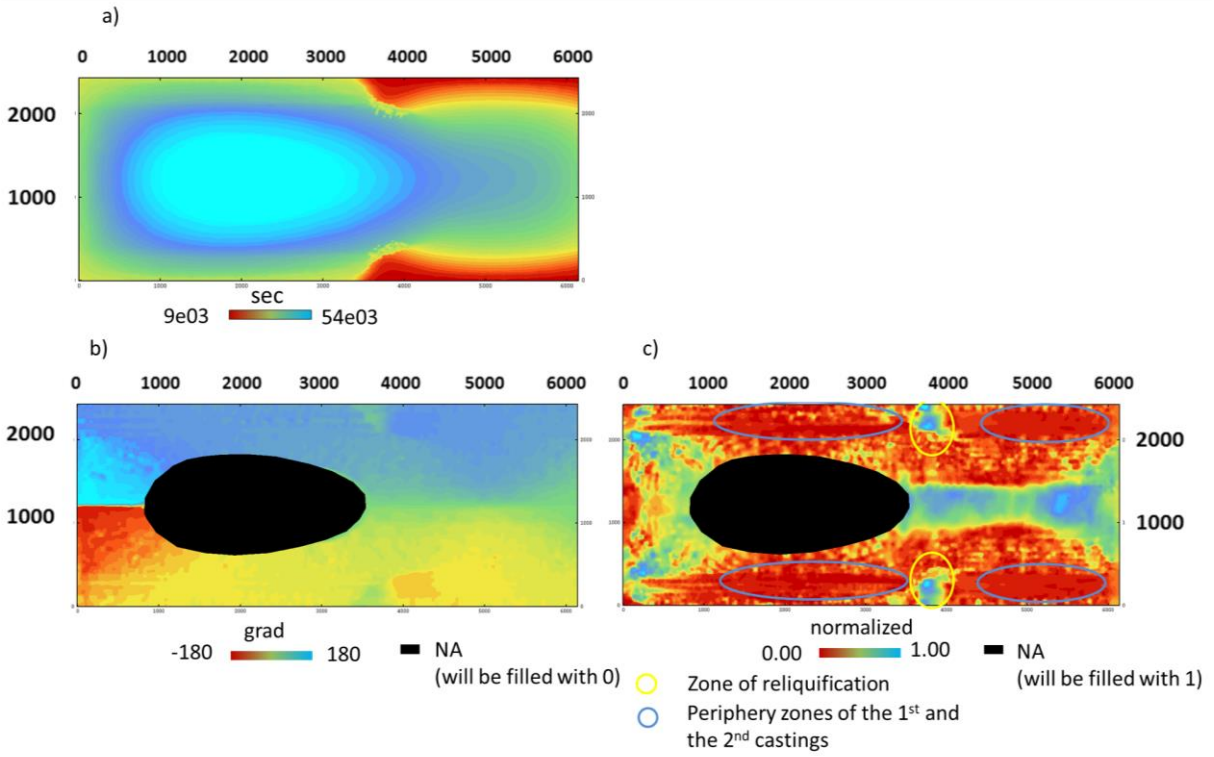

Figure 10 Maps used to introduce anisotropy when constructing fracture network equivalent tessellations.

a) Map of arrival times of solidification front. The solidification fronts were analyzed for all arrival times, from 9 e03 to 54 e03 s after the start of glass being poured into a container, in order to produce maps of the rotation angles and curvature of the front lines.
b) Map of the fronts line rotation angles.
c) Map of the normalized curvature, calculated by using the formula of the Menger curvature for each triple of set of three points of solidification front.

1.5.Geometric and geostatistical modeling

As mentioned in Section 1.3.3, the objective of the segment representation is to enable replication of the block facture network by reproducing its segmented image, with the seeds of the cells and the thickness of borders provided by the geostatistical modeling. In the following section, geostatistical modeling of seed positions and average thickness of the cell borders will be discussed.

To better understand the meaning of these parameters, which will be discussed in Section 1.5.2, we here explain the technique intended to be used for constructing multiple realizations of fracture network equivalent tessellation.

The generation of multiple equivalent realizations of the block fracture network is based upon the geostatistical spatial analysis of the data coming from the image analysis and the information collected from the map of front of solidification.

1.5.1. Creation of fracture network equivalent tessellation

To model an equivalent block fracture network, we used the anisotropic version of Voronoï algorithm (Anton et al. 2009), which represents a version of mesh growth models and delineates mesh boundaries considering the cell scaling factors and the cell rotation matrix.

It should be noted that in the remainder of this paper, the term "cell" is applied as an analogue of the term "segment" by referring to a separate unit of an equivalent representation of the segmented image. Moreover, the term "seed" or "centroid" will be used to replace the term "center" in reference to the origin of the corresponding cell growth.

According to the Voronoï algorithm, a cell **C (P_i)** generated by the growth of P_i centroid (seed) is defined by X_i, Y_i; a^M_i, b^M_i, θ^{*M}_i. It contains all points **M** which are closer to the seed P_i than to any other seed, according to the parameters a^M_i, b^M_i, θ^{*M}_i. Here, X_i, Y_i are coordinates of a cell center, a^M_i, b^M_i are scaling factors, and θ^{*M}_i is the rotation angle defined in all points **M**.

Mathematically, the cell is defined by formula (5):

$$\mathbf{C}(\mathbf{P_i}) = \mathbf{M} \in \mathbf{R^2}\ \forall \mathbf{j}: \frac{\mathbf{d}(\mathbf{M},\mathbf{P_i})}{\mathbf{v}} \leq \frac{\mathbf{d}(\mathbf{M},\mathbf{P_j})}{\mathbf{v}}, \qquad (5)$$

where υ is the constant radial rate of growth equal to 1.

First, the distance $\mathrm{d}(\mathbf{M},\mathbf{P_i})$ between the datum and the target site is computed by considering the rotation matrix $\begin{pmatrix} cos\theta^* & sin\theta^* \\ -sin\theta^* & cos\theta^* \end{pmatrix}$, where $\boldsymbol{\theta^*}$ is the rotation angle specified in all points **M** belonging to the cell.

Next, the scaling (defined by a^M_i, b^M_i) is operated in the rotated system. The component is unchanged if the scaling factor is equal to 1, reduced if it is higher than 1, and increased if it is lower than 1.

Finally, the boundaries of a newly created equivalent tessellation are thickened by considering the results of the geostatistical modeling of the average aperture calculated inside each segment (Section 1.5.2).

The average values of the apertures are attached to the cell seed positions, whereas the rotation angle and scaling factors in all directions[24] are defined on a fine grid.

As presented in Sections 1.3.4 and 1.4, the maps of the rotation angle and the ratio of scaling factor had been obtained by analyzing the map of the arrival times of front of glass solidification, while modeling of seed positions and average aperture of cell boundaries will be covered in the next section.

1.5.2. Geostatistical analysis

It is apparent that the fracture network morphologies and inherent characteristics vary among blocks. The reasons for these variations are numerous and are related mainly to the procedure of block fabrication and some random fluctuations. It is evident that when dealing with only one specimen, it is impossible to evaluate the uncertainty of the altered glass quantity resulting from the variation in parameters related to the fracture network. Therefore, in the next step, we conduct exploratory spatial data analysis followed by geostatistical simulations of two variables. The first is the position of cell seeds. The second is the average aperture assigned to cell seeds that will determine the thickness of the boundaries between the adjacent cells, which in the context of our research represents the fracture average aperture. The results of the simulations will be used to

[24] Two scaling factors (or their ratio as in the example above) if 2D tessellation is build.

construct multiple realizations of an equivalent fracture network based on the Voronoï algorithm explained in the preceding section.

1.5.2.1. Position of cell seeds

Calculation of the point density of the training image is based on the results of the image analysis where the segments centers have been located within the upper part of UMo segmented image (Figure 17a, Y > 1215); the lower part is obtained by a mirror symmetry (the reason why the lower part (Figure 17a, Y < 1215) is discarded is explained in Section 2).

Calculation of the point density of the training image is based on the results of the image analysis, specifically the positions of segment centers of the upper part of the UMo segmented image reflected by mirror symmetry to obtain the lower part. This step includes (i) calculation of the number of centers divided by the surface[25] of counting window with windows of varying dimensions and (ii) regression of these density values against the surface values. This regression analysis is used to evaluate the impact of the moving window size on the density regionalization. Later, the values of point density, determined on the grid support,[26] are migrated to the position of the segment centers. Further, the geostatistical analysis and modeling is based on the values of density collected at 352 segment centers. In the same manner, the values of the solidification front arrival time are migrated to the positions of the segment centers. Next, the values of density are regressed against the values of the solidification front arrival time, and the procedure is iterated for all window sizes. The spatial variability of densities and their residuals are studied by using the experimental variograms and their best-fit theoretical models. Then, the parameters derived from the fitted models for density and residuals, and the values of correlation coefficients are examined to determine the impact of the moving window dimensions on the density values and to eventually determine the density values to be used as the input data for further modeling.

After the residuals are normal-score transformed to correct for the slight skewness of the histogram, the non-conditional simulations (using the turning band method (Matheron 1973)) are conducted to produce N realizations of the spatial distribution of residuals. After the back-transformation to the raw scale and the use of the coefficients of the linear correlation, N maps of the varying Poisson intensity are obtained.

They are subsequently used to generate the spatial Poisson point process with varying intensity (Lantuejoul 2002). Moreover, a rejection step is used to ensure that the simulated seeds are separated by a minimum distance that is equivalent to the minimum distance between the centers of the training image. It should be mentioned that the N realizations of the intensity maps constructed in the previous step are calibrated to the number of the centers in the training image.

1.5.2.2. Averaged apertures assigned to cell seeds

After determining the position for cell seeds, the averaged apertures assigned to cell seeds were modeled. As input data, measurements of the averaged apertures inside segments of the segmented UMo image (Section 1.3.5) were used[27].

[25] Surface of a moving window lying inside an output regular grid.

[26] Procedure is repeated for all maps of density calculated for several sizes of moving window.

[27] Similar to that used to determine the positions of centers, we retained the measurements of the averaged apertures assigned to the centers of segments located in the upper half of the image, and we assigned the same averaged apertures values to the centers of the lower half of the block obtained by mirror reflection.

Next, we verified the correlation between 1) the values of average apertures and the arrival times of the solidification front and 2) the values of average apertures and the values of Poisson density calculated in Section 1.5.2.1.

Because the correlation for both pairs of variables was inadequate, we defined a geostatistical model of averaged which does not involve any explanatory function.

The geostatistical modeling of average aperture on the cell seeds was performed in four steps: 1) normal score transform of the data, 2) calculation of the experimental variogram and determination of its theoretical best-fit model, 3) non-conditional simulation of the aperture average values in the normal space by using the turning band method, and 4) back-transform of simulated values in the original scale.

2. Results

In this section, we first show the results of the fracture network characterization of the UMo training image, and we present the maps obtained by the analysis of the map of the solidification front arrival times. Next, we demonstrate some realizations of the geostatistical modeling of seed positions and average aperture, and we shows the resultant realizations of the equivalent fracture network constructed by considering all previously demonstrated results.

Figure 11 illustrates the fracture network extracted separately from the pullout zones. To select the size of the structuring element necessary to perform the morphological operations, we calculated and analyzed the distribution curves with several types of opening, including a hexagonal opening and that by erosion-reconstruction (Figure 12). When selecting the size of the structuring element, we adhered to the following rules:

1) The chosen size of the opening by erosion-reconstruction is higher than the maximal size of the reflections. According to the distribution curves computed with morphological erosion and with the opening by erosion-reconstruction, light reflections are expected up to 5 pixels
2) The size of the black top hat transformation is chosen with respect to the range of the fracture thicknesses. According to the distribution curves, fractures are expected to be up to 20 pixels in width.
3) The threshold operator is applied to separate the matrix background and the identified fractures. Because the black top hat transformation puts the matrix values close to zero, we fix the threshold to 30, which is slightly higher than the maximal expected fracture width. By doing so, we assumed that the crack depths are greater that their widths.

4) The size of the morphological closing implemented to set apart fractures and pullout zones is equal to the size of the average fracture width, at 10 pixels.

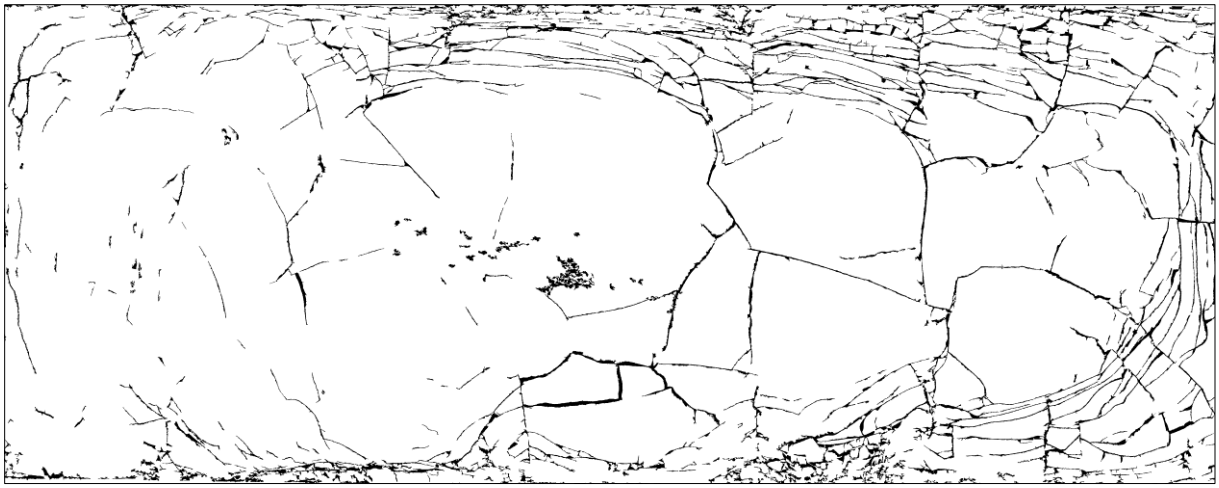

Figure 11 Result of the fracture network extraction (image UMo: dimensions are 1044 mm × 413 mm).

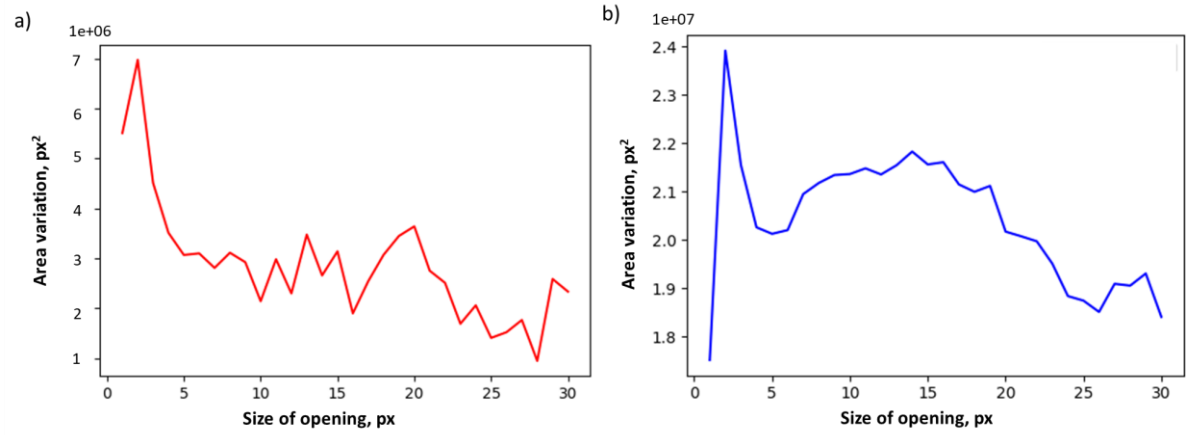

Figure 12 Size distribution curves calculated with a) morphological opening and b) opening by erosion-reconstruction for the 8 bit input UMo image.

The histograms of apertures measured by applying the three proposed approaches are shown in Figure 13 and in Table 2. All approaches gave similar values of fracture aperture; however, the values obtained by the bounding boxes method were discrete more often. With respect to the results, there is no evidence that the bounding boxes approach overestimates the values of fracture thickness, which means that correction for shape curvature made at the stage of results post-processing is justified. Regarding the continuous way of aperture measurement, the use of the distance function read along the traces of simple arcs is considered to be more judicious and gives more accurate results because it does not imply the use of the skeleton by maximal balls, which has technical limitations.

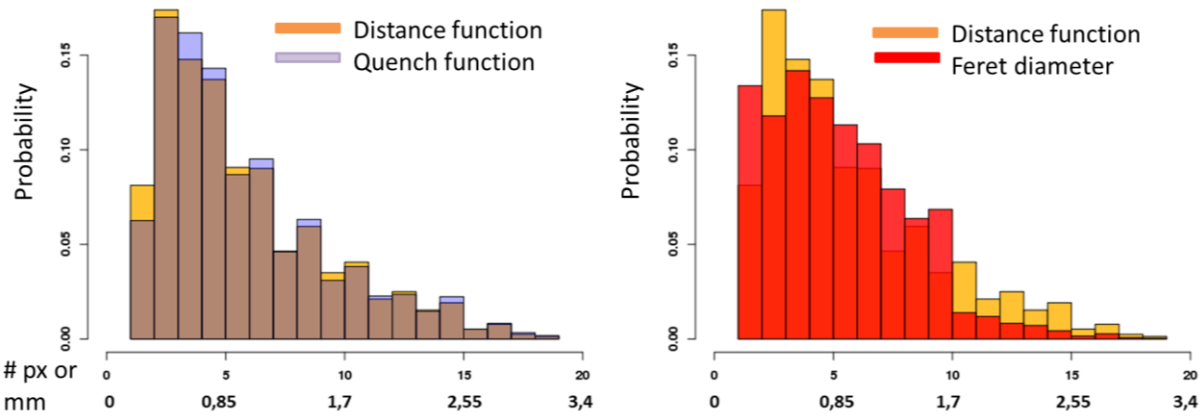

Figure 13 Histograms of apertures computed via distance and quench functions and Feret diameter calculation.

Table 2 Statistical characteristics of aperture distribution obtained by discrete and continuous approaches.

Measurement function / object of application	Max		Min		Mean		Standard deviation	
	# px	mm	# px	mm	# px	mm	# px	mm
Feret diameter/ bounding boxes	19	3.23	1	0.17	5.72	0.97	3.01	0.51
Quench function/ simple arcs	19	3.23	1	0.17	5.92	1.01	3.60	0.61
Distance function/ simple arcs	19	3.23	1	0.17	5.82	0.99	3.60	0.61

The segmentation results are illustrated in Figure 14. The segmentation procedure is realized by marker controlled watershed (see Section 1.3.3) in order to avoid oversegmentation that could have occurred owing to the presence of the spurious minima.

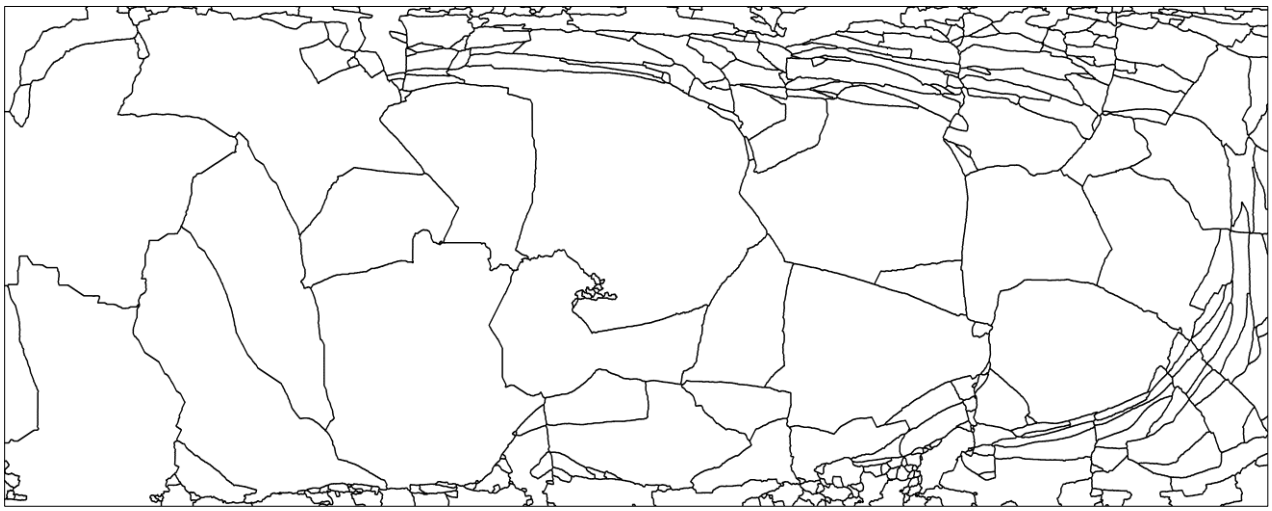

Figure 14 Results of the UMo image segmentation, where the dimensions are 1044 mm × 413 mm. For better visibility, the watershed lines are eroded with size = 3.

Undoubtedly, the choice of the marker image is important because it determines the output. Because our objective was to replace fracture representation with segment representation, it was critical that we obtain a segmented image that has no excessive segments inside the segments to

ensure that the segments were separated exclusively by fractures or their prolongations in the absence of fractures. At this stage, we considered that a satisfactory result was achieved. Therefore, characterization of the segmented image by first- and second-order moment was next conducted.

As was stated in Section 1.3.4, the objective of the segmented image characterization is to determine attributes of the image that must be reproduced in order to mimic the anisotropic nature of fracture network of the glass blocks. The result of the calculation of segment rotation angles and the ratio of their axis lengths is demonstrated in Figure 15 in the form of the maps, where, the calculated parameters are used to fill the segmented image for enhanced visualization.

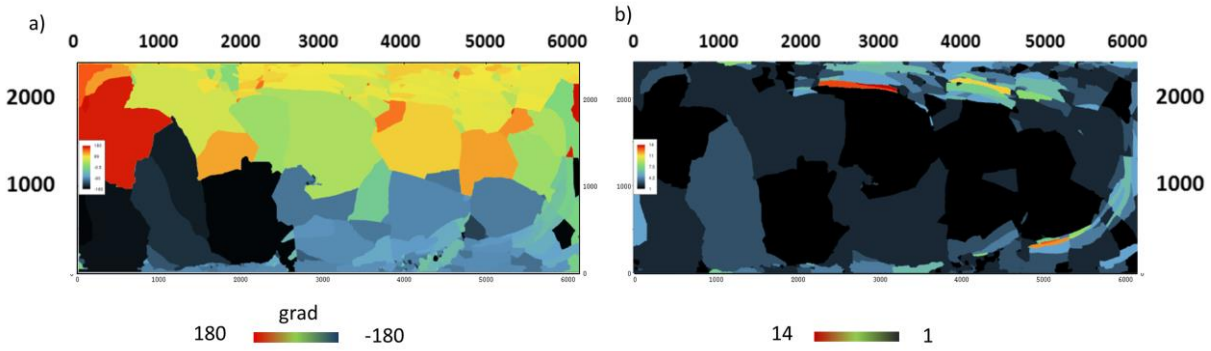

Figure 15 Segmented UMo image in which the segments are filled with the values of a) the rotation angles and b) the ratio of axis lengths (image dimensions are 1044 mm × 413 mm).

Unfortunately, these data were not sufficient for use as input maps needed to effectuate coordinate transformation, including scaling and rotation of the fracture network equivalent tessellations in order to consider fracture network anisotropy. Therefore, we used the soft data presented by the continuous map of solidification front arrival times obtained from the thermo-mechanical simulation.

Figure 10 provides the results of the analysis of the thermo-mechanical parameter representing the transition from liquid to solid state inside the glass. As shown in Figure 10a, the transition from one arrival time to the following arrival time is rather smooth; however, zones were noted in which the transition was sharp such as the abscissa axis, from 3800 to 4000 and the ordinate axis, from 0 to 500 and from 2000 to 2430. These zones are associated with the complex phenomena of recasting at the boundary between the first and the second glass casting. The zones are even more noticeable in the map of the normalized curvature (Figure 10c).

Following calculation of the curvature, estimation of the ratio of scaling factors A/B was performed using the external drift kriging technique. It should be noted that the estimation was conducted inside a specified polygon for one half of the block. Indeed, because the external drift map is symmetric, as the whole model of the thermo-mechanical behavior of a glass block, and some doubt existed on the quality of the fracture network of the lower part of the UMo block[28], we conducted the estimation based only on the A/B measurements for the upper half of the block (Y > 1215, Figure 17a). The lower part (Y < 1215) of the map was obtained by applying the mirror symmetry. Moreover, it should be noted that the polygon did not cover the entire half of the block. The analysis of the segmented image in which the segments are filled with the values of A/B (Figure 17a) and

[28] The lower half of the UMo block was found to be unacceptably damaged. Indeed, several indications of artificial splitting in the fracture network parallel to the block's long wall have been noticed.

some observations of transversal and axial cross-sections of glass blocks (Crevoisier et al. 2011) led us to presume that in the center of the block and close to the upper part of the block, large rather homogeneous segments likely form in which the A/B values could be assigned by default to 1.

Figure 16 represents the scatter plot showing the regression between the values of the external drift (curvature of the solidification front lines) and the available data of the searched variable A/B obtained through image analysis.

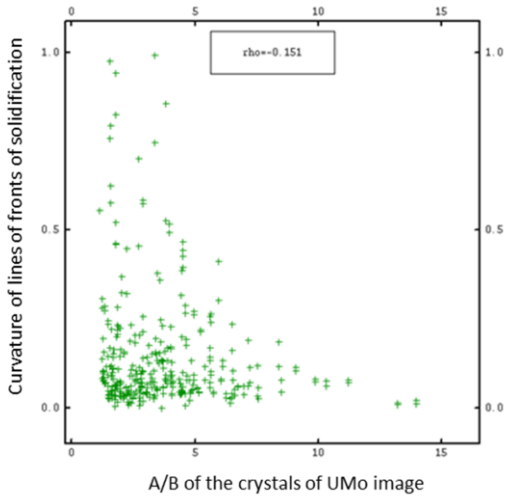

Figure 16 Scatter plot between the values of front line curvature and those of crystal length ratio.

The scatter plot above shows a weak linear correlation (ρ = -0.15) between the values of the curvature and the values of the segment length ratio of the block UMo. In fact, along the long sides of the container in the zones in which the elongated segments are located, some isotropic segments are also present.

Despite the weak correlation, we used the map of normalized curvature as an explanatory deterministic map for construction of the map of the A/B ratio of the scaling factors. It fact, we did not look for an accurate assessment of this ratio because this map served only as a background map while constructing fracture network equivalent tessellations. Nevertheless, for future research, we strongly recommend analysis of the regression of the scaling factor ratio against the values of the normalized curvature for a new block (having ensured integrity).

Figure 17b illustrates the result of the A/B estimation. This map together with the map of the rotation angle, were used to consider the anisotropy.

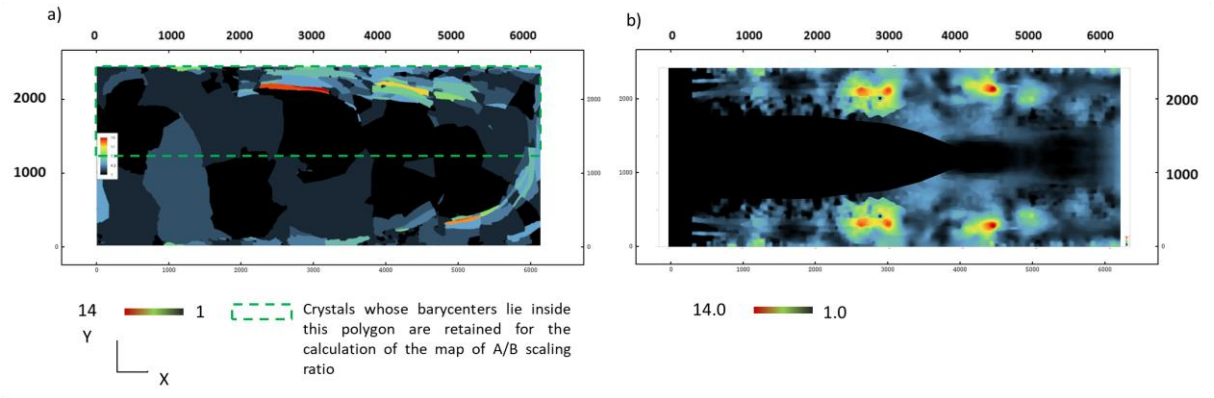

Figure 17 Analysis of A/B ratio of mesh scaling factors.

a) Segmented image in which the segments are filled with the values of ratio axes lengths (UMo image).
b) Upper half of the map of A/B ratio of mesh scaling factors obtained by kriging with external drift. The lower half (Y< 1215) represents the mirror reflection of the upper part (Y> 1215).

Although it is possible to precisely measure the apertures of fracture ramifications, these data are not generally used at the stage of modeling of multiple realizations of equivalent fracture network. Thus, in an attempt to preserve the accuracy of the aperture measurements and to diminish the amount of data to be processed in the course of the geostatistical analysis, fracture aperture averages were computed inside the segments of the upper half of the segmented image and were assigned to their centroids. The same values of the average facture apertures were assigned to the centers of the lower half. The results of the averaged aperture measurements are shown in Figure 18.

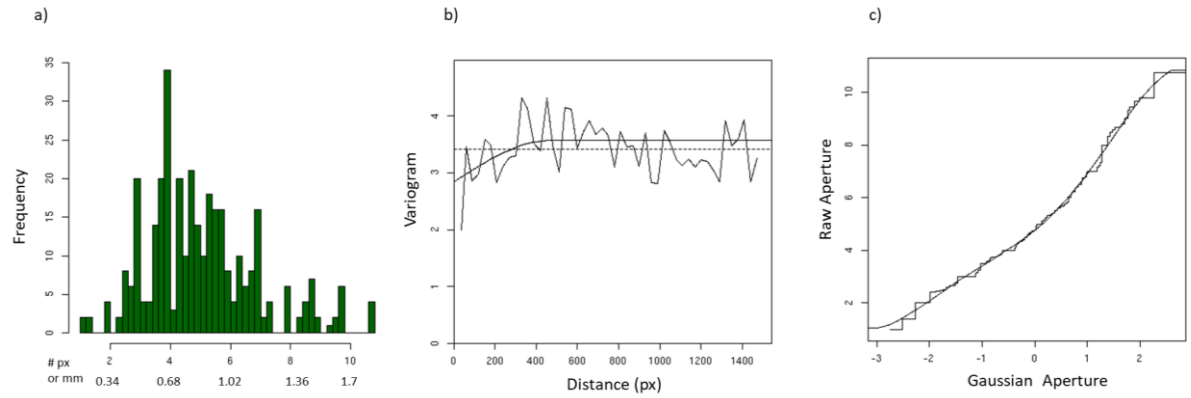

Figure 18 a) Histogram, b) omni-directional variogram, and c) normal score transform of aperture averages computed inside the crystals of the segmented image.

The results of the geostatistical modeling of seed positions and aperture averages that provide information on the thickness of boundaries of equivalent tessellations are given subsequently.

As explained in Section 1.5.2.1, Poisson density modeling is based on the calculation of the segment center density with different moving windows. The results are summarized in Figure 19. From these data, it is clear that by increasing the size of the moving window, the regularization of the density is increased, reflected by a decrease in the sills of the variograms. In consideration of the pros and cons of regularization, specifically variogram sill decrease and better correlation with the explanatory

variables versus loss of the variability, we selected the density values calculated with a moving window size of 13 × 13 blocks, given that the total size of the grid is 123 × 49 blocks.

A theoretical nested model with nugget, exponential and spherical structures fitted to the experimental variogram of residuals, shown by an asterisk in Figure 19c, was used to perform non-conditional simulations of residuals. The parameters of the regression between the density and the explanatory variable, shown by an asterisk in Figure 19b, were involved when computing maps of the Poisson intensity. For each realization of the Poisson intensity map, the seeds were generated so that the minimum distance between seeds is larger than 25 pixels and their total number is close to 350. Both parameters were fixed with reference to the results of the analysis of the training image.

Afterward, for each realization of seeds, aperture average modeling was conducted. The non-conditional simulations were based on the theoretical nested-type model with nugget, exponential and spherical structures fitted on the experimental variogram (Figure 18b) and the model of the normal-score transform (Figure 18c).

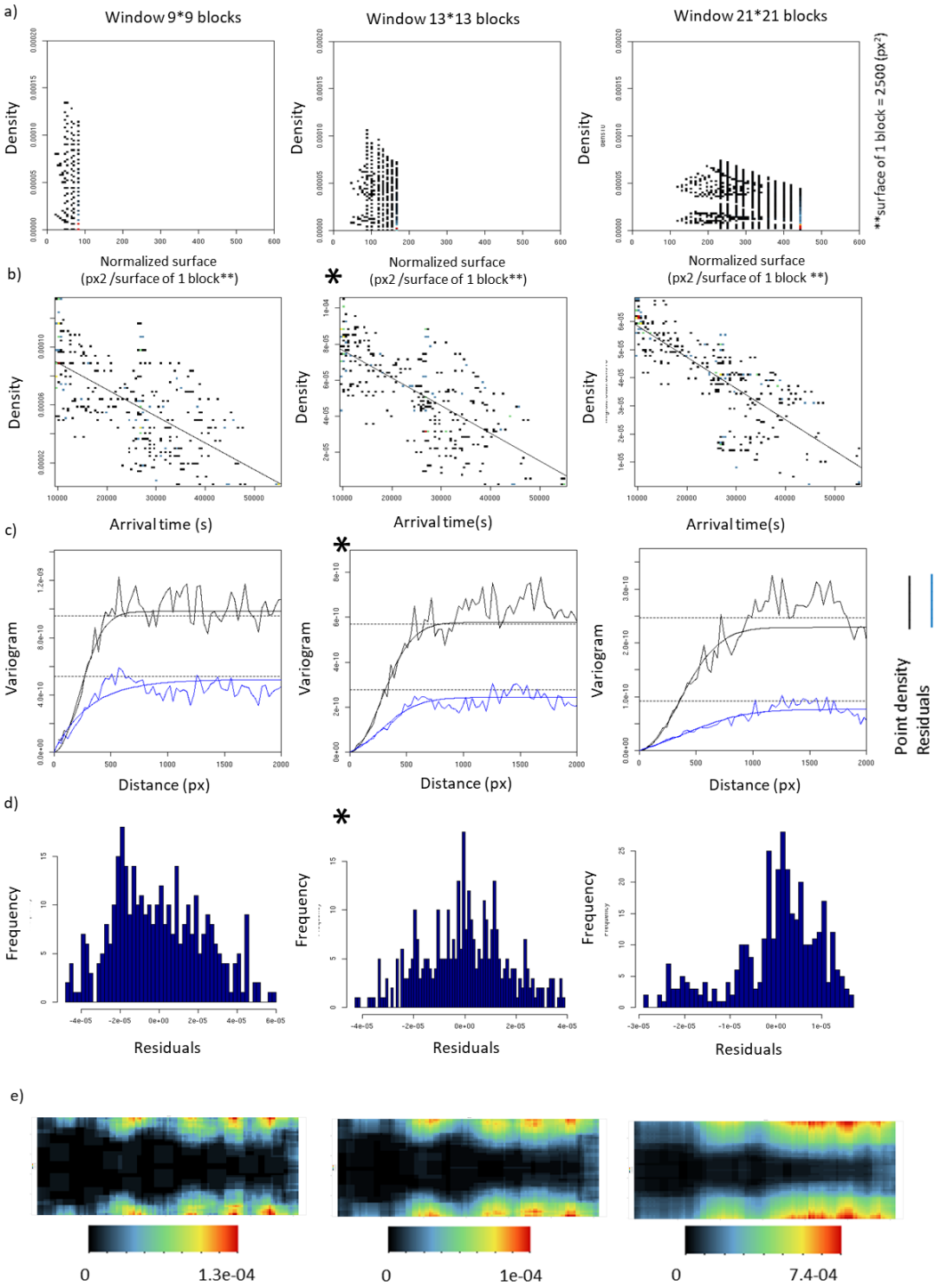

Figure 19 Results of the computation of point density for different sizes of moving windows: a) regression of density against normalized surface (in number of blocks, each block covers 2500 px2); b) regression of density against arrival time of solidification front ; c) omni-directional experimental variograms of point density (black) and residuals (blue) and their theoretical models; d) histograms of residuals; e) map of point density in which values read at the positions of the segment centers were used afterward as input data for the seed generation.

Three realizations of seed positions generated according to a spatial Poisson point process with varying intensity and the histograms of average apertures simulated at the seed locations are given in Figure 20.

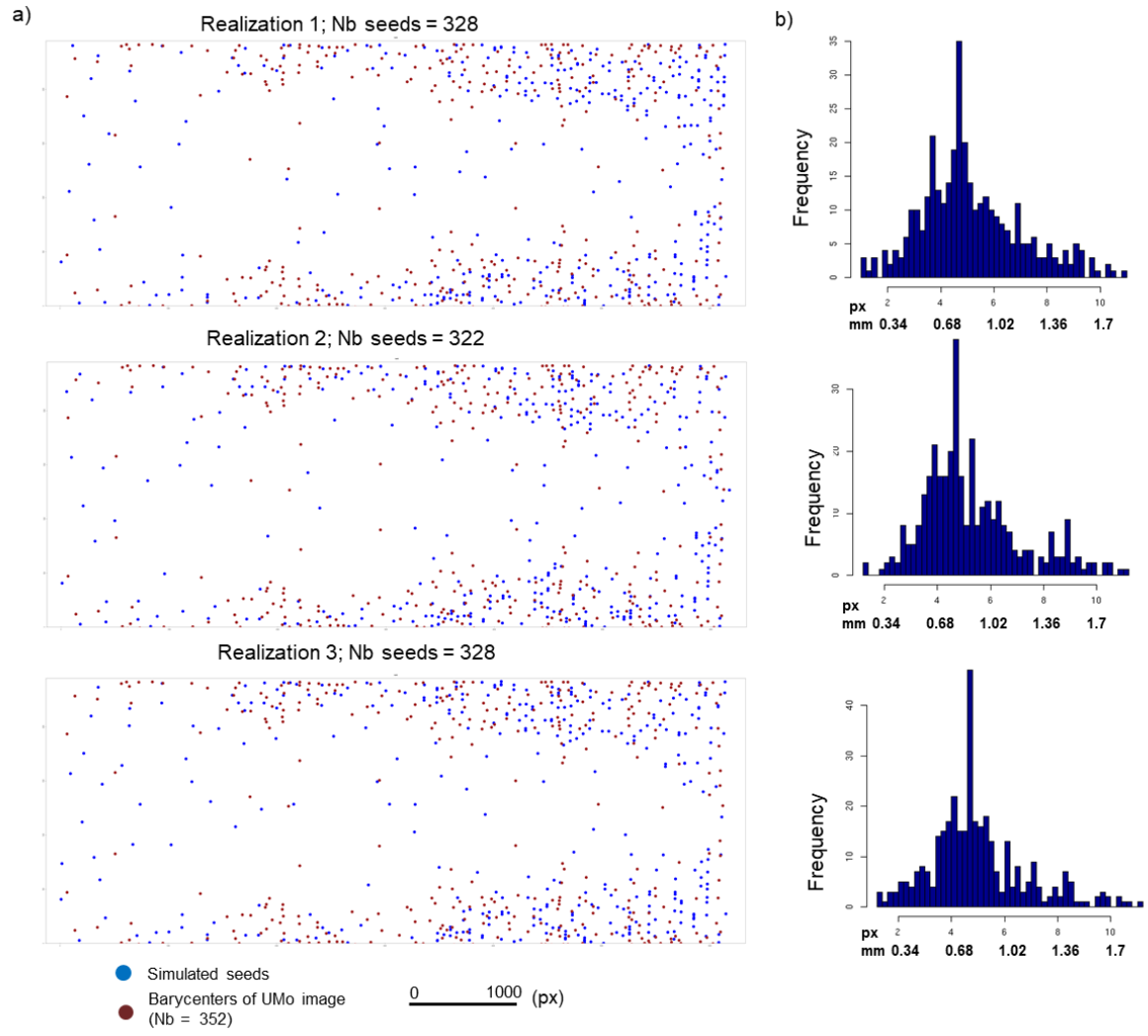

Figure 20 Construction of equivalent fracture network tessellations: a) positions of seeds obtained by Poisson point process (blue) vs. positions of barycenters of UMo image (brown); b) histograms of aperture average.

Figure 21 gives the results of the equivalent tessellations generated using the anisotropic Voronoï algorithm for three realizations of seeds and simulated apertures. In order to evaluate the representativeness of the obtained equivalent tessellations, they were compared with the fracture network of UMo and UOx training images presented in Figure 23. Moreover, to discern the ability of equivalent tessellations in reproducing a 2D nuclear glass fracture network, the results in Figure 22 were analyzed.

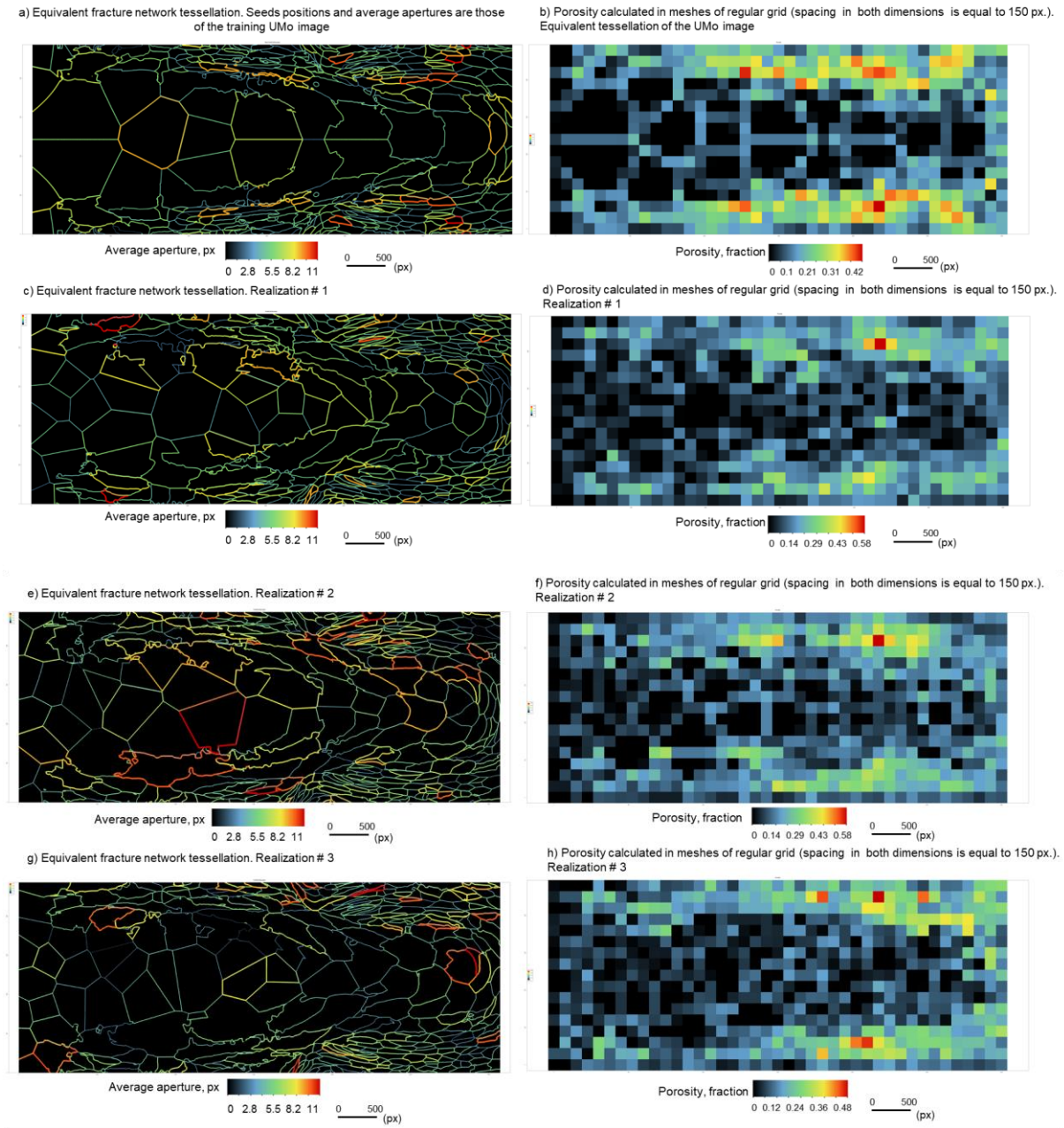

Figure 21 Equivalent fracture network by Voronoï anisotropic tessellation. Left columns including a), c), e), and g): equivalent fracture network tessellation (dimensions are 6145 px ×2430 px with 1 px corresponding to 0.17 mm. Right columns including b), d), f), and h): porosity (defined as the ratio of the surface occupied by fractures to the sum of the surfaces of the glass matrix and the fracture network) calculated for meshes of the 41 × 17 simulation grid.

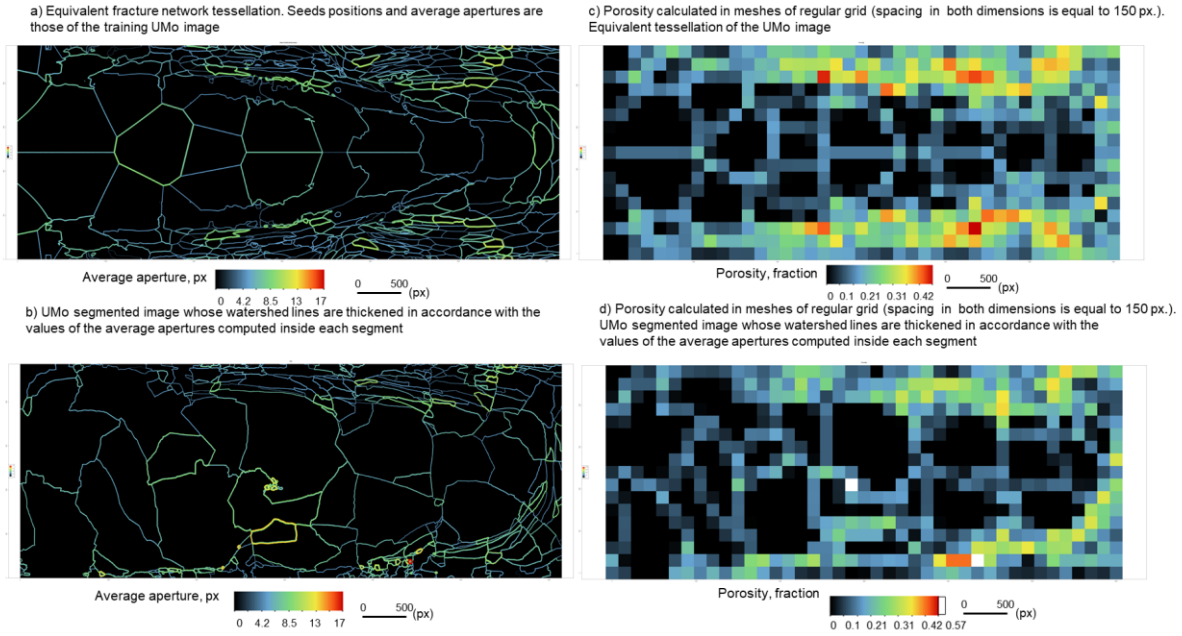

Figure 22 Reproduction of segment representation by equivalent tessellation: a) reproduction of the segmented UMo image by anisotropic Voronoï tessellation; b) UMo segmented image in which watershed lines are thickened in accordance with the values of the aperture averages computed inside each segment (dimensions are 6144 px × 2430 px with 1 px corresponding to 0.17 mm); c), d) their corresponding porosities.

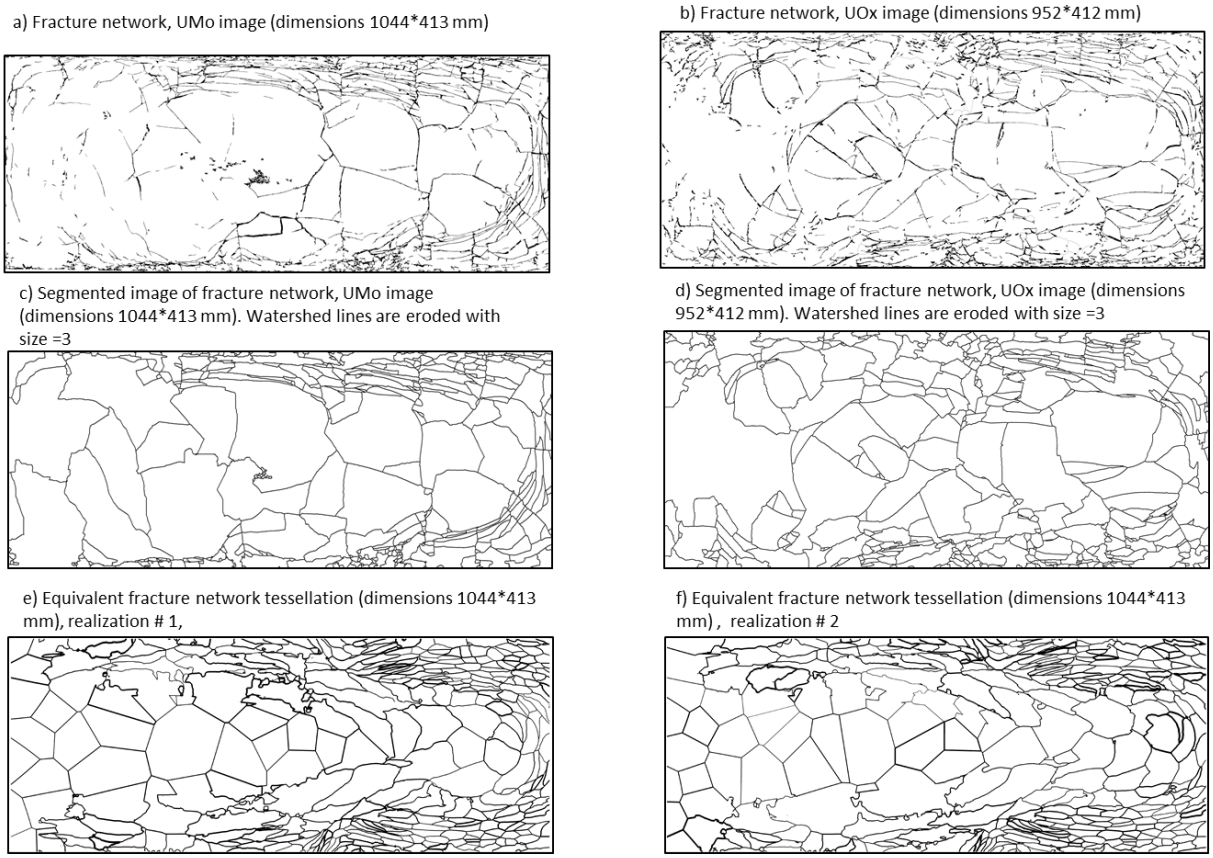

Figure 23 Effect of replacement of fracture network by segment representation and its reproduction by equivalent tessellations. Top left a): UMo; top right b): UOx; middle c), d): segmented images; bottom e), f): equivalent fracture network. Equivalent fracture network tessellations are expected to mimic the structures of

segmented images, whereas fracture apertures are considered by thickening boundaries of equivalent tessellations.

3. Discussion

i. Fracture network extraction

We believe that by having implemented operations for contrast enhancement (black top hat) and noise removal (opening by erosion-reconstruction) with a carefully chosen size of the structuring element, we obtained satisfactory results. Nevertheless, we admit that the resulting fracture network is not a unique representation that could be obtained from the raw image. In fact, changing the size of the structuring element of any operation involved in fracture extraction would certainly give a different result. However, the proposed procedure of fracture network extraction is believed to be useful for future analysis of cross-sections of glass blocks, especially because it offers the possibility of generating multiple realizations of the fracture network model.

ii. Measurement of fracture apertures

Although the results of aperture measurement provided by the three approaches (Figure 13) are compatible, each has weak and strong points that are worth consideration:

Advantages of the discrete method of aperture measurement via the bounding boxes approach:

1. Implementation ease
2. Rapid calculation

Disadvantages of the discrete method of aperture measurement via the bounding boxes approach:

1. The facture network must be disintegrated into non-connected branches at the first step of the measurements.
2. The aperture values are derived from the measurements of the shortest axes of the bounding boxes surrounding the fractures and represent the maximal apertures of these fractures. By applying this method, it is impossible to consider the variability of the fracture aperture. The calculated aperture values are integers. For fractures in which the shapes are significantly curved, the length of the shortest bounding box axis does not reflect the real aperture magnitude. Therefore, to indicate the average aperture, these values of Feret diameter need to be corrected by using the ratio of the area of the object over the length of the longest bounding box axis.

General advantages of the continuous method of aperture measurement:

1. The problem of fracture separation[29] can be bypassed.
2. This method is appropriate for characterizing fractures of non-constant thickness.

Disadvantages of the continuous method of aperture measurement via quench function:

[29] To be precise, fractures are still separated into simple ramifications, but the measurement is applied to the network in which the integrity is preserved, i.e., when we performed aperture measurement by the continuous approach, we apply it to the initial network.

1. The apertures are average values of the quench function found at the intersection of the skeleton of maximal balls and the traces of simple arcs. This could jeopardize the accuracy of the calculations because not all relevant points of the skeleton of maximal balls lie on the same trace as the simple arcs (Figure 6b).
2. The quench function is not secured from parity bias; in certain cases, it is prone to underestimate the real fracture aperture. Moreover, the maximal balls skeleton is not connected and can have thickness of more than 1 pixel, which might increase the error of average aperture estimation (Beucher 1994).

Disadvantages of the continuous method of aperture measurement via distance function:

1. The distance function is not secured from the parity bias, which means that values of average fracture aperture can be also slightly underestimated.

Considering the above-enumerated advantages and disadvantages of the aperture measurement techniques, for further research, the continuous method of aperture measurement via the distance function is recommended to be retained because has been proved to be the most accurate and least biased.

iii. Analysis of the map of front of solidification

A comparison of the values of the rotation angles measured for segments of the training UMo image (Figure 15a) and the map of the front line rotation angles (Figure 10b) revealed their good agreement.

However, the value of the linear correlation coefficient between the values of the curvature and those of the segment length ratio calculated for the training image was rather unsatisfactory. There are several possible explanations for this cohabitation of segments of different levels of lengthening generated in similar thermo-mechanical conditions, according to the map of internal structural relaxation. One is that the block chosen for the image analysis was not fully representative and could have carried imprints of the artificial damage, particularly in fragile peripheral zones, which would have masked the real fracture pattern.

iv. Geostatistical and geometrical modeling

Figure 20a proves that spatial distribution of seeds generated by the Poisson process and the centers of the segmented image are comparable; however, for each realization, the number of seeds generated in the central part of the blocks was higher than in the UMo training image. These small discrepancies are not believed to bias the result, particularly when considering that for the UOx block, more segments were observed in the central part (Figure 23b).

As shown in Figures 23, the resulting realizations of equivalent fracture network tessellation exhibited strong similarities with the fracture networks of nuclear glass block. Moreover, they have the potential for modeling the fracture network at scale 1 and for conducting the reactive transport modeling. However, the demonstrated fracture network equivalent tessellations possess some features that make them different from the real fracture networks. First, on the 2D equivalent network representations, all cells of the tessellations were connected, whereas the analysis of the 2D cross-section of the UMo fracture network showed some dying-out fractures (Figure 11). Second,

although the total number of seeds of equivalent was close to the total number of centers of the training image, the simulated segments were smaller in the central part of the equivalent tessellations than in the average in the training UMo image. On average, the porosity of the presented equivalent tessellations was higher than that of the UMo training image. However analysis of the fracture networks of both UMo and UOx blocks and comparison with the presented equivalent tessellations indicate that simulated tessellations represent effective reproduction of fracture networks at scale 1. Moreover, they enable consideration of network structure variability.

4. Conclusions and perspectives

A crucial issue in reducing the uncertainty associated with a fracture network model is to consider all data that can be of very distinct natures. In our case, a combination of hard and soft data was used. Hard data were presented by the results of the image analysis on one block of nuclear glass, whereas the soft data correspond to the map of the arrival times of the solidification front and some derivatives of this map.

The first part of the workflow, extraction and determination of the fracture characteristics, appeared to be reliable and offered important insight into the meticulous examination of fracture networks at scale of a glass block. However, it should be noted that the block used as a test bed of the workflow application is not fully indicative because its fracture network was damaged in the course of sawing. Thus, the resulting values of the apertures demonstrated here should not be considered as incontestable and characteristic of a real intrinsic fracture network of a block of nuclear glass. In pursuit of more relevant values of fracture apertures, further analysis using the same methodology on carefully prepared sections is advised.

The second part of the work dealing with the geostatistical modeling and construction of fracture network equivalent tessellations is believed to be a practical and rapid method of fracture network simulation allowing the variability of fracture distribution and aperture to be considered.

The presented research is methodological and strives to elaborate the workflow needed to conduct the reactive transport modeling at the scale of the fractured glass package. Nevertheless, in order to demonstrate the feasibility of the proposed procedure, we presented some results of the training image characterization and used them for further modeling. The findings, while preliminary, suggest that at relatively low expense, it is realistic to simulate a fracture network of blocks of nuclear glass by using the proposed anisotropic Voronoï tessellation. Equivalent tessellation is a good approximation and represents object modeling that considers both hard and soft input data. However, the final test of the quality of the model will come from applications: a comparison should be made of the results of reactive-transport simulation on the direct support (training images) and on the realizations of the equivalent tessellation.

Although the characterization and modeling efforts are important, it is critical to improve the quality of glass block preparation by ensuring the integrity of the fracture network or by using noninvasive techniques. At the same time, it could be useful to deepen the understanding of the relationships between thermal damage parameters and fracture distribution and geometries. In fact, the choice of the actual proxy map was based on the fact that the speed of the solidification front makes it possible to dissipate internal stress more or less easily, thus controlling the morphology of the

fracture network. Other types of maps might be useful if they are justified by mechanical considerations.

Although this research focuses on a 2D model, by unifying information obtained by analyzing images of longitudinal and transversal cross-sections of glass canisters, it is realistic to construct a realistic 3D model. This is especially appealing, since almost all tools necessary to accomplish this exercise are already prepared. First, the knowledge of the fracture pattern of a transverse plane of a fracture package can be obtained by applying the proposed workflow. Second, the data required for geostatistical modelling are identified. Moreover, the maps of the solidification front arrival times necessary to support the image analysis results can be procured easily and the way in which they should be analyzed is already known. Besides, the algorithm used to generate the anisotropic Voronoï tessellation (realized in RGeostats package) should potentially be able to do it in 3D after some proper adaptations are made. These additional implementations concern the creation of the connected 3D fracture planes. However, certain caution must be applied because the fracture network is likely to vary along the z-axis owing to the presence of the different thermo-mechanical environments such as a zone of re-liquefaction or a stress-free surface. Nevertheless, it could be interesting to create realizations of 3D equivalent tessellation based on the data obtained by analyzing two transversal cross sections and one longitudinal cross section. The transversal cross sections should belong to two different castings, in order to capture the difference of the fracture network morphology related to the two-stage manufacturing procedure.

As a general conclusion, we emphasize that the workflow presented here, combining (i) image analysis, (ii) analysis of a physical parameter indicative of glass internal structural relaxation, (iii) geostatistical modeling, and (iv) reproduction of equivalent fracture network tessellations is a powerful tool that enables the combination of hard and soft data concerning nuclear glass fracturing at scale 1. As such, it provides the basis for future investigation of the impact of fracturing on the aqueous alteration of borosilicate nuclear glass.

The demonstrated workflow is part of a more complex workflow and data integration process aimed at characterization of fracture network on the scale of a nuclear glass block, upscaling of permeability, diffusion and kinetics governing parameters, and subsequent reactive transport modeling with consideration for variability in the fracture network. Future work includes the use of the model fracture network for reactive transport simulations at the block scale. These simulations will bring quantitative assessment of the degradation of glass and the release of radioanuclides under different scenarios of evolution, bridging the gap between laboratory scale (micrometers, years) and geological repository scale (meters for the block, tens of thousands of years).

Acknowledgements

The authors wish to thank H. Beucher (MINES ParisTech) and S. Beucher (MINES ParisTech) for fruitful discussions at the early stage of the project and during its implementation. We thank the three anonymous reviewers for their constructive critics, suggestions and comments.

Research data availability

The raw/processed data required to reproduce these findings cannot be shared at this time as the data also forms part of an ongoing study. The data that support the findings of this study will be later available from the corresponding author, Frederic Bouyer, upon request.

References

Al-Kharusi, Anwar S., and Martin J. Blunt. 2008. 'Multiphase flow predictions from carbonate pore space images using extracted network models', Water Resources Research, 44.

ANDRA. 2005. "Dossier 2005 Argile - Tome Évolution Phénoménologique du Stockage Géologique." In, edited by ANDRA, 1-523.

Anton, François, Darka Mioc, and Christopher Gold. 2009. 'The Voronoi Diagram of Circles and Its Application to the Visualization of the Growth of Particles.' in Marina L. Gavrilova and C. J. Kenneth Tan (eds.), Transactions on Computational Science III (Springer Berlin Heidelberg: Berlin, Heidelberg).

Barth, N, D. George, S. Ahzi, Y. Rémond, V. Doquet, F. Bouyer, and S. Bétremieux. 2012. 'Modeling and simulation of the cooling process of borosilicate glass', Journal of Engineering Materials and Technology, 134: 041001.1-01.10.

Barth, N., D George, S. Ahzi, Y. Rémond, N. Joulaee, M.A. Khaleel, and F. Bouyer. 2014. 'Simulation of cooling and solidification of three-dimensional bulk borosilicate glass: effect of structural relaxations', Mechanics of Time-Dependent Materials, 18: 81-96.

Barth, Nicolas. 2013. 'Sur la modélisation et la simulation du comportement mécanique endommageable de verres borosilicatés sous sollicitation thermique', Université de Strasbourg.

Beucher, S. 1982. "Watersheds of functions and picture segmentation." In ICASSP '82. IEEE International Conference on Acoustics, Speech, and Signal Processing, 1928-31.

Beucher, Serge. 1994. 'Digital skeletons in Euclidean and geodesic spaces', Signal Processing, 38: 127-41.

Carl I. Steefel, Lauren E. Beckingham, Gautier Landrot. 2015. 'Micro-Continuum Approaches for Modeling Pore-Scale Geochemical Processes', Reviews in Mineralogy and Geochemistry, 80: 217-46.

Chatterjee, Snehamoy, Ashis Bhattacherjee, Biswajit Samanta, and Samir Kumar Pal. 2010. 'Image-based quality monitoring system of limestone ore grades', Computers in Industry, 61: 391-408.

Crevoisier, D., F. Bouyer, and S. Gin. 2011. 'Semi-stochastic generator (FRAGMA) of 2D fractured media by mechanistic analogy. Application to reactive transport in a fractured package of vitrified nuclear waste', Computational Materials Science, 50: 1387-98.

Cvetkovic, Vladimir, S. Painter, N. Outters, and J. O. Selroos. 2004. 'Stochastic simulation of radionuclide migration in discretely fractured rock near the Aspo Hard Rock Laboratory', Water Resources Research, 40: W02404.

Flusser, Jan, Barbara Zitova, and Tomas Suk. 2009. Moments and Moment Invariants in Pattern Recognition (Wiley Publishing).

Frugier, P., S. Gin, Y. Minet, T. Chave, B. Bonin, N. Godon, J.E. Lartigue, P. Jollivet, A. Ayral, L. De Windt, and G. Santarini. 2008. 'SON68 Nuclear glass dissolution kinetics: Current state of knowledge and basis of the new GRAAL model', Journal of Nuclear Materials, 380: 8-21.

Gin, S., A. Abdelouas, L.J. Criscenti, W.L. Ebert, K. Ferrand, T. Geisler, M.T. Harrison, Y. Inagaki, S. Mitsui, K.T. Mueller, J.C. Marra, C.G. Pantano, E.M. Pierce, J.V. Ryan, J.M. Schofield, C.I. Steefel, and J.D. Vienna. 2013. 'An international initiative on long-term behavior of high-level nuclear waste glass', Materials Today, 16: 243-48.

Hudson, Gordon. 1993. 'Kriging Temperature in Scotland using the External Drift Method.' in Amilcar Soares (ed.), Geostatistics Tróia '92: Volume 1 (Springer Netherlands: Dordrecht).

Jan Flusser, Tomas Suk, Barbara Zitova. 2016. '2D and 3D Image Analysis by Moments', Book.

Jouini, M. S., S. Vega, and E. A. Mokhtar. 2011. 'Multiscale characterization of pore spaces using multifractals analysis of scanning electronic microscopy images of carbonates', Nonlin. Processes Geophys., 18: 941-53.

Lantuejoul, Christian. 2002. 'Geostatistical Simulation: Models and Algorithms'.

Lubarda, Vlado A., and Yujia Liu. 2011. 'Areal moments of inertia revisited: on the distinction between the principal directions', Archive of Applied Mechanics, 81: 111-22.

Matheron, G. 1967. 'Eléments pour une théorie des milieux poreux'.

Nykyri, M., H. Nordman, J. Loefman, A. Poteri, N. Marcos, and A. Hautojorvi. 2008. "Radionuclide release and transport RNT-2008." In, 164. Finland.

Pajot, Hevre. 2002. ' Analytic Capacity, Rectifiability, Menger Curvature and the Cauchy Integral.', Lecture Notes in Mathematics, Springer, Berlin, Heidelberg.

Pierce, Eric M., Pierre Frugier, Louise J. Criscenti, Kideok D. Kwon, and Sebastien N. Kerisit. 2014. 'Modeling Interfacial Glass-Water Reactions: Recent Advances and Current Limitations', International Journal of Applied Glass Science, 5: 421-35.

Serra, J. 1969. 'Introduction à la Morphologie Mathématique', Cahiers du Centre de Morphologie Mathématique: 160.

———. 1982. 'Image Analysis and Mathematical Morphology', Academic Press.

Soille, Pierre. 2003. Morphological Image Analysis: Principles and Applications (Springer-Verlag New York, Inc.).

Tokan-Lawal, Adenike, Maša Prodanović, and Peter Eichhubl. 2015. 'Investigating flow properties of partially cemented fractures in Travis Peak Formation using image-based pore-scale modeling', Journal of Geophysical Research: Solid Earth, 120: 5453-66.

Vernaz, Etienne. 2009. 'Nuclear Waste Conditioning', CEA DFN Monographs.

Zhang, Chun-Liang. 2018. 'Thermo-hydro-mechanical behavior of clay rock for deep geological disposal of high-level radioactive waste', Journal of Rock Mechanics and Geotechnical Engineering.

Glossary

Binary image	The value of a pixel of this image is either 1 or 0 depending on whether the pixel belongs to the foreground or to the background.
Black top-hat transformation	Is defined as the difference between the image closing φλ(f) and the image itself f, it extracts black and narrow features. In this study, black top hat transformation was applied to grayscale images at the stage of image pre-processing to remove slow trends and to perform contrast enhancement. This operator brought out fractures whose thickness is half the chosen size of the SE and, as a consequence, it facilitated the separation of the glass matrix and the fracture network.
Bounding box	Smallest enclosing box for an object.
Cell	Applied as an analogue of the term “segment” by referring to a separate unit of an equivalent representation of the segmented image. Synonyme: mesh.
Center	Geodesic center of the segment (shard, crystal). It is obtained by the homotopic full thinning with the double structuring element D (Golay’s alphabet). Synonym: barycenter.
Centroid	Origin of the corresponding cell growth. Synonym: seed.
Closing	The closing of an image f by a structuring element B is denoted by φB(f) and is defined as the dilation of f with a structuring element B followed by the erosion with the reflected SE. The idea behind the morphological closing is to build an operator able to recover the initial shape of the image structures that have been dilated. This is achieved by eroding the dilated image.
Dilation	The dilation of an image f by a structuring element B is denoted by δB(f) and is defined as the maximum of the translation of f by the vectors -b of B. Like for the erosion, the dilated set is the locus of points where the answer to the question is affirmative, however the question slightly changes and becomes: “Does the structuring element hit the set?”
Distance function	Defined as the length of the shortest path drawn on the Euclidian grid between two points. In the digital version, each section at level i of the distance function of a set X corresponds to the erosion of size i-1 of X.
Equivalent tessellation	One realization of the equivalent fracture network constructed by the anisotropic Voronoï algorithm.
Erosion	The erosion of an image f by a structuring element B is denoted by εB(f) and is defined as the minimum of the translations of f by the vectors -b of B. Or to put it simply, the eroded set is the locus of points where the answer to the question "Does the structuring element fit the set?" is affirmative.
Feret diameters	Distances between the parallel planes restricting the object.
Fracture aperture	Defined as the width of the fracture between its two opposite walls on the 2D image. For peripheral part of the longitudinal cross-section, it represents a true fracture width, since here fracture network is perpendicular to the cross-section plane. For central part of the longitudinal cross-section, it differs from the true fracture width by cosα, where α is the angle between the plane parallel to the longitudinal cross-section and the plane orthonormal to the fracture whose aperture is measured. Synonymes: aperture, fracture opening.
Geodesic reconstruction	Allows the reconstruction of all connected components of an image g from a marker image f. It is effectuated by iterating geodesic dilatations of f with respect to g until stability. The opening by reconstruction, in contrast to simple opening, preserves the contours of the objects that have not been removed by the erosion (binary image) and removes unconnected light features (grayscale

	image).
Grayscale image	The range of the values of the pixels of this image is extended from 0 to 2n - 1 for pixel values coded on n bits.
Image segmentation	Its partition into different regions, each one having certain properties.
L-skeleton by homotopic thinning	Obtained by performing the sequential thinning with six rotations of L structuring element (Golay's alphabet) until stability. This skeleton is always connected, of unit thickness and is less prone to generating spurious branches due to irregularities of object frontiers.
Moving window	Rectangle defined by 4 points (x_1,y_1; x_2,y_1; x_2,y_2; x_1,y_2) which includes certain number of samples i so that their coordinates (x_i, y_i) respect the conditions: $x_1 \leq x_i \leq x_2$ and $y_1 \leq y_i \leq y_2$.
Multiple points	Used for detecting connections between one-pixel width curves such as those obtained after the homotopic skeletonisation. They were useful in separating fracture ramifications.
Opening	The opening γ of an image f by a structuring element B is denoted by γB(f) and is defined as the erosion of f by B followed by the dilation with the reflected SE. The idea behind the morphological opening is to dilate the eroded image to recover as much as possible the original image.
Pullout zone	Zone of damage, created during sawing operations.
Quench function	Calculated together with the skeleton by maximal balls, associates the radius of the ball to the ball center.
Rotation matrix	Matrix used by the anisotropic version of Voronoï algorithm to perform a rotation in Euclidean space for defining the anisotropy on distances.
Scaling factor	Number by which the distance along the chosen axis (after possible rotation) is divided.
Seed	Origin of the corresponding cell growth. Synonym: centroid.
Segment	In mathematical terms, it represent a disjoint nonempty set and it is obtained by image segmentation. It the specific case of this research it represents a part of the glass matrix separated by the extracted early fracture network. Synonyms: shard, crystal.
Skeleton	Compact representation obtained by thinning of the object to a set of lines condensing the information of the original object while keeping its homotopy (topology preservation). The skeletal points and their distance to the boundary of the set enable the reconstruction of the set. There are several techniques to perform skeletonisation. In this research, we used a skeleton by maximal balls and a skeleton by homotopic thinning.
Skeleton by maximal balls	Defined by the centers of maximal balls, where a maximal ball B is considered maximal in X object if there exists no other ball included in X and containing B.
Solidification front	Corresponds to the isoline of the delay $\Delta T = T_f - T(t) = 10$ between the fictive temperature (T_f) and the glass temperature at each time step T(t).
Structuring element (SE)	Set of known shape used to probe the analyzed image. There are several types of structuring elements: hexagon, triangle, linear segment etc. The shape of the SE is usually chosen according to some preliminary knowledge about the geometry of the relevant and irrelevant image structures.

Variogram	Function describing the degree of spatial dependence of a spatial random field or stochastic process. It is calculated as a half the average squared difference between all points separated at distance h.

5. From block image analysis to reactive transport modeling (*continued*)

5.3. Parameters upscaling

5.3.1. Effective permeability

5.3.2. Effective diffusion

5.3.3. Geochemical behavior (input parameters for the GRAAL model)

5.3.4. Reactive transport modeling for a synthetic case

5.4. Reactive transport at the scale of the vitrified glass canister

5.4.1. Aqueous alteration experiment of a nonradioactive full-scale SON68 glass block

5.4.2. Reactive transport modeling at the scale of the vitrified glass canister in diffusive and convective modes

Chapters 5.3 and 5.4 are presented in the form of the article entitled "Reactive transport modeling of the glass alteration in a fractured vitrified nuclear glass canister: from upscaling to experimental validation". It was submitted in March 2019. Below some supplementary information on the long-term experiment of a nonradioactive full-scale SON68 glass block aqueous alteration presented in Section 1.1 of the article is provided.

Preparation of the SON68 glass canister

To conduct aqueous alteration tests, a block of SON68 glass was fabricated in 2001. This 400 kg block was made in a perforated stainless steel basket with 10 mm diameter holes occupying 50% of the surface. The thermal scenario that has been imposed was as follows:

i. Canister was installed in the preheating furnace;
ii. Canister was preheated during three hours before the first melted glass discharge took place, with the temperature of the low and the high zones being 450° C and 550°C respectively;
iii. Two glass castings were effectuated at 1200° C during approximately 30 minutes;
iv. Heating was maintained during 10 h after the first casting took place in order to keep up the temperature before pouring the second casting;
v. Heating was stopped at the end of the second casting;
vi. Glass canister was moved out from the oven 2h30 after the second casting and cooled down in the open air condition.

Presentation of the ALISE installation

The ALISE (Appareillage de Lixiviation Statique Electrique) installation has been built in Marcoule, CEA to carry out long-term aqueous alteration tests of industrial scale vitrified glass canisters under static or quasi-static conditions with moderate amount of water available to come in contact with the glass (about 35 L for one block of 400 kg).

The installation was equipped with electric heaters to keep water temperature constant. The temperature was monitored by thermocouples readings, with three thermocouples placed in different places. A sampling valve was used to collect some solution (a few millilitres for each sample) for chemical analysis. The upper part of the reactor, removable to allow exceptional interventions during the test, included an injection plug to add water and a window for real-time observation of the water level and the upper part of the block placed inside the installation.

Soon after its fabrication, the block was placed into the ALISE installation. It stayed there during 2718 days (7.5 years). The initial temperature of the test was set to 106±1° C (the originally planned temperature was 90 ° C but due to a thermocouple calibration error detected in early 2002, the temperature was kept higher, at 106 °C). The initial volume of water in the reactor was 34.7 liters.

In total, over the course of the test 106 samples were collected and analyzed by the inductively coupled plasma atomic emission spectroscopy (ICP / AES) technique on the following elements: Si, B, Na, Li, Mo, Al, and by the inductively coupled plasma mass spectrometry (ICP / MS) on Cs. Before each sample collection, the solution was homogenized using a closed-loop pumping.

It should be noted that there were some interventions: *e.g.* in February 2007, *i.e.* 5.5 years after the beginning of the test, when 8 liters of a synthetic solution was added to compensate for the cumulated evaporated water. Before mixing, the solution composition was adjusted to minimize the chemical disturbance. Composition of the solution in the unit was probed at the end of 2006. It was the following: Si (300 ppm), B (530 ppm), Na (820 ppm), Li (110 ppm), and Mo (80 ppm) (internal communication, Minet et al., 2013).

Some key results of the ALISE test

The evolution of tracer concentrations is shown in Figure 5-1. For the purposes of this research, our attention was brought to the evolution of the tracer elements represented by boron, sodium, and lithium. They are considered good tracers of the glass alteration: they are released by the glass dissolution but are not retained (boron) or slightly retained (sodium, lithium) in the alteration layers. The knowledge of the concentration of these elements made the evolution estimation of the mass of altered glass possible, under the hypothesis that tracer element concentrations were identical in the external solution and in the fractures.

Some other elements, such as silicon, molybdenum, cesium, aluminum and calcium were also analyzed and monitored as they provide information about the alteration layer itself.

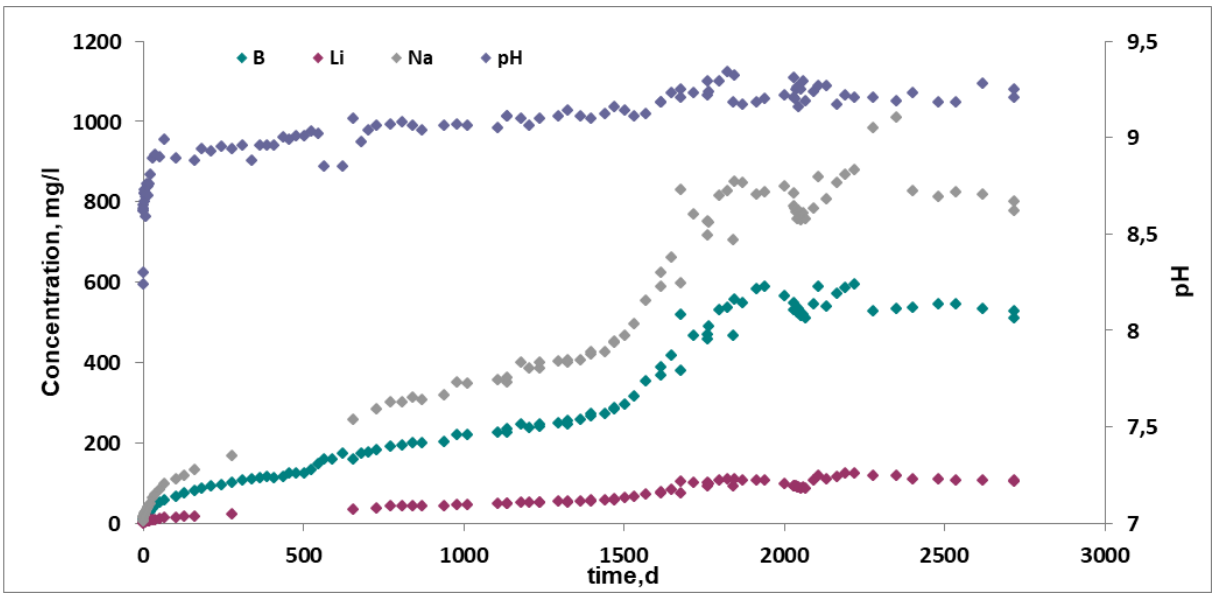

Figure 5-1 Evolution of the tracer-elements concentration and the pH. Modified from Minet et al., 2013.

Figure 5-2 shows the evolution of the mean quantity of altered glass per unit time. Based on the detailed analysis of the concentrations of the analysed elements and the quantity of altered glass, (Minet et al, 2013) reported five phases of alteration.

i. 1-30 days: an initial phase characterized by a rapid transition from the initial rate regime (Section 2.1) to the rate drop regime reflected by the sharp increase of the released QAG per unit time and the quick increase of the pH.
ii. 30-500 days: a phase of gradual decline of the alteration rate characterized by progressive decrease of the QVA and the slow increase of the pH.
iii. 500-1400 days: a phase of the interchange between the regime of the alteration rate recovery and the regime of the alteration rate decline.
iv. 1400-1700 days: a phase of the alteration rate resumption characterized by the increase of the QAG per unit time of almost an order of magnitude, followed by a subsequent decrease. Regarding the pH, it increased too.
v. 1700 to 2700 days: a final phase characterized by the fluctuating alteration rates. This phase of the test was perturbed by external interventions, such as first, the opening of the cover plate to measure the water level, second, the addition of the synthetic solution. Due to the fact that the chemical environment was strongly disturbed, the interpretation of the aqueous alteration behaviour is not unequivocal.

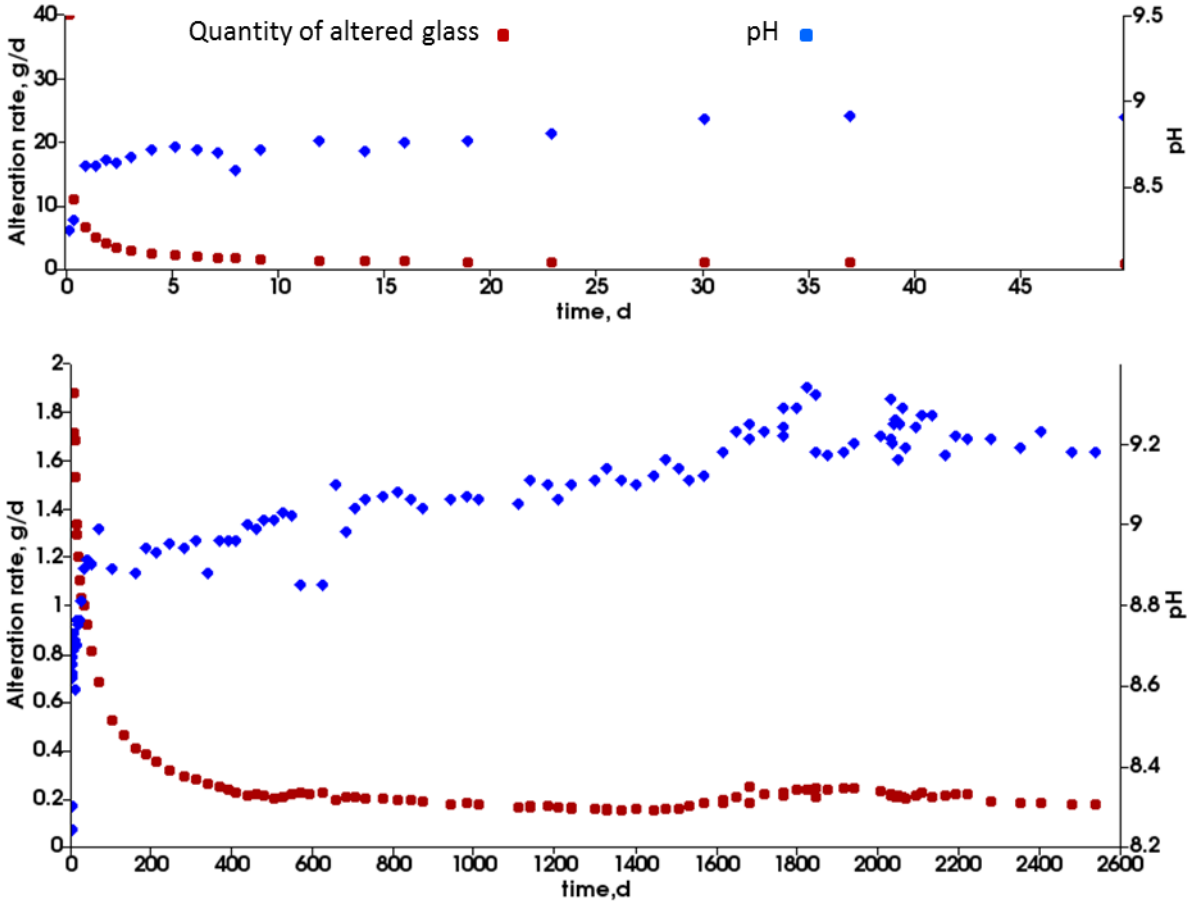

Figure 5-2 Quantity of altered glass per unit time calculated from the concentration of the boron in the solution and pH of the external solution: a) zoom for the first 50 days; b) whole duration of the experiment. Calculated from total dissolved boron concentration obtained from (Minet et al. 2013).

Post-mortem characterization

As mentioned in Section 2.2, after the test had been stopped, the block was coated with an epoxy fluid resin to enhance its mechanical durability before moving ahead with its cutting. As illustrated in Figure 2-9, first, the block was cut in 2 parts along its transversal axis; secondly, the upper half was split into 10 discs of 4 cm thickness each. The discs were numbered from 2 to 10 in a downward direction. At the following stage, the fracture network of the disc number 6, located between 43 and 47 cm from the top of the block was studied in detail. Results of this analysis can be found in Section 2.2.

Comparison with the reactive transport modeling results

For this research, the results of the aqueous alteration of a nonradioactive full-scale SON68 glass block carried out in the ALISE installation were valuable, because it was important to compare them with the results of the RT simulations applied to a series of equivalent fracture network realizations obtained by following the workflow presented in Section 5. Although there were some differences between the conditions in which the ALISE experiment was

realized and the modeled conditions, the QAG calculated from the concentration of the tracer element was similar.

Title: Reactive transport modeling of the glass alteration in a fractured vitrified nuclear glass canister: from upscaling to experimental validation

Authors : Maria Repina[a,b], Frédéric Bouyer[a,30], Vincent Lagneau[b]

[a] CEA, DEN, DE2D , SEVT, LCLT Marcoule, F 30207 BAGNOLS SUR CEZE Cedex, France

[b] MINES ParisTech - PSL Research University, Centre de Géosciences 35, Rue Saint-Honoré F 77305 FONTAINEBLEAU Cedex, France

Abstract

Performance assessment of geological nuclear waste repositories entails modelling of the long-term evolution of the aqueous alterations of the fractured nuclear glass block, because the time scales under consideration are of several thousands of years and hence beyond the range of any direct experimental perspectives. In this study, our objective is to bridge the gap between the reservoir-scale flow and transport simulations and the micron-scale modeling of the glass-water interfacial processes by providing quantitative evaluation of the aqueous alteration of glass at the block scale. In particular, calculations of the equivalent diffusive, hydraulic, and alteration kinetics properties and reactive transport simulations are discussed. Prior to performing reactive transport modeling at the scale of the glass canister, the preferred upscaling techniques were first applied to a synthetic fracture network system with ends to compare the results of the borosilicate glass alteration with the discrete fracture modeling and the equivalent porous medium approach. The evolution of the altered glass obtained from reactive transport modeling applied to several realizations of the equivalent fracture network tessellation was compared to the experimental data of the aqueous alteration test of a nonradioactive full-scale SON68 glass canister. The proposed model agrees with the experimental data and offers, for the first time, an opportunity to better understand the impact of fracturing on the corrosion of nuclear glass as well as the convection due to the radioactivity acting as a heating source.

Keywords

Nuclear glass corrosion, fracture network, glass alteration rate, reactive transport modeling, upscaling, equivalent continuum, kinetic regimes.

Introduction

The vitrification of radioactive waste has been considered as a reliable method to condition high-level long-lived nuclear fission products in geological disposal facilities on time scales of up to millions of years. This process involves calcination of the liquid fission product solutions followed by melting at around 1100 °C in an induction-heated metallic vessel, where the glass frit and the calcinated fission product solution are mixed before being poured into a metallic container. During cooling and solidification of the glass, the increase of tensile stresses resulting from the mechanical equilibrium between the internal liquid and the external (reduced volume) solidified glass causes the development of a network of fractures.

[30] Corresponding author CEA, DEN, DE2D , SEVT, LCLT Marcoule, F 30207 BAGNOLS SUR CEZE Cedex
E-mail address: frederic.bouyer@cea.fr (BOUYER Frederic)

ANDRA, the French national operator for the management of nuclear waste, and numerous academic or national operators worldwide have been carrying out research concerning the feasibility of geological waste disposal. In consideration of the results of several decades of research, the French Parliament opted for deep geological disposal and asked ANDRA to design Cigéo (Centre industriel de stockage géologique) – a deep geological disposal facility for radioactive waste. According to the disposal scenario proposed by ANDRA, the packages of vitrified fractured glass containing high-level long-lived radioactive waste (HLLLW) would be stored in disposal cells in a repository built with Callovo-Oxfordian (COx) clay, located 500 m beneath the Earth surface in Meuse/Haute-Marne, France. With the current concept (which is still in development), these cells would be blind micro-tunnels, 0.7 m in diameter and of 100–150 m total length (Figure 1a). A steel lining is intended to facilitate the placement of packages during the operational phase (and their removal for possible recovery). Finally, a filler material would be injected between the liner and the host rock to enhance mechanical strength and reduce corrosion. The glass canisters made of vitrified glass contained in 53–65 mm thick steel overpacks (Figure 1b) would be positioned separately from one another, such that heat production in the cell is compatible with thermo-hydro-mechanical targets (ANDRA 2016).

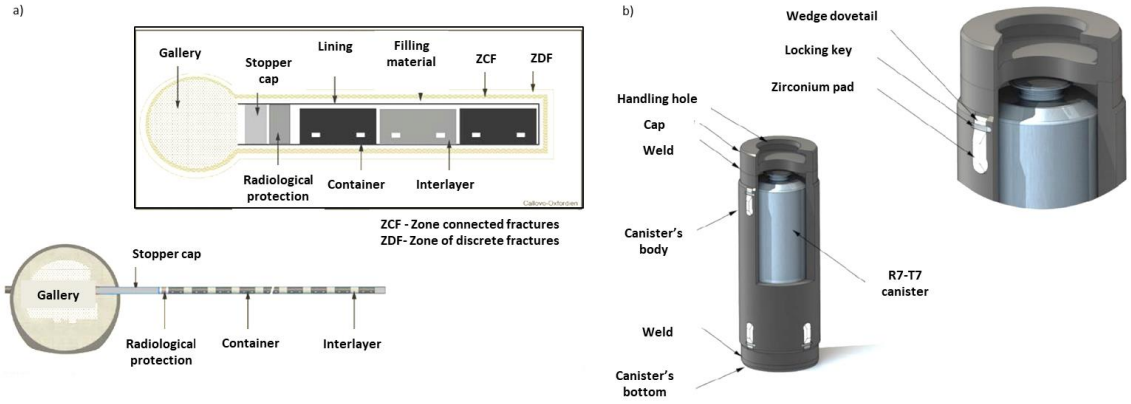

Figure 1 a) Schematic diagram of the high activity HA cell; b) Illustration of an HA storage container for vitrified nuclear waste, primary package type R7T7. High-level long-lived waste disposal gallery in operating configuration. Obtained from (ANDRA 2016).

As mentioned above, the cooling down stage creates numerous fractures in the vitrified glass packages. The fracture network increases the reactive surface areas and creates water pathways within the glass. After re-saturation of the vicinity of the cell, and the eventual corrosion of the canister, water will come into contact with the glass. The water-glass interaction must therefore be studied, both in terms of glass alteration and release-rate of radionuclides.

Despite the advancements made in studies of solute transport and flow of ground water in fractures at the mega-scale (ANDRA 2005; Zhang 2018; Cvetkovic et al. 2004; Nykyri et al. 2008) and discoveries achieved in the domain of borosilicate glass aqueous alteration (Pierce et al. 2014; Gin 2013) at the micro-scale, the reactive transport modeling applied to a scale of one block of fractured borosilicate glass has not been performed to date, to the best of our knowledge.

Although the evolution of reactive transport modeling (RTM) codes is impressive, RTM applied to fractured media of a glass block remains challenging. Particularly, the coupling of the geochemistry of borosilicate glass dissolution with physical flow and transport phenomena within a discrete fracture network is too CPU-intensive. Hence, in order to study nuclear glass degradation at the scale of the

industrial vitrified glass canister, an equivalent fracture network model was constructed, and its hydraulic, diffusive and kinetics controlling parameters were determined.

This study is a further development of our previous research (Repina et al. 2018, accepted in the Journal of Nuclear Materials), where the authors presented an image processing-based fracture network characterization workflow elaborated for the purpose of RTM application to a block of vitrified nuclear glass. The workflow was devised in the following steps: (i) characterization of a glass block fracture network, (ii) establishment of a link between a physical parameter representing an internal state of glass structural relaxation and an internal structure of the block fracture network, and (iii) generation of multiple realizations of fracture networks by considering the variability of fracture network parameters such as fracture distribution and aperture. Based on mapped fracture distribution and aperture, the present paper presents an upscaling workflow and subsequent RTM application as follows: computation of the equivalent hydraulic, diffusive, and glass degradation kinetics- governing parameters, verification of the proposed techniques, their application to several realizations of fracture networks, and reactive transport modeling. The construction of the equivalent continuum model was initiated to overcome the problem of the complexity of the fracture network discrete representations and, as a consequence, to be able to perform RTM at the scale of the industrial glass canister.

RTM was conducted by the HYTEC code (Van der Lee et al. 2003; Lagneau et al. 2010). The kinetics of the international simple glass (ISG) aqueous alteration (Gin 2013), including the passivation effect of porous or dense gel formation, is represented using the Glass Reactivity with allowance for the Alteration Layer (GRAAL) model. ISG glass aqueous alteration was studied under the assumption of full saturation with water in pH conditions preventing alteration resumption. The methodology was tested over synthetic discrete fracture networks, and finally an application is performed at the block scale to simulate a long-term aqueous alteration experiment of a non-radioactive proxy canister.

1. Material

1.1. Aqueous alteration experiment of a nonradioactive full-scale SON68 glass block

French Alternative Energies and Atomic Energy Commission CEA performed an aqueous alteration experiment on a non-radioactive full-scale inert nuclear glass canister (Minet et al. 2013). The experiment was conducted in the ALISE (Appareillage de Lixiviation Statique Électrique) unit built in Marcoule. The objective of this experiment was to produce a set of data on the long-term (seven years) aqueous alteration of an industrial-scale vitrified glass canister under static conditions with a moderate amount of water in contact with the glass (about 35 L for one block of 400 kg). The general schematic of the installation is depicted in Figure 2.

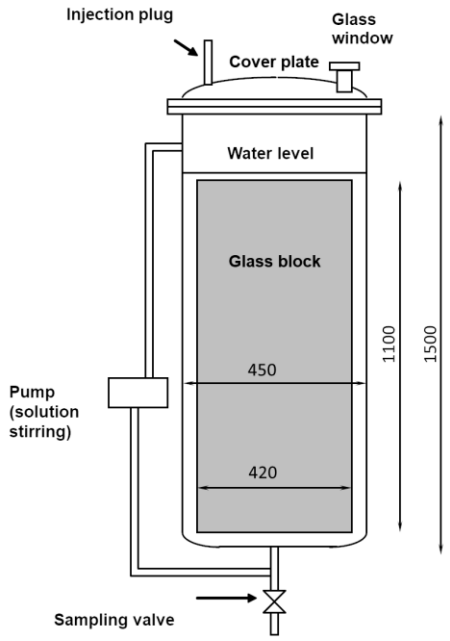

Figure 2 General view of the ALISE unit. Dimensions indicated on the sketch are in mm. Modified from (Minet et al. 2013).

An industrial-scale block of inert nuclear glass was fabricated in a cold crucible in two stages. This 400 kg block was made in a perforated stainless steel basket with 10 mm diameter holes to facilitate water access during the experiment.

Soon after the fabrication of the block, it was placed into the ALISE unit. It remained there for 2718 days (7.5 years). The initial temperature was set to 106 ± 1 °C. The initial volume of water in the reactor was 34.7 liters. In total, over the course of the test, 106 samples were collected and analyzed by ICP/AES for Si, B, Na, Li, Mo, Al, and by ICP/MS for Cs. Prior to each sample collection, the solution was homogenized using closed-loop pumping.

To characterize the glass alteration, the evolution of two parameters was monitored. First, the evolution of the boron[31] tracer element was observed. Secondly, with respect to boron concentration evolution, the alteration rate was estimated using the following equation (1):

$$alteration\ rate = \frac{C_{i(t)} * V}{X_i * t}, \qquad 1$$

where C_i is the concentration of dissolved boron in the solution at time t, x_i is the mass fraction of boron in the glass, and V is the solution volume.

1.2.Glass block section and its fracture network equivalent tessellations

The segmented image of a non-radioactive vitrified glass fracture network (Figure 3a) and three realizations of fracture network equivalent tessellations (Figure 3b–d) presented in (Repina et al. 2018, accepted in the Journal of Nuclear Materials) were used as the input data for this study. The glass fracture network was extracted and characterized using mathematical morphology tools. The

[31] Boron is considered as a tracer of glass dissolution, because it is released completely from the glass during the glass alteration process without being retained in the alteration layer.

input data necessary for the generation of multiple realizations of fracture network equivalent tessellations were obtained by conducting geostatistical modelling based on the results of image analysis and the analysis of a physical parameter indicative of glass internal structural relaxation. The parameters of the four fracture networks are indicated in Table 1.

Table 1 Fracture network parameters impacting glass alteration

Name/ Parameter	Segmented Image	Equivalent Tessellation #1	Equivalent Tessellation #2	Equivalent Tessellation #3
Average porosity	0.08	0.11	0.12	0.11
Length of fracture median axes, m	20.5	51	52.1	49.5
2D fracturing ratio	17.4	42.7	41.8	40.6
Internal fracture surface[32], m^2	26.6	67.7	66.2	66.7

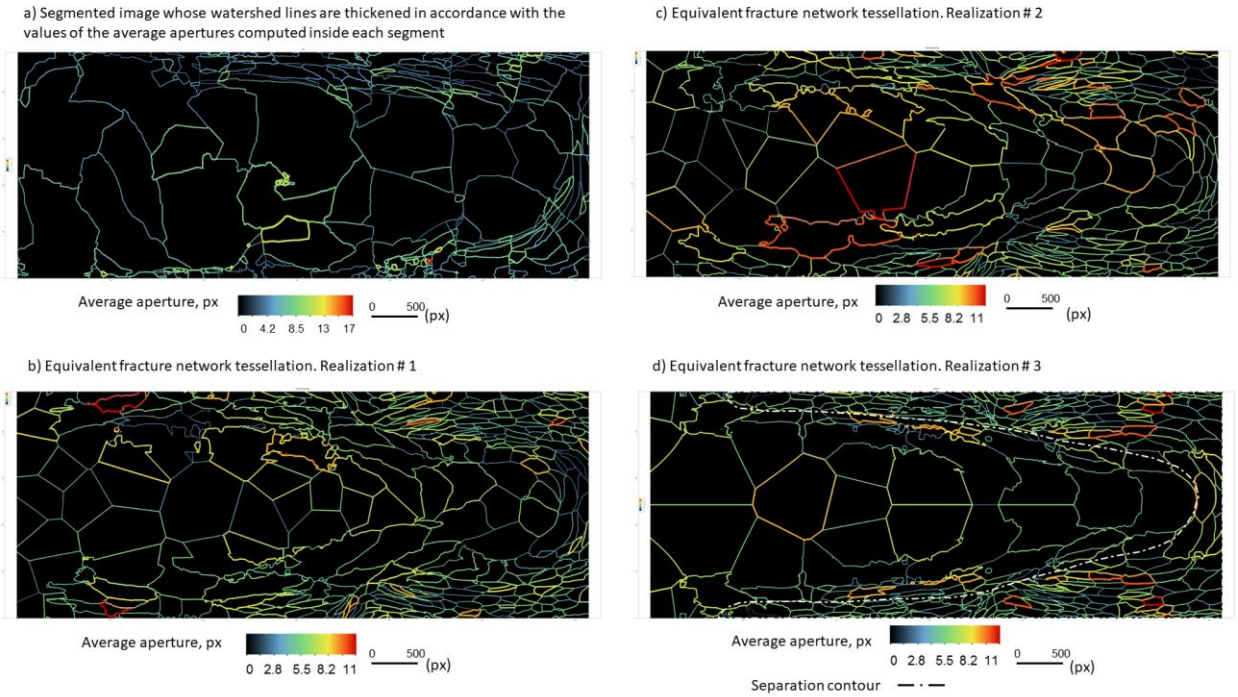

Figure 3 Input images used to calculate equivalent reactive transport parameters: segmented image of the full glass section of the canister (top left), and three equivalent tessellations used in this study. Image dimensions are 6144 px × 2430 px, with 1 px corresponding to 0.17 mm.

1.3. GRAAL geochemical model

The borosilicate nuclear glass alteration was simulated by the glass reactivity with allowance for the alteration layer (GRAAL) model (Frugier et al. 2009; Frugier 2008; Minet et al. 2010). The model pursues a dual objective: (i) coupling between the affinity effects in the kinetic law and the diffusion processes in the alteration layer and (ii) establishment of a precise material balance to calculate the distribution of the elements of the glass between the solution, secondary phases and a developing gel. The first hypothesis of the GRAAL model is the speed of the hydration reaction of the glass at the

[32] Calculated under the hypothesis that fracturing ratio in 2D and in 3D are equal

initial time: this phenomenon causes the elements of the glass (the alkali earth metals, boron) to pass into solution. The hydrolysis of silicon is slower and conditions the initial dissolution rate of the glass. The difference between these two kinetics leads to the formation of a dealkalized hydrated glass layer at the glass-solution interface. This layer or gel is gradually reorganized by hydrolysis / condensation phenomena and is referred to as the passivating reactive interface (PRI). Each silicon atom present in the solution stems from the dissolution of the PRI. Concurrent to its formation, this gel dissolves, given that the solution is not saturated with the elements that constitute it, namely Si, Al, Ca, and Zr. GRAAL proposes a description of the gel formed on the surface of glass by condensation and precipitation of Si, Al, Zr, and Ca. With a relatively simple formalism, the model accounts for the chemistry and solubility of the gel. It assumes that glass alteration is controlled by the PRI, consisting of glass without any mobile elements in its composition.

The transport properties of the PRI are modeled by a spatially and temporally constant diffusion coefficient for the elements of the glass. Thus, the flow of mobile elements transported through the PRI is proportional to the diffusion coefficient and inversely proportional to the thickness of the PRI. GRAAL therefore makes the assumption of a balance between the non-passivating gel and the solution, and between the external interface of the PRI and the solution. GRAAL uses two kinetic equations for the PRI grouped in (2).

$$\frac{dx}{dt} = \mathrm{r}_1 - \mathrm{r}_2 = \frac{D_{PRI}}{\mathrm{x_{PRI}}} - v_0\left(1 - \frac{Q_{PRI}}{K_{PRI}}\right) = \frac{D_0 \times [OH^-]^{n'} \times e^{-\frac{E'_a}{RT}}}{x} - \mathrm{k}^+ \times [H^+]^{\mathrm{n}} \times e^{-\frac{E_a}{RT}} \times \left(1 - \frac{\mathrm{Q_{PRI}}}{\mathrm{K_{PRI}}}\right), \quad 2$$

This equation states that the passivating reaction interface PRI (i) is formed from the glass with a rate r_1, which is a function of its thickness $\mathrm{x_{PRI}}$ and the PRI diffusion coefficient D_{PRI}, and (ii) also dissolves with a rate r_2 according to a classical affinity law in which v_0 is the initial velocity, Q_{PRI} is the ionic product and K_{PRI} is the PRI solubility product. The right hand-side of the equation is the expanded version, indicating the dependence of D_{PRI} and v_0 on pH and T, where D_0 is the interdiffusion constant, E'_a is the activation energy associated to the interdiffusion coefficient, n' is the pH-dependence factor, E_a is the apparent activation energy at the initial rate, n is the pH-dependence factor of the initial rate, k^+ is the dissolution rate of the PRI in pure water, and T is the experiment temperature.

As in the study of (Frugier et al. 2018), in order to limit the formation kinetics of the protective layer, *i.e.* to avoid the appearance of the infinite rate when $\mathrm{x_{PRI}} = 0$, a constant hydration rate is introduced in the definition of r_1 in (3):

$$\mathrm{r}_1 = \frac{\mathrm{D_{PRI}}}{\mathrm{x_{PRI}}} = \frac{\mathrm{r_h}}{1 + \mathrm{x_{PRI}}\frac{\mathrm{r_h}}{\mathrm{D_{PRI}}\frac{\pi}{2}}}, \quad 3$$

where $\mathrm{r_h}$ is the hydration rate, which is higher than the initial dissolution rate. This is fully compatible with the experimental observations: the dissolution rate of mobile ions is higher than the dissolution rate of silicon ions. However, due to the very low diffusion coefficient of nuclear glasses, the hydration rate governs the alteration rate only for a few seconds. The parameter is not measurable experimentally and has almost no effect on the modeling results.

In order to perform a RTM of borosilicate glass alteration, regardless of the modeling approach used (discrete fracture network or the equivalent porous model), some parameters in the law of glass dissolution have to be specified: glass mass per solution volume C_v, glass specific surface S_{sp}, half-

saturation coefficient present in the inhibition function[33] used to account for the interdiffusion rate, molar fractions of elements in the PRI, i_{PRI}, and in the glass, i_{PS}, glass molar density ρ_{PS}, and some other constants, like E^a, k^+, n, E_a', D_0, n' from Equation 2.

Some of the mentioned parameters, such as ρ_{PS}, k^+, i_{PRI}, i_{PS}, T, and the pH-dependence constants, E^a and E_a', are specific to the chemical properties of the glass. The others, such as C_v, S_{sp}, and the half-saturation coefficient, are controlled by the internal structure of the modeled fracture network. Depending on whether the discrete model or the equivalent porous model is applied, the calculation of these parameters changes. The exact formulas and the hypothesis constructed to compute these parameters for equivalent continuum and discrete models are discussed in Section 2.1.3 and Section 3.

In this study, the porosity update due to the precipitation of the secondary minerals in the fracture network was not considered. Indeed, in accordance with the GRAAL model, the alteration is considered isovolumetric: dissolved glass is replaced isovolumetrically by the alteration layer, such that glass alteration has no impact on fracture aperture and hydraulic conductivity.

1.4. Reactive transport modeling in HYTEC coupled code

Reactive transport simulations are performed by the HYTEC code (Van der Lee et al. 2003). HYTEC is a coupled chemistry-transport code that relies on the method of the separation of operators, with a sequential iterative algorithm (Lagneau 2013; Lagneau et al. 2010). The flow module is available in saturated (stationary, transitory regimes), unsaturated, and two-phase forms. It also allows for variable density flow. The variation of water densities as a function of temperatures (motor to thermo-convection) uses the Boussinesq approximation (4):

$$\frac{\rho}{\rho_0} = 1 - \alpha(T - T_0)\,, \qquad 4$$

where α is the thermal expansion coefficient, T_0 is the reference temperature at which the density is ρ_0, and T is the local temperature at which the density is ρ.

In this study, the simulations of the aqueous alteration of the borosilicate ISG glass were conducted in saturated stationary and saturated transient regimes. These simulations were conducted in both diffusive and convective modes. Convection originated from an imposed temperature gradient between the lower and upper parts of the modeled glass canisters. Change in porosity and its effect on the permeability and diffusion, as a consequence of clogging or dissolution, was not considered in the simulations, in agreement with the isovolumetric phase replacement.

The grids of both discrete and equivalent models presented here were created by a three-dimensional mesh generator GMSH (Geuzaine et al. 2009). HYTEC uses this grid for its node-centered finite volume scheme.

The governing equations of the GRAAL model are implemented in HYTEC. The principal requirements for HYTEC to accept GRAAL equations are the availability of the Monod-type equation, the ability to use the concentration of a solid (glass) as a variable of the equation, and an adaptive time step

[33] The inhibition function, representing a special case of the Monod equation, imposes that the interdiffusion rate is only proportional to the diffusion coefficient if half-saturation << instantaneous PRI concentration. When the PRI does not exist, the alteration rate of the glass is maximal.

(Frugier et al. 2018). Thus, the time step needs to be small at the beginning of the calculation when the protective layer is thin to prevent its immediate dissolution. The switch from the GRAAL model to HYTEC is performed by treating (3) as a Monod-type equation and using the general kinetic formulation (van der Lee 1998) to describe the dissolution equation (Table 2):

Table 2 Analogy between the parameters in the GRAAL model and HYTEC code

	GRAAL model	HYTEC code
Parameter	PRI thickness X_{PRI}	PRI concentration $X_{PRI} = \frac{C_{PRI}}{\rho_{PRI} S_{sp} C_v}$
Primary solid alteration rate controlled by protective layer's thickness	$\frac{D_{PRI}}{x_{PRI}} = \frac{r_h}{1 + x_{PRI}\frac{r_h}{D_{PRI}\frac{\pi}{2}}}$ $D_{PRI}(T, pH) = D_0 \times [OH^-]^{n'} \times e^{-\frac{E'_a}{RT}}$	$r_h \frac{half-saturation}{half-saturation+C_{PRI}}$ Monod type equation (inhibition) $half - saturation = \frac{D_{PRI}\frac{\pi}{2}}{r_h} \rho_{PS} \frac{i_{PS}}{i_{PRI}} S_{sp} C_v$ W term specifying the dependence of D_{PRI} on pH
Protective layer's dissolution rate	$k^+ \times [H^+]^n \times e^{-\frac{E_a}{RT}} \times \left(1 - \frac{Q_{PRI}}{K_{PRI}}\right)$	Rate, area , Y- term specifying the dependence on the saturation state , W-term specifying the dependence on the pH

C_{PRI} is the concentration of the protective layer, S_{sp} is the specific surface area of the glass, and C_v is the concentration of the glass in the calculation cell volume.

The thermodynamic data used in this study were taken from the public Common thermodynamic database for speciation models CTDP adapted at the Laboratoire d'étude du Comportement à Long Terme des matériaux de conditionnement (LCLT), CEA Marcoule, by the addition of the definition of glass composites of interest (ISG, SON68, etc.).

2. Methods

2.1. Determination of the equivalent properties

The reactive transport parameters considered in this study are the porosity, tortuosity, diffusion coefficient, hydraulic conductivity, and glass alteration kinetic parameters controlled by the ratio of the contact surface to the solution volume.

It has been long established that flow and transport parameters are scale dependent (de Marsily 1986; Renard 1997a). This results from the existence of multiscale structures of porous medium that induce a hierarchy, which generates the heterogeneity. Consequently, the measurement or calculation of the parameters carried out at one scale cannot be directly applied to another-scale modeling. In fact, to pass to a higher scale, *i.e.* to make model coarser, upscaling techniques need to be employed. Upscaling leads to the replacement of a heterogeneous domain by a homogeneous one that should reproduce an equivalent response with the same imposed boundary conditions. Hence, upscaling transfers parameter values from the small to the larger scale by regularizing the heterogeneities at the smaller scale (Deng 2009). Upscaling has received a lot of attention from various fields, *e.g.* reservoir engineering (Durlofsky 1991; Begg et al. 1989; Christie 1996), hydrology,

(Neuman 1990; Zhou 2008; Cushman et al. 2002), and reactive transport modeling (Fernàndez-Garcia et al. 2005; Deng 2009; Nos et al. 2011).

There are numerous upscaling techniques, that are often sorted in several groups: most notably volume averaging (Whitaker 1967), homogenization (Hornung 1997), renormalization (King 1989; Noetinger 1994), ensemble averaging (Wood et al. 2003), and continuous-time random walk (Nœtinger et al. 2000). Despite the fact that these techniques have a lot of differences, their goal is basically the same: to relate the microscopic-scale structures and properties to the associated effective, or sometimes termed equivalent parameters (Renard P. 1997) considered in the macroscopic transport and flow equations.

In this study, we deal with the construction of an equivalent continuum model, meaning that the issue of the upscaling of permeability and diffusion is tackled. Although the construction of the equivalent continuum model is delicate because of the problematic choice of the representative elementary volume (REV) due to the disparate character of fracture density inside a glass canister, this model is able to provide the first estimate of the impact of fractures on nuclear glass aqueous corrosion in the geologic repository environment. Moreover, upscaling is also necessary for the geochemical description of glass alteration: the geochemical model of the borosilicate glass corrosion (Frugier 2008) is entirely adopted in the equivalent continuum modeling.

In the next sections we address the calculation of the maps of porosity, permeability, and effective diffusion and furthermore, we focus on the calculation of the equivalent glass corrosion kinetic parameters.

2.1.1. Equivalent permeability

The objective here is to calculate the maps of equivalent permeability, which would result in the same total flow of single-phase fluid through the coarse, homogeneous mesh as that obtained from the geometric description of the fracture network. It should be noted, that although there is some evidence that under geo-repository conditions a two-phase flow would take place due to the liberation of hydrogen as a result of the steel corrosion and radiolysis, in this research we considered that both flow and geochemical alteration happen under a water saturated condition.

The equivalent permeability was calculated by the simplified renormalization technique proposed in (Renard 1997b; Renard et al. 2000). As in all renormalization techniques, the studied parameter is considered at several scales, starting from the scale of the initial stage (fine mesh) to the final stage passing through all intermediate steps. At each stage, the map of the considered effective parameter is computed by renormalizing the map of the parameter at the preceding step. The idea of the simplified normalization method is to first assemble cells in groups of N × N cells at each step of the calculation, second, for each assembled group to calculate either the harmonic mean followed by the arithmetic mean or the arithmetic mean followed by the harmonic mean depending on the direction of the calculation with respect to the flow direction, third, at the end of stage before passing to the next level, to compute the geometric mean of the two previous results. The procedure is considered completed when the size of the coarse mesh is reached.

The fracture permeability on the initial map of fracture apertures was obtained using the parallel-plate model. Values of fracture permeability were computed using the relationship derived from the

Hagen-Poiseuille solution of the Navier-Stokes equation, which relates the intrinsic fracture permeability to its aperture as defined in (5):

$$K_f = {a^2}/{12}, \quad 5$$

where a is the fracture aperture.

Matrix permeability was taken as equal to 10^{-18} m^2 with reference to the study on thermo-mechanical cracking effects on elastic wave velocities, mechanical strength, and permeability under pressure (Ougier-Simonin 2010).

2.1.2. Equivalent diffusion

The efficiency of the random walk method applied to solve the diffusion problem is largely recognized (Noetinger 2016). In the random walk techniques, the determination of diffusivity of the media relies on the Einstein relation (Einstein. A. 1956), relating the mean square displacement to the effective diffusion coefficient (6):

$$R^2(t) = \langle (r(t) - r(t=0))^2 \rangle = 2d \times D(t) \times t, \quad 6$$

where d is the system dimensionality, D(t) is the diffusion coefficient, r(t) particle position at t, and r(t=0) is the particle position at t=0. It should be noted, that the square displacement is averaged for all particles.

The self-diffusion coefficient of molecules in a limitless bulk media is independent of time. It is only controlled by the type of molecules and by the fluid in which molecules diffuse. However, this diffusion coefficient becomes time-dependent when calculated in heterogeneous porous media.

Multiple studies have shown (Promentilla et al. 2009; Nakashima et al. 2004; Sen 2004; Gouze et al. 2011) that in the case of heterogeneous media, the convergence of the diffusion coefficient D(t) to its asymptotic value of effective diffusion (D_{eff}) is reached once the squared displacement $R^2(t)$ exceeds the permeability correlation length. In other words, to obtain the information about the true molecule trajectories encoded in the diffusion coefficient, it is necessary to allow the molecules to discover the whole domain. The short-time behavior of the mean squared displacement *vs.* time determines the surface-volume ratio of the porous media, because at short time scales, the molecules do not sense heterogeneities of the media (Sen 2004; Mitra et al. 1993).

In this study, we attempt to evaluate the tortuosity and the effective diffusion coefficient from the images of fracture networks shown in Figures 3 and 4a. This is carried out by modeling a 2D random walk in the percolating fracture space as follows:

1. N_{part} independent particles are placed randomly in each cell of the output grid.
2. At each iteration Δt, they can move to 4 neighboring positions (–X, +X, –Y, +Y) inside the fracture network, over a distance equal to 1. In the case where they encounter the glass, the displacement is not incremented. If particles leave the cell, they continue their paths in the fracture medium created by a mirror (toroidal) reflection.
3. Euclidean distance and directional displacements between the initial and the final locations for each particle are calculated and then averaged for all particles.
4. The regression of the average of the squared distances as a function of the iteration is verified for linearity, and the slope of the linear regression is recorded.

In general, in the case of the particle diffusion in free limitless space, the slope of the mean square displacement (msd) *vs.* time is equal to 1, whereas for the diffusion in fractured systems when motion is restricted by the glass matrix, the slope is less than 1. It reflects the impact of geometrical features on the particle diffusion, such as tortuosity of the porous media. To be precise, the tortuosity that determines the ratio of the effective average path of fluid particles to the corresponding straight and shortest distance along the direction of the flux is equal to the inverse of the slope according to the equations (7–8) given for the directional diffusion tortuosity.

$$\tau_{D_x} = \frac{1}{2}\left[\lim_{t\to\infty} \frac{d\langle (x(t)-x(t=0))^2\rangle}{dt}\right]^{-1}, \quad 7$$

$$\tau_{D_y} = \frac{1}{2}\left[\lim_{t\to\infty} \frac{d\langle (y(t)-y(t=0))^2\rangle}{dt}\right]^{-1}, \quad 8$$

Subsequently, in accordance with the equations (9–10), the directional coefficients of effective diffusion and the average diffusion coefficient are calculated.

$$D_x^e = \phi D_w \frac{1}{\tau_{D_x}}, \quad 9$$

$$D_y^e = \phi D_w \frac{1}{\tau_{D_y}}, \quad 10$$

where ϕ is the porosity of the fracture medium, and D_w is the water self-diffusion coefficient.

Meanwhile, it should be mentioned that it is not recommended to apply the described procedure to a low-density fracture network. In fact, in low density fractured media where fractures are not branched, it is difficult to record the average diffusion coefficient because particles move for a long time only in one direction before discovering the next fracture ramification. For this reason, at the scale of glass canister, the coefficient of effective diffusion for the inner part of the fracture network is calculated with the assumption that $\tau_{D_x} = \tau_{D_y} = 1$. The example of one block partitioning into inner and outer parts is shown in Figure 3d. The separation contour corresponds to the maximum gradient of the map of the arrival times of the solidification front.

Prior to application to a fracture network at the scale of the glass canister, the method is verified by comparing random walk on a discrete fracture network and on the calculated equivalent porous medium. Synthetic fracture networks were created, and the fracture density was chosen in accordance with the target fracture network in the glass canister and the desired upscaling. The evolution of particle concentration (N_{part} in a cell/N_{part}) in each cell of the output grid is recorded and analyzed, in order to investigate the resemblance of particle movement in the synthetic fracture medium and its equivalent porous system. The procedure is the following.

1. For the image in Figure 4a, the limiting slopes of the mean square displacement in X and Y directions ($slope_x^{cell(i)}$, $slope_y^{cell(i)}$) are calculated in accordance with the procedure explained above.
2. The resulting values are assigned to the elementary displacements $\Delta x^{cell(i)} = slope_x^{cell(i)}$, $\Delta y^{cell(i)} = slope_y^{cell(i)}$ that particles can effectuate in X and Y directions in each cell during their walk in the equivalent porous system.
3. The equivalent porous system is created by taking into account the porosity of the discrete fracture medium, *i.e.* the dimensions of each cell of the equivalent porous grid are:

$$dx_{cell} = {}^{a}/_{N_x} \times \sqrt{\Phi_{cell}} \text{ and } dy_{cell} = {}^{b}/_{N_y} \times \sqrt{\Phi_{cell}}$$

where a and b are the dimensions of the fracture network image, N_x and N_y depict the number of cells in x and y directions, and Φ_{cell} is the porosity of the cell where particles are counted.

4. In the case of the discrete fracture network, N particles are placed at the point with the smallest abscissa and ordinate values of the fracture network. They could travel to four neighboring positions inside the fractures during T iterations, with the maximum Δx and Δy elementary displacement being equal to 1.
5. As for the equivalent porous media, the same number N of particles were placed at the (0,0) point. They could travel to four neighboring positions inside the fractures during T iterations. Their elementary displacements were as specified at stage 2. The particles were not allowed to leave the media: they were reflected by the boundaries, and their displacements were incremented in a normal way.
6. At each iteration, the particles present in each cell were calculated and divided by the total number of the particles.

2.1.3. Equivalent glass corrosion kinetic governing parameters

Since the glass aqueous alteration is controlled by the product of the glass mass per solution volume by the glass specific surface ($C_v \times S_{sp}$), which is determined by the internal structure of the fracture network, the goal of this step is to build the grids of the C_v, S_{sp}, half-saturation coefficient according to the equations (11–13):

$$C_v = \frac{M_g}{V_s} = \frac{(1-\Phi)\rho}{\Phi}, \quad 11$$

$$S_{sp} = \frac{2Lc}{M_g} = \frac{2L}{ab(1-\Phi)\rho}, \quad 12$$

$$\text{half saturation} = \lambda \frac{D_{PRI}}{r_h} \rho_{PS} \frac{i_{PS}}{i_{PRI}} \times \frac{1}{\Phi} \times \frac{2L}{ab} = D_o [OH^-]^n \exp(-\frac{E_a}{RT}) \times \frac{\lambda}{r_h} \rho_{PS} \frac{i_{PS}}{i_{PRI}} \times \frac{1}{\Phi} \times \frac{2L}{ab}, \quad 13$$

where Φ is the porosity, L is the total length of the fracture median axes in the XY plane, a, b are the dimensions of one cell of the grid, *c* is the third dimension of the grid that in case of 2D modeling is set to 1 m in 2D, and λ is the coefficient of linear approximation. Note that the formulation of the dependence of D on the pH is valid for pH values between 6 and 10.5 and temperatures between 30 °C and 90 °C.

The fact that the kinetics of glass dissolution is controlled by the product $C_v \times S_{sp}$ implies that the law of the glass dissolution has to be set separately for each cell in the equivalent porous media system.

3. Verification

3.1. Fracture network of a synthetic model: preparation of input data for reactive transport modeling

Although the principal goal of this study was to perform the reactive transport modeling at the scale of the glass canister and verify the applicability of the techniques proposed with the aim to construct

an equivalent fracture model, one synthetic discrete fracture network (Figure 4) was generated by the FRAGMA semi-stochastic generator (Crevoisier et al. 2011).

When modeling the glass aqueous alteration applied to this discrete model, glass and water media were represented in two separate zones: the glass zone (depicted in purple in Figure 4b) and the fracture zone (depicted in green in Figure 4b).

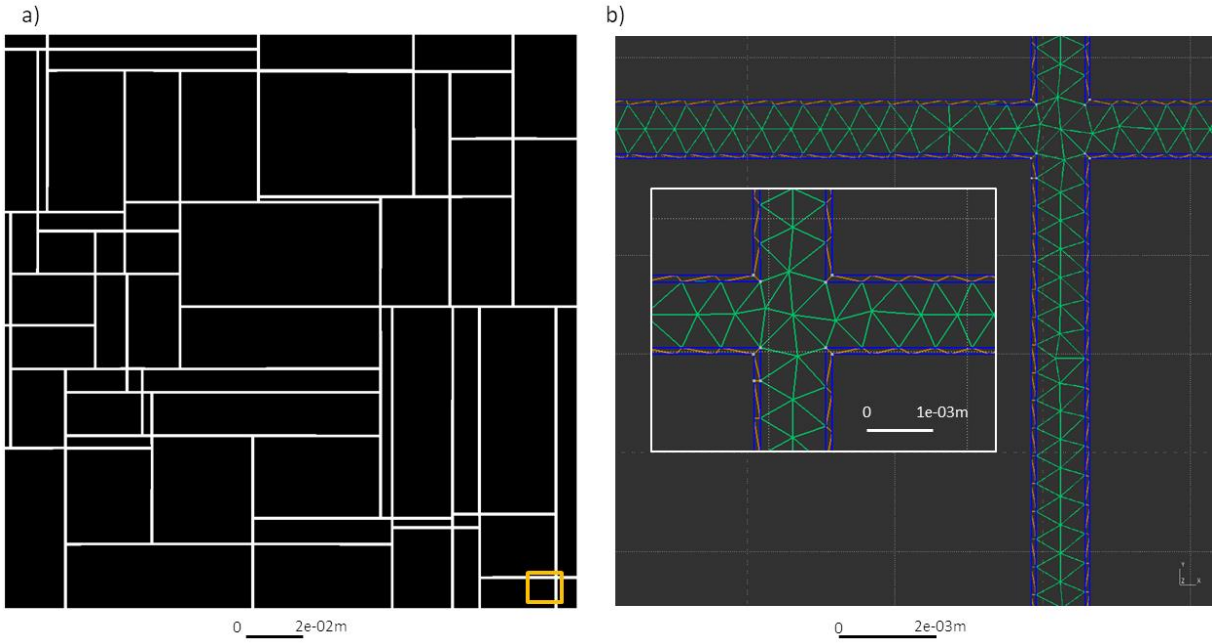

Figure 4 a) Image of the synthetic fracture network. Fractures have a constant aperture equal to 1 mm. The orange box shows the position of the mesh represented in b. Black pixels denote glass matrix, white pixels indicate fractures; b) fragment of the mesh used to run RTM. Cells in green belong to the water geochemical unit, while cells in blue belong to the glass geochemical unit. Total number of cells of the discrete fracture network is 24300. The thickness of the glass film is 0.1 mm. The total length of all walls of the fracture network is 5.93 m.

In accordance with the GRAAL formalism, both water in the fracture zone and glass in the glass zone were represented by liquid media. The glass zone was modeled by a one-mesh thickness layer at the interface with the fracture zone. The glass zone acted as a source of material and had a concentration given by (14):

$$C_v = \frac{\sum M_g}{\sum S * {}^{a}/_{2}}, \quad 14$$

Using the geometrical properties of the fractures, equations (15) and (16) can be modified to yield the two parameters controlling the kinetics of glass dissolution. Depending on the modeled fracture network, these were determined as defined:

$$S_{sp} = \frac{\sum S}{\sum M_g}, \quad 15$$

$$\text{half saturation} = \frac{\lambda D_{PRI} dm_{PRI}}{v_{hyrd}} \times \frac{2}{a} = \frac{\lambda dm_{PRI}}{v_{hyrd}} \times \frac{2}{a} \times D_o [OH^-]^n \exp(-\frac{E_a}{RT}), \quad 16$$

where $a/2$ is the half-aperture of the fracture: only half of the aperture was used to account to the fact that each fracture wall «sees» only half of the solution present in the fracture.

The use of the discrete fracture modeling approach ruled out the necessity of the calculation of the equivalent hydraulic and diffusive parameters. However, it presented a big challenge due to its demand for the fine meshing, and as a consequence, high calculation time.

3.2. Results of the RTM applied to the synthetic case

As a first step, we conducted the RTM applied to the discrete fracture network model and its equivalent porous medium model of the synthetic fracture network to demonstrate the relevance of the techniques used to construct the equivalent continuum model.

The discrete fracture network system consisted primarily of the finely meshed glass fracture and secondly of two reservoirs of dimensions (0.064 m × 0.2 m), connected to both sides of the fracture network (Figure 5a). These two reservoirs were filled with water and interconnected *via* the glass fracture network.

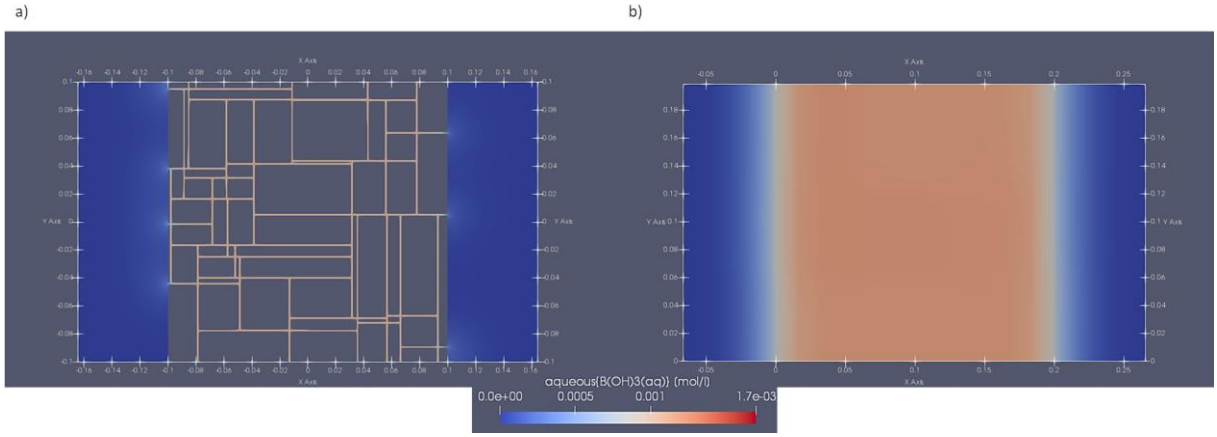

Figure 5 Physical representation of the system comprising two reservoirs and the synthetic facture network in the framework of a) the discrete model and b) the equivalent porous media model. X and Y axes are in m.

Table 3 summarizes the reactive transport input parameters of the discrete fracture network model. Hydraulic conductivity in water was estimated by fluid mechanics modeling from the iterative calculation, taking into account the velocity generated by the temperature differences between two opposite boundaries of the reservoirs separated by three ideal fractures of 1 mm aperture. The glass geochemical unit is represented by a liquid in which all glass is concentrated, and the porosity of this unit is equal to 1. This concentrated glass acts as a source of material readily available at the glass / water interface.

Table 3 Reactive transport parameters used to model the glass aqueous alteration in the synthetic fracture network described explicitly (discrete fracture network approach).

Geochemical unit	Porosity	Pore diffusion coefficient, m2/s	Hydraulic conductivity coefficient at 25°C, m/s	T,°C	C_v, g/l	S_{sp}, m^2/g	Half-saturation, molal
Glass	1	1×10^{-09}	-	90	3.49×10^{-04}	5.73×10^{-09}	3.07×10^{-11}
Water	1	1×10^{-09}	1	90	-	-	-

The equivalent porous medium model was composed of the grids of porosity, equivalent hydraulic conductivity (Figure 6 a–b), equivalent directional diffusion coefficient, and parameters requested to specify the glass dissolution kinetic law, such as equivalent glass concentration, equivalent glass specific surface, and the half-saturation coefficient.

The values of the directional tortuosity were obtained by analyzing the regressions of the directional mean square displacements *vs.* time for each cell of the porous media. The examples of these regressions are illustrated in Figure 7. Subsequently, the tortuosity values were used to calculate the grids of diffusion coefficients shown in Figure 6 c–d.

Figure 8 depicts the results of particle concentration evaluation in the discrete fracture network and in its equivalent porous medium. From the curves of the concentration evolution, it is clear that the particles diffused in a similar manner in both media, and no significant differences were found. A discrepancy in concentration was regularly noticed only in cell (2,2). The results of particle tracking indicated that this cell was visited less frequently when the synthetic fracture network was replaced by its equivalent media. This slight divergence in the obtained concentrations was considered acceptable. Overall, the similarity of the concentration profiles was encouraging and indicated that the proposed approach based on the random walk could be applied for calculating the equivalent diffusion in the fractured zones of the glass block where the fracture density is significant, such as the peripheral parts of glass block fracture networks.

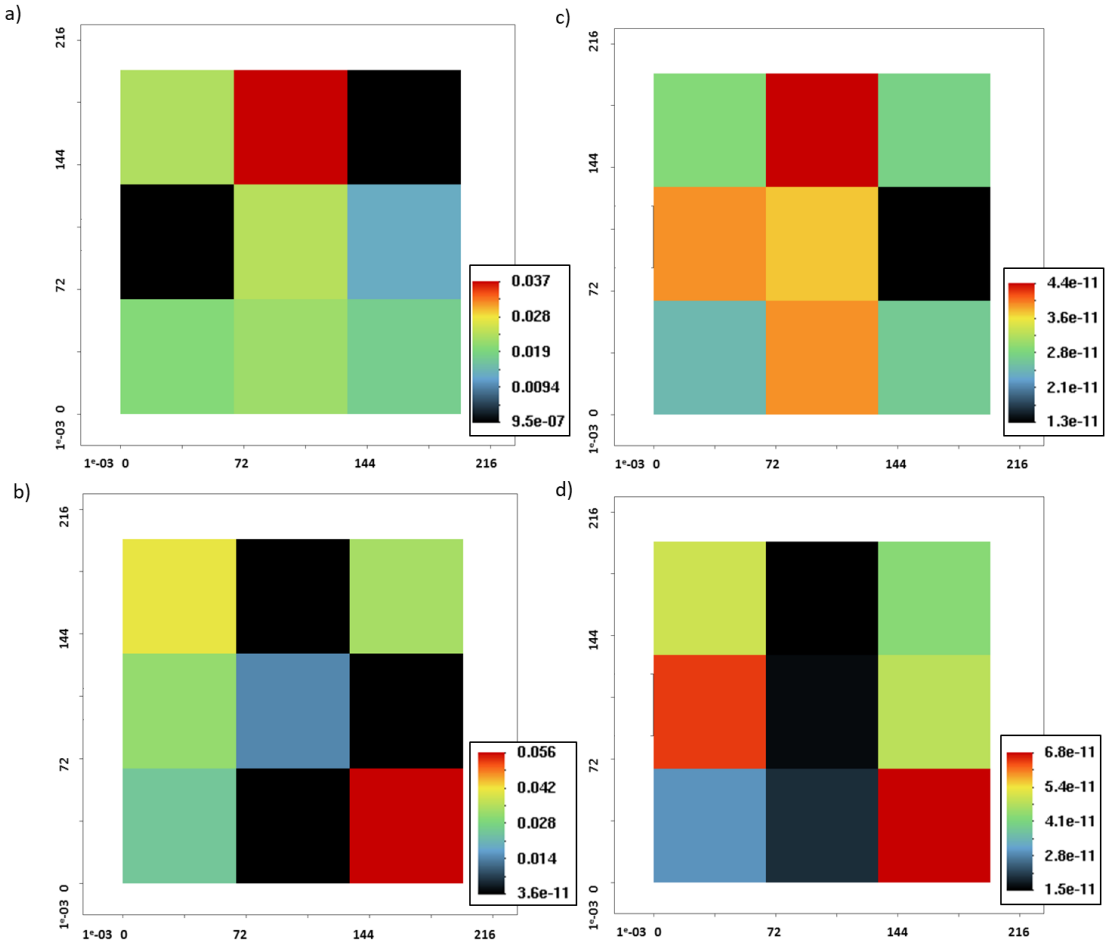

Figure 6 Results of the calculations of the equivalent parameters for the synthetic fracture network. Grids of: a, b) the equivalent directional hydraulic conductivity (m/s) in X and in Y; c, d) the equivalent directional diffusion coefficient (m^2/s) in X and in Y. Both axes are in m.

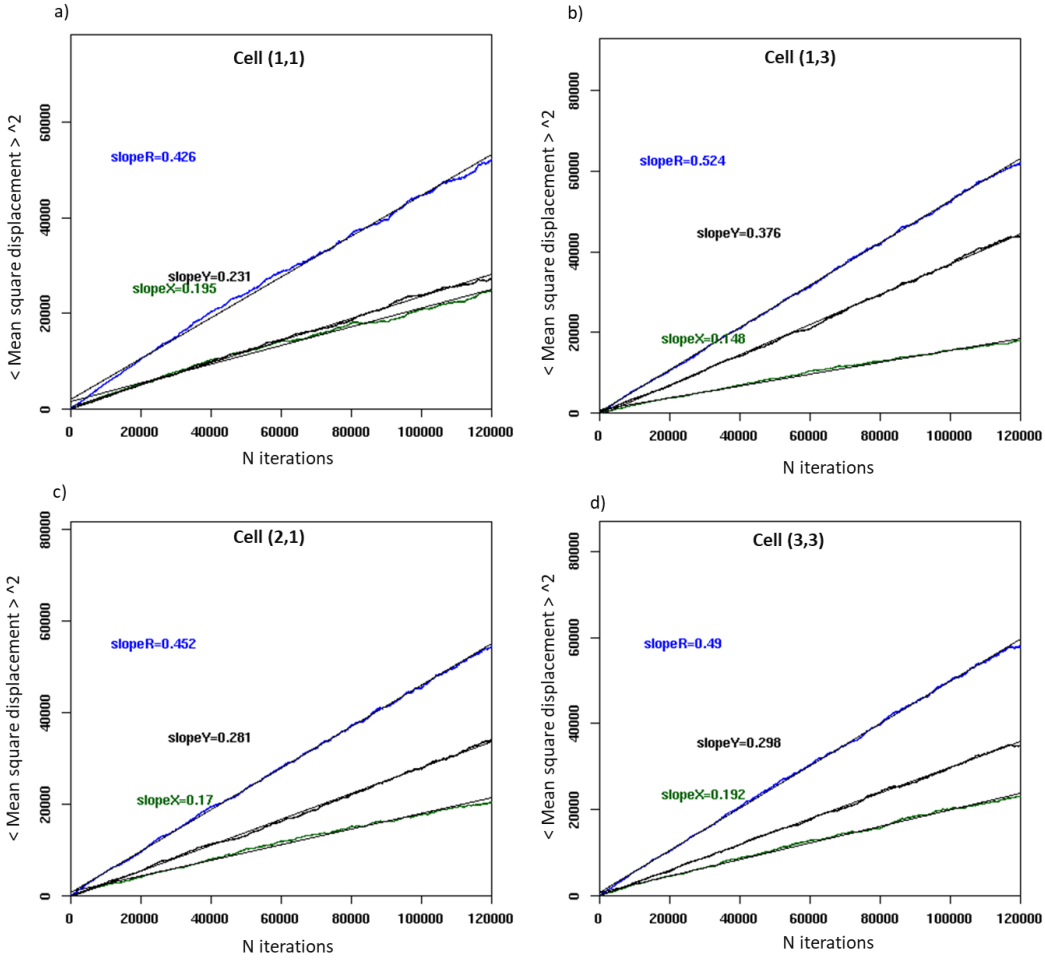

Figure 7 a–e) The mean square displacements ($\langle r^2 \rangle$ - in blue,$\langle x^2 \rangle$ – in green, $\langle y^2 \rangle$ –in black) vs. time of 2000 walkers for the synthetic fracture network. Plots are shown for the cells (1,1), (1,3), (2,1), (3,3) of the output grid presented in Figure 8d.

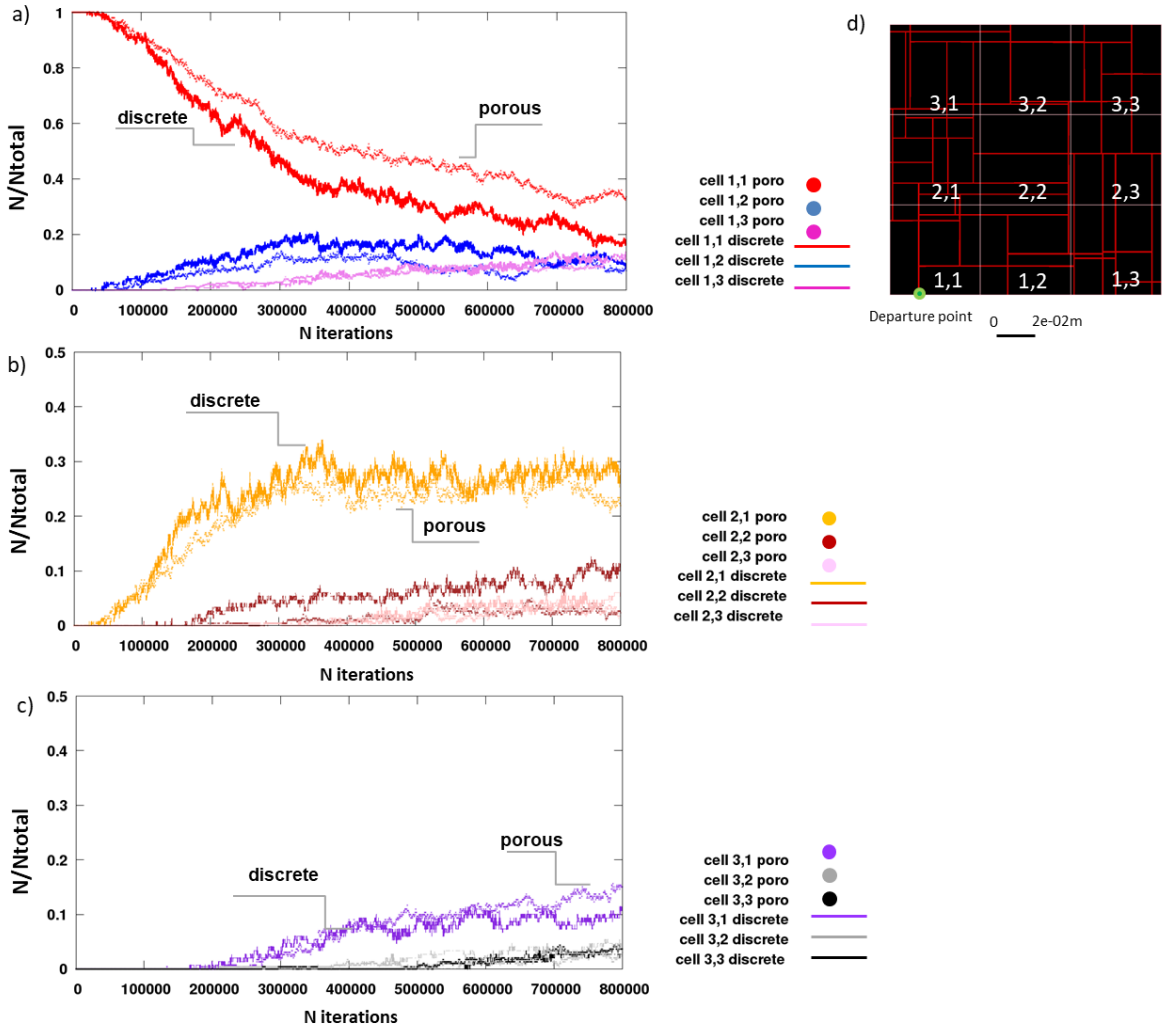

Figure 8 a–c) Evolution of particle concentration in the cells, obtained by tracking 500 independent particles undergoing Brownian motion in the discrete and the equivalent porous media. d) Scheme showing the synthetic discrete fracture network and the positions of the cells used in the legend of the graphics on the left.

Similarly to the discrete fracture network model, two water-bearing zones were added to the left and to the right of the equivalent porous media, such that the same water volume was available for both models in the glass alteration (Figure 5b). These supplementary meshes formed the water geochemical unit and were initialized with the same parameters, namely the diffusion coefficient and the hydraulic conductivity coefficient, as the water geochemical unit of the discrete model (Table 3).

The results of the RTM of ISG aqueous degradation obtained by the discrete and the equivalent continuum approaches are presented in Figure 9. The values of the alteration rate are correctly computed and their evolution can be easily explained in view of the kinetic regimes of the alteration of borosilicate glass reported in (Gin et al. 2012). Specifically, after the initial dissolution rate regime ended around 8 h, a rate drop regime occurred until a residual rate was reached, which is four orders of magnitude lower. The differences of the absolute values of the alteration rate can be explained from the angle of the local chemical effects, *i.e.* saturation in silica was attained faster locally in the case of the discrete model, which leads to the creation of the passivating interface in the middle of cracks and slows down the alteration. In the case of the porous medium model, the alteration progressed more homogeneously. This justification is supported by the results of the modeling when

the kinetics was paralyzed, *i.e.* when the dependence of dissolution rate on pH and saturation was not taken into account. In fact, values of the glass alteration rate found by modeling the alteration at the constant dissolution rate by discrete and equivalent porous models were very close (Figure 14 in Appendix).

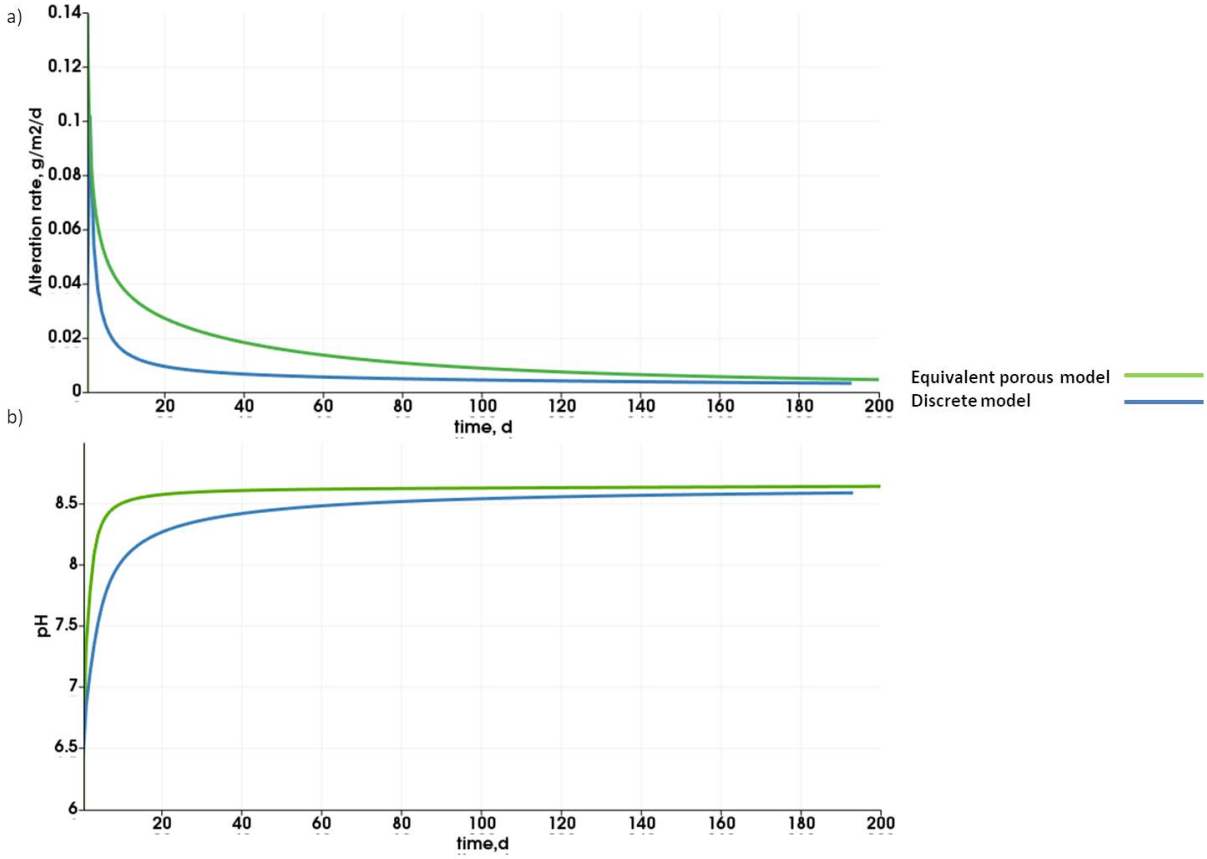

Figure 9 Results of the reactive transport modeling by the discrete fracture approach and by the equivalent continuum approach in the diffusive mode: a) the glass alteration rate obtained from boron concentration averaged over the water zones, b) evolution of the solution pH.

This application was performed to demonstrate the validity of the techniques proposed to compute the equivalent diffusive, hydraulic and alteration kinetics controlling parameters, obtained by comparing the results of the glass aqueous degradation found by the discrete fracture network model and the equivalent porous medium model. Given both the profiles of the alteration rate evolution and the pH evolution, it is evident that the equivalent porous medium model yielded results comparable with those of the discrete fracture network model. This is especially appealing in view of the fact that the rate of the calculation by the equivalent porous medium is much faster. This undoubtedly represents a significant advantage and implies that the model applicable at the industrial glass canister scale, or even under different scenarios of repository evolution. Table 4 presents the values of the time requested to execute simulations of the aqueous alteration applied to the synthetic discrete fracture network and to its equivalent porous media system. The RTM could not be run in convective mode applied to the discrete model of the synthetic case. However, this was realized for the equivalent porous model. The fluid movement in this simulation was generated by the temperature gradient imposed to the left (80 °C) and to the right (90 °C) walls of the water reservoirs. The results of the glass aqueous alteration in convective mode can be found in Figure 15 in the Appendix.

Table 4 Comparison of the time requested to conduct the RTM by the discrete fracture model and the equivalent continuum model. Number of processors was equal to 16 for all modeled cases.

Simulated time, year	Transport	Execution time, d	
		Discrete Fracture Model	Equivalent Continuum Model
1	Diffusion	87	0.22
1	Diffusion+Convection	-	15.1

4. Application

4.1. Application at the scale of the vitrified glass canister in diffusive and convective modes

Although this study focuses on the construction and the application of a 2D model of a nuclear glass fracture network at scale 1, its extension toward a simplified 3D model is feasible. Glass canisters, being perfect cylinders, have a natural axis of symmetry which has been used for the thermo-mechanical simulations at the glass canister scale (Barth 2013). Thus, the use of cylindrical coordinates was opted for in this study (Figure 10a).

The equivalent porous medium models of the training image fracture network and of three realizations of the fracture network equivalent tessellation were used. All models are composed of two geochemical units, the equivalent porous media unit and the water (reservoir) unit. The equivalent porous media unit is described by the map of porosity, equivalent hydraulic conductivity, equivalent directional diffusion coefficient, local direction of anisotropy[34] and parameters defining the glass dissolution kinetic law. Each grid was made up of 4 × 21 meshes, each mesh had dimensions of $5.168 \times 10^{-2} \times 4.964 \times 10^{-2}$ m. The water unit represented a hollow cylinder with a height equal to 1.13244 m and internal and external radii equal to 0.2067 m and 0.2217 m, respectively. The total volume of the water zone was 35 L and reflected the amount of water initially present in contact with the glass canister in the ALISE experiment (Section 1.2). Figure 10 b–c shows the representation of the equivalent porous medium model at the glass canister scale, used to conduct RTM in diffusive and convective modes.

[34] The rotation angle is defined as the angle associated with the largest axis of a fracture and the horizontal plane. The grid of the rotation angle is identical for all modeled cases and was employed to introduce the directional anisotropy of the hydraulic conductivity and the diffusion.

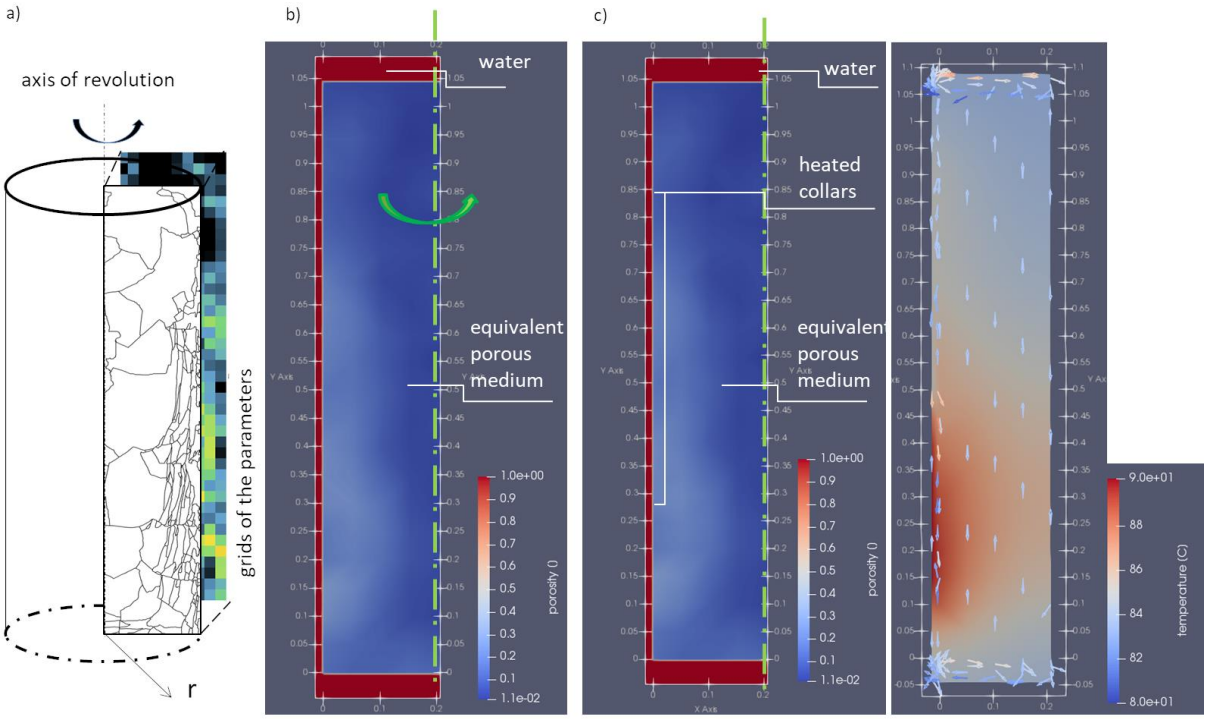

Figure 10 a) Conceptual representation of a simplified 3D model with cylindrical coordinates, b) representation of the equivalent porous medium model used to study the glass aqueous alteration in diffusive mode. The zero flux condition was imposed to the axis of revolution. c) Representation of the equivalent porous medium model used to study the glass aqueous alteration in convective mode. RTM was conducted with consideration of the following limiting conditions: upper heated collar – constant temperature at 80 °C, lower heated collar – constant temperature at 90 °C, axis of revolution – zero flux. X and Y axes are in m.

Results of RTM of the ISG glass aqueous alteration are given in Figure 11 for the diffusive mode and in Figure 12 for coupled diffusive and convective modes. Before proceeding to examine the results of these simulations, it is necessary to look at the interpretation of the experimental data.

4.2. Experimental results from ALISE unit

The results from the ALISE experiment are documented in (Godon et al. 2012; Minet et al. 2013). In total, 106 samples were collected and analyzed by the inductively coupled plasma atomic emission spectroscopy (ICP / AES) technique on the following elements: Si, B, Na, Li, Mo, Al, and by the inductively coupled plasma mass spectrometry (ICP / MS) on Cs. Before each sample collection, the solution was homogenized using closed-loop pumping.

It should be noted that there were some interventions. First, after 1840 d from the beginning of the test, the reactor was opened to estimate the amount of the evaporated solution. Second, after 2030 d, eight liters of a synthetic solution was added to compensate for the cumulated evaporated water. Before mixing, the solution composition was adjusted to minimize the chemical disturbance.

Based on the detailed analysis of the concentration of the boron tracer element, the pH and the glass alteration rate, the study in (Minet et al. 2013) reported five phases of alteration. Phase 1, from 1 to 30 days: the initial phase characterized by a rapid transition from the initial rate regime to the rate drop regime reflected by the sharp increase of the released altered glass per unit time and the quick increase of the pH. Phase 2, from 30 to 500 days: gradual decline of the alteration intensity characterized by progressive decrease of the alteration rate (from ≈0.3 g/d to ≈0.2 g/d) and the slow increase of the pH (from ≈8.9 to ≈9). Phase 3, from 500 to 1400 days: interchange between the

regime of the alteration rate recovery (Fournier et al. 2014) and the regime of the alteration rate drop. Phase 4, from 1400 to 1700 days: recovery of the alteration rate, with an increase of the alteration rate (from ≈0.15 to ≈0.21) and the significant increase of the pH (from ≈9.15 to ≈9.25). The final phase (1700 to 2700 days) involved external interventions, which disturbed the experiment and thus did not allow for a proper interpretation.

4.3. Diffusive mode simulation

The modeling results of the average total dissolved boron concentration in water, the average pH in water, and the glass alteration rate are shown in Figure 11.

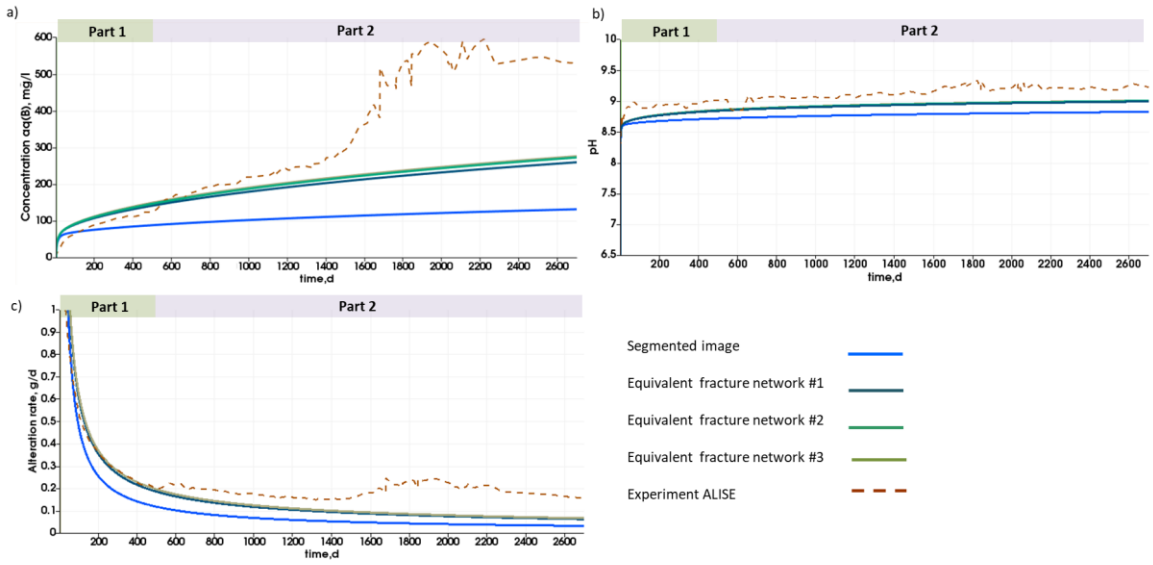

Figure 15 Results of the RTM of the aqueous alteration in the diffusive mode at the scale of the nuclear glass canister: a) average concentration of all aqueous species containing boron present in the solution, b) evolution of the solution pH, and c) overall glass alteration rate obtained by total boron release. Experimental results of the ALISE test are documented in (Minet et al. 2013). It should be noted that the experimental results and the modelling results could be compared only for the first 500 days (part 1 on the figure), because later the ALISE experiment displays phases of (i) the alteration resumption that is not considered in the applied version of the geochemical model and (ii) the impact of the chemical perturbations due to external interventions.

A comparison of these results with experimental data reveals that the first part of the alteration (0–500 d) was correctly reproduced. The simulations in diffusive mode exhibit the same pattern of the alteration regimes transition as the ALISE experiment: a sharp decrease from the initial alteration rate in the first tens of days followed by a period of the gradual alteration rate decline and the stabilization of pH. Moreover, for this first period, the average total dissolved boron concentration for three equivalent fracture networks is close to the experimentally measured boron concentration. However, the results of the RTM applied to the segmented image are less compatible: this less intensive glass alteration is believed to be related to an underestimation of glass fracture surface available for the alteration. Indeed, according to Table 1, internal fracture surface of the segmented image is 2.5 times lower than that of the equivalent tessellations. Unfortunately, the fracture network surface of the ALISE bloc was not determined, such that no comparison with the model is possible.

The second part of the alteration (500–2700 d) was not reproduced by modelling. Indeed, the ALISE experiment displays phases of the alteration resumption from the 500th day, during which the glass is

again significantly altered. This phenomenon was not considered in the GRAAL version that was used, as it is not expected in repository environments. The perturbations of the chemical environment due to maintenance of the apparatus in phase 5 of the experiment are not relevant either.

In summary, the proximity of the results of the RTM applied to the equivalent tessellations with the experimental results enables us to argue that (i) the chosen fracture network equivalent tessellations are representative of the ALISE glass block fracture network, and (ii) the technique proposed to construct glass block equivalent porous model are relevant and could be relied upon.

4.4. Thermo-convective mode simulation

Although there was no fluid movement in the ALISE unit (in absence of a temperature gradient), simulations with thermo-convection were conducted to evaluate the impact of the water convection on the alteration in the fractured nuclear glass blocks. They gave similar overall results (Figure 12), with a fast initial alteration rate and the following rate drop regime to the residual rate. During this time the alteration rate dropped from ~70 g/d (after 12 h) to ~0.065 g/d, and the pH increased from ~8.45 to ~8.94. Figure 13 shows that the initial rate was much higher in the presence of thermo-convection. In fact, once the convection was installed, it stimulated the renewal of water inside the glass fracture equivalent media with fresh water from the outer reservoir. This resulted in the immediate increase of the dissolution rate. Then, when the saturation in silica became high, the reaction affinity diminished, and the rate started to drop. The transition from the initial rate regime to the residual rate regime was shorter for the diffusive case in comparison to the convective case. Although the average total concentration of silica in water was lower in case of pure diffusive transport, the effect of local arrivals on silica saturation was more important.

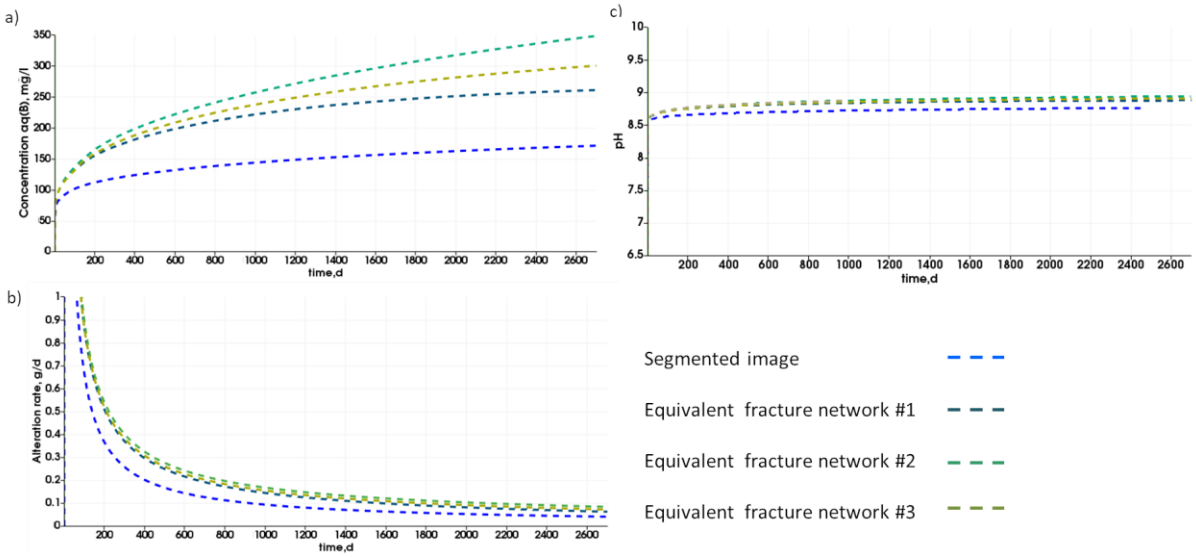

Figure 12 Results of the RTM of the aqueous alteration at the scale of the nuclear glass canister: a) average concentration of all aqueous species containing boron present in the solution, b) evolution of the solution pH, and c) overall glass alteration rate obtained from total boron release. Both diffusion and thermo-convection caused by the imposed temperature difference were considered.

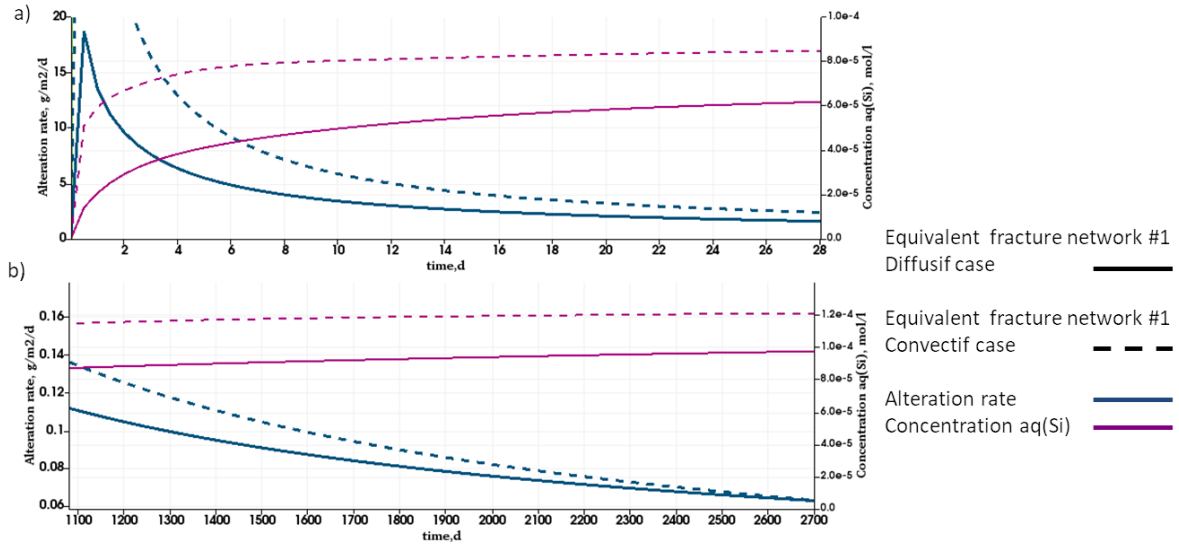

Figure 13 Evolution of the average total concentration of silica present in water and the alteration rate: a) in the short-term and b) in the long-term.

5. Discussion

Regarding the project feasibility study, it is important to consider several scenarios in the geological repository evolution. That is why it is essential to compare the results of the borosilicate glass alteration obtained in diffusive and convective modes. In this study, we do not aim at reproducing a scenario of repository conditions, where the fluid movement would potentially result from the heat release due to radioactivity. Nevertheless, the results of the modeling presented in this paper provide a preliminary idea about the impact of water flow on the intensity of the glass alteration at the scale of one canister.

According to the results presented in Figures 11–13, glass degradation was favored by water convection. Twelve hours from the start of the alteration, the glass alteration rate was four times higher compared to the no-flow case. The effect was, however, less significant once the solution became saturated in alteration products. Indeed, for the fracture tessellation #1, as an example, the glass altered rate in the convective flow conditions at the 20th day of alteration made up only 4.8% of the initial rate and was 1.54 times higher than the alteration rate in the pure diffusive movement conditions. However, it is important to mention that the gradient imposed in the presented case was significant (5 °C) and does not reflect the situation in repository conditions.

In future studies, it would be interesting to conduct reactive transport modeling in conditions that are more representative of the repository. Heat sources could be specified according to specific scenarios: time of water intrusion, spacing between canisters, and heat exchange with the host rock. The methodology developed in this paper could then be extended to 3D simulations. Application to industrial purposes would require further research to understand and quantify the phenomena that would govern (i) the alteration of the borosilicate glass in presence of all the components of the nearby field (*e.g.* iron of the overpack, clay of the COx), (ii) the transport of the alteration products with the COx water in the conditions of the argillite pores clogging, and (iii) the mechanisms of glass alteration and solutes migration in presence of hydrogen originated from radiolysis and corrosion of the overpacks.

According to multiple studies (Carrière 2017; Neill et al. 2017; de Combarieu 2007; Rébiscoul 2013; Arena 2016), in presence of iron, glass alteration is fostered by the precipitation of iron silicate species. The formation of these secondary phases modifies the chemical equilibrium in the aqueous solution, acting as a “silicon pump” and, as a consequence, increases glass alteration. Regarding the interactions with the COx water, studies (Jollivet et al. 2012; Aréna et al. 2017; Debure et al. 2012) show that the pH of the water of the repository site and the availability of magnesium in solution can affect the transient regime, where dissolution rate drops rapidly and the residual rate. In fact, magnesium secondary phases could maintain glass alteration by consuming silicon. Nevertheless, in absence of a renewal of magnesium or in the case of decrease of the pH, the expected residual rate was reported close to that measured in pure water (ANDRA-Collectif 2016; Jollivet et al. 2012).

In accordance with the current vision of the high-level vitrified waste alteration model presented by ANDRA (ANDRA-Collectif 2016), the first phase of glass alteration would take place in unsaturated conditions resulting from partial re-saturation of the vicinity of the cell and the counter-effect of hydrogen release due to radiolysis and anoxic corrosion of metallic components, which could last from several thousand to tens of thousands of years. In consideration of the possibility of a high relative humidity in the storage conditions, studies aiming at the understanding of the mechanisms of glass alteration in the vapor phase have been initiated. From the experimental results conducted so far, it can be understood that the reactions occurring between glass and water are the same for alteration in aqueous medium and unsaturated water vapor. However, the rate controlling reaction mechanism and the driving force for alteration are different in both cases (Abrajano et al. 1989). The difference arises largely from the changes in water chemistry, as a result of the extremely small volume of water available for reaction in the unsaturated case. The various results from vapor hydration experiments suggest that the alteration in vapor phase is not simply an extreme case of glass alteration in aqueous medium at a very high S/V (Abrajano et al. 1986). The precipitation of

secondary phases seems to be the strongest driving force for alteration in vapor phase at high temperature and low solution volume.

Moreover, presently there is no clear vision on the possibility of the gas to coexist with the water. In fact, it is necessary to understand in further detail how the repository re-saturation will happen. Although, according to ANDRA (ANDRA 2013), hydrogen presence will not imply significant overpressure in water, it is still uncertain how the re-saturation will occur precisely in different compartments of the repository, what will be the relative permeability of the hosting rock and the infilling materials of the repository, and how the transport of the solutes in the biphasic condition will differ from that in the saturated condition.

In general, our model can be evolved to take into account the above-cited phenomena. Certainly, in case of the presence of both gas and water phases inside the fracture network of vitrified canisters, it will be mandatory to change the techniques of the permeability and effective diffusion calculation (Savoye et al. 2010; Savoye et al. 2014), and take into the account saturation of both wetting (water) and non-wetting (gas) phases, as well as the capillary pressure (Mualem 1976). Moreover, in the future, the geochemical part of the model should be enhanced, such that the interactions of the elements of the nearby field could be accounted for. This will require an upgrade of the geochemical model and could also require accounting for the change of fracture aperture, since the hypothesis of isovolumetricity would not be valid anymore. Moreover, the temporal porosity change related to the swelling of argillites minerals (Bock 2010; Trotignon et al. 2007) would be probably worth considering when estimating the temporal evolution of the hydraulic/diffusive properties of glass canister fracture network.

Another possible evolution of the upscaling is towards a hybrid model. Indeed, the glass canister fracture network exhibits strong non-stationarity: large sparse fractures in the center, opposed to fine, dense fractures close to the periphery. A hybrid model could be devised, with explicit fractures at the core of the canister and equivalent medium on the finely fractured peripheral area. This change of the modeling approach should be considered with regard to the calculation capabilities of the applied reactive transport code. This is because, at the present time, it is hardly possible to run this type of model at the scale of the glass canister, especially when the convection, originated by temperature gradient, is taken into account.

6. Conclusions

Coupled chemistry-transport models must be used to quantitatively assess the corrosion of the vitrified fractured glass containing long-lived high-level nuclear waste. Having been restricted to laboratory examinations for a long time, the present study gives an example of how such models can be used for geometries (2D and simplified 3D) and time scales (100 000 y) relevant for performance assessment. Given the difficulty of performing reactive transport modeling applied directly to the discrete representation of the glass fracture network at the scale of glass canister, we focused here on the construction of its equivalent porous model. Special attention was paid to the calculation of the reactive transport parameters such as porosity, tortuosity, diffusion coefficient, hydraulic conductivity, and glass alteration kinetic parameters. First, the validation of the applicability of the proposed techniques was accomplished by conducting reactive transport modeling applied to a synthetic two-dimensional fracture network in the scope of the discrete model and the equivalent

porous model. Second, the equivalent porous model was applied to four representations of the glass fracture network. The reactive transport modeling was performed in cylindrical coordinates in diffusive and convective modes. The results of the quantity of altered glass were then compared with experimental results obtained of the long-term aqueous alteration test of a non-radioactive full-scale nuclear glass block. Reasons were provided to explain the minor differences. Although the reproduction of one particular scenario in the conditions of the repository was not the objective of this study, the presented results gave a preliminary indication of the impact of thermo-convection on the glass alteration at the scale of one canister and demonstrated the feasibility of the glass corrosion reactive transport modeling under different scenarios of repository evolution.

The presented model focused on glass-water interaction in conditions that do not correspond to the repository conditions. Nevertheless, the model could be extended or re-adapted such that different scenarios of canister evolution might be considered. The strength of this work, started in (Repina et al. 2018), is within the proposal of a complex workflow and data integration process that allows the estimation of the impact of fracturing on the glass corrosion, by taking account fracture network variability and different limiting conditions.

Acknowledgements

The authors wish to thank P. Frugier (CEA Marcoule) and T. Le Borgne (Rennes-1 University) for fruitful discussions.

Research data availability

The raw/processed data required to reproduce these findings cannot be shared at this time as the data also forms part of an ongoing study. The data that support the findings of this study will be available at a later day from the corresponding author, Frederic Bouyer, upon request.

References

Repina M., Renard D., Bouyer F., Lagneau F. 2018. 'Coupling image analysis and thermo-mechanical simulation results to produce a model of the fracture network in a nuclear glass canister', accepted in the *Journal of Nuclear Materials*.

Abrajano, T., J. K. Bates, and C.D. Byers. 1986. 'Aqueous corrosion of natural and nuclear waste glasses I. Comparative rates of hydration in liquid and vapor environments at elevated temperatures', *Journal of Non Crystalline Solids*, 84: 251-57.

Abrajano, T.A., Jr., J.K. Bates, and J.J. Mazer. 1989. 'Aqueous corrosion of natural and nuclear waste glasses. II. Mechanisms of vapor hydration of nuclear waste glasses', *Journal of Non-Crystalline Solids*, 108: 269-88.

ANDRA-Collectif. 2016. "Dossier d'options de sûreté - Partie après fermeture (DOS-AF)." In, 1-467. ANDRA.

ANDRA. 2005. "Dossier 2005 Argile - Tome Évolution Phénoménologique du Stockage Géologique." In, edited by ANDRA, 1-523.

———. 2013. 'Projet Cigéo : Revues techniques de préparation à la Demande d'Autorisation de Création (DAC) Revue Finale des Modèles et des Données - première partie (RFMD-1) : Bilan des connaissances phénoménologiques et incertitudes résiduel'.

———. 2016. 'Rapport Andra CG-TE-D-NTE-AMOA-SR1-0000-15-0060 – « Dossier d'options de sûreté - Partie exploitation »'.

Aréna, H., N. Godon, D. Rébiscoul, P. Frugier, and R. Podor, Garcès, E., Cabie, M., Mestre, J. P. 2017. 'Impact of iron and magnesium on glass alteration: Characterization of the secondary phases and determination of their solubility constants', *Applied Geochemistry*, 82: 119-33.

Arena, Helene. 2016. *Effets cumulatifs et compétitifs des éléments chimiques sur l'altération des verres nucléaires*.

Barth, Nicolas. 2013. 'Sur la modélisation et la simulation du comportement mécanique endommageable de verres borosilicatés sous sollicitation thermique', Université de Strasbourg.

Begg, S., R. R. Carter, and P. Dranfield. 1989. *Assigning effective values to simulator grid-block parameters*.

Bock, Helmut et al. 2010. 'Self-sealing of Fractures in Argillaceous Formations in the Context of Geological Disposal of Radioactive Waste'.

Carrière, C. 2017. 'Influence de la corrosion du fer sur les processus d'altération du verre : approche analytique multi-échelle.', Université Pierre et Marie Curie - Paris VI.

Christie, M. A. 1996. 'Upscaling for Reservoir Simulation', *Journal of Petroleum Technology*, 48: 1004-10.

Crevoisier, D., F. Bouyer, and S. Gin. 2011. 'Semi-stochastic generator (FRAGMA) of 2D fractured media by mechanistic analogy. Application to reactive transport in a fractured package of vitrified nuclear waste', *Computational Materials Science*, 50: 1387-98.

Cushman, John H., Lynn S. Bennethum, and Bill X. Hu. 2002. 'A primer on upscaling tools for porous media', *Advances in Water Resources*, 25: 1043-67.

Cvetkovic, Vladimir, S. Painter, N. Outters, and J. O. Selroos. 2004. 'Stochastic simulation of radionuclide migration in discretely fractured rock near the Aspo Hard Rock Laboratory', *Water Resources Research*, 40: W02404.

de Combarieu, G. 2007. 'Altération du verre de confinement de déchets type R7T7 en condition de stockage géologique.', Université Paris XI - UFR Scientifique d'Orsay.

de Marsily, G. 1986. 'Quantitative Hadrogeology: Groundwater Hydrology for Engineers'.

Debure, M., P. Frugier, L. De Windt, and S. Gin. 2012. 'Borosilicate glass alteration driven by magnesium carbonates', *Journal of Nuclear Materials*, 420: 347-61.

Deng, H. 2009. 'Upscaling Reactive Transport Parameters for Porous and Fractured Porous Media', *Dissertation*.

Durlofsky, Louis J. 1991. 'Numerical calculation of equivalent grid block permeability tensors for heterogeneous porous media', *Water Resources Research*, 27: 699-708.

Einstein. A., Fürth. R. 1956. 'Investigations on the theory of Brownian movement'.

Fernàndez-Garcia, Daniel, Tissa H. Illangasekare, and Harihar Rajaram. 2005. 'Differences in the scale dependence of dispersivity and retardation factors estimated from forced-gradient and uniform flow tracer tests in three-dimensional physically and chemically heterogeneous porous media', *Water Resources Research*, 41.

Fournier, M., S. Gin, and P. Frugier. 2014. 'Resumption of nuclear glass alteration: State of the art', *Journal of Nuclear Materials*, 448: 348-63.

Frugier, P., T. Chave, S. Gin, and J.E. Lartigue. 2009. 'Application of the GRAAL Model to Leaching Experiments with SON68 Nuclear Glass in Initially Pure Water', *Journal of Nuclear Materials*, 392: 552-67.

Frugier, P., Gin, S., Minet, Y., Chave, T., Bonin, B., Godon, N.,Lartigue, J.E., Jollivet, P., Ayral, A., De Windt, L., Santarini, G. 2008. 'SON68 Nuclear glass dissolution kinetics: Current state of knowledge and basis of the new GRAAL model', *Journal of Nuclear Materials*, 380: 8-21.

Frugier, Pierre, Yves Minet, Natarajan Rajmohan, Nicole Godon, and Stéphane Gin. 2018. 'Modeling glass corrosion with GRAAL', *npj Materials Degradation*, 2: 35.

Geuzaine, Christophe, and Jean Francois Remacle. 2009. 'Gmsh: A 3-D finite element mesh generator with built-in pre- and post-processing facilities', *International Journal for Numerical Methods in Engineering*, 79: 1309-31.

Gin, S., Abdelouas, A., Criscenti, L.J., Ebert, W.L., Ferrand, K., Geisler, T., Harrison, M.T., Inagaki, Y., Mitsui, S., Mueller, K.T., Marra, J.C., Pantano, C.G., Pierce, E.M., Ryan, J.V., Schofield, J.M., Steefel, C.I., Vienna, J.D. 2013. 'An international initiative on long-term behavior of high-level nuclear waste glass', *Materials Today*, 16: 243-48.

Gin, S., X. Beaudoux, F. Angeli, C. Jegou, and N. Godon. 2012. 'Effect of composition on the short-term and long-term dissolution rates of ten glasses of increasing complexity from 3 to 30 oxides', *Journal of Non-Crystalline Solids*, 358: 2559-70.

Godon, N., S. Peuget, F. Bouyer, F. Angeli, S. Depierre, O. Pinet, M. Tribet, B. Boizot, J.M. Delaye, J.L. Dussossoy, N. Ollier, S. Gin, C. Jégou, and Ribet I. 2012. "Référentiel scientifique sur le comportement à long terme des déchets vitrifiés : résultats de la R&D menée en collaboration avec les producteurs de déchets." In, edited by CEA, 1-425.

Gouze, Philippe, and Linda Luquot. 2011. 'X-ray microtomography characterization of porosity, permeability and reactive surface changes during dissolution', *Journal of Contaminant Hydrology*, 120-121: 45-55.

Hornung, Ulrich (ed.)^(eds.). 1997. *Homogenization and porous media* (Springer-Verlag).

Jollivet, P, P. Frugier, G. Parisot, J.-P. Mestre, E. Brackx, S. Gin, and S. schumacher. 2012. 'Effect of clayey groundwater on the dissolution rate of the simulated nuclear waste glass SON68', *Journal of Nuclear Materials*, 420: 508-18.

King, P. R. 1989. 'Transp Porous Med', *Kluwer Academic Publishers*.

Lagneau, V. 2013. 'Simulation of coupled geochemical reactions and hydynamical processes in porous media -- application to CO2 storage and Uranium exploitation', Université Pierre et Marie Curie - Paris VI.

Lagneau, Vincent, and Jan van der Lee. 2010. *Operator-splitting-based reactive transport models in strong feedback of porosity change: The contribution of analytical solutions for accuracy validation and estimator improvement*.

Minet, Y., B. Bonin, S. Gin, and P. Frugier. 2010. 'Analytic implementation of the GRAAL model: Application to a R7T7-type glass package in a geological disposal environment', *Journal of Nuclear Materials*, 404: 178-202.

Minet, Y., JL. Chouchan, and JP. Mestre. 2013. "Altération du bloc SON68 01FID07/2 dans Alise à 106°C: résultats de l'essai longue durée (7,5 ans) et observations post mortem." In, edited by CEA, 1-67.

Mitra, Partha P., Pabitra N. Sen, and Lawrence M. Schwartz. 1993. 'Short-time behavior of the diffusion coefficient as a geometrical probe of porous media', *Physical Review B*, 47: 8565-74.

Mualem, Yechezkel. 1976. 'A new model for predicting the hydraulic conductivity of unsaturated porous media', *Water Resources Research*, 12: 513-22.

Nakashima, Yoshito, Tsukasa Nakano, Koichi Nakamura, Kentaro Uesugi, Akira Tsuchiyama, and Susumu Ikeda. 2004. 'Three-dimensional diffusion of non-sorbing species in porous sandstone: computer simulation based on X-ray microtomography using synchrotron radiation', *Journal of Contaminant Hydrology*, 74: 253-64.

Neill, Lindsey, Stéphane Gin, Thomas Ducasse, Trilce De Echave, Maxime Fournier, Patrick Jollivet, Alkiviadis Gourgiotis, and Nathalie A. Wall. 2017. 'Various effects of magnetite on international simple glass (ISG) dissolution: implications for the long-term durability of nuclear glasses', *npj Materials Degradation*, 1: 1.

Neuman, Shlomo P. 1990. 'Universal scaling of hydraulic conductivities and dispersivities in geologic media', *Water Resources Research*, 26: 1749-58.

Noetinger, B. 1994. 'The effective permeability of a heterogeneous porous media', *Transp. Porous Media*: 99-127.

Nœtinger, B., and T. Estebenet. 2000. 'Up-Scaling of Double Porosity Fractured Media Using Continuous-Time Random Walks Methods', *Transport in Porous Media*, 39: 315-37.

Noetinger, B., Roubinet, D., Russian, A. et al. 2016. 'Random Walk Methods for Modeling Hydrodynamic Transport in Porous and Fractured Media from Pore to Reservoir Scale', *Transp Porous Med*.

Nos, Jeremy, Vincent Lagneau, and Valérie Langlais. 2011. *Reactive transport upscaling at the Darcy scale: A new flow rate based approach raises the unsolved issue of porosity upscaling*.

Nykyri, M., H. Nordman, J. Loefman, A. Poteri, N. Marcos, and A. Hautojorvi. 2008. "Radionuclide release and transport RNT-2008." In, 164. Finland.

Ougier-Simonin, Audrey. 2010. 'Propriétés mécaniques et de transport des verres fissurés', Université Denis Diderot - Paris 7.

Pierce, Eric M., Pierre Frugier, Louise J. Criscenti, Kideok D. Kwon, and Sebastien N. Kerisit. 2014. 'Modeling Interfacial Glass-Water Reactions: Recent Advances and Current Limitations', *International Journal of Applied Glass Science*, 5: 421-35.

Promentilla, M. A. B., T. Sugiyama, T. Hitomi, and N. Takeda. 2009. 'Quantification of tortuosity in hardened cement pastes using synchrotron-based X-ray computed microtomography', *Cement and Concrete Research*, 39: 548-57.

Rébiscoul, Diane, Burger, Emilien, Bruguier, Florence, Godon, Nicole, Chouchan, Jean-Louis, Mestre, Jean-Pierre, Frugier, Pierre, Lartigue, Jean-Eric, Gin, Stephane. 2013. 'Glass-Iron-Clay interactions in a radioactive waste geological disposal: a multiscale approach', *MRS Proceedings*, 1518: 185-90.

Renard, P. 1997a. 'Modélisation des écoulements en milieux poreux hétérogènes', Paris Mines.

Renard P., de Marsily G. . 1997. 'Calculating equivalent permeability: a review', *Advances in Water Resources*, 20: 253-78.

Renard, P., de Marsily, G. 1997b. 'Calculating equivalent permeability: a review', *Advances in Water Resources*, 20: 253-78.

Renard, P., G. Le Loc'h, E. Ledoux, G. Marsily, and R. Mackay. 2000. 'A fast algorithm for the estimation of the equivalent hydraulic conductivity of heterogeneous media', *Water Resources Research*, 36: 3567-80.

Savoye, S., C. Imbert, A. Fayette, and D. Coelho. 2014. 'Experimental study on diffusion of tritiated water and anions under variable water-saturation and clay mineral content: comparison with the Callovo-Oxfordian claystones', *Geological Society, London, Special Publications*, 400: 579-88.

Savoye, S., J. Page, C. Puente, C. Imbert, and D. Coelho. 2010. 'New experimental approach for studying diffusion through an intact and unsaturated medium: a case study with Callovo-Oxfordian argillite', *Environ Sci Technol*, 44: 3698-704.

Sen, P. 2004. 'Time‐dependent diffusion coefficient as a probe of geometry', *Concepts in Magnetic Resonance Part A*, 23A: 1-21.

Trotignon, L., V. Devallois, H. Peycelon, C. Tiffreau, and Xavier Bourbon. 2007. *Predicting the long term durability of concrete engineered barriers in a geological repository for radioactive waste*.

van der Lee, J. 1998. "Thermodynamic and mathematical concepts of CHESS." In, edited by Ecole des Mines de Paris and Fontainebleau.

Van der Lee, Jan, Laurent De Windt, Vincent Lagneau, and Patrick Goblet. 2003. 'Module-oriented modeling of reactive transport with HYTEC', *Computers & Geosciences*, 29: 265-75.

Whitaker, Stephen. 1967. 'Diffusion and dispersion in porous media', *AIChE Journal*, 13: 420-27.

Wood, Brian D., Fabien Cherblanc, Michel Quintard, and Stephen Whitaker. 2003. 'Volume averaging for determining the effective dispersion tensor: Closure using periodic unit cells and comparison with ensemble averaging', *Water Resources Research*, 39.

Zhang, Chun-Liang. 2018. 'Thermo-hydro-mechanical behavior of clay rock for deep geological disposal of high-level radioactive waste', *Journal of Rock Mechanics and Geotechnical Engineering*.

Zhou, Quanlin; Liu, Hui Hai; Molz, Fred J. et al. 2008. 'Field-Scale Effective Matrix Diffusion Coefficient for Fractured Rock: Results From Literature Survey'.

Appendix

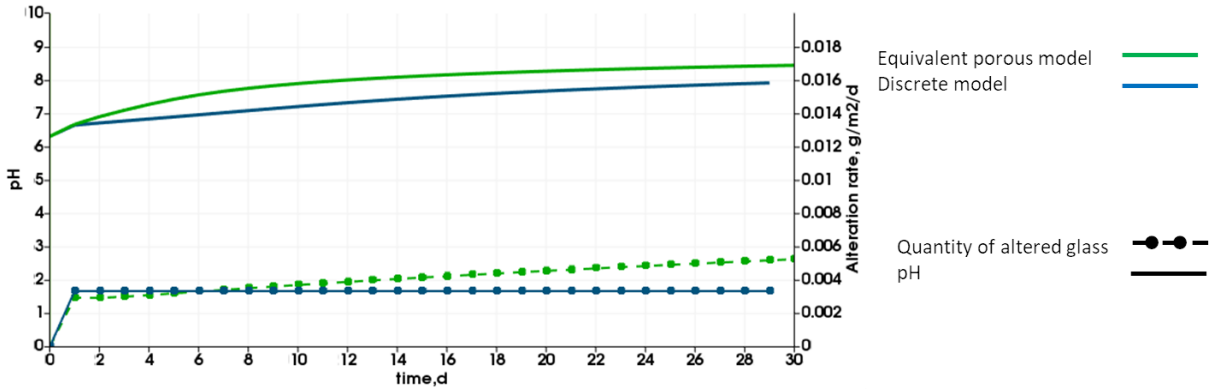

Figure 14 Results of the reactive transport modeling in the case where the impact of the pH and of the affinity term on the glass dissolution rate were not considered: quantity of altered glass obtained from boron concentration averaged over the water zones and evolution of the solution pH.

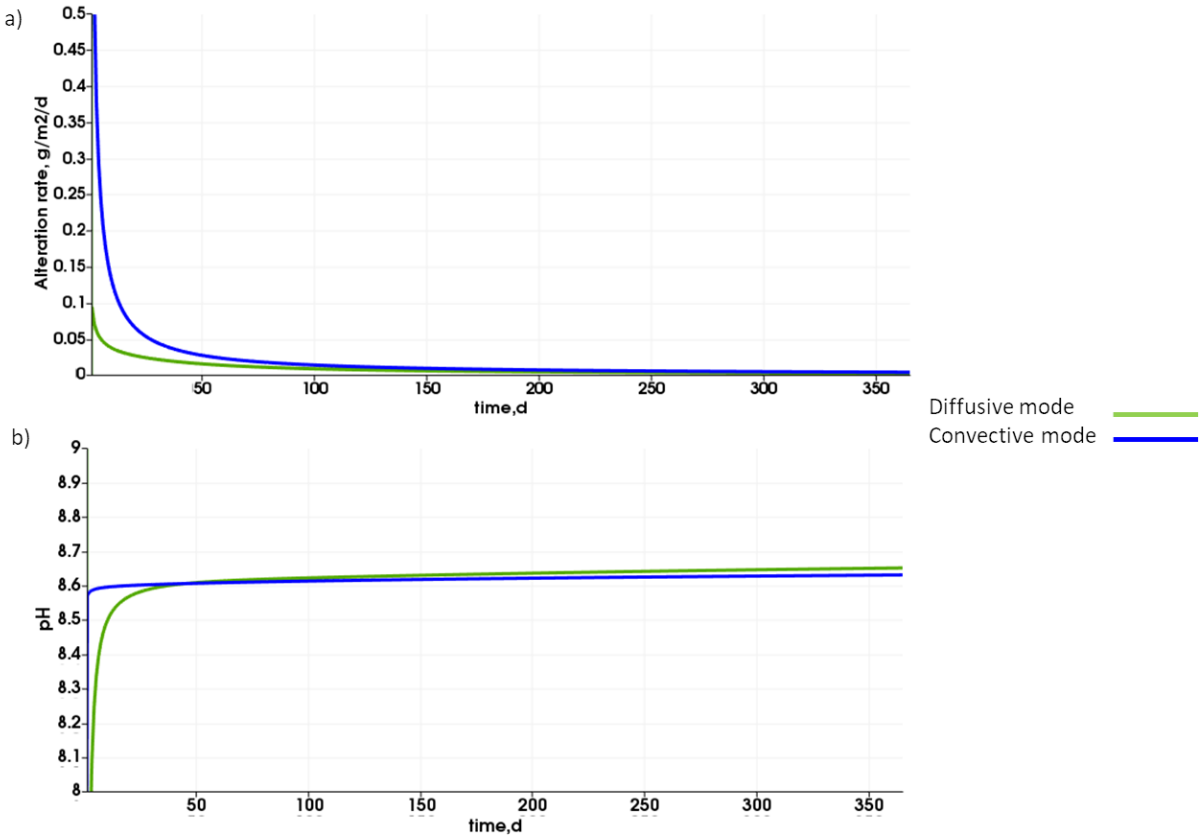

Figure 15 Results of the reactive transport modeling by the equivalent continuum approach in diffusive and convective modes: a) quantity of altered glass obtained from boron concentration averaged over the water zones, b) evolution of the solution pH.

5. From block image analysis to reactive transport modeling (*continued*)

5.5. Reactive transport modeling at the scale of the vitrified glass canister in conditions close to repository conditions

The goal of this section is to present the results of the RTM of the glass aqueous alteration of one glass canister in conditions closer to what could occur in underground geological repository.

As mentioned earlier, in glass packages in repository conditions, convection would result from the heat source due to radioactive decay. The heat would diffuse, giving rise to a temperature gradient within a package. Differences in water density and resulting gravity instabilities would lead to the formation of rolls, named Rayleigh-Bénard cells.

We did not expect to capture fully the impact of the thermo-convective movement on the glass alteration by applying our vertical 2D-radial model: indeed, current concepts favor horizontal deposition of the canisters along the storage cells. Nevertheless, the results of the presented below cases provide interesting insights on the impact of the heat release on the glass corrosion at 1,000; 5,000 and 10,000 y. That means that we make the hypothesis that the corrosion of the canister happens 1,000; 5,000 or 10,000 y after its disposal in the HA cell.

As before, the system was composed of two parts: free water around the canister and the equivalent porous medium model of one realization of fracture network equivalent tessellation for the glass canister itself. The equivalent porous medium unit was comprised of the grids of porosity, equivalent hydraulic conductivity, equivalent directional diffusion coefficient, rotation angle and parameters specified in the glass dissolution kinetic law. Each grid was made up of 21 × 8 meshes, the total size being 1.04244 × 0.41344 m. In comparison with the previous cases, the block position was horizontal, as expected in Cigéo. The water unit surrounded the equivalent porous medium and had dimensions 2.9624 × 0.45344 m. These dimentions were chosen with respect first, to a HL canister size (0.6 m in diameter, 1.6 m in height (ANDRA 2016)), and second, to the considered configuration of a waste cell: wastes packages would be separated by free space to account for the heat diffusion constraint in the host rock. By chosing the water unit length equal to 2.9624 m, we supposed that free space still exist in the cell at the time of corrosion of the canister (1,000 or 5,000 or 10,000 y).

Figure 5-3 shows the equivalent porous medium model representation, used to conduct RTM in conditions resembling the repository conditions.

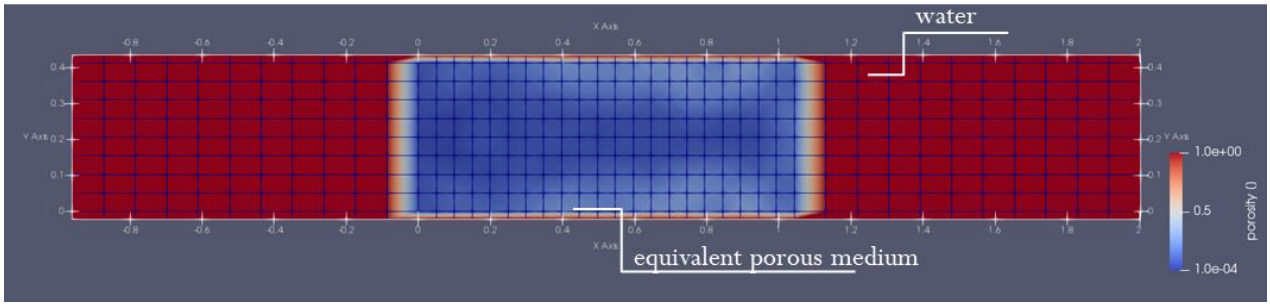

Figure 5-3 Representation of the equivalent porous medium model used to study the glass aqueous alteration in thermo-convective mode with term source.

Initial and limiting conditions, such as initial temperature in water and equivalent porous medium units, temperature at the boundaries of the water unit and the thermal power density of package used in the calculations are displayed in Table 5-1. They were obtained from (Bouyer 2017, internal CEA communication), (ANDRA-Collectif 2016; Godon 2004), presented in Section 2.3.2. The assumption of equality of temperature at the boundaries of the overpack and at the water unit boundaries was made.

Table 5-1 Initial and limiting conditions used for RTM

Name of the case	«Convective 1,000»	«Diffusive 1,000»	«Convective 5,000»	«Diffusive 5,000»	«Convective 10,000»	«Diffusive 10,000»
Initial temperature in water / equivalent porous medium units, °C	51	51	33	33	29	29
Temperature fixed at the boundaries of the water unit, °C	51	-	33	-	29	-
Thermal power density set in cells of equivalent porous medium model, W×m^{-3}	173	-	96	-	0.266	-
Flow condition at the boundaries of the water unit	No flow	No flow	No flow	No flow	No flow	No flow
Transport condition at the boundaries of the water unit	Zero gradient	Zero gradient	Zero gradient	Zero gradient	Zero gradient	Zero gradient

The results of the RTM of the ISG aqueous alteration in thermo-convective and diffusive modes applied to one realization of fracture network equivalent tessellation are demonstrated in Figure 5-4.

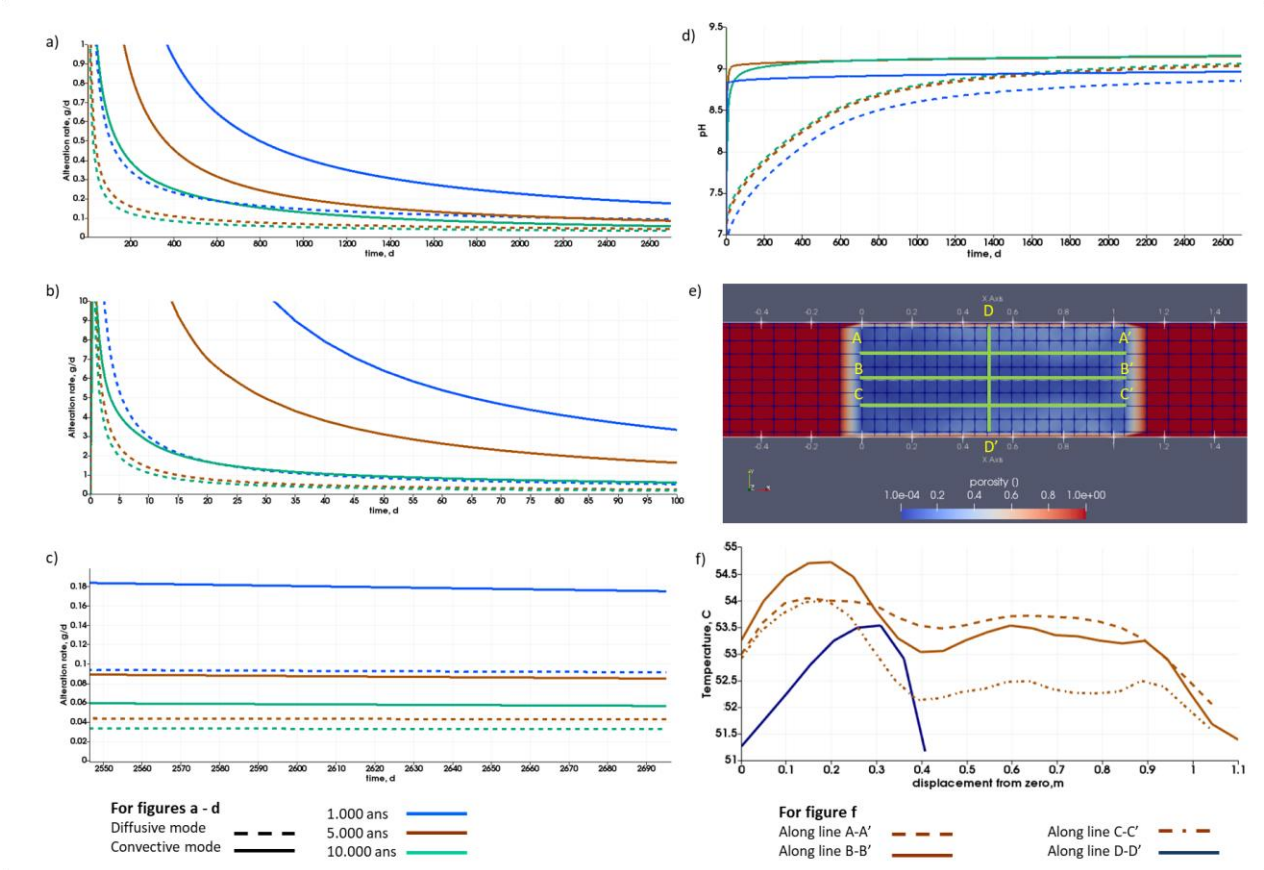

Figure 5-4 Results of the RTM for the cases "Convective 1,000" and "Diffusive 1,000" (time 0 in the simulation corresponds to canister failure after 1,000 y); "Convective 5,000" and "Diffusive 5,000" (time 0 in the simulation corresponds to canister failure after 5,000 y) ; "Convective 10,000" and "Diffusive 10 000" (time 0 in the simulation corresponds to canister failure after 10,000 y): a-c) rate of glass alteration obtained from boron concentration averaged over the water unit: for the first 2700 d, for the first 100 d, from 2560 to 2700 d, d) evolution of the solution pH, e) profiles of temperature for the case "Convective 1,000" after 150 d.

Evolution of three main parameters such as, the temperature distribution inside the canister, the rate of alteration obtained from the concentration of boron containing elements and the pH were looked at while analyzing the results. It was found that maximum difference between the walls of the canister and the center of the canister was equal to 3.2° C (54.7° C against 51.5° C) for the case "Convective 1,000" and 0.0105° C (29.0105° C against 29° C) for the case "Convective 10,000".

For the three treated cases (Convective 1,000; Convective 5,000; Convective 10,000), the calculated fluid flow was significant (Figure 5-5b) and led to the amplified solution homogenization and postponed the achievement of the solution saturation with respect to silica. In the end, it resulted in the prolongation of the initial dissolution rate regime. According to Figure 5-4, even for the case "Convective 10,000" with the smallest temperature gradient, during the first 500 days of alteration, the rate of alteration was three times higher for the case in convective mode compared to the diffusive mode. The transition from the initial dissolution rate regime to the residual dissolution rate regime lasted near 2000 d for

the case "Convective 10,000" in comparison to only 400 d for the case when only diffusive transport was modeled. As regards the value of the residual rate, it was close to 0.06 g/d for the case "Convective 10,000". Or, given that the fracturing ratio of the modeled glass canister is equal to 40.6 (Table 5-2), the residual rate amounted to ≈ 9E-04 g/m2/d. Regarding the case with the highest temperature gradient (assuming that ground water arrival time is 1000 y), the alteration rate was close to 2.7E-03 g/m2/d after 7 years of alteration.

Table 5-2 Calculation of 2D fracturing ratio

Parameter	Value
Length of fracture median axes, m	49.5
Perimeter, m	2.50
2D fracturing ratio	40.6
Block external surface, m^2	1.62
Block internal surface, m^2	64.3

Note to the Table 5-2: The fracturing ration was calculated as the ratio of the doubled total length of fracture median axes over the canister perimeter.

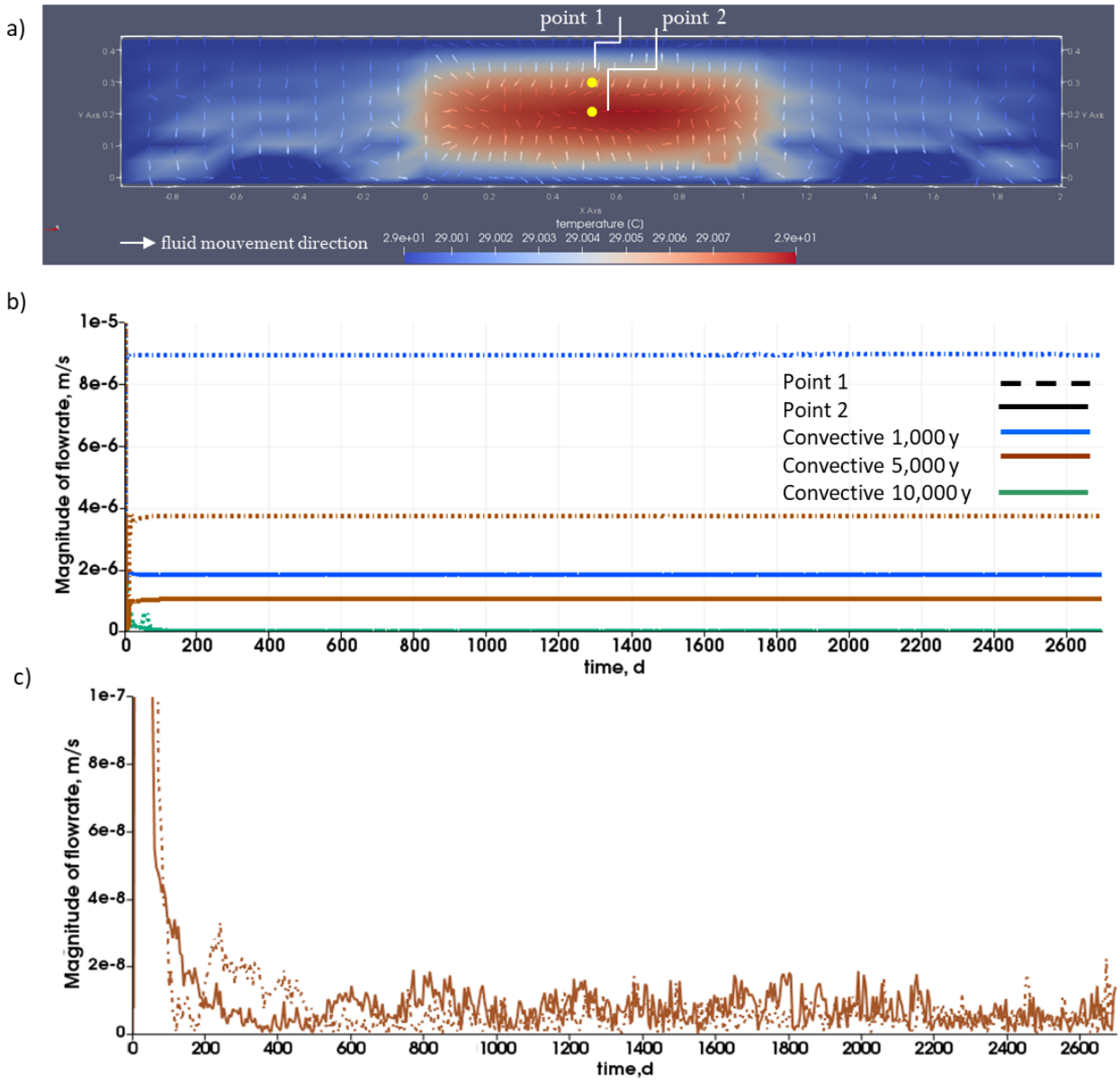

Figure 5-5 a) Modeled case "Convective 10.000", temperature distribution at 20th day from the beginning of the alteration when the system arrived at equilibrium, Rayleigh-Bénard cells originated due to the existence of the density gradient between the top and the bottom, gravity force acted against viscous force trying to pull the cooler, denser liquid from the top to the bottom; b) flowrate evolution for two points of the equivalent porous medium vs. time c) case "Convective 10.000", zoom on the flowrate evolution for two points of the equivalent porous medium vs. time

Dimensionless numbers Péclet and Damkhöler (Eq. from 5-1 to 5-3) are interesting means to identify the regime in the system, and compare the relative contributions of reaction kinetics, molecular diffusion and convection:

$$Pe = {}^{UL}/_{D} \quad 5\text{-}1,$$

$$Da = {}^{k}/_{U} \quad 5\text{-}2,$$

$$Pe \times Da = {}^{kL}/_{D} \quad 5\text{-}3,$$

where U is the velocity magnitude, L is the characteristic length taken equal to the radius of the modeled glass canister, D is the diffusion coefficient, k is the kinetic constant equal to the initial glass dissolution rate. Input parameters used of the computations are demonstrated in Table 5-3.

Table 5-3 Parameter values used to analyze the transport pattern via Damköhler and Péclet numbers.

Ground water arrival Mode	1 000 y	5 000 y	10 000 y
	Convective	Convective	Convective
Velocity magnitude (U, m/s)	1.80E-06	1.00E-06	1.00E-08
Characteristic length (L, m)	2.07E-01	2.07E-01	2.07E-01
Diffusion (D, m2/s)	5.00E-11	5.00E-11	5.00E-11
Kinetic constant (k, m/s)	1.12E-12	2.14E-13	1.44E-13
Damköhler (Da)	6.24E-07 < 1	2.14E-07 < 1	1.44E-05 < 1
Péclet (Pe)	7.44E+03 > 1	4.13E+03 > 1	4.13E+01 > 1
Product (Da × Pe)	4.65E-03 < 1	8.84E-04 < 1	5.95E-04 < 1
Influence order	Dissolusion < Diffusion< Convection		

The comparison of these dimensionless numbers at 1 000 y, 5 000 y and 10 000 y revealed that the convective effect on the solute transport was dominant in comparison to the molecular diffusion effect ($Pe > 1$). The effect of convection also dominated the dissolution effect (Da<1). Damköhler and Péclet product was lower than 1, which indicated that the reaction effect was subordinate in comparison to the diffusion effect. Overall, these findings were expected, taking in consideration the evolution of the QAG. There was an influence of the convective flow on the initial phase of glass alteration, this influence, however, becomes weaker with time once the solution becomes saturated with silica.

Nevertheless, it should be remembered that these findings should be taken with prudence. They are very likely to be only partially indicative of the glass corrosion in repository condition (even for the scenario of glass alteration in the saturated regime). Like discussed for the ALISE experiment, cautions should be exerted on these simulation results: complete repository conditions should incorporate exchange with COx water and more accurate description of the geometry and interfaces around the canister.

References

Abrajano, T., J. K. Bates, and C.D. Byers. 1986. 'Aqueous corrosion of natural and nuclear waste glasses I. Comparative rates of hydration in liquid and vapor environments at elevated temperatures', *Journal of Non Crystalline Solids*, 84: 251-57.

Abrajano, T.A., Jr., J.K. Bates, and J.J. Mazer. 1989. 'Aqueous corrosion of natural and nuclear waste glasses. II. Mechanisms of vapor hydration of nuclear waste glasses', *Journal of Non-Crystalline Solids*, 108: 269-88.

Advocat, Dussossoy, and Petitjean. 2008. 'Vitrification des déchets radioactifs', *Techniques de l'ingénieur Cycle du combustible nucléaire : combustibles usés et déchets radioactifs*, base documentaire : TIB457DUO.

Al-Kharusi, Anwar S., and Martin J. Blunt. 2008. 'Multiphase flow predictions from carbonate pore space images using extracted network models', *Water Resources Research*, 44.

ANDRA-Collectif. 2016. "Dossier d'options de sûreté - Partie après fermeture (DOS-AF)." In, 1-467. ANDRA.

ANDRA. 2005a. "Dossier 2005 Argile - Tome Architecture et Gestion du Stockage Géologique." In, edited by ANDRA, 1-497.

———. 2005b. "Dossier 2005 Argile - Tome Évolution Phénoménologique du Stockage Géologique." In, edited by ANDRA, 1-523.

———. 2010. "2006 - 2009 - 4 ans de recherches scientifiques à l'Andra pour les projets de stockage." In, edited by ANDRA, 1-48.

———. 2013. 'Projet Cigéo : Revues techniques de préparation à la Demande d'Autorisation de Création (DAC) Revue Finale des Modèles et des Données - première partie (RFMD-1) : Bilan des connaissances phénoménologiques et incertitudes résiduel'.

———. 2016. 'Rapport Andra CG-TE-D-NTE-AMOA-SR1-0000-15-0060 – « Dossier d'options de sûreté - Partie exploitation »'.

andra.fr, collectif. "Site internet de l'ANDRA." In.

Anton, François, Darka Mioc, and Christopher Gold. 2009. 'The Voronoi Diagram of Circles and Its Application to the Visualization of the Growth of Particles.' in Marina L. Gavrilova and C. J. Kenneth Tan (eds.), *Transactions on Computational Science III* (Springer Berlin Heidelberg: Berlin, Heidelberg).

Aréna, H., N. Godon, D. Rébiscoul, P. Frugier, and R. Podor, Garcès, E., Cabie, M., Mestre, J. P. 2017. 'Impact of iron and magnesium on glass alteration: Characterization of the secondary phases and determination of their solubility constants', *Applied Geochemistry*, 82: 119-33.

Arena, Helene. 2016. *Effets cumulatifs et compétitifs des éléments chimiques sur l'altération des verres nucléaires*.

Barth, N, D. George, S. Ahzi, Y. Rémond, V. Doquet, F. Bouyer, and S. Bétremieux. 2012. 'Modeling and simulation of the cooling process of borosilicate glass', *Journal of Engineering Materials and Technology*, 134: 041001.1-01.10.

Barth, N., D George, S. Ahzi, Y. Rémond, N. Joulaee, M.A. Khaleel, and F. Bouyer. 2014. 'Simulation of cooling and solidification of three-dimensional bulk borosilicate glass: effect of structural relaxations', *Mechanics of Time-Dependent Materials*, 18: 81-96.

Barth, Nicolas. 2013. 'Sur la modélisation et la simulation du comportement mécanique endommageable de verres borosilicatés sous sollicitation thermique', Université de Strasbourg.

Battiato, Ilenia, Daniel M. Tartakovsky, Alexandre M. Tartakovsky, and Timothy Scheibe. 2011. *Hybrid models of reactive transport in porous and fractured media*.

Beckingham, L., C. Peters, W. Um, K. Jones, and W. Lindquist. 2013. *2D and 3D imaging resolution trade-offs in quantifying pore throats for prediction of permeability*.

Begg, S., R. R. Carter, and P. Dranfield. 1989. *Assigning effective values to simulator grid-block parameters*.

Berkowitz, B. 2002. 'Characterizing flow and transport in fractured geological media: A review', *Advances in Water Ressources*, 25: 861-84.

Beucher, S. 1982. "Watersheds of functions and picture segmentation." In *ICASSP '82. IEEE International Conference on Acoustics, Speech, and Signal Processing*, 1928-31.

Beucher, Serge. 1994. 'Digital skeletons in Euclidean and geodesic spaces', *Signal Processing*, 38: 127-41.

Bock, Helmut et al. 2010. 'Self-sealing of Fractures in Argillaceous Formations in the Context of Geological Disposal of Radioactive Waste'.

Bonniaud, R., A. Jouan, and C. Sombret. 1980. 'Large scale production of glass for high level radioactive waste', *Nuclear and Chemical Waste Management*, 1: 3-16.

Bourbiaux B., Basquet R., Cacas M-C, Sarda S. 2002. 'An Integrated Workflow to Account for Multi-Scale Fractures in Reservoir Simulation Models: Implementation and Benefits', *Conference and oil show*.

Bouyer, F, Véronique Doquet, Céline Mallet, Nicolas Barth, Emmanuelle Chabert, Neji Ben Ali, Andrei Constantinescu, Jérôme Fortin, Yves Guéguen, Daniel George, Yves Rémond, and Saïd Ahzi. 2014. "Synthèse sur la fracturation thermomécanique des verres R7T7 - Bilan du programme 2011-2014." In, edited by CEA, 1-201.

Cailleteau, C. 2008. 'Influence de la morphologie du gel sur la cinétique d'altération des verres nucléaires: rôle du calcium et du zirconium.', Thèse de l'école polytechnique de Paris.

Carl I. Steefel, Lauren E. Beckingham, Gautier Landrot. 2015. 'Micro-Continuum Approaches for Modeling Pore-Scale Geochemical Processes', *Reviews in Mineralogy and Geochemistry*, 80: 217-46.

Carrière, C. 2017. 'Influence de la corrosion du fer sur les processus d'altération du verre : approche analytique multi-échelle.', Université Pierre et Marie Curie - Paris VI.

Caubit, C., G. Hamon, A. P. Sheppard, and P. E. Øren. 2009. 'Evaluation Of The Reliability Of Prediction Of Petrophysical Data Through Imagery And Pore Network Modelling', *Petrophysics*, 50: 13.

Chatterjee, Snehamoy, Ashis Bhattacherjee, Biswajit Samanta, and Samir Kumar Pal. 2010. 'Image-based quality monitoring system of limestone ore grades', *Computers in Industry*, 61: 391-408.

Chomat, L. 2008. 'Compréhension de l'altération à long terme des colis de verre R7T7 : étude du couplage chimie transport dans un milieu fissuré', Université Paris VI.

Christian, Thiery. 2013. 'Tomographie à rayons X', *Techniques de l'ingénieur CND : méthodes globales et volumiques*, base documentaire : TIB585DUO.

Christie, M. A. 1996. 'Upscaling for Reservoir Simulation', *Journal of Petroleum Technology*, 48: 1004-10.

Crevoisier, D., F. Bouyer, and S. Gin. 2011. 'Semi-stochastic generator (FRAGMA) of 2D fractured media by mechanistic analogy. Application to reactive transport in a fractured package of vitrified nuclear waste', *Computational Materials Science*, 50: 1387-98.

Cushman, John H., Lynn S. Bennethum, and Bill X. Hu. 2002. 'A primer on upscaling tools for porous media', *Advances in Water Resources*, 25: 1043-67.

Cvetkovic, Vladimir, S. Painter, N. Outters, and J. O. Selroos. 2004. 'Stochastic simulation of radionuclide migration in discretely fractured rock near the Aspo Hard Rock Laboratory', *Water Resources Research*, 40: W02404.

Davy, Philippe, Olivier Bour, Jean-Raynald de Dreuzy, and Caroline Darcel. 2006. *Flow in multiscale fracture networks*.

De Chiffre, L., Simone Carmignato, J. P. Kruth, Robert Schmitt, and Albert Weckenmann. 2014. *Industrial applications of computed tomography*.

de Combarieu, G. 2007. 'Altération du verre de confinement de déchets type R7T7 en condition de stockage géologique.', Université Paris XI - UFR Scientifique d'Orsay.

de Dieuleveult, C., J. Erhel, and M. Kern. 2009. 'A global strategy for solving reactive transport equations', *Journal of Computational Physics*, 228: 6395-410.

de Dreuzy, Jean-Raynald. 2008. 'Modélisation des écoulements et du transport dans les milieux fortement hétérogènes et fracturés - Mémoire HDR', Université de Rennes 1.

de Marsily, G. 1986. 'Quantitative Hadrogeology: Groundwater Hydrology for Engineers'.

De Windt, Laurent, Rabia Badreddine, and Vincent Lagneau. 2007. 'Long-term reactive transport modelling of stabilized/solidified waste: from dynamic leaching tests to disposal scenarios', *Journal of Hazardous Materials*, 139: 529-36.

Debure, M., P. Frugier, L. De Windt, and S. Gin. 2012. 'Borosilicate glass alteration driven by magnesium carbonates', *Journal of Nuclear Materials*, 420: 347-61.

Deng, H. 2009. 'Upscaling Reactive Transport Parameters for Porous and Fractured Porous Media', *Dissertation*.

Dran, J.C., G. Della Mea, A. Paccagnella, J.C. Petit, and Laurent Trotignon. 1988. 'The aqueous dissolution of alkali silicate glasses : reappraisal of mechanisms by H and Na depth profiling with high energy ion beams', *Physics and Chemistry of Glasses*, 29: 249-55.

Dube, Martine, Veronique Doquet, Andrei Constantinescu, Daniel George, Yves Remond, and Said Ahzi. 2010. 'Modeling of thermal shock-induced damage in a borosilicate glass', *Mechanics of Materials*, 42: 863-72.

Durlofsky, Louis J. 1991. 'Numerical calculation of equivalent grid block permeability tensors for heterogeneous porous media', *Water Resources Research*, 27: 699-708.

Einstein. A., Fürth. R. 1956. 'Investigations on the theory of Brownian movement'.

Fernàndez-Garcia, Daniel, Tissa H. Illangasekare, and Harihar Rajaram. 2005. 'Differences in the scale dependence of dispersivity and retardation factors estimated from forced-gradient and uniform flow tracer tests in three-dimensional physically and chemically heterogeneous porous media', *Water Resources Research*, 41.

Flusser, Jan, Barbara Zitova, and Tomas Suk. 2009. *Moments and Moment Invariants in Pattern Recognition* (Wiley Publishing).

Fournier, M. 2015. 'Etude des mécanismes à l'origine des reprises d'altération. Modélisation et évaluation de l'impact sur les verres de confinement.', Université de Montpellier.

Fournier, M., S. Gin, and P. Frugier. 2014. 'Resumption of nuclear glass alteration: State of the art', *Journal of Nuclear Materials*, 448: 348-63.

Frugier, P., T. Chave, S. Gin, and J.E. Lartigue. 2009. 'Application of the GRAAL Model to Leaching Experiments with SON68 Nuclear Glass in Initially Pure Water', *Journal of Nuclear Materials*, 392: 552-67.

Frugier, P., S. Gin, Y. Minet, T. Chave, B. Bonin, N. Godon, J.E. Lartigue, P. Jollivet, A. Ayral, L. De Windt, and G. Santarini. 2008. 'SON68 Nuclear glass dissolution kinetics: Current state of knowledge and basis of the new GRAAL model', *Journal of Nuclear Materials*, 380: 8-21.

Frugier, P., Gin, S., Minet, Y., Chave, T., Bonin, B., Godon, N.,Lartigue, J.E., Jollivet, P., Ayral, A., De Windt, L., Santarini, G. 2008. 'SON68 Nuclear glass dissolution kinetics: Current state of knowledge and basis of the new GRAAL model', *Journal of Nuclear Materials*, 380: 8-21.

Frugier, Pierre, Yves Minet, Natarajan Rajmohan, Nicole Godon, and Stéphane Gin. 2018. 'Modeling glass corrosion with GRAAL', *npj Materials Degradation*, 2: 35.

Geisler, T., A. Janssen, D. Scheiter, T. Stephan, J. Berndt, and A. Putnis. 2010. 'Aqueous corrosion of borosilicate glass under acidic conditions: A new corrosion mechanism', *Journal of Non-Crystalline Solids*, 356: 1458-65.

Geuzaine, Christophe, and Jean Francois Remacle. 2009. 'Gmsh: A 3-D finite element mesh generator with built-in pre- and post-processing facilities', *International Journal for Numerical Methods in Engineering*, 79: 1309-31.

Ghogomu, N. F., and René Therrien. 2000. *Reactive mass transport modeling in discretely-fractured porous media*.

Gin, S., A. Abdelouas, L.J. Criscenti, W.L. Ebert, K. Ferrand, T. Geisler, M.T. Harrison, Y. Inagaki, S. Mitsui, K.T. Mueller, J.C. Marra, C.G. Pantano, E.M. Pierce, J.V. Ryan, J.M. Schofield, C.I. Steefel, and J.D. Vienna. 2013. 'An international initiative on long-term behavior of high-level nuclear waste glass', *Materials Today*, 16: 243-48.

———. 2013. 'An international initiative on long-term behavior of high-level nuclear waste glass', *Materials Today*, 16: 243-48.

Gin, S., X. Beaudoux, F. Angeli, C. Jegou, and N. Godon. 2012. 'Effect of composition on the short-term and long-term dissolution rates of ten glasses of increasing complexity from 3 to 30 oxides', *Journal of Non-Crystalline Solids*, 358: 2559-70.

Gin, S., and J.P. Mestre. 2001. 'SON 68 nuclear glass alteration kinetics between pH 7 and pH 11.5', *Journal of Nuclear Materials*, 295: 83-96.

Glassley, William, John Nitao, and Charles Grant. 2003. *Three-dimensional spatial variability of chemical properties around a monitored waste emplacement tunnel*.

Godon, N. 2004. "Dossier de Référence sur le Comportement à Long Terme des Verres Nucléaires." In, edited by CEA, 292.

Godon, N., S. Peuget, F. Bouyer, F. Angeli, S. Depierre, O. Pinet, M. Tribet, B. Boizot, J.M. Delaye, J.L. Dussossoy, N. Ollier, S. Gin, C. Jégou, and Ribet I. 2012. "Référentiel scientifique sur le comportement à long terme des déchets vitrifiés : résultats de la R&D menée en collaboration avec les producteurs de déchets." In, edited by CEA, 1-425.

Goebbels, J., P. Reimers, M. Aouri, P. Jollivet, E. Vernaz, C. Lierse, K. Krebs, E. Kaciniel, and W. Stöwer. 1998. "Non-destructive examination of nuclear radioactive waste packages by advanced radiometric methods." In, edited by Commission européene, 97.

Gouze, Philippe, and Linda Luquot. 2011. 'X-ray microtomography characterization of porosity, permeability and reactive surface changes during dissolution', *Journal of Contaminant Hydrology*, 120-121: 45-55.

Grambow, B., and R. Muller. 2001. 'First-order dissolution rate law and the role of surface layers in glass performance assessment', *Journal of Nuclear Materials*, 298: 112-24.

Guy, Lauriat, and Gobin Dominique. 2008. 'Convection naturelle Cas particuliers', *Techniques de l'ingénieur Modélisation mécanique*, base documentaire : TIB400DUO.

Hellmann, R., S. Cotte, E. Cadel, S. Malladi, L.S. Karlsson, S. Lozano-Perez, M. Cabie, and A. Seyeux. 2015. 'Nanometre-scale evidence for interfacial dissolution-reprecipitation control of silicate glass corrosion', *Nature Materials*, 14: 307-11.

Hornung, Ulrich (ed.)^(eds.). 1997. *Homogenization and porous media* (Springer-Verlag).

Hudson, Gordon. 1993. 'Kriging Temperature in Scotland using the External Drift Method.' in Amilcar Soares (ed.), *Geostatistics Tróia '92: Volume 1* (Springer Netherlands: Dordrecht).

J. Bourbiaux, B., M. C. Cacas, S. Sarda, and J. C. Sabathier. 1997. *A Fast and Efficient Methodology to Convert Fractured Reservoir Images Into a Dual-Porosity Model*.

Jan Flusser, Tomas Suk, Barbara Zitova. 2016. '2D and 3D Image Analysis by Moments', *Book*.

Jegou, C., S. Gin, and F. Larche. 2000. 'Alteration kinetics of a simplified nuclear glass in an aqueous medium: effects of solution chemistry and of protective gel properties on diminishing the alteration rate', *Journal of Nuclear Materials*, 280: 216-29.

Jercinovic, M.J., S.A. Kaser, R.C. Ewing, and W. Lutze. 1990. 'Comparison of surface layers formed on synthetic basaltic glass, French R7T7 and HMI borosilicate nuclear waste form glasses-materials interface interactions tests, Waste Isolation Pilot Plant.' in V.M. Oversby and P.W. Brown (eds.), *Scientific Basis for Nuclear Waste Management XIII* (Mater. Res. Soc: Pittsburgh, PA, USA).

Jollivet, P, P. Frugier, G. Parisot, J.-P. Mestre, E. Brackx, S. Gin, and S. schumacher. 2012. 'Effect of clayey groundwater on the dissolution rate of the simulated nuclear waste glass SON68', *Journal of Nuclear Materials*, 420: 508-18.

Jouini, M. S., S. Vega, and E. A. Mokhtar. 2011. 'Multiscale characterization of pore spaces using multifractals analysis of scanning electronic microscopy images of carbonates', *Nonlin. Processes Geophys.*, 18: 941-53.

Kang, Qinjun, Peter C. Lichtner, and Dongxiao Zhang. 2007. 'An improved lattice Boltzmann model for multicomponent reactive transport in porous media at the pore scale', *Water Resources Research*, 43.

Kang, Qinjun, Dongxiao Zhang, and Shiyi Chen. 2003. 'Simulation of dissolution and precipitation in porous media', *Journal of Geophysical Research: Solid Earth*, 108.

King, P. R. 1989. 'Transp Porous Med', *Kluwer Academic Publishers*.

Lagneau, V. 2013a. *Développement d'un module écoulements densitaires dans Hytec*.

———. 2013b. 'Simulation of coupled geochemical reactions and hydynamical processes in porous media -- application to CO2 storage and Uranium exploitation', Université Pierre et Marie Curie - Paris VI.

———. 2014. "Gestion fine pas de temps et sorties dans HYTEC." In, 1-13.

Lagneau, Vincent, and Jan van der Lee. 2010. *Operator-splitting-based reactive transport models in strong feedback of porosity change: The contribution of analytical solutions for accuracy validation and estimator improvement*.

Lantuejoul, Christian. 2002. 'Geostatistical Simulation: Models and Algorithms'.

Lichtner, Peter. 2000. *Critique of dual continuum formulations of multicomponent reactive transport in fractured porous media*.

Lichtner , Steefel, Oelkers. 1996. *Reactive Transport in Porous Media* (Mineralogical Society of America).

Lubarda, Vlado A., and Yujia Liu. 2011. 'Areal moments of inertia revisited: on the distinction between the principal directions', *Archive of Applied Mechanics*, 81: 111-22.

MacQuarrie, K.T.B., and K.U. Mayer. 2005. 'Reactive transport modeling in fractured rock: A state-of-the-scieence review', *Earth-science Reviews*, 72: 189-227.

Manneville. 2006. 'Rayleigh-Bénard Convection: Thirty Years of Experimental, Theoretical, and Modeling Work.'.

Matheron, G. 1967. 'Eléments pour une théorie des milieux poreux'.

Meakin, Paul, and Alexandre M. Tartakovsky. 2009. 'Modeling and simulation of pore-scale multiphase fluid flow and reactive transport in fractured and porous media', *Reviews of Geophysics*, 47.

Minet, Y., B. Bonin, S. Gin, and P. Frugier. 2010. 'Analytic implementation of the GRAAL model: Application to a R7T7-type glass package in a geological disposal environment', *Journal of Nuclear Materials*, 404: 178-202.

Minet, Y., JL. Chouchan, and JP. Mestre. 2013. "Altération du bloc SON68 01FID07/2 dans Alise à 106°C: résultats de l'essai longue durée (7,5 ans) et observations post mortem." In, edited by CEA, 1-67.

Minet, Y., and N. Godon. 1999. "Synthèse des connaissances sur la fracturation des blocs de verre de type R7T7 et AVM." In, edited by CEA, 1-53.

———. 2003. "Leaching full-scale fractured glass blocks." In *American Ceramic Society - 104th meeting*, 275-82.

Mitra, Partha P., Pabitra N. Sen, and Lawrence M. Schwartz. 1993. 'Short-time behavior of the diffusion coefficient as a geometrical probe of porous media', *Physical Review B*, 47: 8565-74.

Moncouyoux, J.P., A. Aure, and C. Ladirat. 1991. "Investigation of full scale high-level waste containment glass blocks - Task 3 : Characterization of radioactive waste forms - A series of final reports (1985-89)-N°24." In, edited by Commission of the European Communities, 1-91.

Moynihan, Cornelius T., Allan J. Easteal, Mary A. DeBolt, and Joseph Tucker. 1976. 'Dependence of the Fictive Temperature of Glass on Cooling Rate', *Journal of the American Ceramic Society*, 59: 12-16.

Mualem, Yechezkel. 1976. 'A new model for predicting the hydraulic conductivity of unsaturated porous media', *Water Resources Research*, 12: 513-22.

Nakashima, Yoshito, Tsukasa Nakano, Koichi Nakamura, Kentaro Uesugi, Akira Tsuchiyama, and Susumu Ikeda. 2004. 'Three-dimensional diffusion of non-sorbing species in porous sandstone: computer simulation based on X-ray microtomography using synchrotron radiation', *Journal of Contaminant Hydrology*, 74: 253-64.

Narayanaswamy, O.S. 1971. 'A Model of Structural Relaxation in Glass', *Journal of the American Ceramic Society*, 54: 491-98.

Neill, Lindsey, Stéphane Gin, Thomas Ducasse, Trilce De Echave, Maxime Fournier, Patrick Jollivet, Alkiviadis Gourgiotis, and Nathalie A. Wall. 2017. 'Various effects of magnetite on international simple glass (ISG) dissolution: implications for the long-term durability of nuclear glasses', *npj Materials Degradation*, 1: 1.

neimagazine.com, collectif of. 2011. 'cold crucible retrofit', *site of Nuclear Engineering International*.

Neuman, Shlomo P. 1990. 'Universal scaling of hydraulic conductivities and dispersivities in geologic media', *Water Resources Research*, 26: 1749-58.

Noetinger, B. 1994. 'The effective permeability of a heterogeneous porous media', *Transp. Porous Media*: 99-127.

Nœtinger, B., and T. Estebenet. 2000. 'Up-Scaling of Double Porosity Fractured Media Using Continuous-Time Random Walks Methods', *Transport in Porous Media*, 39: 315-37.

Noetinger, B., Roubinet, D., Russian, A. et al. 2016. 'Random Walk Methods for Modeling Hydrodynamic Transport in Porous and Fractured Media from Pore to Reservoir Scale', *Transp Porous Med*.

Nos, Jeremy, Vincent Lagneau, and Valérie Langlais. 2011. *Reactive transport upscaling at the Darcy scale: A new flow rate based approach raises the unsolved issue of porosity upscaling*.

Nykyri, M., H. Nordman, J. Loefman, A. Poteri, N. Marcos, and A. Hautojorvi. 2008. "Radionuclide release and transport RNT-2008." In, 164. Finland.

Ougier-Simonin, Audrey. 2010. 'Propriétés mécaniques et de transport des verres fissurés', Université Denis Diderot - Paris 7.

Pajot, Hevre. 2002. ' Analytic Capacity, Rectifiability, Menger Curvature and the Cauchy Integral.', *Lecture Notes in Mathematics*, Springer, Berlin, Heidelberg.

Perez, Jr.J.M., and J.H.Jr. Westsik. 1989. "Effects of cracks on glass-leaching." In, edited by PNL, 1-19.

Pierce, Eric M., Pierre Frugier, Louise J. Criscenti, Kideok D. Kwon, and Sebastien N. Kerisit. 2014. 'Modeling Interfacial Glass-Water Reactions: Recent Advances and Current Limitations', *International Journal of Applied Glass Science*, 5: 421-35.

Promentilla, M. A. B., T. Sugiyama, T. Hitomi, and N. Takeda. 2009. 'Quantification of tortuosity in hardened cement pastes using synchrotron-based X-ray computed microtomography', *Cement and Concrete Research*, 39: 548-57.

Rebiscoul, D., F. Rieutord, F. Né, P. Frugier, R. Cubitt, and S. Gin. 2007. 'Water penetration mechanisms in nuclear glasses by X-ray and neutron reflectrometry.', *Journal of Non-Crystalline Solids*, 353: 2221-30.

Rébiscoul, Diane, Burger, Emilien, Bruguier, Florence, Godon, Nicole, Chouchan, Jean-Louis, Mestre, Jean-Pierre, Frugier, Pierre, Lartigue, Jean-Eric, Gin, Stephane. 2013. 'Glass-Iron-Clay interactions in a radioactive waste geological disposal: a multiscale approach', *MRS Proceedings*, 1518: 185-90.

Renard, P. 1997a. 'Modélisation des écoulements en milieux poreux hétérogènes', Paris Mines.

Renard P., de Marsily G. . 1997. 'Calculating equivalent permeability: a review', *Advances in Water Resources*, 20: 253-78.

Renard, P., de Marsily, G. 1997b. 'Calculating equivalent permeability: a review', *Advances in Water Resources*, 20: 253-78.

Renard, P., G. Le Loc'h, E. Ledoux, G. Marsily, and R. Mackay. 2000. 'A fast algorithm for the estimation of the equivalent hydraulic conductivity of heterogeneous media', *Water Resources Research*, 36: 3567-80.

Repina, M. 2016. 'Reactive transport modelling in the glass cracks media'.

Savoye, S., C. Imbert, A. Fayette, and D. Coelho. 2014. 'Experimental study on diffusion of tritiated water and anions under variable water-saturation and clay mineral content: comparison with the Callovo-Oxfordian claystones', *Geological Society, London, Special Publications*, 400: 579-88.

Savoye, S., J. Page, C. Puente, C. Imbert, and D. Coelho. 2010. 'New experimental approach for studying diffusion through an intact and unsaturated medium: a case study with Callovo-Oxfordian argillite', *Environ Sci Technol*, 44: 3698-704.

Sen, P. 2004. 'Time‐dependent diffusion coefficient as a probe of geometry', *Concepts in Magnetic Resonance Part A*, 23A: 1-21.

Sené, M.R., M. Bailey, B. Illerhaus, J. Goebbels, O. Haase, A. Kulish, and J.L. Chouchan. 1999. "Characterisation of accessible surface area of HLW glass monoliths by high energy accelerator tomography and comparison with conventional techniques." In, edited by European Commission, 1-99.

Serra, J. 1969. 'Introduction à la Morphologie Mathématique', *Cahiers du Centre de Morphologie Mathématique*: 160.

———. 1982. 'Image Analysis and Mathematical Morphology', *Academic Press*.

Soille, Pierre. 2003. *Morphological Image Analysis: Principles and Applications* (Springer-Verlag New York, Inc.).

Steefel, C., L. Beckingham, and G. Landrot. 2015. 'Micro-Continuum Approaches for Modeling Pore-Scale Geochemical Processes', *Reviews in Mineralogy and Geochemistry*, 80: 217-46.

Steefel, C., Beckingham, L., Landrot G. 2015. 'Micro-Continuum Approaches for Modeling Pore-Scale Geochemical Processes', *Reviews in Mineralogy and Geochemistry*, 80: 217-46.

Steefel, C. I., C. A. J. Appelo, B. Arora, D. Kalbacher, O. Kolditz, V. Lagneau, P. C. Lichtner, K. U. Mayer, J. C. L. Meeussen, S. Molins, D. Moulton, D. Shao, J. Simunek, N. Spycher, S. B. Yabusaki, and G. T. Yeh. 2015. 'Reactive transport codes for subsurface environmental simulation', *Computational Geosciences*, 19: 445-78.

Steefel, C.;, S.; Molins, and D. Trebotich. 2013. *Pore Scale Processes Associated with Subsurface CO2 Injection and Sequestration*.

Steefel, Carl I., Donald J. DePaolo, and Peter C. Lichtner. 2005. 'Reactive transport modeling: An essential tool and a new research approach for the Earth sciences', *Earth and Planetary Science Letters*, 240: 539-58.

Steefel, Carl, and Antonio Lasaga. 1994. *A Coupled Model for Transport of Multiple Chemical-Species and Kinetic Precipitation Dissolution Reactions with Application to Reactive Flow in Single-Phase Hydrothermal Systems*.

Sterpenich, J. 1998. 'Altération des vitraux médiévaux - Contribution à l'étude du comportement à long terme des verres de confinement', Doctorat, Université Henri Poincaré.

Tokan-Lawal, Adenike, Maša Prodanović, and Peter Eichhubl. 2015. 'Investigating flow properties of partially cemented fractures in Travis Peak Formation using image-based pore-scale modeling', *Journal of Geophysical Research: Solid Earth*, 120: 5453-66.

Trotignon, L., V. Devallois, H. Peycelon, C. Tiffreau, and X. Bourbon. 2007a. 'Predicting the long term durability of concrete engineered barriers in a geological repository for radioactive waste', *Physics and Chemistry of the Earth, Parts A/B/C*, 32: 259-74.

Trotignon, L., V. Devallois, H. Peycelon, C. Tiffreau, and Xavier Bourbon. 2007b. *Predicting the long term durability of concrete engineered barriers in a geological repository for radioactive waste*.

van der Lee, J. 1998. "Thermodynamic and mathematical concepts of CHESS." In, edited by Ecole des Mines de Paris and Fontainebleau.

Van der Lee, Jan, Laurent De Windt, Vincent Lagneau, and Patrick Goblet. 2003. 'Module-oriented modeling of reactive transport with HYTEC', *Computers & Geosciences*, 29: 265-75.

Vernaz, Etienne. 2009. 'Nuclear Waste Conditioning', *CEA DFN Monographs*.

Vernaz, Étienne, and Jérôme Bruezière. 2014. 'History of Nuclear Waste Glass in France', *Procedia Materials Science*, 7: 3-9.

Verney-Carron, A. 2009. 'Etude d'analogues archéologiques pour la validation des modèles de comportement à long terme des verres nucléaires', Institut national polytechnique de Lorraine.

Verney-Carron, A., S. Gin, and G. Libourel. 2008. 'A fractured roman glass block altered for 1800 years in seawater: Analogy with nuclear waste glass in a deep geological repository', *Geochimica et Cosmochimica Acta*, 72: 5372-85.

Weinan E., and Bjorn E. 2003. 'The Heterognous Multiscale Methods', *Commun. Math. Sci.*, 1: 87-132.

Whitaker, Stephen. 1967. 'Diffusion and dispersion in porous media', *AIChE Journal*, 13: 420-27.

Wood, Brian D., Fabien Cherblanc, Michel Quintard, and Stephen Whitaker. 2003. 'Volume averaging for determining the effective dispersion tensor: Closure using periodic unit cells and comparison with ensemble averaging', *Water Resources Research*, 39.

www.bp.com. 2017. 'BP Statistical Review of World Energy'.

Xiao, Y.; Whitaker, F.; Xu, T.; Steefel, C. 2018. 'Reactive Transport Modeling: Applications in Subsurface Energy and Environmental Problems ': 540.

Zhang, Chun-Liang. 2018. 'Thermo-hydro-mechanical behavior of clay rock for deep geological disposal of high-level radioactive waste', *Journal of Rock Mechanics and Geotechnical Engineering*.

Zhou, Quanlin; Liu, Hui Hai; Molz, Fred J. et al. 2008. 'Field-Scale Effective Matrix Diffusion Coefficient for Fractured Rock: Results From Literature Survey'.

Chapter 6: Discussions, perspectives

Résumé du chapitre

Dans ce chapitre, la question de l'applicabilité du modèle dans le contexte du stockage des blocs de verre fracturé contenant les déchets nucléaires de haute activité est posée. Nous mettons en évidence les problèmes techniques rencontrés lors de l'application de la méthodologie et nous réfléchissons sur la possibilité d'évolution de cette méthodologie pour qu'elle puisse, premièrement, être élargie vers le 3D et, deuxièmement, prendre en compte des conditions de stockage plus réalistes que celles modélisées dans cette thèse.

6. Discussions, perspectives

6.1. Back to the industrial objectives

In view of the results presented in the preceding sections, it is possible to argue that the proposed image processing-based fracture network characterization workflow elaborated for the purpose of RTM applied to a block of vitrified nuclear glass allows us (i) to unite hard data obtained by direct measurement of the fracture network and soft physics-based explanatory data, (ii) to considers the variability in the fracture network, (iii) to create a defendable model that represents glass fracture network as a homogenized porous medium, (iv) to decrease the computational effort needed to solve complex transport-flow-chemistry interactions, (v) to account for thermo-convection at the scale of the glass canister, (vi) to obtain results compatible with experimental data. Undoubtedly, glass fracture network characterization and modeling efforts are significant; the proposed methodology offers the industry an excellent opportunity to better understand and quantify the impact of fracturing on the corrosion of nuclear glass.

However, this methodology and/or the presented applications have some weak points that could be important to consider in the future.

In Section 5.1-5.2 it was mentioned that the quality of the blocks used as test-beds for the application of the first part of the methodology had some issues. Indeed, in the future it is recommended to improve preparation of new canisters and ensure preservation of the fracture network during their cutting. In addition, with a view to expand towards 3D modelling, analysis of the fracturing on transversal cuttings will be mandatory: after preparation of the cuttings, the analysis can be performed using the same techniques (Section 5.1 - 5.2). Some adaptations will need to be performed: as indicated in Section 3.2.3, as per the date of the thesis writing, the anisotropic Voronoï tessellation used to create realizations of fracture network equivalent tessellation is only available in 2D. 3D tessellation of equivalent fracture network can be performed based on the knowledge of position of cell centers and scaling factors in 3 directions and, maybe, some supplementary hypothesis, *e.g.* that fracture planes grow radially toward the canister axis. Overall, it should be feasible, given that the techniques of the 3D Voronoï tessellation construction are well-established (Ledoux 2007; Okabe et al. 1992).

On top of that, when the preservation of the fracture networks will be ensured, it will be essential to take photos of higher resolution, *i.e.* to work on the reconstruction of multiple photos with the ambition to be able to capture finer fractures. The fact that some trustworthy data on additional fractures is included would (i) help mitigate the issue of the REV size selection, (ii) avoid the necessity of making the assumption of the tortuosity isotropy of the inner canister part, (iii) could potentially improve the regression between the values of the proxy model variables (thermo-mechanical data of the arrival times of the solidification front, curvature of the solidification front lines etc.) and the data obtained through image analysis, that could open some new potentials to the geostatistical modeling.

Regarding the use of the 3D model in the HYTEC reactive transport code, it is neither possible at the time of the thesis writing, because the vertex centered scheme has not yet been coded in 3D in HYTEC. However, it should not bring any serious problem, because the whole structure of HYTEC code is fully adapted for being functional in 3D. Nevertheless, it will be necessary to ensure that HYTEC version is stable and capable of performing RTM in 3D with the considered initial and limiting conditions.

As it was seen in the previous chapter, the intensity of the glass alteration was characterized by the quantity of altered glass that could potentially release from the canister over time. However, to date, no link between the quantity of altered glass and the quantity of radionuclides[35] that could possibly be liberated from the glass matrix has been discussed. Indeed, this point is still unclear. According to the current (high level) vitrified waste alteration model, presented by ANDRA (CG.NT.ASCM.16.0009), radionuclide release is considered congruent, that is, radionuclides are expected to go into solution at the same rate than tracer elements at both initial and residual rate regimes. This statement is however disputable because the experimental data show that certain elements, including the actinides are well retained in the alteration film (Godon et al. 2012; Jollivet 1998) – in a way, the congruent dissolution hypothesis is at least conservative in terms of radionuclide release. The retention rates of rare earths and actinides are highly dependent on pH, Eh, solution composition and composition of the alteration layer. Nevertheless, at the time of writing, there is no single clear vision on the related processes and potential complexing agents that could be present in solution in repository conditions. That is why no position was taken during this study to estimate radionuclide release based on mass of altered glass.

The objective of the proposed methodology is to give a quantitative assessment of the degradation of glass fractured canister and of the release of radionuclides under different scenarios of evolution, bridging the gap between laboratory scale and geological repository. That is, it is only focused on the study of the interactions of water with one isolating barrier – glass matrix. However, as per the adopted multi-barrier disposal concept, in the long run, a

[35] In the nominal composition of R7T7 French nuclear glass, fission products and actinide oxides make up 13,7 % by weight, while in the SON68 nominal composition simulated fission products and actinide oxides amounts to 10.7 7 % by weight.

whole series of engineered and natural barriers (clay, container, buffer material around the container, metal envelops, sealing systems), should be considered, as they will work together to contain and isolate fission products and actinide from the environment. That means that the proposed model represents a first constituting element of the bigger model that should integrate major barriers together and account for the interactions between them. Reactive transport codes (and modelers) are well prepared to perform this task: several interfaces are already well studied so far, so that integrating several zones with different properties around the model of fracture glass would be facilitated. Some specific problems concern (i) the alteration of the borosilicate glass in presence of elements of the nearby field, *i.e.* iron of the overpack, silica and aluminum or calcium and magnesium from clay of the COx, (ii) the transport of the alteration products with the COx water, and (iii) mechanisms of glass alteration and solutes migration in presence of hydrogen originated from radiolysis or corrosion of the overpacks.

Finally, in-depth reflection on the interaction scenario should be carried out: particularly time of the package corrosion (and correlated heat power of the waste), water saturation in the various components of the storage at that time.

The above-enumerated phenomena are considered separately and are discussed in the following Section.

6.2. From laboratory scale (micrometer, months/years) to block scale (meter, n×10,000's years)

In Section 5, some applications of the methodology were demonstrated. It was seen that several environmental conditions (T from 25 to 90°C, source term, static *vs* dynamic hydrological regimes of glass alteration) were possible to take into account. In general, it was noted that the progress of alteration of the glasses of the chosen composition depends on environmental conditions (pH, temperature, water renewal). Nevertheless, as mentioned in the discussion part of the second article, the shown applications represent only one part of the integrated modeling that will be necessary to consider in the future. In addition to the considered glass-water interactions in saturated flow regime under different T, pH conditions, the effect of the species in solution (e.g. Ca, Mg, Fe of COx water), the effect of the non-saturated conditions (due to the anoxic corrosion of the cell metal liner and the overpacks of the canisters), possible effect of glass fracture clogging by precipitation of clay mineral etc. could be integrated in the model in the future.

In fact, in the last several years, studies aiming at the understanding of phenomena covering conditions representative of the geological storage, particularly clay medium, have been initiated. They showed that initial dissolution rate measured in COx water in renewal condition was up to five times higher than that measured in pure water, mainly because of the presence of calcium (Dove et al. 1997; Jollivet, Gin, et al. 2012); internal CEA

communication, Jollivet, 2011. The explanation of this increase was related to the formation of sites making the Si-O bonds of glass broken more easily. At the same time, the evidence was provided that at basic pH, calcium tends to integrate into the alteration gel and to reduce the transport (Mercado-Depierre et al. 2013; Chave et al. 2011). The dissolution rate decrease occurs more quickly and more efficient in the presence of calcium (Jegou 1998; Gin et al. 2001; Godon et al. 2012). Also, it was demonstrated that the pH of the COx water and the availability of magnesium in solution affect the rate drop regime and the value of the residual rate. Thus, according to (Jollivet, Frugier, et al. 2012; Aréna et al. 2017; Debure et al. 2012), the precipitation of secondary magnesium phases sustains the dissolution of the passivating layer of the glass, lowers the pH, and as a consequence, increases the diffusivity of this protective interphase. Authors also showed that the precipitation of magnesium phases is not limited by their precipitation kinetics, but is rather controlled by their solubility and the release rate of silicon from glass dissolution. Regarding iron effect, it was argued (de Combarieu et al. 2011; Rébiscoul 2013) that its incorporation in the alteration layer is penalizing, *i.e.* it tends to deplete the alteration gel and to remove its passivating property. Moreover, iron presence fosters glass alteration by means of precipitation of iron silicate species (Aréna et al. 2017; Dillmann et al. 2016). In fact, it was demonstrated that the formation of these newly formed phases modifies the chemical equilibrium in the aqueous solution, consumes silicon and, as a consequence, increases the glass alteration.

Given these results, it is clear that the reactivity and the transport of elements of the surrounding components to the glass canister field could have a significant impact on the long-term behavior of the glass and thereby, should be considered in the integrated model.

In the proposed model, glass alteration was supposed isovolumetric, *i.e.* dissolved glass is considered replaced by the alteration layer of same volume and no feedback of minerals precipitation or dissolution in fractures was taken into account. That, however, could be debatable, given some demonstrations (Bock 2010; ANDRA-Collectif 2016) that in presence of free water argillaceous material tends to increase its volume and, by consequence, clogs partially or entirely pores and fractures of the host-rock (clay). Likewise, glass fracture clogging could also result from the precipitation of secondary phases rich in elements of the COx water, like evidenced on natural glass corrosion (Verney-Carron 2009).

Aside from these geochemical interactions of glass corrosion products with the elements of the nearby field, the question of the hydrological regime that would occur in repository conditions is worth addressing. Although at this stage all scenarios (normal evolution, altered evolution and "What-if" scenario) proposed by ANDRA consider the solute transport by water in saturated condition, the elaboration of the scenario that will include the transient regime (hydraulic-gas) is envisaged for the DAC (demande d'autorisation de creation). It is important because the geological repository is likely to stay for a long time in non-saturated conditions: primarily due to the long time of resaturation of the vicinity of the storage, and the counter-effect of H_2 gas production by radiolysis and anoxic corrosion of metal

components. Thus, according to ANDRA, the formation of hydrogen will slow the resaturation of the storage. With respect to their first estimations, the resaturation could last around 100,000 years for the HL zone and a few hundred thousand years for the medium level waste (ML) area. In this connection, the following questions have to be tackled before being able to conduct RTM of borosilicate glass alteration in transient regime:

1. How and at what speed will the resaturation of the HL compartment and, in particular, HL canisters take place?
2. How interfaces can modify locally capillary forces and influence liquid water transfer and distribution between tiny (10 nm) pore host-rock, bentonitic cement filling, corroded liner and overpack, and small (μm) to medium size (mm) fractures?
3. How will water come in contact with glass canister (what will its state be: fine recondensed layer covering fractures walls *vs*. vapor)? What are the mechanisms and the principal driving forces of glass alteration of such alteration?
4. What will the temperature be when water comes into contact of the glass?

As for the first two questions, the preparation of its answer is ongoing (ANDRA-Collectif 2016), it will be based on the knowledge gained on hydrogen production (that is a function of corrosion rate that, in its turn, depends on the presence of liquid water or vapor and temperature) as well as gas transfer characteristics in different storage areas and their possible interfaces. First estimations (ANDRA 2013) indicate that in HL zone the saturations will evolve from the initial saturation, close to 70% to 80% to reach a complete saturation towards 40.000 years to 50.000 years after the storage closure.

Regarding the last two questions, the reaction of glass with water vapor has been studied in Argonne National laboratory (ANL), PacificNorthwest National Laboratory (PNNL), Savannah River Laboratory (SRL) and are currently under study in French Alternative Energies and Atomic Energy Commission (CEA), Orano, Subatech, French National Research Agency (ANR), etc. So far, it is acknowledged that the scientific database on the vapor hydration of nuclear glasses has still the potential to be enlarged. According to the current vision, the precipitation of secondary phases seems to be the strongest driving force for alteration in vapor phase at high temperature (Abrajano et al. 1986; Abrajano et al. 1989); internal CEA communications Narayanasamy, 2017, 2018. Indeed, at high temperatures and low solution volume that gets saturated rapidly, the conditions are thermodynamically favorable for the precipitation of secondary phases. As for the question whether, from the chemical perspective, the glass corrosion process can be emulated by an aqueous solution with a high S/V ratio, at the time of writing there is no single opinion. The answer will decide whether the current version of the GRAAL model could be applied to model glass corrosion in vapor phase or not (whether it will be equal to modeling with high S/V or it will be necessary to adapt the geochemical model). In any case, once the scenario treating the transient regime is established, data about relative permeability, capillary pressure, saturation of both wetting (water) and non-wetting (gas) phases will be requested firstly, for

the COx clay, then for all barriers, glass fracture network included. Afterwards, it will be necessary to think about the techniques that could be applied to perform permeability and effective diffusion upscaling (Savoye et al. 2014; Savoye et al. 2010; Mualem 1976; Crotti et al. 2003; Fouda 2016) at the scale of one block and for the ensemble of glass canister surrounding materials.

To sum up, the proposed image processing-based fracture network characterization workflow was elaborated for the purpose of RTM applied to a block of vitrified nuclear glass. It allowed us to unite data obtained by image analysis and by thermo-mechanical simulations with the aim of creating multiple realizations of glass fracture network. It focused on the upscaling of the reactive transport parameters, such as permeability, diffusion and parameters governing the kinetics of glass dissolution in the context of the equivalent porous media approach. It enabled the modeling of glass aqueous alteration by taking into account fracture network variability and different limiting conditions. The results obtained by applying the workflow are totally in agreement with the experimental results of alteration of a vitrified glass block. Although, it concerned only the interactions of water with the borosilicate glass, it could be potentially expanded in order to be able to consider diverse interactions of the glass with the other barriers of the repository.

References

Abrajano, T., J. K. Bates, and C.D. Byers. 1986. 'Aqueous corrosion of natural and nuclear waste glasses I. Comparative rates of hydration in liquid and vapor environments at elevated temperatures', *Journal of Non Crystalline Solids*, 84: 251-57.

Abrajano, T.A., Jr., J.K. Bates, and J.J. Mazer. 1989. 'Aqueous corrosion of natural and nuclear waste glasses. II. Mechanisms of vapor hydration of nuclear waste glasses', *Journal of Non-Crystalline Solids*, 108: 269-88.

ANDRA-Collectif. 2016. "Dossier d'options de sûreté - Partie après fermeture (DOS-AF)." In, 1-467. ANDRA.

ANDRA. 2013. 'Projet Cigéo : Revues techniques de préparation à la Demande d'Autorisation de Création (DAC) Revue Finale des Modèles et des Données - première partie (RFMD-1) : Bilan des connaissances phénoménologiques et incertitudes résiduel'.

Aréna, H., N. Godon, D. Rébiscoul, P. Frugier, and R. Podor, Garcès, E., Cabie, M., Mestre, J. P. 2017. 'Impact of iron and magnesium on glass alteration: Characterization of the secondary phases and determination of their solubility constants', *Applied Geochemistry*, 82: 119-33.

Bock, Helmut et al. 2010. 'Self-sealing of Fractures in Argillaceous Formations in the Context of Geological Disposal of Radioactive Waste'.

CG.NT.ASCM.16.0009, Note Andra. 'Comportement des déchets en stockage - Modèles de relâchement des radionucléides'.

Chave, T., P. Frugier, S. Gin, and A. Ayral. 2011. 'Glass-water interphase reactivity with calcium rich solutions', *Geochimica and Cosmochimica Acta*, 75: 4125-39.

Crotti, M. A., and R. H. Cobenas. 2003. "Upscaling of Relative Permeability Curves for Reservoir Simulation: An Extension to Areal Simulations Based on Realistic Average Water Saturations." In *SPE Latin American and Caribbean Petroleum Engineering Conference*, 6. Port-of-Spain, Trinidad and Tobago: Society of Petroleum Engineers.

de Combarieu, G., M. Schlegel, D. Neff, E. Foy, D. Vantelon, P. Barboux, and S. Gin. 2011. 'Glass-iron-clay interactions in a radioactive waste geological disposal : An Integrated laboratory-scale expériment', *Applied Geochemistry*, 26: 65-79.

Debure, M., P. Frugier, L. De Windt, and S. Gin. 2012. 'Borosilicate glass alteration driven by magnesium carbonates', *Journal of Nuclear Materials*, 420: 347-61.

Dillmann, P., S. Gin, D Neff, D. Rebiscoul, and L GENTAZ. 2016. 'Effect of natural and synthetic iron corrosion products on silicate glass alteration processes', *Geochimica et Cosmochimica Acta*: 287-305.

Dove, P.M., and C.J. Nix. 1997. 'The influence of the alkaline earth cations, magnesium, calcium, and barium on the dissolution kinetics of quartz', *Geochimica et Cosmochimica Acta*, 61: 3329-40.

Fouda, Mohamed Ali Gomaa. 2016. 'Relative permeability upscaling for heterogeneous reservoir models'.

Gin, S., and C. Jegou. 2001. "Limiting mechanisms of borosilicate glass alteration kinetic:effect of glass composition." In *Water-Rock Interaction*, edited by A.A. Balkema, 279-82. Vilasimius, Italie.

Godon, N., S. Peuget, F. Bouyer, F. Angeli, S. Depierre, O. Pinet, M. Tribet, B. Boizot, J.M. Delaye, J.L. Dussossoy, N. Ollier, S. Gin, C. Jégou, and Ribet I. 2012. "Contribution CEA au référentiel de comportement des déchets vitrifiés." In, edited by CEA, 1-503.

Jegou, C. 1998. 'Mise en évidence expérimentale des mécanismes limitant l'altération du verre R7T7 en milieu aqueux. Critique et proposition d'évolution du formalisme cinétique.', Montpellier II.

Jollivet, P, P. Frugier, G. Parisot, J.-P. Mestre, E. Brackx, S. Gin, and S. schumacher. 2012. 'Effect of clayey groundwater on the dissolution rate of the simulated nuclear waste glass SON68', *Journal of Nuclear Materials*, 420: 508-18.

Jollivet, P. 1998. "Synthèse des connaissances sur les gels nucléaires R7T7." In, edited by CEA, 1-36.

Jollivet, P., S. Gin, and S. Schumacher. 2012. 'Forward dissolution rate of silicate glasses of nuclear interest in clay-equilibrated groundwater', *Chemical Geology*, 330: 207-17.

Ledoux, Hugo. 2007. *Computing the 3D Voronoi Diagram Robustly: An Easy Explanation*.

Mercado-Depierre, S., F. Angeli, F. Frizon, and S. Gin. 2013. 'Antagonist effects of calcium on borosilicate glass alteration', *Journal of Nuclear Materials*, 441: 402-10.

Mualem, Yechezkel. 1976. 'A new model for predicting the hydraulic conductivity of unsaturated porous media', *Water Resources Research*, 12: 513-22.

Okabe, Atsuyuki, Barry Boots, and Kokichi Sugihara. 1992. *Spatial tessellations: concepts and applications of Voronoi diagrams* (John Wiley \& Sons, Inc.).

Rébiscoul, Diane, Burger, Emilien, Bruguier, Florence, Godon, Nicole, Chouchan, Jean-Louis, Mestre, Jean-Pierre, Frugier, Pierre, Lartigue, Jean-Eric, Gin, Stephane. 2013. 'Glass-Iron-Clay interactions in a radioactive waste geological disposal: a multiscale approach', *MRS Proceedings*, 1518: 185-90.

Savoye, S., C. Imbert, A. Fayette, and D. Coelho. 2014. 'Experimental study on diffusion of tritiated water and anions under variable water-saturation and clay mineral content: comparison with the Callovo-Oxfordian claystones', *Geological Society, London, Special Publications*, 400: 579-88.

Savoye, S., J. Page, C. Puente, C. Imbert, and D. Coelho. 2010. 'New experimental approach for studying diffusion through an intact and unsaturated medium: a case study with Callovo-Oxfordian argillite', *Environ Sci Technol*, 44: 3698-704.

Verney-Carron, A. 2009. 'Etude d'analogues archéologiques pour la validation des modèles de comportement à long terme des verres nucléaires', Institut national polytechnique de Lorraine.

RÉSUMÉ

Comprendre l'altération du verre nucléaire dans un réseau de fracture au sein d'un bloc de verre vitrifié est important pour la sûreté du conditionnement des déchets nucléaires (quantification des risques associés au relâchement des radionucléides). L'évaluation de la performance du stockage géologique des déchets nucléaires passe obligatoirement par la modélisation de l'altération aqueuse d'un bloc de verre nucléaire fracturé, l'échelle de temps envisagée (plusieurs milliers d'années) dépassant toute possibilité d'expérience directe. Cette thèse vise donc à combler le fossé entre les simulations d'écoulement et de transport à l'échelle du réservoir et la modélisation à l'échelle micrométrique des processus interfaciaux verre-eau, en apportant l'évaluation quantitative de la dégradation aqueuse du verre à l'échelle d'un bloc.

Pour aborder ce problème, les objectifs principaux de cette thèse ont été fixés comme suit : (i) la reproduction des résultats expérimentaux obtenus précédemment (pour quelques fractures modélisées de manière discrète en mode diffusif), (ii) l'analyse de l'impact des géométries de fractures sur la quantité de verre altéré pour quelques fissures modélisées de manière discrète, (iii) l'étude de la possibilité d'adaptation du modèle géochimique à la modélisation dans le cadre de l'approche milieu équivalent, (iv) la mise au point d'une méthodologie de caractérisation, (v) la modélisation géostatistique et géométrique de réseau de fractures à l'échelle d'un conteneur de verre, (vi) le calcul des paramètres équivalents diffusifs, hydrauliques et les paramètres qui contrôlent la cinétique de dissolution de verre, et au final, (vii) la modélisation de transport réactif à l'échelle d'un conteneur.

À titre illustratif, la méthodologie de la caractérisation de réseau fracturé proposée, basée sur le traitement des images, a été appliquée aux images bidimensionnelles (2D) de haute résolution de deux blocs de verre. Cette application a permis de mettre en œuvre à la fois les données directes obtenues par mesures des paramètres d'un réseau fracturé de verre vitrifié et les données indirectes explicatives issues des simulations thermomécaniques. L'application a abouti à la création de multiples réalisations de tessellation de réseaux fracturés équivalents qui ont ensuite été utilisées comme représentations physiques pour les calculs de la perméabilité équivalente, de la diffusion équivalente et des paramètres contrôlant la cinétique de dissolution de verre borosilicaté. L'évolution de la quantité de verre altéré obtenue en effectuant la modélisation de transport réactif appliquée à plusieurs réalisations de la tessellation de réseau fracturé équivalent a été comparée aux données expérimentales d'un essai d'altération aqueuse d'un conteneur non radioactif de verre nucléaire. Les résultats montrent que la méthodologie conçue offre une opportunité pour mieux comprendre l'impact de la fracturation sur l'altération aqueuse du verre vitrifié et constitue un outil fiable permettant de prendre en compte différents scénarios d'évolution du stockage.

MOTS CLÉS

Modélisation, corrosion du verre nucléaire, réseau de fractures, analyse d'images, changement d'échelle, milieu poreux équivalent

ABSTRACT

Understanding the alteration of nuclear glass in a fracture network of a vitrified glass block is important for the safe conditioning of nuclear waste (quantification of the risks associated with radionuclide release). Performance assessment of geological nuclear waste repositories entails modelling of the long-term evolution of the fractured nuclear glass block aqueous alteration, because the considered time scale, of several thousands of years, is beyond the range of any direct experimental perspectives. This dissertation aims then to bridge the gap between the reservoir-scale flow and transport simulations and the micron-scale modeling of the glass-water interfacial processes, by bringing the quantitative evaluation of the glass aqueous degradation at the block scale.

To tackle this issue, the main objectives of this thesis were fixed as follows: (i) reproduction of the experimental results previously obtained (for some fractures modeled in a discrete way in the diffusive mode), (ii) analysis of the impact of fractures geometries on the quantity of altered glass at the scale of some fractures modeled in a discrete way, (iii) investigation of the possibilities of the geochemical model adaptation for the equivalent homogenous modeling, (iv) establishment of a methodology for glass block fracture network characterization, (v) geostatistical and geometric modeling, (vi) calculation of the equivalent diffusive, hydraulic and glass dissolution kinetics controlling properties and (vii) upcoming reactive transport modeling at the scale of one canister.

As an illustrative example, the proposed image processing-based fracture network characterization methodology was applied to two-dimensional (2D) high-resolution images of two blocks of vitrified glass. This application brought into service both hard data obtained by direct measurement of the fracture network and soft physics-based explanatory data and resulted in the creation of multiple realizations of fracture network equivalent tessellation that were further used as physical representation for the calculation of the equivalent hydraulic, diffusive, and alteration kinetics - controlling properties. The evolution of the quantity of altered glass obtained by conducting reactive transport modeling applied to several realizations of the equivalent fracture network tessellation was compared with the experimental data of the aqueous alteration test of a non-radioactive full-scale nuclear glass canister. The results show that implementation of the devised procedure presents an opportunity for better understanding the

KEYWORDS

Modeling, nuclear glass corrosion, fracture network, image analysis, upscaling, equivalent porous medium